Universidade do Estado do Rio de Janeiro
Centro de Tecnologia e Ciências
Faculdade de Geologia

Bárbara Santos Queiroz

Processos petrogenéticos e geodinâmicos relacionados às seções magmáticas de poços na Bacia de Santos

Rio de Janeiro
2025

Bárbara Santos Queiroz

Processos petrogenéticos e geodinâmicos relacionados às seções magmáticas de poços na Bacia de Santos

Tese apresentada, como requisito parcial para obtenção do título de Doutor, ao Programa de Pós-Graduação em Geociências, da Universidade do Estado do Rio de Janeiro. Área de concentração: Geociências.

Orientador: Prof. Dr. Anderson Costa dos Santos

Coorientadores: Prof.ª Dra. Monica da Costa Pereira Lavalle Heilbron

Prof. Dr. Sérgio de Castro Valente

Rio de Janeiro

2025

CATALOGAÇÃO NA FONTE
UERJ/REDE SIRIUS/CTCC

Q384 Queiroz, Bárbara Santos.
Processos petrogenéticos e geodinâmicos relacionados às seções magmáticas de poços na Bacia de Santos / Bárbara Santos Queiroz.– 2025.
128 f. : il.

Orientador: Anderson Costa dos Santos.
Tese (Doutorado) – Universidade do Estado do Rio de Janeiro, Faculdade de Geologia**.**

1. Vulcanismo – Teses. 2. Petrografia – Teses. 3. Magmatismo - Teses. 4. Geoquímica- Isótopos – Teses. 5. Gestão ambiental – Teses. I. Santos, Anderson Costa dos. II. Universidade do Estado do Rio de Janeiro. Faculdade de Geologia. III. Título.

CDU: 551.21

Bibliotecária Responsável: Priscila Freitas Araujo/ CRB-7: 7322

_____ _____

Assinatura Data

Bárbara Santos Queiroz

Processos petrogenéticos e geodinâmicos relacionados às seções magmáticas de poços na Bacia de Santos

Tese apresentada, como requisito parcial para obtenção do título de Doutor, ao Programa de Pós-Graduação em Geociências, da Universidade do Estado do Rio de Janeiro. Área de concentração: Geociências

Aprovada em 14 de Março de 2025.

Orientador: Prof. Dr. Anderson Costa dos Santos

Faculdade de Geologia - UERJ

Coorientadora: Prof.ª Dra. Monica da Costa Pereira Lavalle Heilbron

Faculdade de Geologia – UERJ

Prof. Dr. Sérgio de Castro Valente

Instituto de Geociências - UFRRJ

Banca Examinadora: _____

Prof. Dr. Lucas M. Rossetti

Faculdade de Geociências - UFMT

_____

Prof. Dr. Rommulo Vieira Conceição

Instituto de Geociências – UFRGS

_____

Prof. Dr. Valdecir de Assis Janasi

Instituto de Geociências – USP

_____

Prof. Dr. Egberto Pereira

Faculdade de Geologia – UERJ

_____

Prof. Dr. Sérgio Bergamaschi

Faculdade de Geologia – UERJ

Rio de Janeiro

2025

DEDICATÓRIA

Aos meus pais.

AGRADECIMENTOS

Agradeço aos meus pais, Vera e Demézio, por estarem sempre ao meu lado em todas as decisões que eu tomei. Desde escolher a geologia até ir para o outro lado do planeta. Obrigada por me ensinarem a ter resiliência. Obrigada por nunca desistirem da ideia de ter uma filha com ensino superior. Pai, obrigada por todas as noites intermináveis de trabalho no bar para sustentar a nossa casa e os nossos sonhos. Mãe, obrigada por cuidar das nossas vidas. Eu só cheguei até aqui porque tenho vocês.

Além do título, o doutorado me trouxe o Júlio, meu marido, amigo e colega de profissão. Obrigada, meu amor, por me ajudar a não desistir da ciência, por segurar na minha mão nas horas que precisei enfrentar meus monstros e por me exaltar sempre. Obrigada por todas as tardes e noites de conversas geológicas e vinho. Você tornou essa jornada mais fácil e mudou a minha vida.

Minhas amigas do LabMEG, Amanda Martoni, Edjane Silva, Giovana Medeiros, Mayara Reis e Victoria Verdugo, obrigada por todas as conversas, fofocas e risadas. Edjane, Gio, e Vic, muito obrigada por confiarem em mim a responsabilidade de orientá-las na iniciação científica e na monografia.

Agradeço aos meus orientadores Anderson Costa, Monica Heilbron e Sergio Valente pela orientação, pelas oportunidades dadas a mim e todo conhecimento transmitido.

Agradeço especialmente ao Valente por se tornar um grande amigo e por confiar tanto no meu trabalho. Aquece meu coração olhar para trás e ver que hoje eu trabalho com o professor que eu tanto admirava durante a graduação e que segue sendo a minha inspiração profissional. Eu aprendi muito e ainda tenho muito que aprender com você, SV. Uma vez meu pai me disse ‘Valente é um pai pra você e pro Júlio, né?’. Impossível discordar.

Por fim, agradeço à UERJ pela oportunidade de realizar o doutorado, bem como à CAPES pela bolsa de estudos. Agradeço ano CNPq e ao Instituto GeoAtlântico pela oportunidade do doutorado-sanduíche na Curtin University (Austrália). Agradeço ao LabMEG (UFRuralRJ) por toda estrutura e espaço concedidos. Agradeço ao Projeto EQUIMAG e à Empresa EQUINOR, pelo financiamento da pesquisa. Agradeço também à ANP pela disponibilidade do perfil composto e das amostras para a realização deste trabalho.

RESUMO

QUEIROZ, Bárbara Santos. **Processos petrogenéticos e geodinâmicos relacionados às seções magmáticas de poços na Bacia de Santos**. 2025. 150 f. Tese (Doutorado em Geociências) – Faculdade de Geologia, Universidade do Estado do Rio de Janeiro, Rio de Janeiro, 2025.

A Bacia de Santos é uma bacia de margem passiva localizada na margem sudeste do Brasil e detém as maiores reservas de óleo e gás do país. Eventos magmáticos vulcânicos e plutônicos são registrados nas fases rifte, pós-rifte e drifte da bacia. Este trabalho apresenta dados petrofísicos e petrográficos de seções magmáticas dos poços 6-BG-6P-SPS, 3-BRSA-1267A-RJS e 1-BRSA-886-RJS no intervalo pré-sal da Bacia de Santos, bem como novos dados geoquímicos, isotópicos e geocronológicos de amostras de rochas magmáticas do poço 6-BG-6P-SPS. A correlação entre os dados petrográficos e petrofísicos permitiu a identificação de eventos vulcânicos explosivos e efusivos félsicos e efusivos máficos no poço 6-BG-6P-SPS. Este é o primeiro registro de magmatismo félsico na Bacia de Santos. Adicionalmente, identificou-se ocorrência de vulcanismo subaquoso no poço 3-BRSA-1267A-RJS e magmatismo intrusivo pré-Albiano com feições cumuláticas no poço 1-BRSA-886-RJS. O poço 6-BG-6P-SPS registra eventos vulcânicos com idades entre 135 e 121 Ma. As rochas máficas e félsicas deste poço são subalcalinas, com afinidade toleítica. A análise de processos evolutivos indicou que as rochas vulcânicas ácidas e básicas do poço 6-BG-6P-SPS não são cogenéticas por cristalização fracionada ou AFC. A modelagem de processos evolutivos mostrou que pelo menos uma suíte básica evoluiu por cristalização fracionada com assimilação da crosta superior até composições intermediárias. A origem das rochas ácidas foi atribuída a processos de fusão parcial da crosta superior félsica. A modelagem de fusão parcial do manto permite concluir que a gênese das rochas básicas menos evoluídas e não contaminadas está relacionada a fontes mantélicas litosféricas e sublitosféricas de diferentes composições. As composições isotópicas (Sr-Nd-Pb) das rochas vulcânicas básicas, intermediárias e ácidas são condizentes com a participação de componente enriquecido do tipo EMII do manto litosférico subcontinental. A origem deste componente enriquecido foi atribuída aos processos de subdução dos vários ciclos de Wilson que culminaram com a amalgamação do Gondwana no Proterozoico e início do Fanerozoico. A modelagem de mistura binária corrobora a participação dos reservatórios mantélicos tipo pluma de Tristão da Cunha e EMII. Episódios de dois eventos vulcânicos máficos e félsicos registrados no poço 6-BG-6P-SPS impuseram diferentes regimes térmicos desde o Hauteriviano até o Aptiano que podem explicar algumas das características dos sistemas petrolíferos do pré-sal da Bacia de Santos.

Palavras-chave: Bacia de Santos; vulcanismo bimodal; magmatismo; vulcanismo; Tristão da Cunha; EMII; MLSC; petrofísica.

ABSTRACT

QUEIROZ, Bárbara Santos. **Petrogenetic and geodynamic processes related to magmatic sections of wells in the Santos Basin**. 2025. 150 f. Tese (Doutorado em Geociências) – Faculdade de Geologia, Universidade do Estado do Rio de Janeiro, Rio de Janeiro, 2025.

The Santos Basin is a passive margin basin located on the southeastern margin of Brazil and detain the largest reserves of oil and gas in the country. Volcanic and plutonic magmatic events are recorded in the rift, post-rift and drift phases of the basin. This work presents petrophysical and petrographic data from magmatic section of wells 6-BG-6P-SPS, 3-BRSA-1267A-RJS and 1-BRSA-886-RJS in the pre-salt sedimentary sequence of the Santos Basin, as well as new geochemical, isotopic and geochronological data from magmatic rock samples from well 6-BG-6P-SPS. The correlation between the petrographic and petrophysical data allowed the identification of explosive and effusive felsic and effusive mafic events in well 6-BG-6P-SPS. This is the first record of felsic magmatism in the Santos Basin. In addition, subaqueous volcanism was identify in well 3-BRSA-1267A-RJS and pre-Albian intrusive magmatism with cumulatic features in well 1-BRSA-886-RJS. Well 6-BG-6P-SPS records volcanic events with ages between 135 and 121 Ma. The mafic and felsic rocks of this well are subalkaline, with tholeiitic affinity. An analysis of evolutionary processes indicated that the acid and basic volcanic rocks of well 6-BG-6P-SPS are not cogenetic by fractional crystallization or AFC. Evolutionary process modelling showed that at least one basic suite evolved by fractional crystallization with upper crustal assimilation to intermediate compositions. The origin of the acid rocks was attributed to partial melting processes of the felsic upper crust. The partial melting modelling of the mantle allowed to conclude that the genesis of the least evolved and uncontaminated basic rocks is related to lithospheric and sublithospheric mantle sources of different compositions. The isotopic compositions (Sr-Nd-Pb) of the basic volcanic rocks, intermediate and acid rocks are consistent with the participation of an enriched EMII-type component of the subcontinental lithospheric mantle. The origin of this enriched component was attributed to the subduction processes of the Wilson Cycles that culminated in the amalgamation of Gondwana in the Proterozoic and early Phanerozoic. The binary mixing modelling corroborates the participation of Tristan da Cunha plume-type and EMII-type mantle reservoirs. Episodes of two mafic and felsic volcanic events recorded in well 6-BG-6P-SPS imposed different thermal regimes from the Hauterivian to the Aptian that may explain some characteristics of the pre-salt petroleum systems of the Santos Basin.

Keywords: Santos Basin; bimodal volcanism; magmatism; volcanism; Tristan da Cunha; EMII; SCLM; petrophysic

LISTA DE FIGURAS

LISTA DE TABELAS

SUMÁRIO

INTRODUÇÃO

Sistemas tectono-magmáticos em margens vulcânicas são formados a partir de interações entre a litosfera e a astenosfera antes, durante e depois da ruptura continental, com controles relevantes sobre a formação dos paleoambientes, a distribuição de recursos minerais e exploração de hidrocarbonetos (Eldholm *et al.*, 1995, 2000). O magmatismo em zonas de rifteamento continental, margens vulcânicas relacionadas e províncias de derrames de basalto continental (*Continental Flood Basalts* - CFB) envolve dinâmicas de convecção do manto e de *hotspot* sob vários regimes térmicos (Bailey, 1983; White & McKenzie, 1989; Eldholm & Grue, 1994; Nielsen & Hopper, 2002; Gholamrezaie *et al.*, 2018; Lu & Huismans, 2021). Por sua vez, os regimes térmicos evoluem durante os estágios sin-rifte e pós-rifte da ruptura continental e posterior deriva devido ao regime de extensão, espessura da camada sedimentar e migração da deformação, afetando a subsidência da bacia e a transição de bacias sedimentares do tipo rifte para o tipo de margem passiva (Wolfenden *et al.*, 2005; Armitage *et al.*, 2010; Levell *et al.*, 2010; Biari *et al.*, 2021; Stanton *et al.*, 2014; Pérez-Gussinyé *et al.*, 2024).

O acúmulo de sucessões sedimentares e magmáticas espessas durante o estágio pré-rifte e posterior evolução da bacia é muito reconhecido ao longo das margens vulcânicas do Atlântico Norte e Sul, bem como a correlação temporal entre o magmatismo onshore e offshore (Eldholm, 1991; Hinz *et al.*, 1993; Eldholm & Grue, 1994; Gladczenko *et al.*, 1997; Menzies *et al.*, 2002; Eide *et al.*, 2017a,b; Gordon *et al.*, 2023a; Ferreira *et al.*, 2023; He *et al.*, 2025). As bacias de margem passiva são amplamente exploradas por empresas de petróleo e gás em todo o mundo (por exemplo, Levell *et al.*, 2010; Pimentel & Reis, 2016; Zhixin *et al.*, 2016; Zalan, 2017; Schinteie *et al.*, 2023). Desta forma, o magmatismo se tornou um tópico relevante de estudo para exploração de petróleo e gás, considerando seus efeitos nos processos de geração, migração, armazenamento, aprisionamento e selagem em sistemas petrolíferos em bacias sedimentares em todo o mundo (Archer *et al.*, 2005; Senger *et al.*, 2017; Jackson *et al.*, 2020; Zeng *et al.*, 2023; Mangione *et al.*, 2024).

Diferentes configurações de *emplacement* (por exemplo, plutônico e vulcânico), bem como ambientes vulcânicos (por exemplo, subaéreos e subaquáticos; efusivos e explosivos) podem afetar as características das rochas do sistema petrolífero (Archer *et al.*, 2005; Senger *et al.*, 2017; Jackson *et al.*, 2020; Zeng *et al.*, 2023; Mangione *et al.*, 2024). Por exemplo, seções magmáticas em bacias sedimentares podem não ser reconhecidas usando métodos sísmicos, levando a uma subestimação volumétrica de rochas plutônicas e vulcânicas dentro de poços individuais (Poprawa *et al.*, 2023). Tais desafios foram parcialmente superados nos últimos anos pela correlação de

dados sísmicos 3D, experimentos de laboratório, dados petrofísicos de registros de poços e trabalho de campo que permitem a distinção entre fluxos basálticos vulcânicos espessos e intrusões de diferentes formas (Schofield *et al.*, 2016; Gao *et al.*, 2017; Muirhead *et al.*, 2017; Mark *et al.*, 2024).

Outro aspecto envolve a ascensão de CO_2 do manto da Terra e a coacumulação de CO_2 e petróleo bruto, a qual ocorre em larga escala na Bacia de Santos (Ferraz *et al.*, 2019; Freitas *et al.*, 2022). As causas que levaram à ocorrência de quantidades altamente variáveis de CO_2 em muitos campos de petróleo vizinhos à Bacia de Santos ainda são uma questão de debate (Gamboa *et al.*, 2019), apesar do consenso sobre a origem do CO_2 dentro do manto da Terra, similarmente a outras bacias em outras partes do mundo (Liu *et al.*, 2017; Zhu *et al.*, 2018; Liu *et al.*, 2023). O hidrotermalismo relacionado ao magma sob altos gradientes geotérmicos, além do afinamento regional da crosta, falhas profundas, alta densidade de falhas e intrusões ígneas estão entre os processos e parâmetros que desempenham um papel na ascensão do CO_2 do manto para a crosta e podem afetar a formação de reservatórios de hidrocarbonetos do pré-sal da Bacia de Santos (Farias *et al.*, 2019. Gamboa *et al.*, 2019; Freitas *et al.*, 2022; Yang *et al.*, 2022; Oliveira *et al.*, 2024; Plawiak *et al.*, 2024).

A origem da Bacia de Santos está relacionada aos processos de ruptura do Supercontinente Gondwana durante o Eocretáceo Inferior, que culminaram com a formação de uma margem vulcânica rifteada no sudeste do Brasil (Chang *et al.*, 1988; Cainelli & Mohriak, 1999; Moreira *et al.*, 2007). Abundantes rochas magmáticas plutônicas e vulcânicas máficas são intercalados com as rochas sedimentares do Pré-sal na Bacia de Santos (Louback *et al.*, 2021; 2023; Scribelk & Valente, 2023). No entanto, seções magmáticas em poços na Bacia de Santos são comumente descritas como rochas ígneas não discriminadas. O vulcanismo basáltico efusivo é o processo magmático pré-ruptura mais usual em margens vulcânicas, sendo o magmatismo bimodal raro (por exemplo, Morris *et al.*, 2024). O mesmo pareceu se aplicar à Bacia de Santos com base em publicações anteriores (Scribelk & Valente, 2023; Gordon *et al.*, 2023b).

Esta tese apresenta correlações entre dados petrográficos e petrofísicos de seções magmáticas de três poços do pré-sal: 6-BG-6P-SPS, 3-BRSA-1267A-RJS e 1-BRSA-886-RJS, perfurados em águas profundas nas porções central e norte da Bacia de Santos, SE do Brasil. Os poços compreendem seções com rochas magmáticas máficas plutônicas e vulcânicas, efusivas (subaéreas e subaquáticas), bem como rochas vulcânicas félsicas efusivas e explosivas. Adicionalmente, esta tese apresenta novos dados litogeoquímicos, isotópicos (Sr-Nd-Pb) e geocronológicos (U-Pb) obtidos para amostras recuperadas de uma seção magmática do poço 6-BG-6P-SPS (também conhecido como Corcovado 1). Este é o primeiro relato de vulcanismo

bimodal na Bacia de Santos, o qual possivelmente representa a porção offshore do magmatismo contemporâneo que ocorre na Província Magmática Paraná-Etendeka.

A abordagem petrofísica mostrou que litotipos máficos e félsicos podem ser discriminados por alguns dados geofísicos de poços, conforme proposto em trabalhos anteriores. Também foi possível discriminar rochas magmáticas plutônicas, bem como efusivas e explosivas vulcânicas, subaéreas e subaquáticas, baseado em uma abordagem qualitativa. E, desta forma, inferir paleoambientes vulcânicos associados aos diferentes eventos magmáticos. O estudo geoquímico apontou que as rochas vulcânicas félsicas e máficas na seção magmática do poço 6-BG-6P-SPS não são cogenéticas por nenhum processo de diferenciação possível. A modelagem geoquímica é consistente com a não cogeneticidade entre rochas máficas e félsicas e destacou o papel da crosta superior como contaminante dos líquidos básicos e fonte para rochas félsicas e ácidas, por meio de fusão parcial. O modelo geodinâmico proposto implica no envolvimento da pluma mantélica Tristão da Cunha e do reservatório mantélico EMII na gênese das rochas máficas básicas. As interações manto-crosta estabeleceram um regime térmico durante o Eocretáceo Inferior na área, o que pode explicar o hidrotermalismo variável, mas generalizado, e o influxo de CO_2 registrados ao longo da sequência sedimentar do pré-sal na Bacia de Santos.

1 **OBJETIVOS**

O objetivo geral da tese de doutorado é propor um modelo petrogenético para o magmatismo pré-Albiano de uma parte da Bacia de Santos. Os objetivos específicos incluem:

a) Avaliar se o modelo petrogenético é coerente com os modelos geodinâmicos existentes para a bacia ou propor cenários tectônicos alternativos;

b) Avaliar qualitativamente a correlação entre as propriedades petrofísicas de rochas vulcânicas e dados petrográficos, com foco em determinar possíveis padrões correspondentes de ambientes magmáticos.

2 **JUSTIFICATIVA**

A Bacia de Santos é foco de diversos estudos e o debate acerca da influência dos eventos magmáticos nos seus sistemas petrolíferos está em crescimento, devido ao seu elevado potencial petrolífero e por abranger a maior área do Pré-Sal do país (Souza & Sgarbi, 2019). Por exemplo, a condução térmica gerada a partir das câmaras magmáticas estacionadas no embasamento, bem como através das intrusões na sequência sedimentar, pode influenciar os processos de geração relacionados aos sistemas petrolíferos de bacias sedimentares e modificar propriedades petrofísicas das rochas selantes e reservatório na bacia. Além disso, é também possível que as características petrofísicas das rochas magmáticas reflitam as condições prevalecentes nos seus ambientes de formação e alocação (Thomaz Filho *et al.*, 2000; Thomaz Filho *et al.*, 2008; Miranda *et al.*, 2018; Cioccari & Mizusaki, 2019).

A despeito da sua importância, os processos petrogenéticos dos eventos magmáticos da Bacia de Santos ainda são pouco estudados. Estudos petrogenéticos foram realizados em poucas amostras da Formação Camboriú (fase rifte), sugerindo que a gênese desses basaltos toleíticos está associada à mistura de fonte empobrecida, N-MORB e uma fonte fértil, tipo pluma (Ascensão, Tristão da Cunha ou Bouvet; Fodor *et al.*, 1980; Fodor *et al.*, 1983; Fodor & Vetter, 1984). O papel das plumas mantélicas em modelos geodinâmicos propostos para o magmatismo do Eoceno Inferior ainda está em debate (Oreiro *et al.*, 2008; Louback *et al.*, 2021). No entanto, a escassez de publicações também se aplica aos estudos petrogenéticos para os eventos magmáticos das fases pós-rifte e drifte na Bacia de Santos.

3 **LOCALIZAÇÃO**

A Bacia de Santos está localizada na margem continental adjacente aos estados do Rio de Janeiro, São Paulo, Paraná e Santa Catarina, cobrindo uma área de aproximadamente 352.000 km² com mais de 10.000 m de rochas sedimentares (Abelha, 2017). Esta pesquisa conta com 3 poços, poço 6-BG-6P-SPS (Poço A), poço 3-BRSA-1267A-RJS (Poço B) e poço 1-BRSA-886-RJS (Poço C). Os poços, objetos desse estudo, estão situados nas porções norte e central da bacia (Figura 1).

O limite norte da Bacia de Santos é dado pelo Alto de Cabo Frio e o limite sul pelo Alto de Florianópolis (Figura 1), representando as fronteiras com as bacias de Campos e Pelotas, respectivamente. O limite oeste da bacia é dado pela Charneira de Santos (ou Charneira Cretácea, Figura 1), que corresponde a um sistema de falhamento normal que comporta a sedimentação Cretácea, com direção concordante com a linha de costa (Nunes *et al.*, 2004). Por fim, a bacia é limitada a leste pelo sopé do Platô de São Paulo em águas profundas (Figura 1). Essa feição fisiográfica corresponde a um arcabouço do embasamento, de natureza continental, reativado na fase rifte (Macedo, 1989; Dias, 1993).

Figura 1: Mapa de localização da Bacia de Santos, com o polígono do Pré-sal e a localização dos poços 6-BG-6P-SPS, 3-BRSA-1267A-RJS e 1-BRSA-886-RJS.

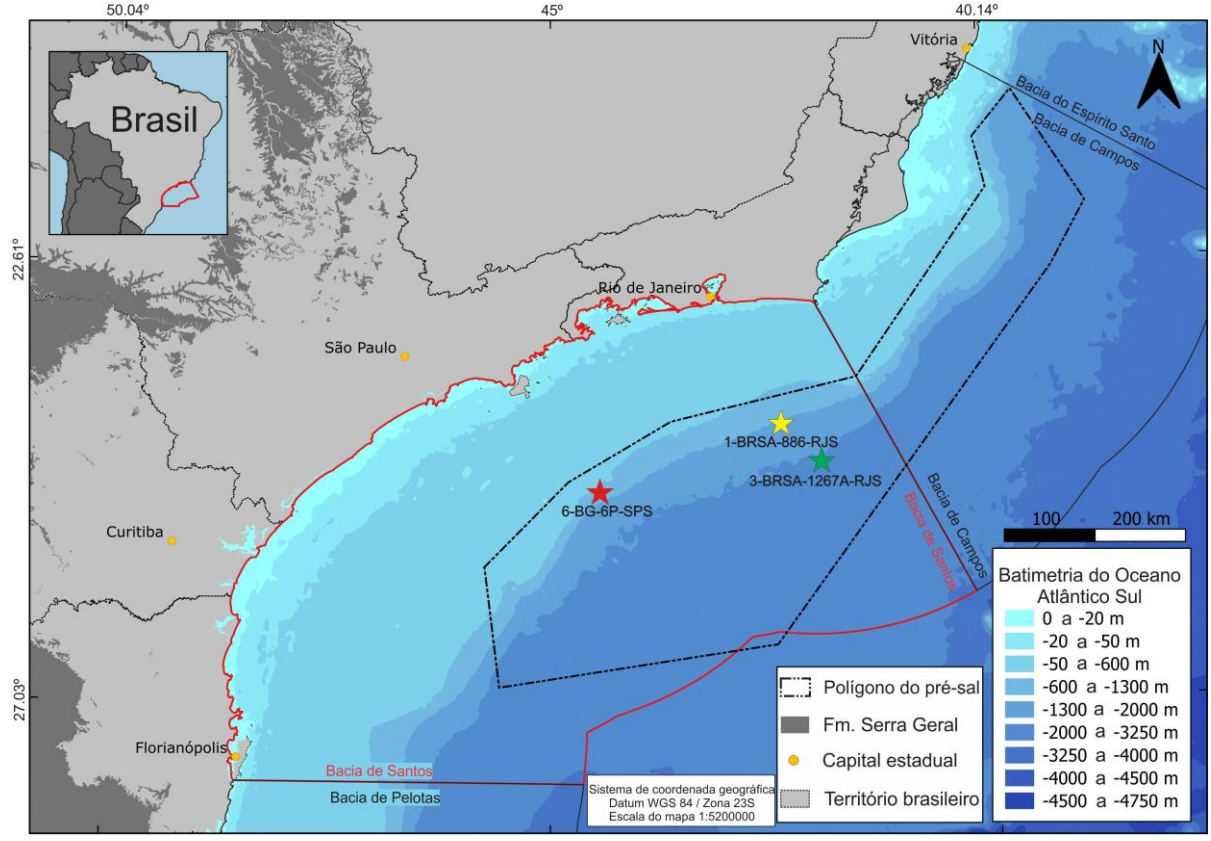

Fonte: A autora, 2025

4 MATERIAIS E MÉTODOS

A pesquisa está vinculada ao Projeto EQUIMAG do Laboratório de Modelagem e Evolução Geológica (LabMEG) da UFRuralRJ. As atividades realizadas, os métodos e materiais utilizados nesta pesquisa são descritos a seguir:

a) Obtenção de amostras e perfil composto: A etapa inicial da pesquisa consistiu na obtenção de perfis e amostras de seções magmáticas de poços exploratórios junto à Agência Nacional do Petróleo (ANP);

b) Levantamento bibliográfico: O levantamento bibliográfico consistiu na leitura de publicações técnico-científicas acerca das ferramentas e propriedades petrofísicas com foco em rochas ígneas, evolução cronoestratigráfica e tectônica da Bacia de Santos, bem como do magmatismo das fases rifte, pós-rifte e drifte da bacia;

c) Interpretação dos perfis compostos: Esta pesquisa conta com os poços 6-BG-6P-SPS (denominado Poço A no Artigo 1, Tópico 6.1), 3-BRSA-1267A-RJS (denominado Poço B no Artigo 1, Tópico 6.1) e poço 1-BRSA-886-RJS (denominado Poço C no Artigo 1, Tópico 6.1). O poço 6-BG-6P-SPS apresenta seção magmática com cerca de 800 m de espessura, sem intercalação com rochas sedimentares. O poço 3-BRSA-1267A-RJS é composto por 625 m de rochas básicas intercaladas com coquinas da Formação Itapema. Para essa pesquisa, considerou-se apenas a terceira seção magmática do poço, com 83 m de espessura. O poço 1-BRSA-886-RJS é formado por 720 m de rocha ígnea e vulcanoclástica intercaladas, abaixo de uma extensa camada de rochas sedimentares composta por argilito, folhelho, arenito, marga, calcilutito, halita e anidrita. Apenas a primeira seção magmática do poço foi estudada neste projeto, com cerca de 150 m de espessura. Os critérios de escolha das seções de interesse dos poços 3-BRSA-1267A-RJS e 1-BRSA-886-RJS foram: a) boa amostragem; b) amostragem em intervalos com padrões petrofísicos distintos. Todos os poços estudados estão inseridos em seções do pré-sal da Bacia de Santos. Estimativas das composições, texturas e estruturas das rochas foram feitas a partir de dados petrofísicos registrados nos perfis compostos dos poços, discriminando-se distintos padrões representativos de eletrofácies. A análise qualitativa dos perfis petrofísicos foi realizada a partir dos dados de Raio Gama (GR), Resistividade (R), Sônico (Δt), Porosidade Neutrão (Φ) e Densidade (ρ). A interpretação petrofísica do poço 6-BG-6P-SPS está inserida no Apêndice A e no Artigo 2 (Tópico 6.2) e as interpretações das seções representativas dos poços 3-BRSA-1267A-RJS e

1-BRSA-886-RJS estão inseridas no Artigo 1 (Tópico 6.1);

d) Análises macroscópica e microscópica: As fases de seleção, preparação, descrição e envio das amostras para análises foram realizadas nas dependências do LabMEG, vinculado ao Departamento de Petrologia e Geotectônica, do Instituto de Geociências da UFRuralRJ. 125 amostras laterais do poço 6-BG-6P-SPS, 10 amostras da seção de interesse do poço 3-BRSA-1267A-RJS e 11 amostras da seção de interesse do poço 1-BRSA-886-RJS foram selecionadas para descrição macroscópica. As amostras foram catalogadas, descritas sob escala macroscópica e fotografadas sobre bancada e sob lupa estereoscópica. Concomitante a essa fase, realizou-se a seleção de 76 amostras do poço 6-BG-6P-SPS, 10 amostras do poço 3-BRSA-1267A-RJS e 11 amostras do poço 1-BRSA-886-RJS para confecção de lâminas petrográficas. As amostras foram enviadas para o Laboratório PETROGRAFIA-BR em Contagem, MG. Posteriormente, as lâminas foram catalogadas, descritas e fotografadas sob microscópio de luz transmitida AXIOSCOP do Departamento de Petrologia e Geotectônica da UFRuralRJ. As descrições das amostras dos poços 3-BRSA-1267A-RJS e 1-BRSA-886-RJS foram realizadas por alunas de mestrado e graduação da UFRuralRJ, respectivamente, vinculadas ao LabMEG e ao Projeto EQUIMAG. Todos os dados petrográficos foram inseridos na Plataforma LabMEG (labmeg.com), disponíveis no Apêndice B;

e) Seleção e preparação de amostras para análise litogeoquímica: Apenas o poço 6-BG-6P-SPS foi escolhido para os estudos litogeoquímicos. 30 amostras foram selecionadas com o objetivo de determinar as concentrações dos elementos maiores, traços e terras-raras de interesse petrogenético. Os critérios utilizados de maneira combinada para a seleção foram: (1) menor grau de alteração das amostras, (2) ausência ou menor quantidade de amígdalas observadas em escala macroscópica e (3) espaçamento de cerca de 27 m entre amostras de uma mesma seção magmática. As amostras laterais são pequenos cilindros de cerca de 3 cm de diâmetro, coletadas por uma broca inserida perpendicularmente na parede do poço. O processo de coleta dessas amostras envolve um sistema hidráulico capaz de quebrar, por torção, um plugue (formato de rolha) de até 5 cm de comprimento. Em uma mesma descida no poço, a ferramenta coleta amostras em diferentes profundidades, sendo possível separar e organizar a amostragem. Entretanto, esse processo, assim como outros envolvendo perfurações, requer o uso de lama e fluidos de perfuração. Deste modo, as amostras coletadas chegam em superfície impregnadas por esse material. O processo de preparação das amostras para esta pesquisa envolveu, inicialmente, lavagem

manual e secagem das amostras, a fim de retirar ao máximo a lama impregnada. Entretanto, tal procedimento foi satisfatório apenas para análises macroscópica e microscópica. Para análises geoquímicas foi necessário retirar toda a lama impregnada, a fim de evitar contaminação. Para tanto, as amostras foram fragmentadas em tamanhos centimétricos a milimétricos, separadas em alíquotas maiores que 5 g (quando possível) e inseridas em uma lavadora ultrassônica, com 750 ml de água. Este aparelho produz vibrações ultrassônicas no líquido, causando movimentação e, em contato com a amostra, gera atrito que remove os resíduos. Esse processo é estritamente físico, logo, não afeta quimicamente as amostras. O tempo de permanência das amostras na lavadora variou de acordo com o tipo de amostra, em uma média de 6 minutos a 30 ºC. Após essa etapa, as amostras foram lavadas com água destilada e secadas. Os fragmentos secos foram separados sob lupa estereoscópica e as porções contendo impurezas ou feições que poderiam afetar a qualidade das análises químicas foram descartadas. Além da capa formada pelo fluido de perfuração, outros elementos eliminados das amostras foram amígdalas e marcações em caneta. Por fim, alíquotas com cerca de 5 g foram separadas e enviadas para o *Actvation Laboratories* Ltd. (ACTLAB, Canadá), onde foram pulverizadas em moinhos de bolas de aço. A moagem é rotineiramente monitorada pelo laboratório, o que garante não haver contaminação das amostras por Ni ou Cr do moinho. As análises litogeoquímicas dos elementos maiores foram realizadas por espectrometria por emissão ótica acoplado a plasma induzido (ICP-OES, *Inductively Couple Plasma-Optical Emission Spectrometry*) e os elementos traços foram analisados por espectrometria de massa acoplado a plasma induzido (ICP-MS, *Inductively Couple Plasma-Mass Spectrometry*). Detalhes sobre os procedimentos utilizados na análise litogeoquímica são descritos no Artigo 2 (Tópico 6.2);

f) Seleção de amostras para análise isotópica: Apenas o poço 6-BG-6P-SPS foi escolhido para análise isotópica. Quinze amostras foram selecionadas para análise isotópica (Sr-Nd-Pb) e enviadas para o *Thermal Ionization Mass Spectrometry Laboratory* (Universidade do Novo México - EUA). A análise no laboratório foi realizada por espectrometria de massa por ionização térmica (*Thermal Ionization Mass Spectrometry* – TIMS). As amostras selecionadas para a análise isotópica foram lixiviadas sob HCl a fim de remover o Sr oriundo da contaminação marinha e de outros possíveis interferentes. As amostras foram enviadas diretamente do ACTLAB (Canadá) para o laboratório no Novo México (EUA) de modo a otimizar o tempo de trânsito das amostras e, assim, utilizar o material pulverizado remanescente das

análises litogeoquímicas. Isso se fez necessário devido à pouca quantidade (em peso) das amostras laterais disponíveis (problema comum para esse tipo de amostragem) e a necessidade de devolver as alíquotas para a Agência Nacional de Petróleo (ANP). Os critérios gerais para seleção foram: pelo menos 1 amostra de cada seção baseada na análise microscópica, baixos valores de LOI (*Lost on Ignition*) determinado na análise litrogeoquímica, baixo grau de alteração de acordo com análise petrográfica. Critérios específicos foram determinados para os diferentes tipos de rochas no poço 6-BG-6P-SPS. O critério de escolha para as rochas de seções félsicas foi o caráter efusivo. Nas seções máficas, os critérios foram: pouca ou nenhuma amígdala/veio; amostras com maior e menor valor de MgO; relação MgO x La/Yb_N (amostras com mesmo valor de MgO e La/Yb_N diferentes ou amostras com valor de MgO diferente e La/Yb_N semelhantes). Detalhes sobre os procedimentos utilizados na análise isotópica são descritos no Artigo 2 (Tópico 6.2);

g) Seleção de amostras para análise geocronológica (U-P *in situ*):

Apenas o poço 6-BG-6P-SPS foi escolhido para análise geocronológica. Oito lâminas petrográficas foram selecionadas para análise geocronológica U-PB *in situ* de 32 grãos de zircão no laboratório LSP-LLA – CPGeo (USP). As análises foram realizadas por ICP-MS. Detalhes sobre os procedimentos utilizados na análise litogeoquímica são descritos no Artigo 2 (Tópico 6.2).

5 **REVISÃO TEMÁTICA**

5.1 **Evolução cronoestratigráfica da Bacia de Santos**

A história evolutiva e a estratigrafia da Bacia de Santos foram compartimentadas nas fases (ou megasequências) rifte, pós-rifte e drifte, além do embasamento cristalino formado por rochas graníticas e gnáissicas de idade pré-cambriana do Orógeno Colisional (ou Faixa) Ribeira (Moreira *et al.*, 2007; Figura 2).

A fase rifte (138-122 Ma) teve início no Hauteriviano e os seus andares cronoestratigráficos locais são chamados de Rio da Serra Superior, Aratu, Buracica e Jiquiá. Essa fase corresponde às primeiras manifestações da ruptura do Supercontinente Gondwana, sendo composta pelas formações Camboriú, Piçarras e Itapema, pertencentes ao Grupo Guaratiba (Moreira *et al.*, 2007). A deposição sedimentar ocorreu em ambiente continental de clima árido, caracterizado por depósitos de leques aluviais, deltaicos e lagos interiores salinos e alcalinos, com deposição biogênica continental (Chang *et al.*, 1988; Cainelli e Mohriak, 1999).

A Formação Camboriú (Sequência K20-K34) é formada por basaltos toleíticos associados ao magmatismo Paraná-Etendeka. O extravasamento ocorreu no Hauteriviano (136,4-130 Ma; andares locais Rio da Serra Superior e Aratu). Esses basaltos são correlacionados aos basaltos da Formação Cabiúnas, na Bacia de Campos, os quais são caracterizados por vulcanismo subaquoso lacustre e vulcanismo subaéreo explosivo (Mizusaki *et al.*, 1992). A Formação Piçarras (sequência 36) está sobreposta aos basaltos da Formação Camboriú e é formada por arenitos, siltitos e folhelhos de composição talco-estevensítica, ricos em matéria orgânica. A deposição dessa formação ocorreu em ambiente lacustre salino no Barremiano (136-126,4 Ma), correspondente aos andares locais Aratu Superior e Buracica (Chang *et al.*, 2008). Acima, nos andares Buracica Superior e Jiquiá, de idade neobarremiana a eoaptiana (126,4-123,1 Ma) está a Formação Itapema (sequência K38), composta por intercalações entre fragmentos de conchas de bivalves (coquinas), rochas carbonáticas bioclásticas (*wackestone* e *packstones*), folhelhos carbonáticos e folhelhos escuros ricos em matéria orgânica (Moreira *et al.*, 2007). A deposição das formações Piçarras e Itapema ocorreu em ambiente lacustre com interação com fluidos hidrotermais das rochas basálticas, o que elevou as condições alcalinas do meio. Porém, a ocorrência de bivalves na Formação Piçarras e um aumento de pH nos ambientes sedimentares da Formação Itapema sugere que houve uma diminuição da alcalinidade no ambiente lacustrino. Tal diminuição pode estar relacionada a um aprofundamento tectônico do lago, somado a um clima mais úmido (Leite *et al.*,

2020). O segundo registro magmático da fase rifte, inserido na Formação Piçarras, corresponde às intercalações de basaltos subaquosos de 130-121 Ma (Moreira *et al.* 2007).

A passagem para a fase pós-rifte (122-113 Ma) é marcada, no início do Aptiano, pela discordância Pré-Alagoas, que marca o limite dos andares locais Jiquiá (base) e Alagoas (topo) há cerca de 122 Ma. A fase pós-rifte é transicional entre o ambiente continental e o marinho raso, em um contexto de quiescência tectônica (fase *sag* da bacia). O clima predominante nessa fase era árido e quente, sob condições neríticas rasas e ambiente euxínico salino (Chang *et al.*, 1988; Cainelli e Mohriak, 1999; Moreira *et al.*, 2007). A deposição sedimentar ocorreu em um ambiente restrito lagunar, resultando na formação de pacotes de rochas carbonáticas e rochas evaporíticas, correspondentes às formações Barra Velha (sequências K44 e K46-K48) e Ariri (Sequência K50), respectivamente, ambas inseridas no Grupo Guaratiba (Moreira *et al.* 2007).

A Formação Barra Velha está sobreposta discordantemente à Formação Itapema. O pacote sedimentar formou-se durante o Aptiano (123,1-113 Ma) e é caracterizado por calcários microbiais, estromatólitos, laminitos microbiais e folhelhos, depositados em ambientes alcalinos com ocorrência de coquinas. Essa formação é dividida em Formação Barra Velha Superior e Inferior, separadas pela discordância Intra-Alagoas de 117 Ma, síncrona ao magmatismo registrado nessa fase (Moreira *et al.*, 2007). A Formação Ariri é composta por evaporitos tais como halita e anidrita, e sais mais solúveis como taquidrita, carnalita e silvinita, depositados durante o Neoaptiano (Andar Alagoas Superior), com tempo de deposição impreciso devido à mobilidade do sal (Moreira *et al.*, 2007). Entretanto, Dias (1998) e Garcia *et al.* (2012) estimam que o tempo de deposição tenha sido entre 0,5-0,7 a 1 Ma.

O pacote sedimentar registrado nas fases rifte e pós-rifte corresponde ao chamado Pré-Sal da Bacia de Santos. O sistema petrolífero Piçarras-Itapema/Barra Velha é caracterizado por rochas geradoras, representadas por intercalação de folhelhos lacustres e carbonatos da Formação Piçarras, rochas-reservatórios carbonáticas (coquinas, estromatólitos e, possivelmente, travertinos) das formações Itapema e Barra Velha, e rocha selante representada pelo pacote de sal da Formação Ariri (Abelha, 2017; Fernandez & Santos, 2017).

A fase drifte iniciou-se no Albiano (113 Ma), e abrange os processos sedimentares até o recente e corresponde à efetiva separação dos continentes sul-americano e africano, com entrada definitiva do mar e a criação de crosta oceânica (Figura 2). O ambiente marinho foi restrito até o Turoniano, com variação entre clima quente e seco e deposição de sedimentos em ambiente nerítico hipersalino. Em seguida, ocorreu um afogamento da plataforma, com deposição de sedimentos efetivamente marinhos e aumento da diversidade biológica. A fase drifte compreende ao maior pacote deposicional da Bacia de Santos, abrangendo aos grupos Camburi, Frade e Itamambuca (Chang *et al.*, 1988; Cainelli e Mohriak, 1999; Moreira *et al.*, 2007).

O Grupo Camburi, de idade albiana-cenomaniana (113-91,2 Ma), representa uma fase de transgressão até a deposição de folhelhos anóxicos na transgressão Turoniana. Os pacotes sedimentares dessa fase são representados pelas formações Florianópolis, Guarujá e Itanhaém, além do Membro Tombo (sequências K60, K70 e K82-K86; Moreira *et al.*, 2007).

A Formação Florianópolis é composta por conglomerados, arenitos e folhelhos associados aos leques aluviais e deltaicos. A Formação Guarujá corresponde à implantação da plataforma carbonática ao longo do Albiano e é dividida em interna e externa com presença de carbonatos, margas e folhelhos escuros. A Formação Itanhaém é limitada na porção inferior por folhelhos radioativos do Marco Beta (porção basal do Albiano Superior) e margas sobrejacentes, e na porção superior por folhelhos radioativos do Marco Turoniano (evento anóxico global), com sedimentos finos e conteúdo carbonático. Essa formação registra um padrão retrogradante, com subida relativa do nível do mar e afogamento da plataforma rasa, a qual marca o fim do Cretáceo Inferior. O Membro Tombo ocorre interacamadado na Formação Itanhaém, sendo caracterizado por depósitos arenosos de fluxos gravitacionais densos (turbiditos; Moreira *et al.*, 2007).

O Grupo Frade é limitado, na base, pelo Marco Turoniano (91,2 Ma) e, no topo, pela passagem do Cretáceo para o Paleógeno (65 Ma). Esse grupo representa um padrão regressivo que deslocou a quebra da plataforma costa afora (cerca de 200 km) para a região a oeste da Charneira cretácica. Esse deslocamento é marcado pelo evento erosivo de 85,8 Ma (Santoniano), considerado um dos mais expressivos da bacia. O Grupo Frade abrange as formações Santos, Itajaí-Açu, Jureia e o Membro Ilhabela (Moreira *et al.*, 2007).

A Formação Santos é composta por arenitos conglomeráticos continentais, que se interdigitam com os arenitos plataformais da Formação Jureia. Por sua vez, a Formação Jureia é composta por sedimentos arenosos, folhelhos e siltitos em ambientes continentais e porções distais da plataforma. Há registros de intenso vulcanismo interacamadado à Formação Jureia no Santoniano, associado às feições vulcânicas presentes no continente, bem como às estruturas tais como a Elevação do Rio Grande e a Zona de Deformação Cruzeiro do Sul. Esses processos vulcanosedimentares coincidem com o aumento da taxa de subsidência na bacia e surgimento da Serra do Mar. A Formação Itajaí-Açu é representada por sedimentos pelíticos, siltitos, folhelhos e argilitos cinza-escuros depositados em ambiente de plataforma distal, talude e sopé. O Membro Ilhabela é formado por arenitos do Andar Turoniano, gerados a partir de fluxos turbidíticos densos, associados a deltas e expressivas escavações no talude e na plataforma (Moreira *et al.*, 2007).

As primeiras movimentações do sal ocorreram no início da fase drifte (Neoaptiano e Eoalbiano), como resposta à sobrecarga sedimentar do Grupo Camburi (Garcia *et al.*, 2012). Isso gerou uma tectônica do sal bastante complexa, com almofadas de sal, diápiros, falhas compressionais e extensionais e controle da sedimentação em calhas associadas à movimentação

do sal (Figueiredo & Mohriak, 1984). No final do Cenomaniano (parte superior do Grupo Camburi) houve uma resistência à mobilidade do sal e acomodação dos sedimentos do Grupo Frade. Desta forma, a plataforma avançou em direção à bacia. Ao final do Cretáceo (parte superior do Grupo Frade), a mobilidade lateral do sal era praticamente nula e cerca de 90% da deformação salífera havia ocorrido. Por fim, a partir do Paleógeno (64 Ma), a deposição do Grupo Itamambuca estabeleceu uma deformação compressiva (Garcia *et al.*, 2012).

No pacote Pós-Sal, há dois principais sistemas petrolíferos: (1) Piçarras-Guarujá e (2) Itajaí-Açu-Ilhabela. O primeiro corresponde às rochas geradoras da Formação Piçarras da fase rifte e às rochas reservatórios carbonáticas da Formação Guarujá. O segundo compreende o pacote sedimentar da Formação Itajaí-Açu como rocha geradora e o Membro Ilhabela como rocha reservatório (Fernandez & Santos, 2017).

O último grupo do pacote deposicional da Bacia de Santos é o Grupo Itamambuca, com início na passagem do Cretáceo para o Paleógeno (65 Ma). Esse grupo é representado pelas formações Ponta Aguda, Iguape, Marambaia, Sepetiba e Membro Maresias (Moreira *et al.*, 2007).

A Formação Ponta Aguda registra a deposição desde o limite Cretáceo-Paleógeno (65 Ma) até o limite Plioceno-Pleistoceno (1,6 Ma), caracterizada por arenitos vermelhos depositados em ambiente de leques aluviais, sistemas fluviais e depósitos costeiros. O pacote sedimentar da Formação Iguape teve início no Oligoceno (33,9 Ma) e fim na passagem Plioceno-Pleistoceno (1,6 Ma), sendo representado por uma plataforma carbonática com calcarenitos e calcirruditos bioclastos intercalados com argilito cinza-esverdeado, siltito e margas. A plataforma carbonática alcança seu maior desenvolvimento no Mioceno (Serravaliano), com ocorrência local e predomínio de sedimentos siliciclásticos na plataforma e talude (Peixoto, 2004). A Formação Marambaia foi depositada nas regiões de plataforma distal, talude e sopé, a partir do Paleoceno (65 Ma) e é formada por siltitos, folhelhos, diamictitos e margas. O Membro Maresias é composto por arenitos resultantes de fluxos turbidíticos fortemente canalizados em cânions que cortam e interdigitam os sedimentos da Formação Marambaia. Por fim, a Formação Sepetiba, com início no Pleistoceno (1,6 Ma), é representada por arenitos cinza-esbranquiçados, coquinas de moluscos, briozoários e foraminíferos (Moreira *et al.*, 2007).

O Grupo Itamambuca é marcado por importantes discordâncias. Uma discordância no Mioceno Inferior (20,4 Ma) marca o desenvolvimento de uma tendência transgressiva, que culmina no Mioceno Médio (Serravaliano), em uma superfície de inundação. Esse período representa a maior variação relativa do nível do mar a partir do Mioceno, sendo responsável pela grande deposição de sedimentos nas porções costeiras e interior da placa sul-americana. No Mioceno Superior (11 Ma), uma outra discordância registra uma queda eustática global, conhecida como Marco Cinza na Bacia de Campos (Moreira *et al.*, 2007).

O magmatismo da fase drifte é registrado por dois eventos. O primeiro magmatismo data do Santoniano-Campaniano, sendo marcado por intenso vulcanismo extrusivo interacamadado aos depósitos da Formação Jureia, do Grupo Frade. O segundo registro magmático pertence ao Eoceno Inferior. Esse magmatismo é caracterizado por basalto alcalino com caráter extrusivo, constituído por hialoclastitos e rochas vulcaniclásticas. Essa ocorrência é representada por cones vulcânicos e derrames submarinos, principalmente na parte norte da Bacia de Santos, na região do Alto de Cabo Frio (Oureiro, 2006). Há também magmatismo intrusivo, representado por soleiras de diabásio, com forma de vitória-régia na sísmica (Moreira *et al.*, 2007).

Figura 2: Carta cronoestratigráfica da Bacia de Santos.

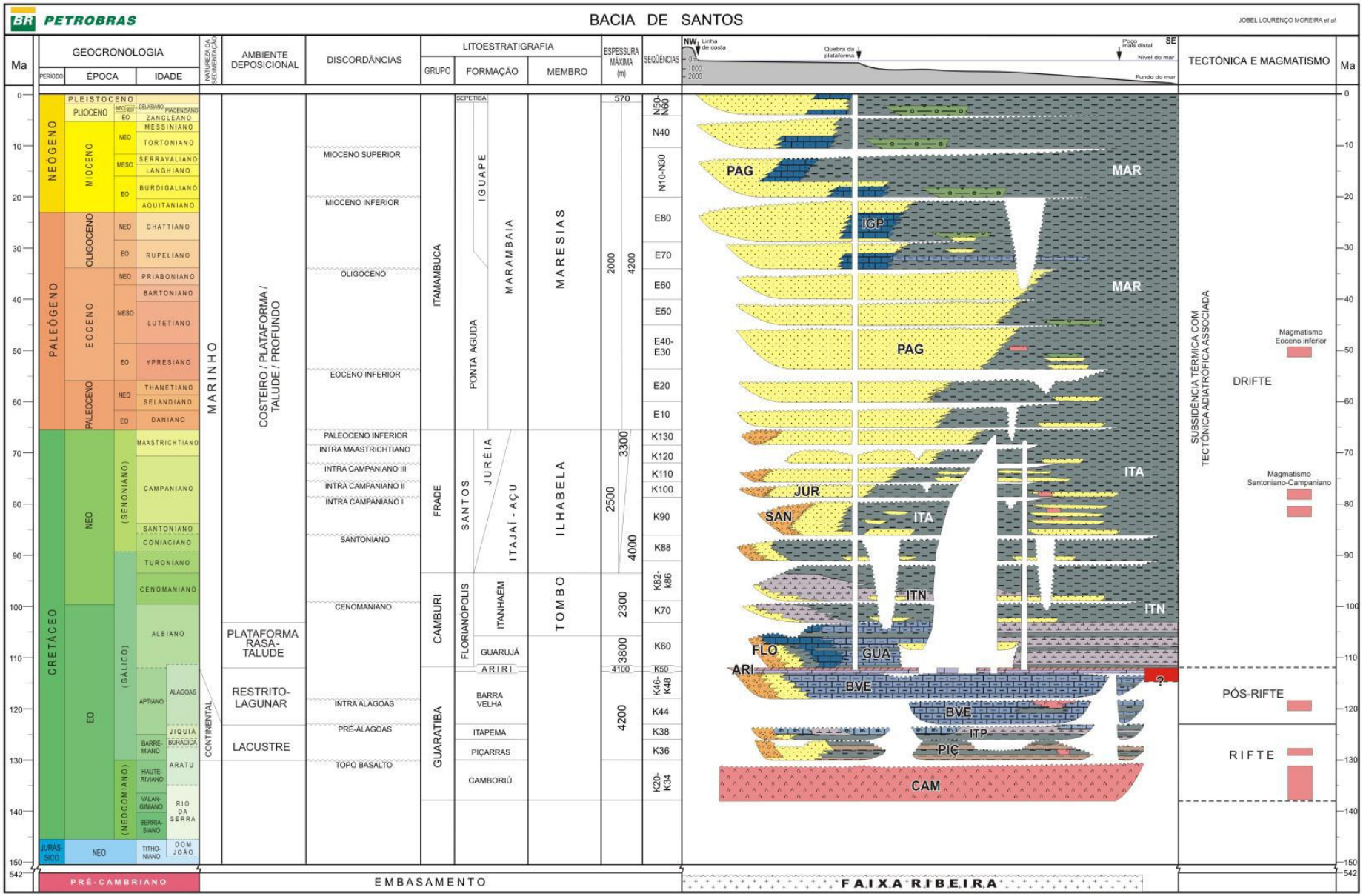

Fonte: Moreira *et al.*, 2007.

5.2 **O magmatismo da Bacia de Santos**

A coluna estratigráfica da Bacia de Santos registra eventos magmáticos em todas as suas fases evolutivas relacionadas às supersequências tectono-sedimentares. Apesar das ocorrências, o magmatismo da bacia ainda é pouco estudado, principalmente no que tange os estudos petrológicos. Moreira *et al.* (2007) dividem as ocorrências magmáticas em pré-Albianas e pós-Aptianas. O magmatismo pré-Albiano corresponde aos eventos das fases rifte e pós-rifte registrados no Hauteriviano, Barremiano e Aptiano. O magmatismo pós-Aptiano compreende os eventos da fase drifte, registrados no Santoniano-Campaniano e no Eoceno Inferior. Estudos geofísicos recentes sugerem que o magmatismo da Bacia de Santos ocorreu em 3 ciclos magmáticos correlacionados com as fases pré-rifte (135 a 132-130 Ma), syn- e pós- rifte (132-130 a 123 Ma e 123 a 113-112 Ma, respectivamente) e drifte (110 a 40 Ma; Gordon *et al.*, 2023a).

O primeiro magmatismo pré-Albiano registrado é representado pelos basaltos toleíticos da Formação Camboriú, com idade Hauteriviana, datado em 138 ± 3,5 Ma pelo método K-Ar em rocha total (Fodor *et al.*, 1983). Esses basaltos são cronocorrelatos aos basaltos toleíticos do magmatismo da Província Paraná-Etendeka (Peate, 1997) e aos basaltos da Formação Cabiúnas da Bacia de Campos (Mizusaki *et al.*, 1992). Os basaltos da Formação Camboriú são pouco alterados pela água do mar e apresentam coloração avermelhada típica de oxidação. As poucas amostras estudadas apresentam veios de carbonato e são amigdaloidais, com preenchimento de carbonato e mineral silicoso de cor verde (Fodor & Vetter, 1985). De maneira geral, os basaltos são cinza-escuros, holocristalinos e de granulometria média (Moreira *et al.*, 2007). A assembleia mineral é composta, principalmente, por plagioclásio, augita e pigeonita, comumente alterados, e óxidos de Fe-Ti e vidro hidratado, alterado e/ou parcialmente devitrificado. As texturas comumente encontradas são ofítica, intergranular e diktitaxítica. Tais texturas sugerem uma correlação com basaltos de derrames continentais, como os basaltos da Formação Serra Geral, na Bacia do Paraná (Fodor & Vetter, 1985; Moreira *et al.*, 2007). Dados de química mineral em grãos de augita mostraram aumento de Fe e diminuição de Ca, variação composicional típica de basaltos toleíticos (Fodor & Vetter, 1985).

Há poucos estudos geoquímicos acerca dos basaltos toleíticos da Formação Camboriú. Fodor & Vetter (1984) analisaram amostras da margem sudeste brasileira, sendo quatro delas localizadas na Bacia de Santos, mas apenas duas pertencentes à Formação Camboriú. As amostras são consideradas enriquecidas e moderadas a altamente evoluídas, com concentração de TiO_2 alta (2-3,5 wt.%), podendo ser relacionadas aos basaltos do Magmatismo Serra Geral. Os valores de MgO são elevados (5,83-9,32 wt.%) e as razões FeO*/MgO são baixas (FeO* = 11,99 e 12,90;

FeO*/MgO = 2,04 e 1,38, respectivamente), o que pode sugerir que a alta concentração de MgO esteja relacionada à presença de carbonatos ricos em Mg. As duas amostras analisadas têm razões de elementos incompatíveis imóveis diferentes (Zr/Nb = 10,5 e 3,4; Y/Nb = 2,4 e 0,52, respectivamente) e consideradas baixas quando comparadas com as amostras estudadas na Bacia de Campos. Os dados indicam que a gênese desses basaltos toleíticos representativos da Formação Camboriú esteja associada à mistura de fonte empobrecida do tipo N-MORB e uma fonte fértil, tipo pluma (possivelmente Tristão da Cunha devido a posição do sul do país no Jurássico), sem evidências de contaminação crustal. Tal mistura pode justificar a heterogeneidade entre os elementos incompatíveis imóveis vistos nas duas amostras analisadas (Fodor *et al.*, 1980; Fodor *et al.*, 1983; Fodor & Vetter, 1984).

O segundo evento magmático pré-Albiano inserido na fase rifte compreende basaltos subaquosos com menos de 130 Ma (Barremiano; Moreira *et al.*, 2007), mas não há dados geoquímicos desse magmatismo disponíveis na literatura. O estudo petrográfico de uma amostra relacionada a este evento magmático, que ocorre intercalada com a Formação Piçarras, registrou a presença de olivina palagonitizada e fragmentada, carbonato como produto de alteração, texturas pouco preservadas similares a *fiammés* e aspecto de tufo (Lutonda, 2014).

O terceiro e último magmatismo pré-Albiano é registrado na fase pós-rifte. A ocorrência magmática abrange basaltos com idade de cerca de 117 Ma (Aptiano, andar Alagoas), estando associados à discordância Intra-Alagoas, na Formação Barra Velha (Moreira *et al.*, 2007). Não há estudos petrológicos deste magmatismo. De acordo com Lutonda (2014), análises petrográficas de rochas ígneas pré-albianas intercaladas à Formação Barra Velha evidenciaram magmatismo alcalino, com ankaramitos (variação porfirítica de basanitos, contendo fenocristais de piroxênio e olivina), basanitos, lamprófiros e basaltos alcalinos.

Cronologicamente, o magmatismo da fase pós-rifte na Bacia de Santos pode ser relacionado ao Magmatismo Alagoas da Bacia de Campos, inserido na parte superior do Grupo Lagoa Feia (Winter *et al.*, 2007). A assembleia mineral das rochas magmáticas desse evento na Bacia de Campos é formada por fenocristais de plagioclásio, clinopiroxênio e olivina, com presença de plagioclásio, clinopiroxênio e minerais opacos na matriz, podendo conter porções desvitrificadas. As texturas das rochas desse magmatismo são típicas de rochas basálticas, como glomeroporfirítica, intersertal, amigdaloidal, ofítica e subofítica. As rochas do Magmatismo Alagoas são caracterizadas como basaltos subalcalinos, de afinidade toleítica a transicional, com baixas concentrações de TiO_2 e valores elevados de MgO. Os padrões de elementos terras raras (ETR) e elementos traços são comparáveis aos basaltos de baixo-Ti da Formação Serra Geral, enquanto o padrão isotópico é comparável aos basaltos de alto-K_2O da Bacia de Campos (Mizusaki *et al.*, 1992; Dani *et al.*, 2017).

O primeiro magmatismo pós-Aptiano na Bacia de Santos compreende o evento magmático do Santoniano-Campaniano (85-75 Ma), constituído por hialoclastitos e rochas vulcaniclásticas em eventos subaquosos e subaéreos (Moreira *et al.*, 2006, 2007). Esse magmatismo é reconhecido por interpretações sísmicas e marcado por cones vulcânicos, diques alimentadores subverticais a verticais, diques anelares e derrames de lava na região do Alto de Cabo Frio, localizada no limite norte da Bacia de Santos (Moreira *et al.*, 2006, 2007; Oreiro *et al.*, 2008; Figura 1). Os dados geofísicos indicam que os cones vulcânicos apresentam rochas com densidades e velocidades distintas e são formados por mais de um pulso magmático. Os diques observados apresentam composição alcalina e intrudem sedimentos albianos-cenomanianos. Além disso, há diques extensos, desde a base do sal até as rochas sedimentares do Cenomaniano. Os derrames de lava são paralelos à estratificação e são representados por basaltos amigdaloidais. A matriz desses basaltos é vítrea com minerais ricos em Ti e plagioclásio. As amígdalas são preenchidas por calcita, clorita e material criptocristalino rico em Ti. Adicionalmente, na base deste basalto foi reconhecida uma seção de brecha vulcaniclástica, de cor verde, com matriz vítrea cloritizada/serpentinizada, granulometria grossa e amigdaloidal (Moreira *et al.*, 2006).

No campo de Libra, localizado no norte da bacia, foram identificadas intrusões de diabásio, basalto, gabro e lamprófiros, ocorrendo como lacólitos, ou em meio à seção evaporítica ou como complexos ramificados de soleiras (Rancan *et al.*, 2018). A ocorrência desse evento magmático no sul da Bacia de Santos é caracterizada por soleiras de geometria planar e em pires, plútons, edifícios vulcânicos e diques alimentadores em ambiente subaquoso, associada a fase inicial desse vulcanismo (Schattner & Mahiques, 2020). Não há estudos petrogenéticos envolvendo amostras desse magmatismo.

O magmatismo mais recente registrado na Bacia de Santos, inserido no pós-Aptiano, é o magmatismo do Eoceno Inferior (50 Ma). A ocorrência deste magmatismo pode estar restrita à região do Alto de Cabo Frio, não tendo sido registrada na região central e sul da Bacia de Santos e ocorrendo raramente na região central e norte da Bacia de Campos, onde é denominado Membro Cabo Frio da Formação Emborê (Oreiro, 2006; Rangel, 2006; Moreira *et al.*, 2007; Oreiro *et al.*, 2008; Mohriak & Fainstein, 2012). O magmatismo do Eoceno Inferior é representado por sequência vulcanosedimentar intercalada com derrames e intrusões basálticas alcalinas (Oreiro, 2006). A ocorrência vulcaniclástica é marcada por rochas epiclásticas, brechas autoclásticas, tufos piroclásticos e hialoclastitos intercalados com pacote sedimentar composto por folhelhos, siltitos e calcissiltitos. Essas ocorrências sugerem períodos de quiescência alternados a atividade vulcânica, por vezes, subaquosa (Mizusaki & Mohriak, 1993; Rangel, 2006; Mohriak, 2020). As estruturas vistas nas seções sísmicas são formadas por edifícios vulcânicos cônicos ou abaulados, diques verticais a subverticais, soleiras em forma de vitória-régia e derrames basálticos (Mizusaki &

Mohriak, 1993; Moreira *et al.,* 2007; Oreiro, 2006; Rangel, 2006; Oreiro *et al.*, 2008; Souza, 2010). Modelos geodinâmicos propõem que o magmatismo não pode ser associado à participação de plumas, mas sim à reativação de falhas profundas (Oreiro *et al.*, 2008). No entanto, estudo petrológico de intrusões de lamprófiros e fonolito na seção Pré-sal, datadas em 41,06 ± 0,02 Ma e 38,62 ± 0,02 Ma, associou este magmatismo à mistura de componente litosférico tipo EB1 (*enriched mantle type 1*) e a pluma de Trindade (Louback *et al.*, 2021). Entretanto, a participação de componentes relacionados à pluma de Trindade implica em grande amplitude de impacto da pluma, desde a região sul de Abrolhos até a Bacia de Santos, com derrames basálticos como ocorre globalmente em impactos de plumas dessa dimensão (Wilson, 1986).

5.3 **Evolução tectônica da Bacia de Santos**

O contexto evolutivo da Bacia de Santos está inserido nos processos de fragmentação do Supercontinente Gondwana e posterior abertura do Oceano Atlântico Sul. A formação do Supercontinente Gondwana ocorreu durante o Neoproterozoico com diversas aglutinações de terrenos arqueanos e paleoproterozoicos, culminando na formação de orógenos colisionais (ou faixas móveis) nas bordas de terrenos cratônicos (Brito Neves & Cordani, 1991; Brito Neves *et al.*, 1995; Miller & Grote, 1998; Campos Neto, 2000; Carvalho *et al.*, 2000; Trouw *et al.*, 2000; Stanistreet & Charlesworth, 2001; Heilbron *et al.*, 2004, 2008). A quebra de Gondwana começou no Mesozoico (*ca.* 147 Ma) e tem sido associada à pluma mantélica de Tristão da Cunha (White & Mckenzie, 1989; Gibson *et al.*, 1999; Meisling *et al.*, 2001, Thomaz Filho *et al.*, 2005). A ascensão do manto e consequente afinamento litosférico causado pela pluma teriam contribuído para o rifteamento, que resultou em intenso magmatismo continental e progrediu até a criação de crosta oceânica e abertura do oceano Atlântico Sul, com a separação dos atuais continentes sul-americano e africano, há *ca.* 104 Ma (Feijó, 1996; Bueno, 2004).

De acordo com Thomaz Filho *et al.* (2000), a ruptura entre a América do Sul e África e a abertura do oceano Atlântico tiveram início na margem equatorial da Guiana Francesa até a Foz do Amazonas/Bacia do Marajó, entre 230 e 170 Ma. Ao mesmo tempo, na porção sul da América do Sul ocorria um rifteamento de sul para norte que atingiu as bacias de San Julian e norte das Malvinas na costa argentina. Até 120 Ma, o rifte seguiu seu processo de abertura até atingir a região da Bacia do Espírito Santo. Concomitantemente a essa abertura, a América do Sul rotacionou no sentido horário, promovendo deslocamentos transcorrentes dextrais na margem equatorial brasileira. O deslocamento final dos continentes ocorreu por volta de 90 Ma e a

separação continua até os tempos atuais, com picos de atividade magmática no Eoceno e Oligoceno (Thomaz Filho *et al.*, 2000; Mizusaki & Thomaz Filho, 2004). O centro de espalhamento meso-atlântico localiza-se mais próximo da margem africana, o que aumentou a extensão do rifte no lado brasileiro e implicou em caráter assimétrico na formação das bacias. A assimetria do rifte do Atlântico Sul colaborou para a formação das bacias evaporíticas, como a Bacia de Santos, que acomoda a maior parte do sal aptiano (Leyden, 1976; Szatmari *et al.*, 1985; Macedo, 1989; Chang *et al.*, 1992; Szatmari, 2000).

Importantes eventos magmáticos estão associados à ruptura de Gondwana, como o magmatismo de Karoo (190-178 Ma, Eojurássico; Riley *et al.*, 2005) e Paraná-Etendeka (135-131 Ma, Neocretáceo; Thompson *et al.*, 2001; Thiede & Vasconcelos, 2010). Houve também uma expressiva formação de enxames de diques no final do Jurássico-Eocretáceo que controlaram a disseminação do magma e a evolução das bacias de rifte da margem sudeste do Brasil (Valente *et al.*, 2009).

Almeida *et al.* (2013) compilaram dados geocronológicos das atividades magmáticas associadas à margem sudoeste do Gondwana e apontaram dois picos de idades, 179 Ma e 132 Ma, relacionados a Karoo e Paraná-Etendeka, além de grupos de atividades magmáticas entre 119-139 Ma e 173-187 Ma. Os autores apontaram a importância do embasamento no processo de ruptura do supercontinente, uma vez que o mesmo episódio magmático ocorreu nos três continentes (África, Antártida e América do Sul), indicando que está relacionado ao enfraquecimento da litosfera, e que enxames de diques de diferentes idades nos continentes sul-americano e africano seguem zonas de fraqueza de mesma direção do embasamento cratônico. De acordo com os autores, o Atlântico Sul Meridional é uma margem altamente vulcânica (*magma-rich* ou *volcanic rifted margin*), com o vulcanismo Paraná-Etendeka apresentando distribuição assimétrica (maior ocorrência na América do Sul). Ademais, os autores sugerem que os fluxos de lavas nas bacias *offshore* da margem sudeste do Brasil provavelmente foram alimentados por diques de direção NW na Bacia do Paraná.

As bacias da margem sudeste brasileira (Bacia de Santos, Campos e Espírito Santo) são consideradas de margem passiva pobre em magma (*magma-poor*; Zalán *et al.*, 2011), o que implica em uma formação relacionada apenas à deriva de placas e estiramento litosférico, com produção de material magmático no estágio final de abertura, quebra do continente e implantação de crosta oceânica. Diferentemente, a Bacia de Pelotas, ao sul da Bacia de Santos, é considerada de margem passiva rica em magma ou margem passiva vulcânica (*magma-rich* ou *volcanic rifted margin*; Zalán *et al.*, 2011), com grande volume de magma produzido. A formação de bacias de margens vulcânicas está relacionada aos processos mantélicos geradores de magma, adicionalmente ao estiramento litosférico por deriva de placas, estando associadas à LIPs (*Large*

Igneous Province) em estágio pré-rifte e SDRs (*Seaward Deeping Reflectors*) formados em estágio sin-rifte (Bullock e Minshull, 2005; Lavier e Manatschak, 2006; Pérez-Gussinyé *et al.*, 2006; Reston, 2009; Zalán *et al.*, 2011; Stica *et al.*, 2014).

Os primeiros modelos de formação de bacias do tipo rifte admitiam uma distensão crustal gerando riftes simétricos por cisalhamento puro (Mckenzie, 1978) ou com falhas profundas cortando toda crosta e gerando riftes assimétricos por cisalhamento simples (Wernick, 1985; Lister *et al.*, 1986). Sabe-se atualmente que esses modelos não são suficientes para explicar toda complexidade estrutural encontrada nas bacias de margem do tipo rifte. A grande extensão (> 600km) da Bacia de Santos, quando comparada com as bacias adjacentes, implica em modelos de estiramentos complexos e que ainda estão em debate. A estruturação aqui adotada para a Bacia de Santos considera o modelo proposto por Rigoti (2015), desenvolvido com base nos modelos presentes no trabalho de Peron-Pinvidic *et al.* (2013).

De acordo com Rigoti (2015), os eventos tectônicos relacionados ao rifteamento na Bacia de Santos podem ser divididos em Domínio Proximal, *Necking*, Domínio Distal, Domínio Alóctone e Domínio Oceânico (Tabela 1 e Figura 3). O Domínio Distal é subdividido em Rifte Interno, Bloco Resistente e Rifte Externo. Cada domínio ou subdomínio é inserido em fases tectônicas. A fase de estiramento acomoda as primeiras estruturas distensivas e tem tempo de evolução limitado pelo avanço da abertura do sistema e migração da deformação para o centro do rifte. A fase de afinamento representa a focalização da deformação no centro da bacia, se sobrepondo à fase de estiramento. A fase de exumação corresponde ao ápice da distensão, hiperestirando a crosta e expondo materiais de níveis profundos, como crosta inferior ou manto litosférico subcontinental. A fase de oceanização representa o processo de criação de crosta oceânica, com atividade magmática causada pelo rompimento da litosfera continental (Peron-Pinvidic *et al.*, 2013). As fases de estiramento, afinamento e exumação são inseridas na fase rifte, e a fase de oceanização está inserida da fase drifte.

Tabela 1: Fases e domínios presentes no modelo geotectônico proposto por Rigoti (2015) para a Bacia de Santos.

<table>
<tr><th>Fase</th><th>Fase tectônica</th><th colspan="2">Domínio</th><th>Crosta</th></tr>
<tr><td rowspan="6">Rifte</td><td>Estiramento</td><td colspan="2">Proximal</td><td rowspan="5">Continental</td></tr>
<tr><td rowspan="3">Afinamento</td><td colspan="2">Necking</td></tr>
<tr><td rowspan="3">Distal</td><td>Rifte Interno</td></tr>
<tr><td>Bloco Resistente</td></tr>
<tr><td rowspan="2">Exumação</td><td>Rifte Externo</td></tr>
<tr><td colspan="2">Alóctone</td><td>Natureza transicional</td></tr>
<tr><td>Drifte</td><td>Oceanização</td><td colspan="2">Oceânico</td><td>Oceânica</td></tr>
</table>

Fonte: A autora, 2025.

O Domínio Proximal está restrito à plataforma continental, com grabens e *half-grabens*.

Este domínio acomoda a deformação rúptil, envolve estruturas de estiramento iniciais e é composta por seção sedimentar siliciclástica e/ou magmática correlacionada à Bacia do Paraná. O Domínio *Necking* é a fase de afinamento crustal, onde a crosta passa de 40 km para 15 km de espessura e separa o Domínio Proximal do Domínio Distal. O limite entre o Domínio Proximal e o *Necking* é representado pela charneira da bacia.

O Domínio Distal é o de maior extensão, onde a crosta continental é hiperestirada. Os possíveis mecanismos para o hiperestiramento a crosta são: falhamentos polifásicos (Reston, 2009), falhamento sequencial (Ranero & Pérez-Gussinyé, 2010) ou falhas de descolamento com grande movimentação horizontal (Manatschal, 2004; Lavier e Manatschal, 2006; Antobreh *et al.*, 2009; Péron-Pinvidic, 2010; Zalán *et al.*, 2011; Huismans e Beaumont, 2011; Sutra & Manatschal, 2012; Peron-Pinvidic *et al.*, 2013).

No subdomínio Rifte Interno é desenvolvida a primeira estrutura de descolamento do tipo *Core-Complex*, envolvendo a crosta inferior. Essa estrutura é formada por movimentos horizontais de grandes extensões, responsáveis pela formação de bacias do tipo rifte. O Rifte Interno é marcado por falhas normais com mergulho em direção ao centro do rifte e é limitado pelo Alto Externo, que marca o fim da fase tectônica de afinamento (Rigoti, 2015).

O subdomínio Rifte Externo é a primeira manifestação da fase de exumação. É formado por uma segunda estrutura de descolamento do tipo *Core-Complex*, desta vez envolvendo o manto superior. Segundo Rigoti (2015), nesta fase há exumação do manto superior serpentinizado por infiltração de água no sistema, uma vez que a crosta inferior e o manto superior estão acoplados em regime rúptil. Evain *et al.* (2015) consideram, através de dados geofísicos, que o Rifte Externo pode ter composição de crosta oceânica ou continental. Para o caso de crosta oceânica, deve ser atípica sem a camada basáltica. Considerando crosta continental, a camada superior pode ser formada por crosta superior com intrusões máficas ou manto alterado exumado.

O Rifte Externo é considerado um centro de espalhamento abortado, pois representa uma tentativa mal-sucedida de *breakup*. A formação do Rifte Externo individualizou uma parte do Rifte Interno, gerando o Bloco Resistente, o qual apresenta as mesmas características estruturais do Rifte Interno. Uma transcorrência tardia no sentido horário no Bloco Resistente foi responsável pela forma em ‘V’ do Rifte Externo (Rigoti, 2015).

O Domínio Alóctone representa a transição entre crosta continental e crosta oceânica, chamada de COT (*Continental-Oceanic Transition*), formado por crosta proto-oceânica de composição gabroica, associada à fase de exumação. Interpreta-se que não houve implementação de um sistema magmático capaz de gerar crosta oceânica típica, uma vez que não houve afinamento crustal na fase final de rifteamento, devido à rotação do Bloco Resistente e ao componente transcorrente sinistral para o *breakup*. A exumação ocorreu com a segunda estrutura

de descolamento do tipo *Core-Complex* (envolvendo o manto superior, associada ao Rifte Externo), que produziu um movimento horizontal na ordem de 100 km (Rigoti, 2015). Zalán *et al.* (2011) definem o Domínio Alóctone como manto subcontinental exumado e o limita (COB – *Continental-Oceanic Boundary*) a leste da zona de transição. Klingelhoefer *et al.* (2014) o definem como de natureza oceânica, com COB a oeste da zona de transição.

Por fim, o Domínio Oceânico ocorre ao sul da Zona de Fratura de Florianópolis e é formado por crosta oceânica (Rigoti, 2015).

Figura 3: Modelo geotectônico (superior) e geofísico-geológico (inferior) para Bacia de Santos, com os principais domínios tectônicos e feições estruturais em planta e em seção.

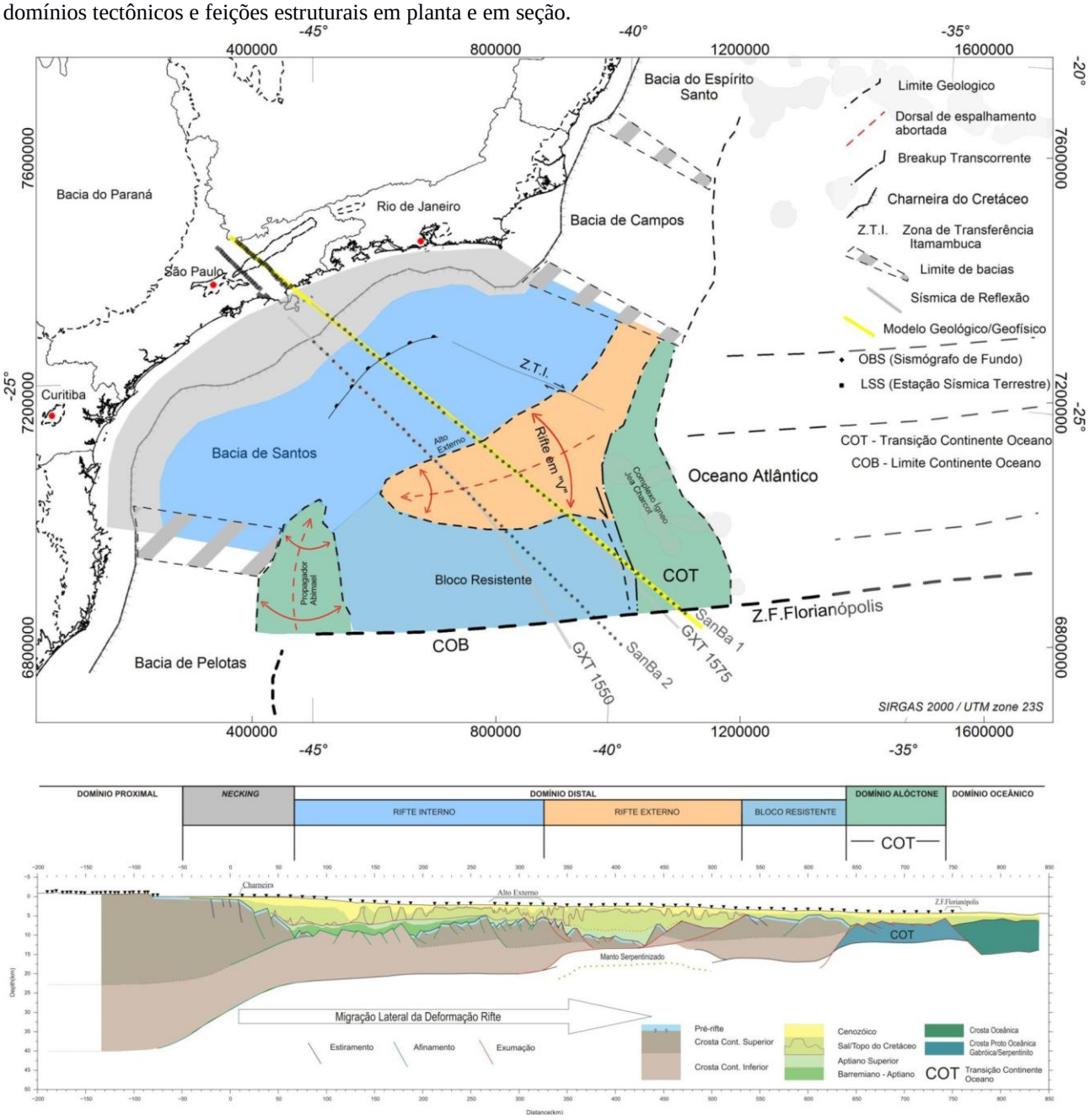

Fonte: Rigoti, 2015.

5.4 **Propriedades e ferramentas petrofísicas**

A petrofísica é o estudo das propriedades físicas da rocha e sua interação com os fluidos. Na indústria petrolífera, esse ramo de estudo é muito utilizado para descrever rochas-reservatórios de petróleo, gás e água. Para rochas vulcânicas, a aplicabilidade das ferramentas petrofísicas ainda é pouco difundida, porém muito discutida uma vez que as respostas obtidas pelas ferramentas podem auxiliar na discriminação de ambientes magmáticos, possíveis reservatórios não-convencionais e estruturação do corpo ígneo.

As principais propriedades utilizadas no estudo da petrofísica básica envolvem porosidade, permeabilidade e densidade. A porosidade indica os espaços vazios na rocha, formado pelos poros que podem conter fluidos (água, óleo ou gás). Os perfis petrofísicos disponibilizam a porosidade total, mas ela pode ser dividida em porosidade primária e secundária. A porosidade primária está relacionada aos elementos texturais da rocha, como tamanho, forma, seleção e arranjo dos grãos, sendo formados durante a ascensão e colocação do magma, durante intrusão, erupção, resfriamento e/ou cristalização. Já a porosidade secundária envolve processos que atuaram durante a diagênese da formação, como intemperismo, fraturamento, dissolução, desvitrificação, ou seja, processos posteriores à deposição. A permeabilidade está relacionada à facilidade com a qual os fluidos se movem através dos poros interconectados presentes na rocha. Quanto maior a permeabilidade da formação, mais fácil para o fluido atravessar o corpo rochoso. A presença de fraturas está diretamente relacionada a uma maior permeabilidade. A densidade da rocha está estritamente relacionada à porosidade. Essa propriedade é estimada através da soma dos dados de matriz e fluidos. Na petrofísica, entende-se como matriz tudo que não é poro. Desde modo, através dos valores de densidade da matriz e dos fluidos, pode-se estimar a porosidade da formação (Boyer & Mari, 1997; Rider, 2000; Taib & Donaldson, 2003; Flores *et al.*, 2006; Ellis & Singer, 2008; Zou *et al.*, 2013; Ran *et al.*, 2014).

Uma das ferramentas utilizadas para o cálculo da porosidade é o Neutrão - NPHI (Φ). Esta ferramenta emite nêutrons que interagem com a rocha e fluidos, sendo absorvidos. Os elementos químicos que não absorvem ou tendem a não absorver os nêutrons geram ausência de detecção na ferramenta, gerando o Índice de Hidrogênio (IH). A associação entre o IH e a porosidade se dá uma vez que parte do H (e outros elementos como Cd, B, Cl, Gd e Ba) presente nas formações está associado aos fluidos contidos nos poros (Millward *et al.*, 2002, Rider, 2000; Ellis & Singer, 2008). Esses poros podem ser vesículas, espaços intersticiais entre grãos e/ou cristais, poros intracristalino, poros formados pela dissolução mineral, pela desvitrificação, cavidades de dissolução ou fraturas (Zou *et al.*, 2013; Ran *et al.*, 2014).

Para o cálculo da densidade é usado o parâmetro RHOB (ρ). O funcionamento envolve a emissão de raios gama (^{137}Cs), que interagem com a formação (matriz + fluido) e retornam para a ferramenta. O resultado da densidade depende dos minerais formadores da rocha da formação, podendo ser utilizado para indicar a litologia, identificar minerais e estimar a porosidade (Rider, 2000; Ellis & Singer, 2008). Os valores médios de densidade para rochas basálticas são entre 2,7 e 3,2 g/cm³, entretanto, a presença de alteração, fraturas, vesículas e amígdalas podem diminuir os valores de densidade da rocha (Rider, 2000).

Outras propriedades físicas das rochas que são analisadas nos perfis petrofísicos envolvem radioatividade, acústica e eletricidade. As propriedades radioativas ou a radioatividade natural das rochas permite inferir a mineralogia e a litologia da formação através do perfil de raios gama (Gamma-ray – GR). A ferramenta emite ondas eletromagnéticas e mede a presença de isótopos de ^{238}U (Urânio), ^{232}Th (Tório) e ^{40}K (Potássio), em conjunto ou separadamente (Boyer & Mari, 1997; Rider, 2000; Taib & Donaldson, 2003; Flores *et al.*, 2006;). O padrão de GR é muito utilizado na interpretação de rochas magmáticas. Rochas básicas apresentam baixos valores de K, quando comparadas com rochas ígneas ácidas. Entretanto, quando passam por alteração hidrotermal ou intemperismo podem apresentar aumento nos teores de K devido a remobilização do elemento (Planke, 1994; Bartetzko, 2005). A presença de minerais ricos em K, Th ou U também podem alterar os valores, como zeólita e celadonita, minerais comumente encontrados preenchendo espaços vazios de rochas ígneas básicas.

As propriedades acústicas estão relacionadas ao perfil sônico (Dt), o qual mede o tempo que a onda sonora leva para percorrer a formação, chamado de tempo de trânsito. Esse parâmetro está associado à composição, textura, estrutura, minerais presentes na rocha e suas dimensões e distribuição na matriz (Wyllie *et al.*, 1956). A combinação de Dt e ρ pode auxiliar na inferência da presença de fraturas. Em rochas densas e maciças, a onda sonora se propagará mais rapidamente. Isso implica em um tempo de trânsito (Dt) menor, onde a densidade é inversamente proporcional ao tempo de trânsito (Boyer & Mari, 1997; Rider, 2000; Taib & Donaldson, 2003; Flores *et al.*, 2006; Ellis & Singer, 2008). Por meio desta ferramenta também é possível estimar a porosidade da formação, através da presença de poros interconectados ou amígdalas.

As propriedades elétricas envolvem a resistividade, ou seja, a capacidade da formação impedir a condução de corrente elétrica. Quanto mais fácil a passagem da corrente elétrica na rocha, menor será o valor da resistividade. Os dados de resistividade dependem da presença de fluidos intersticiais condutivos presentes em amígdalas e fraturas. Desta forma, a resistividade é diretamente associada à porosidade (Boyer & Mari, 1997; Rider, 2000; Taib & Donaldson, 2003; Flores *et al.*, 2006; Ellis & Singer, 2008). Entretanto, baixos valores de resistividade podem estar associados a presença de condutores metálicos precipitados devido circulação de sulfetos, como a

pirita (Theys, 1991).

A composição, as texturas e estruturas presentes nas rochas vulcânicas são fatores que afetam as ferramentas utilizadas nos estudos das propriedades petrofísicas, implicando em padrões e respostas distintas. A estrutura típica de inflação de derrame, formada por base-núcleo-crosta, apresenta respostas marcantes no perfil petrofísicos, tornando possível a delimitação dos diferentes fluxos de lava. No geral, a base e o núcleo maciços apresentam altos valores de densidade e resistividade, em oposição à baixos valores de porosidade, GR e Dt. Enquanto a crosta amigdaloidal/vesicular e fraturada apresenta baixos valores de densidade e resistividade, com altos valores de porosidade, GR e Dt. A presença de minerais nas amígdalas e fraturas podem acentuar os padrões, afetando os valores de GR pelo aumento na concentração de K e aumentando os valores de porosidade pelo Índice de H, uma vez que esses minerais são, em geral, hidratados (Planke 1994; Jerram *et al.*, 2009; Nelson *et al.*, 2009; Nelson *et al.*, 2015; Millett *et al.*, 2016; Rossetti *et al.*, 2019; Millett *et al.*, 2021a, 2021b).

6 **RESULTADOS E DISCUSSÕES**

6.1 **Artigo científico 1 (publicado): Petrophysical and petrographic data correlation and the discrimination of magmatic environments and processes in Santos Basin, offshore SE Brazil.**

DOI: https://doi.org/10.1016/j.jsames.2024.105095

Journal of South American Earth Sciences 147 (2024) 105095

Contents lists available at ScienceDirect

Journal of South American Earth Sciences

journal homepage: www.elsevier.com/locate/jsames

Petrophysical and petrographic data correlation and the discrimination of magmatic environments and processes in Santos Basin, offshore SE Brazil

Bárbara Santos Queiroz [a,*], Sergio de Castro Valente [b], Anderson Costa dos Santos [c,e], Monica Heilbron [d,e]

[a] Rio de Janeiro State University (UERJ), Faculty of Geology (UERJ), São Francisco Xavier Street, 524 – 4033A, Rio de Janeiro (RJ), Brazil
[b] Federal Rural University of Rio de Janeiro, Department of Petrology and Geotectonics, Seropédica, Rio de Janeiro 23890-000, Brazil
[c] Rio de Janeiro State University (UERJ), Faculty of Geology (UERJ), Department of Mineralogy and Igneous Petrology (DMPI), São Francisco Xavier Street, 524 – 4033A, Rio de Janeiro (RJ), Brazil
[d] Rio de Janeiro State University (UERJ), Faculty of Geology (UERJ), Department of Regional Geology and Geotectonics (DGRG). São Francisco Xavier Street, 524 – 4033A, Rio de Janeiro (RJ), Brazil
[e] Tektos and GeoAtlântico groups (UERJ), Brazil

ARTICLE INFO

Keywords:
Magmatic environment
Explosive
Effusive
Subaqueous
Offshore magmatism
Well log data
Felsic rock
Mafic rock

ABSTRACT

The igneous rocks in the context of oil & gas exploratory sedimentary basins have been a paradigm and challenge for industry and academia due to the difficulty of reconnaissance and interpretation using indirect methods, *e.g.* geophysical data. We presented the combination of the petrographic and well log data of distinct magmatic sections from wells of Santos Basin, SE Brazil. Effusive and explosive felsic rocks, mafic volcanic subaerial and subaqueous and plutonic mafic rocks were recognized by petrography and petrophysics proprieties data, as radioactive (GR), electric resistivity (R), acoustic property (Δt), porosity (Φ) and density (ρ), showed different patterns along sections. This enables the division on magmatic subsections and allowed the recognition of rock types and igneous setting. The compositional influences are clearly distinguished by GR, as felsic and mafic rocks, presence of amygdales in mafic effusive rocks and inter-pillow intervals in subaqueous environments, can interfere with GR patterns. In plutonic environment, GR can show evidence of magmatic differentiation. Δt and Φ are directly proportional with similar pattern and both are inversely proportional to R and ρ. Felsic rocks, effusive or explosive, and inter-pillow intervals makes Φ and ρ curves closer. Less dense and more porous rocks, as explosive, tend to imprint the Φ and ρ pattern to the left of the log. Welding processes are distinguished by gradual decrease of Φ and increase of ρ. Otherwise, denser mafic rocks, volcanic or plutonic, tend to show separate Φ and ρ curves on the right of the log, while amygdaloidal portions are lighter and more porous than the massive one, showing the separate pattern on the left. The subaqueous mafic volcanic rocks imprint GR, ρ and Φ intermediate patterns between mafic massive and amygdaloidal. The recognition of the type of magmatic rock, the environment and the physical properties can aid to improve not only the decisions of exploration and production but also the elaboration of a geodynamic context for offshore sedimentary basins.

1. Introduction

Igneous rocks, either volcanic or plutonic, occur in petroleum systems in sedimentary basins worldwide (Farooqui et al., 2009; Eide et al., 2017a; Fornero et al., 2019; Descovi et al., 2021, Louback et al., 2021; Curtis et al., 2022; Marins et al., 2022; Zhang et al., 2023). Plutonic and volcanic magmatic processes are often related with the origin of rift basins and become recurrent during their evolution to passive margin sedimentary basins, such as in SE Brazil (*e.g.* Moreira et al., 2007; Winter et al., 2007; Amarante et al., 2023). Different emplacement settings (*e.g.*, plutonic and volcanic) as well as volcanic environments (*e.g.*, subaerial and subaqueous; effusive and explosive) may affect charge, migration, reservoir, trap and seal characteristics in any petroleum system (*e.g.*, Archer et al., 2005; Senger et al., 2017; Jackson et al., 2020; Zeng et al., 2023; Mangione et al., 2024). Additionally, igneous rocks present significant technical and scientific geological challenges for oil and gas

* Corresponding author.
E-mail addresses: b.queiroz18@hotmail.com (B.S. Queiroz), labmeg.ufrrj@gmail.com (S. de Castro Valente), andersonsantos@dmpi.com.br (A. Costa dos Santos), monica.heilbron@gmail.com (M. Heilbron).

https://doi.org/10.1016/j.jsames.2024.105095
Received 14 May 2024; Received in revised form 18 July 2024; Accepted 13 August 2024
Available online 17 August 2024

6.1.1 Abstract

The igneous rocks in the context of oil & gas exploratory sedimentary basins have been a paradigm and challenge for industry and academia due to the difficulty of reconnaissance and interpretation using indirect methods, e.g. geophysical data. We presented the combination of the petrographic and well log data of distinct magmatic sections from wells of Santos Basin, SE Brazil. Effusive and explosive felsic rocks, mafic volcanic subaerial and subaqueous and plutonic mafic rocks were recognized by petrography and petrophysics proprieties data, as radioactive (GR), electric resistivity (R), acoustic property (Δt), porosity (Φ) and density (ρ), showed different patterns along sections. This enables the division on magmatic subsections and allowed the recognition of rock types and igneous setting. The compositional influences are clearly distinguished by GR, as felsic and mafic rocks, presence of amygdales in mafic effusive rocks and inter-pillow intervals in subaqueous environments, can interfere with GR patterns. In plutonic environment, GR can show evidence of magmatic differentiation. Δt and Φ are directly proportional with similar pattern and both are inversely proportional to R and ρ. Felsic rocks, effusive or explosive, and inter-pillow intervals makes Φ and ρ curves closer. Less dense and more porous rocks, as explosive, tend to imprint the Φ and ρ pattern to the left of the log. Welding processes are distinguished by gradual decrease of Φ and increase of ρ. Otherwise, denser mafic rocks, volcanic or plutonic, tend to show separate Φ and ρ curves on the right of the log, while amygdaloidal portions are lighter and more porous than the massive one, showing the separate pattern on the left. The subaqueous mafic volcanic rocks imprint GR, ρ and Φ intermediate patterns between mafic massive and amygdaloidal. The recognition of the type of magmatic rock, the environment and the physical properties can aid to improve not only the decisions of exploration and production but also the elaboration of a geodynamic context for offshore sedimentary basins.

Keywords: Magmatic environment; Explosive; Effusive; Subaqueous; Offshore magmatism; Well log data; Felsic rock; Mafic rock

6.1.2 Introduction

Igneous rocks, either volcanic or plutonic, occur in petroleum systems in sedimentary basins worldwide (Farroqui *et al.*, 2009; Eide *et al.*, 2017a; Fornero *et al.*, 2019; Descovi *et al.*, 2021, Louback *et al.*, 2021; Curtis *et al.*, 2022; Marins *et al.*, 2022; Zhang *et al.*, 2023). Plutonic and volcanic magmatic processes are often related with the origin of rift basins and become recurrent during their evolution to passive margin sedimentary basins, such as in SE Brazil (e.g. Moreira *et al.*, 2007; Winter *et al.*, 2007; Amarante *et al.*, 2023). Different emplacement settings (e.g., plutonic and volcanic) as well as volcanic environments (e.g., subaerial and subaqueous; effusive and explosive) may affect charge, migration, reservoir, trap and seal characteristics in any petroleum system (e.g., Archer *et al.*, 2005; Senger *et al.*, 2017; Jackson *et al.*, 2020; Zeng *et al.*, 2023; Mangione *et al.*, 2024). Additionally, igneous rocks present significant technical and scientific geological challenges for oil and gas exploration (Millett *et al.*, 2016). For instance, magmatic sections in sedimentary basins may not be recognized using seismic surveys leading to a volumetric underestimation of plutonic and volcanic rocks within individual wells (Poprawa *et al.*, 2023). Problems can be even enhanced where felsic magmatic rocks occur as opposed to the more common mafic rocks drilled in the sedimentary basins due to the low density and compressional velocity of the former (Mark *et al.*, 2017). Such challenges have been partly overcome in more recent years by the correlation of 3D seismic data, laboratory experiments, petrophysical well log data and field work that allow the distinction between thick volcanic basaltic flows and intrusions of different shapes (Schofield *et al.*, 2016; Gao *et al.*, 2017; Muirhead *et al.*, 2017; Mark *et al.*, 2024).

Petrophysical data concerning porosity, permeability and density of rocks are often obtained by geophysical tools during well drilling for oil and gas exploration since they provide valuable information about their trapped fluids. In addition, gamma ray (GR, radioactive property), resistivity (R, electric property), sonic (Δt, acoustic property), neutron porosity (Φ) and density (ρ) data provide good approximations to the composition of rocks whereas sonic and density data provide information on textures and structures of rock formations (Boyer & Mari, 1997; Rider, 2000; Tiab & Donaldson, 2003; Flores *et al.*, 2006; Ellis & Singer, 2008). However, a different and cautious approach must be taken concerning magmatic rocks since those tools have been mostly used to probe sedimentary rocks. For instance, parameters like porosity and permeability can be related with the presence of vesicles and amygdales, veins and their respective mineral infillings rather than diagenetic structures. Another major issue is the alteration processes of magmatic rocks since low acoustic parameters due to alteration of mafic lavas can be mistaken

for overpressure (Osborne & Swarbrick, 1997; Curtis *et al.*, 2022), for instance.

The Santos Basin in SE Brazil originated as a rift basin during the Gondwana breakup in the Lower Cretaceous and evolved to a passive margin sedimentary basin now located offshore SE Brazil (Moreira *et al.*, 2007). It contains the most voluminous oil and gas reserves in Brazil, particularly within the reservoir rocks below its thick salt sequences (the so-called Pre-salt reservoirs). Abundant mafic plutonic and volcanic magmatic rocks, and minor felsic lithotypes, are interbedded with the Pre-salt sedimentary rocks in Santos Basin (Louback *et al.*, 2021; 2023; Scribelk & Valente, 2023) . Nevertheless, magmatic sections in wells in Santos Basin are commonly described as non-discriminated igneous rocks. This paper presents correlations between petrographic and petrophysical data of three wells drilled in Santos Basin, SE Brazil. The wells comprise magmatic sections with mafic plutonic and volcanic, effusive (subaerial and subaqueous) magmatic rocks, as well as felsic effusive and explosive volcanic rocks. The study of the thick magmatic sections in these three wells showed that mafic and felsic lithotypes can be discriminated by some petrophysical data obtained during drilling (e.g. Gamma-ray data) as proposed in previous works. However, in detail, it is also possible to discriminate plutonic as well as effusive and explosive volcanic, both subaerial and subaqueous, magmatic rocks based on a purely qualitative approach. It is expected that the application of the proposed methodology will reduce risks and costs during petroleum exploration in rift-to-drift sedimentary basins elsewhere.

6.1.3 Geology and tectonic setting of Santos Basin

The Santos sedimentary basin is located offshore SE Brazil (Figure 4). It is currently the main hydrocarbon exploratory basin of Brazil, particularly within the so-called Pre-salt reservoirs (Fernandez, 2017). It is a rift basin related with the break-up of Gondwana Supercontinent that evolved to a passive margin sedimentary basin during the opening of the South Atlantic Ocean (Chang *et al.*, 1988; Cainelli e Mohriak, 1999).

The depositional history of the Santos Basin begins at the Lower Cretaceous with the formation of the continental sedimentary rocks of the Rift Megasequence (Figure 5), following the intense volcanism coeval to the Paraná-Etendeka continental flood basalts (Peate, 1997). The Post-rift Megasequence (122-113 Ma) records the sedimentary deposition on restrict lagoon environments during tectonic quiescence, culminating with the formation of thick (up to 2,000 m) salt (halite and anhydrite) layers in the Late Aptian. The Drift Megasequence marks the progress of the open ocean stage, with marine sedimentation and formation of oceanic crust (Moreira *et al.*,

2007). There are four main magmatic events recorded in the chronostratigraphic chart of the basin, referred as such: the rift-related, Camboriú tholeiitic basalts, the poorly-known, post-rift-related magmatism, and the two drift-related, alkaline magmatic events that took place in the Campanian-Santonian and the Eocene (Figure 5).

Figure 4: Location of Santos Basin offshore SE Brazil. The voluminous hydrocarbon reservoirs of Santos Basin are within the Pre-Salt polygon (hachured).

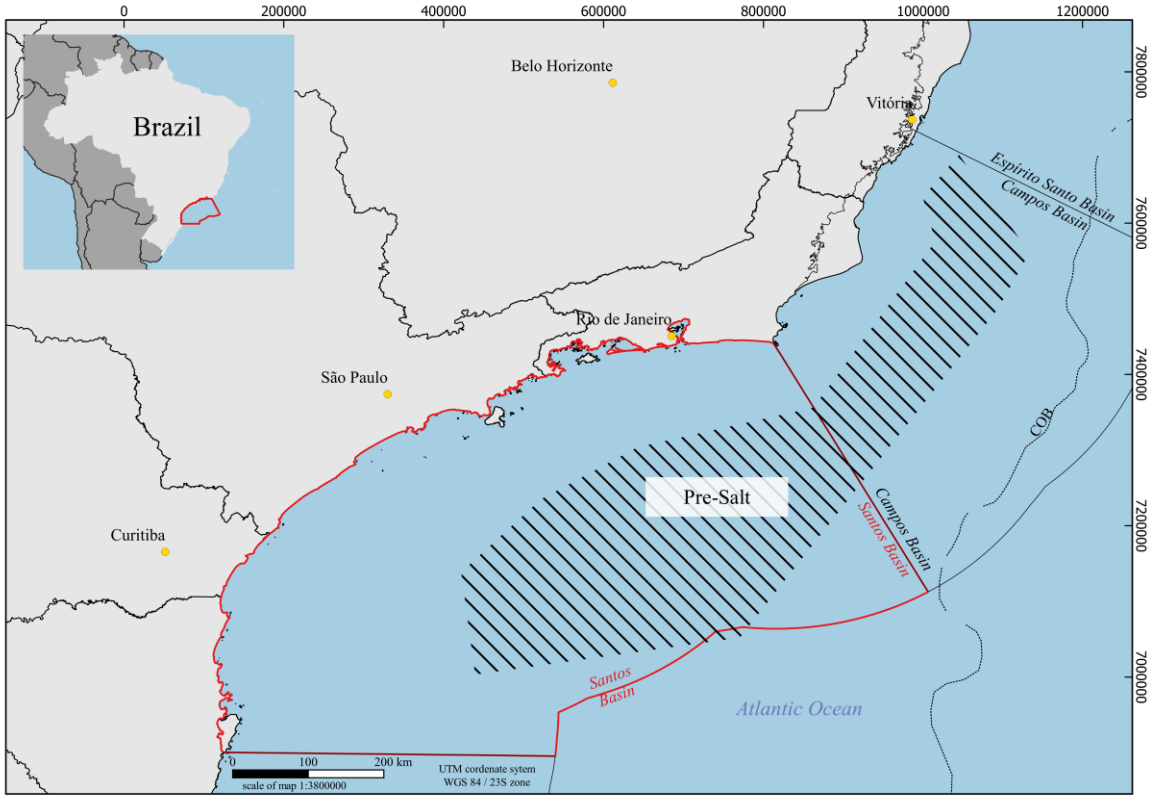

Reference: The author, 2024

6.1.4 Well log data and magmatic settings: a brief review

Gamma ray (GR, radioactive property), resistivity (R, electric property), sonic (Δt, acoustic property), neutron porosity (Φ) and density (ρ) are possibly the commonest data produced by different tools used to probe the petrophysical parameters of drilled sections (Rider, 2000). These well log data are used to obtain information not only on petrophysics but also on alteration processes due to hydrothermalism at contacts between sedimentary host rocks and plutonic magmatic rocks (Delpino & Bermudez, 2009).

Figure 5: Stratigraphic chart of the Santos Basin SE Brazil.

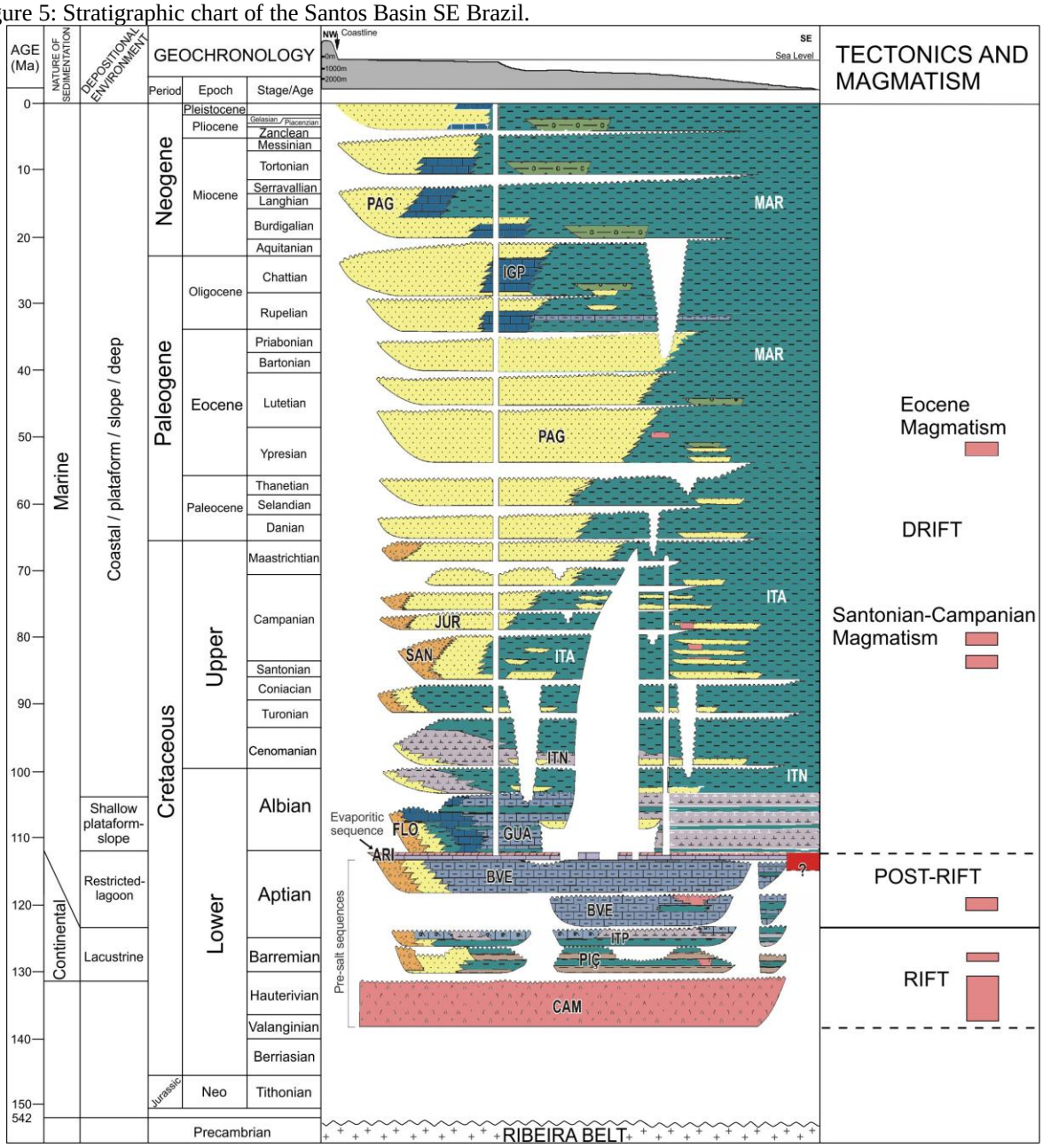

Note: The possible place of the initial occurrence of continental-oceanic boundary is marked by (?). The evaporitic sequence is pointed by a black arrow (Ariri Formation – ARI). The Pre-salt sequences represent the formations deposited before the evaporitic sequence: Camboriú (CAM), Piçarras (PIÇ), Itapema (ITP) and Barra Velha (BVE) formations.
Reference: Modified from Moreira *et al.* (2007).

The GR data provide the record of the naturally emitted radiation from minerals in a rock formation due to presence of 40K, 238U and 232Th isotopes (Rider, 2000). The qualitative evaluation of a GR log can give valuable information on the composition of the magmatic rocks in any given formation. For instance, GR values are higher in felsic acid and intermediate magmatic rocks than in mafic magmatic rocks since the former are richer in K, U and Th than the latter (Keys, 1979; Sanyal *et al.*, 1980). However, GR values of altered mafic magmatic rocks and weathered tops on K-rich lava flows are respectively higher and lower than those of their typical

unaltered counterparts because K is a mobile element (Planke, 1994; Bartetzko *et al.*, 2005; Millett *et al.*, 2021a). In addition, contacts between plutonic magmatic rocks and their respective wall rocks or between felsic and mafic magmatic lava flows can be depicted by abrupt changes in GR patterns (Delpino & Bermúdez, 2009).

The neutron porosity log records the Hydrogen Index (HI) of a rock formation, being directly related with the presence of fluids, as oil, gas or water (bound water, chemically bound water or free pore-water; Millward *et al.*, 2002; Rider, 2002). As such, it gives a good estimate of the rock porosity since most of the H, B, Gd, Sm in the formation is associated with fluids in the pores (Millward *et al.*, 2002). For igneous rocks the pores can be vesicles, intergranular pores, intercrystalline and intracrystalline pores, condensed contraction pores, devitrified pores, dissolved pores (from feldspars, volcanic ashes and carbonate-rich rocks), dissolved cavities, and fractures. The primary porosity is formed during the magma ascent and its emplacement, during intrusion, eruption, quenching, and crystallization. The secondary porosity is formed by post-emplacement processes, such as weathering, alteration, matrix and crystal dissolution, devitrification, and fractures (Zou, 2013; Rossetti *et al.*, 2019).

Resistivity logs record electrical currents passing through a rock formation. Resistivity data depends mostly on the presence of conductive, interstitial fluids in vesicles, amygdales, and joints. Therefore, there is a close relationship between resistivity and porosity (Rider, 2002). The easier an electrical current passes through the rock, the lower the resistivity of the formation, a fundamental characteristic of porous and permeable rocks. However, low values of resistivity may also be associated with the metallic conductivity due to the presence of sulfides, particularly pyrite, as opposed to the conductivity of fluids (Theys, 1991; Hamada *et al.*, 2001).

Density logs provide a continuous record of the apparent density (solid matrix plus fluids) of a rock formation. The results depend mostly on the density of the rock-forming minerals in a certain formation. Therefore, the density log is a good indicator of the lithology and may be used to identify rock forming minerals. Density values of basalts are between 2.7 and 3.2 g/cm^3, but typical values change due to the presence of alteration products, jointing, vesicles and amygdales (Rider, 2000).

The sonic log provides the traveling time of acoustic waves through a rock formation. It is affected by the composition and texture of the rocks, particularly when evaluated together with resistivity logs, since they are inversely correlated parameters. The more massive and less porous a rock, the greater the velocity of the acoustic wave and consequently the lower its traveling time or sonic value. Combined sonic and density values can also provide good information on the presence of joints in a rock formation. The way the acoustic wave travels through a rock is also closely related with its minerals, their sizes and the distributions and their cement and glassy

materials (Wyllie *et al.*, 1956).

Magmatic rocks vary in composition, texture and structure depending on their emplacement environment, regardless plutonic or volcanic. Sills, laccoliths and dikes are the most common plutonic structures in sedimentary basins (Schofield *et al.*, 2015, 2016; Eide *et al.*, 2017b, Mark *et al.*, 2018). Subaqueous volcanic environments give rise to basaltic pillow lavas, lobes and sheet lavas, associated with hyaloclastite, and inter-pillow clayish material (Walker, 1992). Subaerial flows originate different types of structures depending on the composition, viscosity and temperature of the lava, the presence of volatiles, the effusion rate and the topography (Rossetti *et al.*, 2018). Altogether, these volcanic structures observed in mafic and felsic magmatic rocks, as well as their textures, allow the reconstruction of magmatic paleoenvironments based on their plutonic and volcanic facies and facies associations (Walker, 1971; Waichel *et al.*, 2006, 2007, 2012; Nelson *et al.*, 2009; Tucker & Scott, 2009; Watton *et al.*, 2014; White *et al.*, 2015).

Variations in well log patterns are related with distinctive compositions, textures and structures of magmatic rocks (Bartetzko *et al.*, 2005; Trodstorf *et al.*, 2014). For instance, combined decreasing resistivity and density is related with high volume of joints, vesicles and amygdales of effusive, volcanic rocks which, in turn, may be associated with the cooling history, composition and volatile contents of their respective lavas. The GR patterns are also controlled by the composition of unaltered igneous rocks, either plutonic or volcanic (Bartetzko *et al.*, 2005).

Dolerite sills and dikes are the commonest shallow intrusions in sedimentary basins worldwide and their well log data strongly contrast with those of their sedimentary host rocks. For instance, the density of dolerite varies between 2.75 and 3.00 g/cm^3 and their sonic velocity is in excess of 5000 m/s, much lower than values for shales and sandstones (Bell & Butcher, 2002). GR values for dolerite are typically 35-45 API, but increasing GR patterns are attributed to a coarser grain size at the upper third of thick (> 50 m) sills that lack high amounts of glass, whereas an abrupt, box-shaped decreasing GR pattern has been attributed to dikes (Francis, 1982; Trodstorff *et al.*, 2014). In general, the sonic log (Δt) and porosity present low values for intrusions. Basic intrusions are associated with high resistivity values, although they can be low due to the presence of sulfides, particularly pyrite (Theys, 1991). In situ crystal accumulation may happen in sills thicker than 50 m. The GR pattern is directly proportional to the amount of SiO2 and incompatible elements such as K, Th and U and will become concave/decrease and convex/increase in sectors of crystal accumulation of mafic minerals and evolved differentiates within the sill, respectively (Millward *et al.*, 2002; Delpino & Bermudez, 2009; Marsh, 2015).

Gamma-ray logs can be used to obtain information about contacts between the sills and laccoliths and host sedimentary rocks by sharp change in the log curve. Apophysis detection is not possible by analyzing cuttings or by seismic studies but seems to produce abrupt increasing

gamma-ray patterns. The commonest alteration products of dolerite intrusions are chlorite and clay minerals, decreasing and increasing GR values, respectively (Delpino & Bermudez, 2009).

In subaqueous basaltic flows, the structure of the lava pile is vertically heterogeneous with pillows of variable dimensions and different amounts of inter-pillow material, particularly hyaloclastite (Macdonald, 1953; Walker, 1992). This heterogeneity is reflected in petrophysical logs with typical zigzag features in GR and density patterns. In general, GR average values are 7 GAPI, despite the association with K-rich alteration products from reactions with seawater. The porosity increases with intense fracturing and large inter-pillow space. The seawater and clay minerals fill that space, decreasing the resistivity and density values when compared to massive subaerial basalts (Pezard, 1990; Bartetzko *et al.*, 2003).

The pāhoehoe and ′a′ā are the two main types of subaerial basalts flows whose structures depend on the advance of the flow which, in turn, is controlled by temperature, viscosity, effusion rate, gas diffusion and topography (Macdonald, 1953; Walker, 1971; Duraiswami *et al.*, 2014). The pāhoehoe lava is typical formed at low effusion rates. The flow units inflate due to continuous eruptions and movement of the lava under a surface crust, creating an undulating surface. The internal structure of pāhoehoe flows comprises a jointed base with few amygdale/vesicle pipes, a massive and dense core, and an amygdaloidal/vesicular crust due to the volatile escape process. The inflation process generally gives rise to a continuum variation of the pāhoehoe flows, as hummocky-, sheet-, slabby-, rubbly-pāhoehoe and ′a′ā. The ′a′ā lava is marked by a viscous and slow flow, formed by a clinkery crust and a massive core. The base is formed by brecciated fragments of the crust and the frontal lobe (Macdonald, 1953; Walker, 1971; Self *et al.*, 1998; Duraiswami *et al.*, 2003, 2008, 2014).

The most striking difference between the subaerial pāhoehoe and ′a′ā lava lithofacies is the position of the amygdales/vesicles and the massive portion and the brecciated layer into the volcanic body. In general, the abundance of amygdales/vesicles and joints increase the porosity, GR and traveling time of the acoustic wave (Δt), while the density and resistivity decrease. The amount of amygdales/vesicles and joints is directly proportional to the intensity of the variation of the petrophysical data. However, the presence of minerals that fill the amygdales and joints can accentuate these typical patterns. Zeolite and celadonite can increase the amount of K affecting the GR data and increase the H index of neutron porosity for being hydrated minerals (also clay and chlorite). On the other hand, the massive portion is marked by high density, high resistivity, low porosity, low GR and low Δt (Planke 1994; Jerram *et al.*, 2009; Nelson et al, 2009, 2015; Millett *et al.*, 2016; Rossetti *et al.*, 2019; Millett *et al.*, 2021a,b).

Studies mostly performed in China have proved the success of using wireline data, often combined with elemental capture spectroscopy (ECS) and formation microresistivity imaging

(FMI), for interpreting felsic volcanic rocks in boreholes (Dezhi *et al.*, 1991; Ning *et al.*, 2009; Sun *et al.*, 2022). Volcanic felsic rocks present higher values of GR than mafic rocks (Zou *et al.* 2013; Ran *et al.*, 2014) due to the abundant presence of K, Th and U in their composition. The porosity of felsic rocks depends on the volatile content and the effusive/explosive character of the volcanism, decreasing and increasing in cohesive and non-cohesive rocks, respectively. However, welding can change porous pyroclastic rocks in tuffs with very low porosity. Felsic rocks are also less dense than mafic rocks, explosive ones being the lightest. The Δt values are greater for explosive felsic rocks than for effusive ones. Effusive felsic rocks have higher resistivity values than their explosive counterparts (Dellius *et al.*, 1998). Table 2 summarizes the main features presented in this section.

6.1.5 Materials and Methods

Magmatic sections of three wells (A, B and C) drilled in Santos Basin in SE Brazil were studied in this work. All sections occur at depths below the salt layers in Santos, i.e., are within the so-called Pre-salt sedimentary sequence. Thirty-five sidewall core samples of magmatic rocks recovered from drilling were selected for petrographic descriptions, being 14 from well A, 10 from well B and 11 from well C. Samples were washed under tap and distilled water before thin section preparation. The mineral compositions and respective modes, textures and structures of the samples were described under macroscopic and microscopic scales following the typical methodology applied to petrographic work. Textures were described according to Mackenzie *et al.* (1982) and McPhie *et al.* (1993). Rocks are aphanitic and preliminary classification under macroscopic scale was made based on simple criteria such as colour and magnetism (basalt being magnetic and black, dacite and rhyolite being non-magnetic and respectively grey and pinkish). This preliminary classification was further checked under microscopic scale based on mineral composition, either in the groundmass or as phenocrysts. Quartz-bearing rocks were classified as dacite or rhyolite whenever alkalifeldspar and plagioclase could be identified in combination with quartz, respectively. Rocks were classified as basalt whenever plagioclase and pyroxene were identified in the rocks. The geophysical logs of the wells were provided by the Petroleum National Agency of Brazil (Achronome in Portuguese is ANP which stands for Agência Nacional de Petróleo, gás natural e biocombustíveis) and include Gamma Ray (GR), Resistivity (R), Sonic log (Δt), Neutron porosity (NPHI - Φ) and Density (RHOB - ρ) data.

Table 2: Types of magmatic rocks, their geochemical compositions, structures and likely environments discriminated by typical well log patterns.

Log pattern	Rock types	Composition	Structure	Environment
Increasing GR	Unaltered[(1)] andesite to rhyolite and their respective shallow intrusions.	Felsic, intermediate ($52 < SiO_2 < 65$ wt.%) to acid ($SiO_2 > 65$ wt.%).		Subaerial effusive volcanism.
Decreasing GR	Unaltered[(1)] basalt and their respective shallow intrusions (*i.e.*, dolerite).	Mafic and basic ($45 < SiO_2 < 52$ wt.%).		Subaerial, effusive fissural volcanism.
Increasing Φ; increasing Δt decreasing R[(2)]	Amygdaloidal and veined basalt and their respective intrusions (*i.e.* dolerite). Volcanic tuffs.	Gd- and Sm-rich felsic alkaline and felsic acid.	Vesicles, joints and corroded megacrysts.	Top-bottom sections and entablature or colonnade sections of thick basaltic flows of subaerial, effusive fissural volcanism. Subaerial explosive volcanism.
Decreasing Φ; decreasing Δt increasing R	Massive basalt and their respective intrusions (*i.e.* dolerite). Welded volcanic tuffs.	From mafic basic to felsic, intermediate to acid.	Massive and strongly welded.	Middle sections of thick basaltic flows of subaerial, effusive fissural volcanism. Subaerial, strongly explosive volcanism typical of PDC.
Increasing ρ	Unaltered basalt and their respective shallow intrusions (*i.e.*, dolerite).	Mafic and basic ($45 < SiO_2 < 52$ wt.%).	Massive.	Middle sections of thick basaltic flows of subaerial, effusive fissural volcanism.
Decreasing ρ	Unaltered[(1)] andesite to rhyolite and their respective shallow intrusions. Volcanic tuffs.	Felsic, intermediate ($52 < SiO_2 < 65$ wt.%) to acid ($SiO_2 > 65$ wt.%).	Massive.	Subaerial, effusive or explosive volcanism.

Caption: PDC = pyroclastic density currents (i.e. flows and surges); Gamma Ray (GR), Resistivity (R), Sonic log (Δt), Neutron porosity (NPHI - Φ) and Density (RHOB - ρ). Log patterns refer to increasing or decreasing patterns, either abrupt or continuous, along well logging.
Note: (1) – Alteration due to hydrothermalism and weathering may change typical GR and ρ values. *(2)* – Presence of sulfides and oxides may change typical resistivity values.
Reference: The author, 2024

6.1.6 Well logs data

6.1.6.1 Well A

Felsic (andesite, rhyolite and dacite) and mafic (basalt) rocks occur in a thick (895 m) magmatic section in well A (AF and AM sections, respectively; Figure 6). The nearly 100 m-thick felsic section (AF) has been divided in 3 subsections (bottom, middle and top) on the basis of their different log data. The top subsection (10 m thick) shows GR values from 30 to 120 API, R values

from 1 to 20 ohm.m, and Δt from 60 to 90 μs/ft. The Φ varies from 15% to 39% and ρ from 2.2 to 2.5 g/cm³. The Φ and ρ curves overlap along the AF section, exception made for the very top subsection (Figure 6). The R and ρ patterns increase while Δt and Φ decrease gradually in the middle subsection. The GR values vary from 105 to 135 API, Δt from 60 to 80 μs/ft, Φ varies from 9% to 21% and ρ varies from 2.3 g/cm³ to 2.6 g/cm³, and R values from 3 to 20 ohm.m. The bottom subsection shows regular vertical patterns. The GR values are high (105-135 API) as well as R values (20-300 ohm.m). Δt and Φ present low values, between 50 and 60 μs/ft and 3-15%, respectively. Values of ρ varies from 2.5 g/cm³ to 2.6 g/cm³.

The mafic section (AM) of well A has been divided into 3 subsections (Figure 6). The highest GR (45-60 API), Δt (60-80 μs/ft) and Φ (21-27%) values and the lowest R (2-10 ohm.m) and ρ (2.5-2.6 g/cm³) values are those in the top subsection. Values of R (6-30 ohm.m), Δt (50-60 μs/ft), Φ (9-15%) and ρ (2.8-3.0 g/cm³) vary gradually and imprint oblique log patterns along the middle subsection, whereas GR values are lower and less variable (30-45 API) than along the top subsection. Log patterns along the bottom subsection are less variable and nearly vertical, exceptions made for R.

6.1.6.2 Well B

Well B is composed of 625 m of mafic rocks interbedded with coquinas from the Itapema Formation. One representative section of magmatic rocks (B section; Figure 7a) with 10 samples was selected for study. Magmatic section B is 83 m in thickness, being underlain and overlain by mudstone and coquinas (Figure 7a). GR patterns are irregular, with intermediate to high values (30 to 75 API, but locally as low as 15 API). The R values are highly variable, ranging from 10 to 1000 ohm.m, with a predominance at 20 to 100 ohm.m. The Δt values are regular at 50-60 μs/ft. The density values vary from 2.5 g/cm³ to 2.8 g/cm³. The Φ varies from 9% to 15%, with a local highest peak at 21%.

Figure 6: AF and AM magmatic section of well A with their respective GR (gamma-ray), R (resistivity), Δt (sonic), Φ (porosity) and ρ (density) parameters.

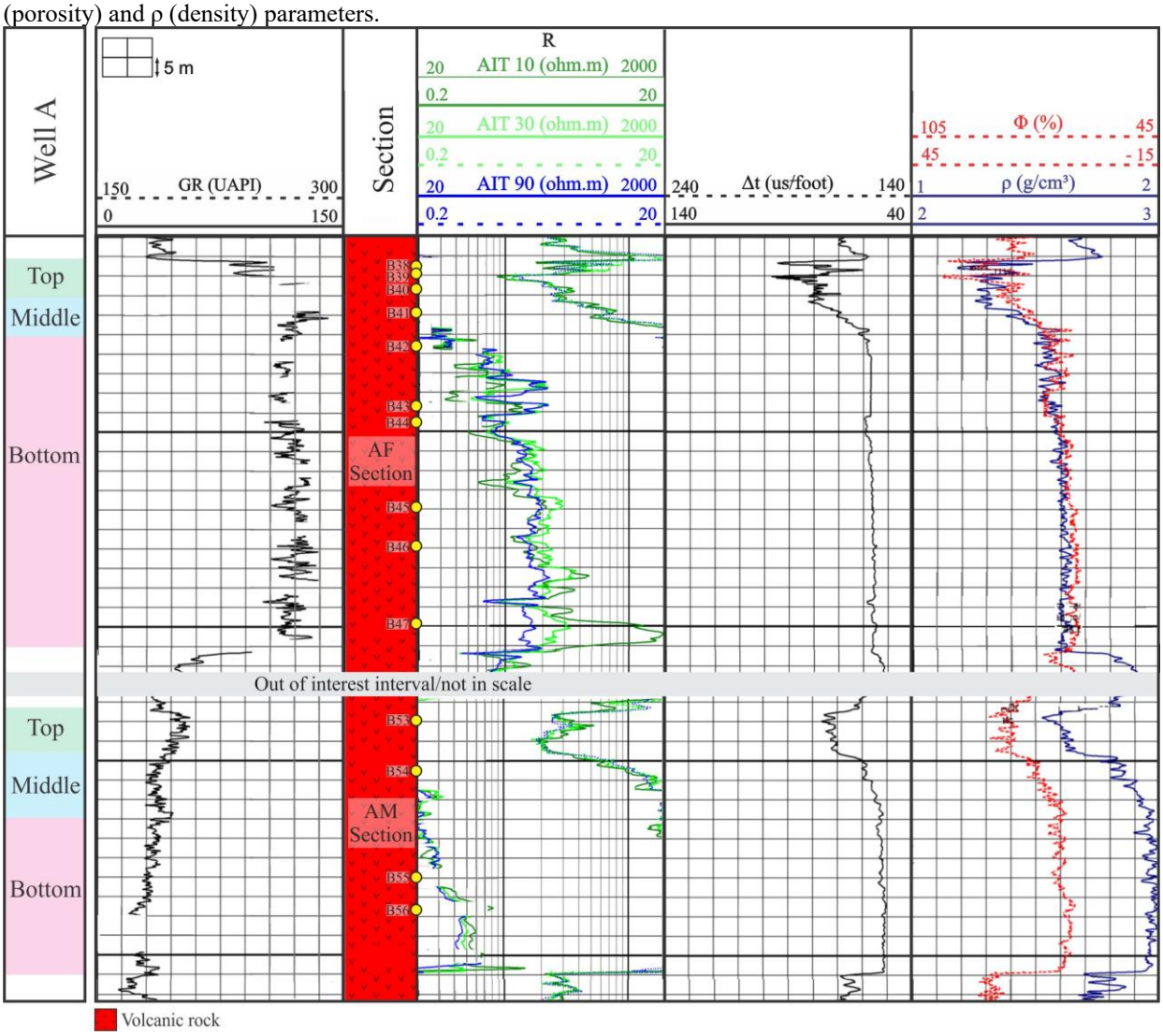

Note: Samples indicated by yellow dots.
Reference: The author, 2024

6.1.6.3 Well C

Well C is formed by 720 m of interbedded magmatic and volcaniclastic rocks below a thick sequence of sedimentary rocks composed of claystone, shale, sandstone, marl, calcilutite, halite and anhydrite. Eleven sidewall core samples from a 150 m-thick magmatic section (C section) were selected for this study (Figure 7b). There is a notable change of patterns allowing the discrimination of two subsections. The top subsection presents higher and more variable GR, Δt values as well as slightly lower Φ values and more variable density values than the bottom subsection (Figure 7b). The GR values vary between 15-30 API showing a sudden peak at 75 API and a gradual return to around 30 API towards the well top. The Δt values are lower than 50 μs/ft at

the bottom of the section, changing to higher than 50-60 µs/ft towards the top. The Φ values show few variations (9-15%) along the log. The ρ parameters present an irregular and gradual decrease from 3.0-2.9 g/cm³ to 2.9-2.8 g/cm³ at its bottom portion, followed by peaks at values higher than 3 g/cm³ and lower than 2.5 g/cm³ which coincide with GR highest peaks. The density values show an irregular and gradual increase from 2.6 to 2.9 g/cm³ until the top of the section. The R parameters show values between 1-10 ohm.m at the bottom portion of the section, with a gradual decrease to 0.4 ohm.m followed by a continuous increase to 3 ohm.m towards the top.

Figure 7: Magmatic sections of wells B and C with their respective GR (gamma-ray), R (resistivity), Δt (sonic), Φ (porosity) and ρ (density) parameters.

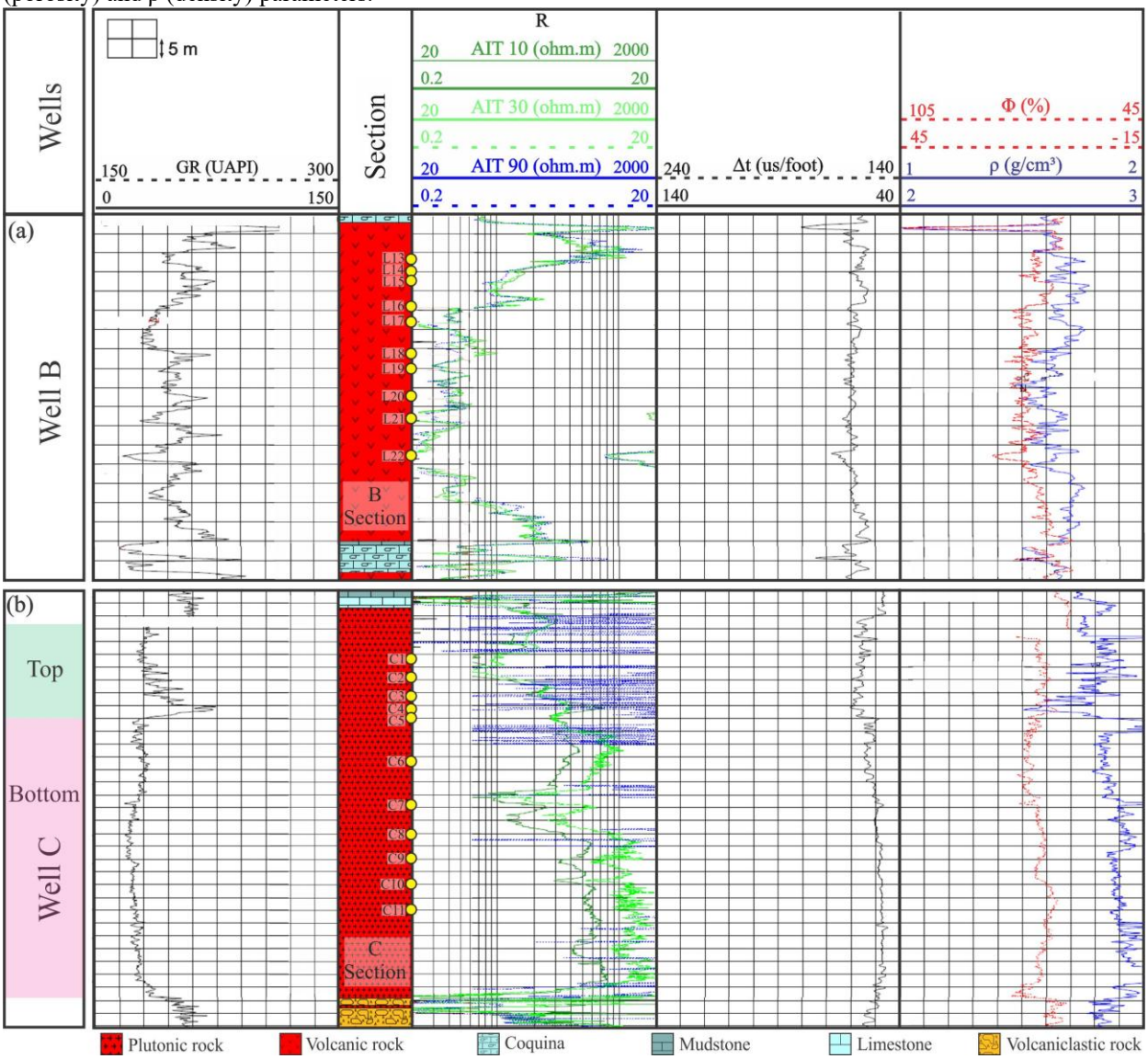

Caption: (a) - B section in well B. (b) – C section in well C.
Note: Samples indicated by yellow dots.
Reference: The author, 2024

6.1.7 Petrography

6.1.7.1 Well A

Samples in AF and AM magmatic sections in well A are volcanic rocks attested by the presence of abundant devitrified glass as spherulites. Both effusive and explosive volcanic rocks occur at upper part of the AF section, with tuff and welded tuff associated with volcaniclastic rocks at some depth intervals. The remaining of the section is composed of effusive rocks only, represented by dacite and rhyolite. In turn, massive and amygdaloidal basalts comprise the AM mafic section in well A.

The volcanic rocks along the AF section are essentially formed by quartz, feldspar, pyroxene, amphibole, and plagioclase (Figure 8a). The Fe-Ti oxides, apatite and zircon occur as accessories minerals. The most common alteration products are carbonate, zeolite, calcite, saussurite, chlorite, talc and sericite. The rocks are inequigranular and porphyritic, with feldspar megacrystals. Both effusive and explosive rocks have broken/fragmented grains. The texture of the matrix is hypohyaline with fine grained and subhedral to anhedral minerals (Figure 8b). The main textures of the volcanic rocks are ophitic and subophitic, besides perlitic and welded. Amygdales, carbonate veins and flow banding are common, mostly among the explosive rocks. The main difference noted between dacite and rhyolite samples is the bedding, with different amounts of spherulite, devitrified glass or shards in layers which are present in the rhyolite samples. The tuffs and welded tuffs present the most striking features of fragmentation and reworking. The welded tuffs have eutaxitic textures, flow banding, feldspar grains arranged parallel to bedding and clasts of basalts (Figure 8c).

The mafic rocks within the AM section are basalts composed of plagioclase, pyroxene and olivine (or as pseudomorphs of iddingsite and soponite) in addition to altered volcanic glass. The accessory minerals are Fe-Ti oxides and leucoxene. Carbonate, chlorite and zeolite fill amygdales or fractures. Basalts are either hypohyaline or hypocrystalline, plagioclase or pseudomorphic olivine-phyric rocks with porphyritic and glomeroporphyritic textures. The matrix is vitreous or fine grained, with undercooling textures like swallow-tail and skeletal plagioclase crystals. The main textures are intersertal, intergranular, subophitic and synneusis. Massive and amygdaloidal basalts occur along the section. The massive ones occur in the middle of the section (Figure 8d). The amygdaloidal rocks are concentrated on top of the section AM (Figure 8e), with amygdales of various formats (circular, sub-circular or irregular) and sizes. Connected amygdales is a very common feature (Figure 8f), as micro-amygdales restrict to the interstices of the matrix. The

amygdaloidal texture is related with the degree of crystallinity; the more vitreous, the more amygdaloidal the rock is.

Figure 8: Photomicrographs of main petrographic features of samples in the magmatic sections of well A.

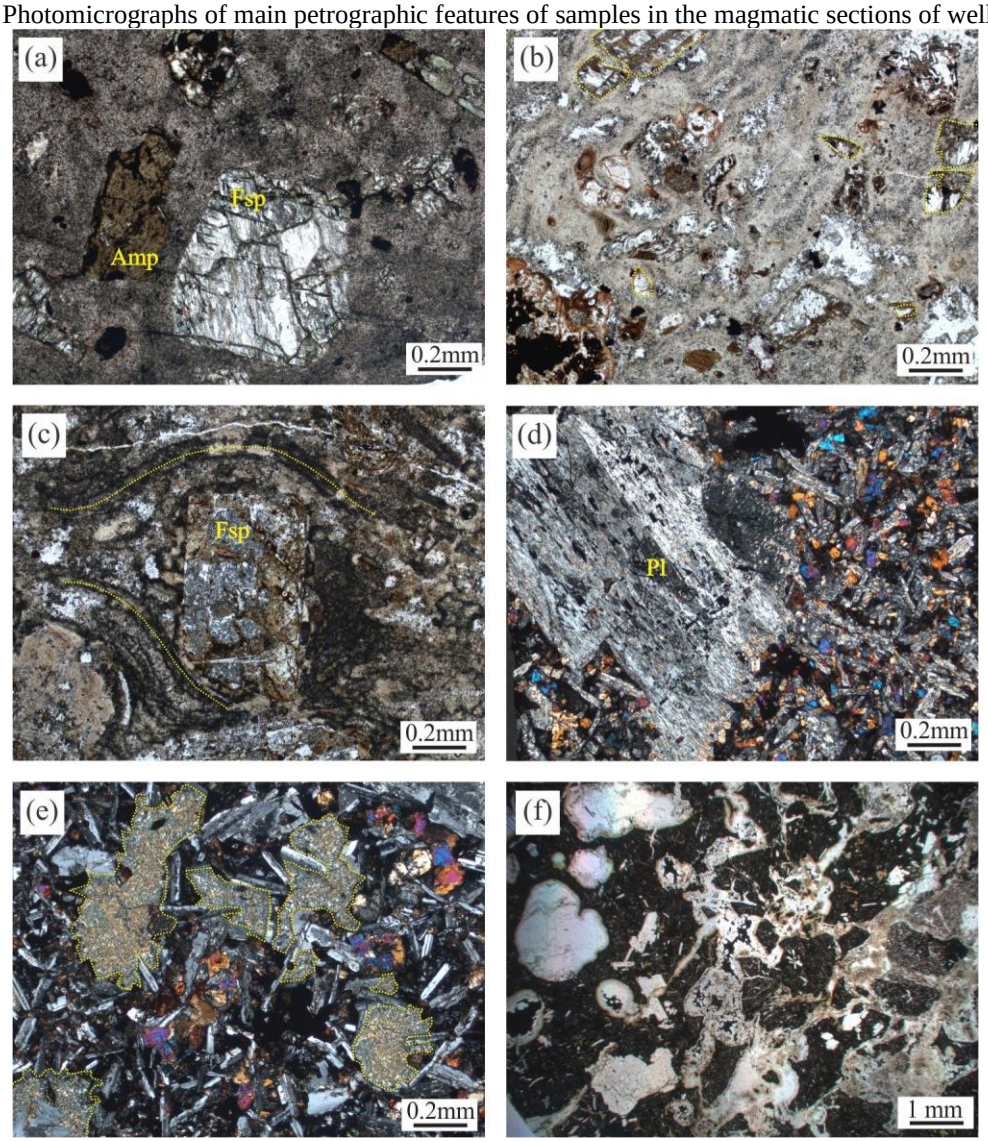

Caption: AF section: a) matrix of dacite with feldspar and amphibole crystal (sample B47), b) matrix of rhyolite with fragmented crystals (sample B42) and c) tuff with flow banding around altered feldspar (sample B41); AM section: d) massive plagioclase-phyric basalt (sample B55), e) amygdaloidal basalt (sample B54) and (f) connected amygdales partially filled by zeolite (sample B53).
Note: Parallel Nicol: (a), (b), (c) and (f); Cross Nicol: (d) and (e).
Reference: The author, 2024.

6.1.7.2 Well B

The B magmatic section in well B is formed by very altered micro-amygdaloidal, and brecciated basalts. The samples are either hypohyaline or hypocrystalline depending on the amount of altered volcanic glass. The basalts are inequigranular, porphyritic and

glomeroporphyritic rocks with a megacryst assemblage composed by plagioclase and pseudomorphic olivine. The matrix is fine grained and composed by plagioclase, altered olivine, pyroxene and abundant glass. The glass is devitrified and/or altered to palagonite. Quenching textures are notable (Figure 9a), as swallow-tail and skeletal ones. Other typical textures of these basalts are ophitic/subophitic, intergranular and intersertal. The basalts of the B section show different types of undercooling matrix in the same sample. The textures differ by the amount of glass and crystal sizes. The contact between these distinctive matrixes is irregular, with one encompassing each other. Usually, this contact is marked by ripform plagioclase crystals of the coarser portion of the matrix arranged tangentially to the finer portion (Figure 9b). A holohyaline or hypohyaline, undercooling margin is common around amygdales, veins and fractures.

The presence of amygdales is a remarkable characteristic of basalts in section B. They are filled by carbonate and occur in variable shapes and sizes, such as small (< 2mm) and irregular and bigger (up to 4 mm), spherical-to-elliptical. Another common feature in all samples is the presence of carbonate and pyrite. Carbonates occur filling fractures, amygdales and interstices but also as batches in contact with the magmatic rock. In the first case, the carbonate is fine to very fine, anhedral, beige or gray. In the last case, the carbonate batches are fine, subhedral to euhedral, typically beige with pastel tones and pleochroic. There are volcanic clasts on carbonate batches (Figure 9c).

6.1.7.3 Well C

The magmatic section C in well C comprises glass-free, medium-to-coarse grained basalts, hereby classified as dolerites. The essential mineral composition is plagioclase and pyroxene with opaque minerals and apatite as accessory phases. There are three types of plagioclase crystals: i) fine- to medium-grained, subhedral crystals enclosed by large pyroxene crystals; ii) medium-grained, euhedral, tabular, aligned crystals; iii) coarse-grained, subhedral crystals in irregular contact with coarse-grained pyroxene. The plagioclase crystals often are zoned (Figure 9d) and/or with multiple twinning. The pyroxene crystals are coarse grained, with some subordinated medium-grained crystals. The coarser pyroxene crystals enclose the finer minerals, mainly fine- and medium-grained plagioclase crystals but also medium- and coarse-grained apatite, imprinting a poikilitic texture to some samples (Figure 9e). Some pyroxenes crystals show fractures and reaction rims. The simple twinning is a very common feature in these minerals. The presence of biotite is common as an alteration phase along the rims or even in fully pyroxene

crystals. The opaque minerals are most abundant in rocks at shallower depths of section C. They are medium- to coarse-grained minerals with skeletal habit, being commonly related with pyroxene or biotite. The apatite crystals are medium- to coarse-grained, euhedral, tabular or acicular. The medium-grained apatite crystals are enclosed by pyroxene.

Dolerites at deeper portions of magmatic section C are finer than those at shallower depths. The poikilitic texture is more frequent in dolerites at deeper levels. Furthermore, the medium-to coarse-grained plagioclase crystals of dolerites at deeper intervals are often mutually aligned. On the other hand, dolerites at shallower depths are coarser and often lack poikilitic textures. Some of these dolerites present textures akin to cumulative processes (Figure 9f).

Figure 9: Photomicrographs of main petrographic features of samples in the magmatic sections of well B and C.

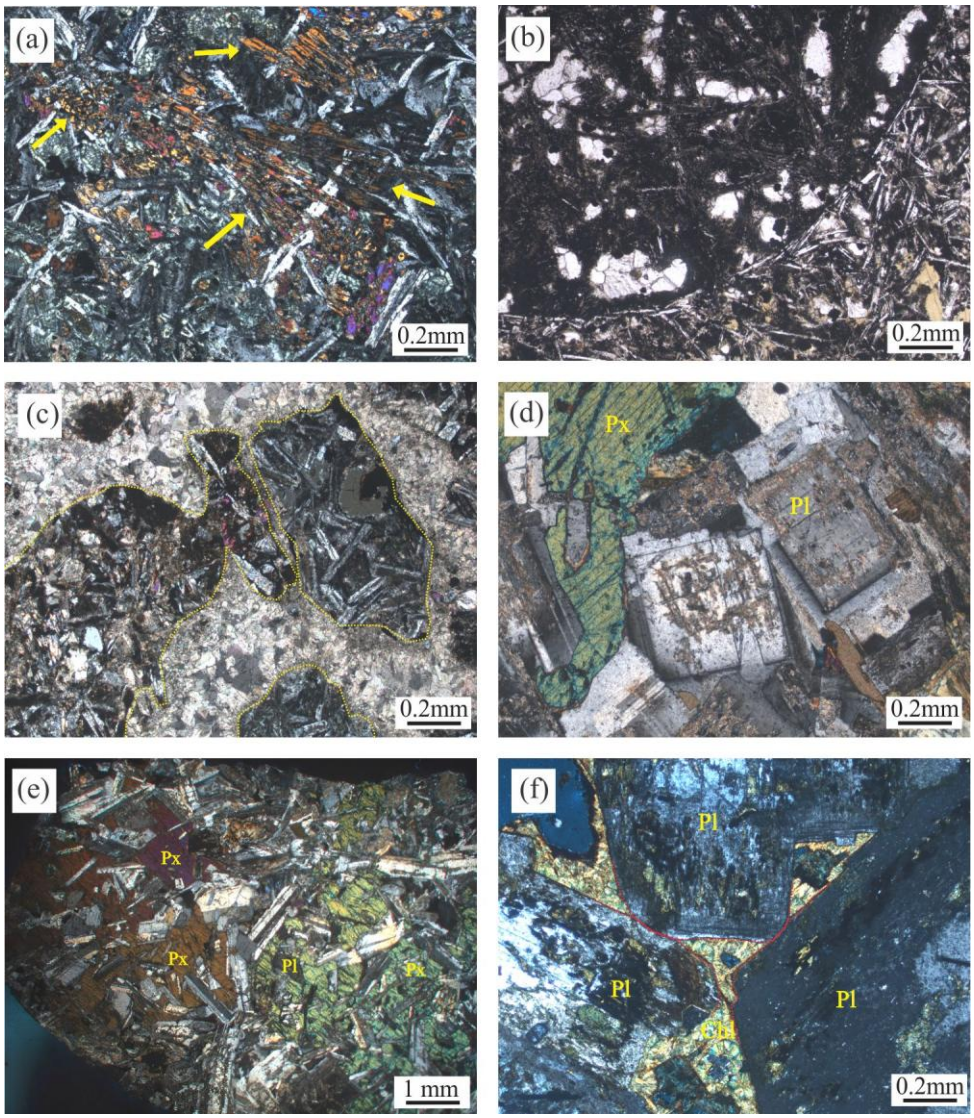

Caption: Well B – B section: a) quenching texture depicted by elongated/skeletal pyroxene crystals (sample L17), b) different undercooling textures with fine plagioclase laths tangentially arranged around the finer portion of the matrix (sample L14) and c) volcanic clasts in carbonate batches (sample L18); Well C – C section: d) zoned plagioclase crystals (sample C8), e) poikilitic texture with plagioclase crystals enclosed by pyroxene (sample C11) and f) plagioclase megacrystals imbrication with trapped material altered to chlorite (sample C5).
Note: Parallel Nicol: (a), (b), (c), (f) and (h); Cross Nicol: (d), (e), (g), (i), (j), (k) and (l).
Reference: The author, 2024

6.1.8 Discussions

Magmatic sections AF, AM, B and C contain different volcanic rocks, from felsic to mafic as well as from explosive to effusive and even plutonic mafic ones as depicted by petrographic data. Mafic, effusive volcanic rocks (basalts) occur in both AM sections of well A, and B section of well B. On the other hand, mafic plutonic rocks (dolerites) occur along magmatic section C of well C. In addition, felsic volcanic rocks (mostly dacite and rhyolite), both effusive and explosive, occur along section AF in well A. Differences in values of geophysical parameters and their respective log patterns, such as GR, can be promptly related with the different compositions of the rocks along AM and AF sections (Figure 6), as noted in previous works (e.g. Bartetzko *et al.*, 2005; Trodstorf *et al.*, 2014). However, more subtle variations in log values and patterns for felsic and mafic rocks themselves cannot be solely related with different lithotypes and probably result from distinctive fabrics (i.e. textures and structures) due to generation in different magmatic environments (e.g. volcanic x plutonic; explosive x effusive), as discussed in the following sections.

6.1.8.1 Explosive *versus* effusive felsic volcanism

The AF Section (Figure 6) has been divided in three subsections (top, middle and bottom) according to petrographic and petrophysical differences. The top and middle subsections comprise explosive rocks (hereafter AF*ex* interval; Figure 10) such as non-welded tuff (sample B38) and welded tuff (B41), whereas the bottom subsection is formed by effusive dacite (B45) and rhyolite (B43) (hereafter AF*ef* interval; Figure 10). The GR, R and ρ values are lower but Δt and Φ are higher along AF*ex* when compared with AF*ef* (Figure 6). GR values are much more variable along AF*ex* than along AF*ef* although values at the bottom of AF*ex* tend to equal those along AF*ef*. Therefore, it may be difficult to distinguish felsic volcanic explosive and effusive rocks based on GR values only. In detail, it may be noted that R, ρ, Δt and Φ vary gradually along the middle subsection within AF*ex*. The gradual increase in values of R and ρ and gradual decrease in values of Δt and Φ is possibly a consequence of increasing welding of the tuffs in AF*ex*.

Despite the natural low density of volcanic felsic rocks due to their mineralogical composition, as much as 20% (ca. 2.2 to 2.6 g/cm^3) increment in ρ values and nearly three times reduction in Φ values (average 27% to 10%) (Figure 10) may be related with different volcanic environments of felsic rocks. Ash-rich, pyroclastic rocks such as tuffs, originated in explosive

settings, are fine grained, light materials with lower density and higher porosity when compared with their effusive, cohesive compositional counterparts such as dacite and rhyolite. Welding processes associated with explosive volcanic environments can decrease porosity, closing spaces by rapid volume reduction due to amalgamation and cooling whereas porosity reduction in cohesive volcanic rocks is highly dependent on the existence of fractures, vesicles or amygdales that are not always found in effusive volcanic felsic rocks (Sruoga *et al.*, 2004). As a result, there will be a tendency for Φ and ρ logs to shift to the right along log sections, sometimes gradually, when felsic, explosive volcanic rocks give place to felsic, effusive volcanic rocks from top to bottom of well profiles (Figure 10).

Effusive and explosive, felsic volcanic rocks can also be distinguished by patterns of the Δt log (Figure 6). The explosive rocks have textures that result in more variable and higher time travelling than those of the effusive volcanic rocks. As such, the sonic log pattern will tend to shift to the right in sections where explosive volcanic felsic rocks overlain the effusive ones, as with the Φ, ρ and R patterns. The sonic log patterns will decrease gradually with increasing welding of the explosive rocks (Figure 6).

The effusive rocks along the AF*ef* interval vary in textures but such differences are difficult to be related with the well log patterns (Figure 10). The matrix of the effusive dacite and rhyolite at the top of the AF*ef* interval are heterogeneous, with patches of glass with variable alteration (samples B42 and B43). These rocks are underlain by effusive dacite with homogeneous, massive matrix that, in turn, overlain effusive dacite with slightly layered structures. In detail, the dacite and rhyolite at the top have more variable, superimposed and slightly higher Φ and lower ρ values than dacites at the bottom of AF*ef* interval (Figure 6). Similarly, Φ and ρ patterns tend to be lesser mutually superimposed towards the slightly layered dacite at the very bottom of AF*ef* interval (Figure 6). Nevertheless, all these differences in log patterns along the AF*ef* interval are subtle and further inference may be too speculative. The main discriminating log values and patterns to distinguish explosive from effusive, volcanic felsic rocks are listed in Table 3.

Figure 10: The AF magmatic section of well A with respective porosity (Φ) and density (ρ) logs and photographs and microphotographs of representative samples.

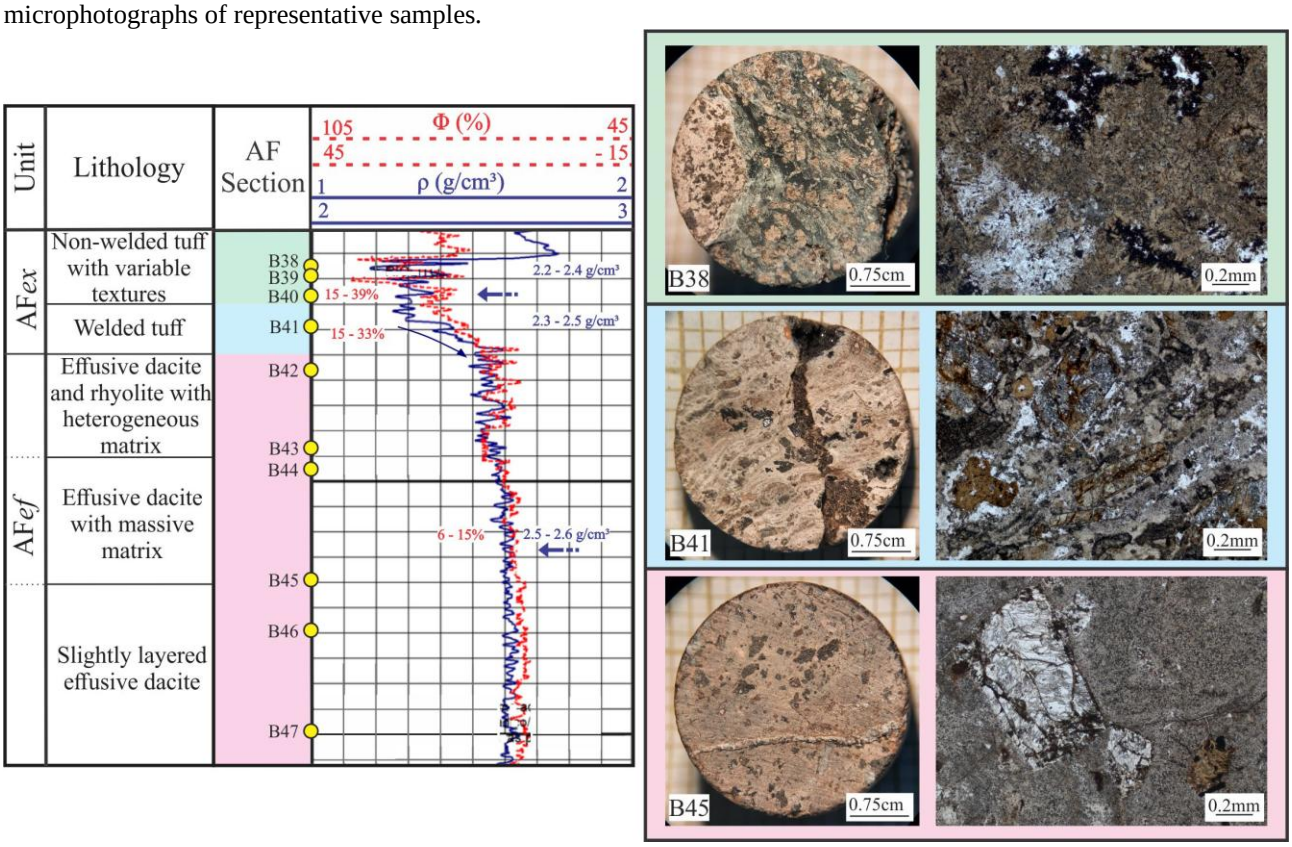

Note: The AF*ex* interval with high Φ and low ρ is represented by a non-welded tuff (sample B38) and welded tuffs with fiammes (sample B41). The AF*ef* interval is represented by massive dacite (sample B45) and rhyolite.
Reference: The author, 2024

Table 3: GR, R, Δt, Φ and ρ patterns discriminated for felsic and mafic rocks, as well as volcanic and plutonic, explosive and effusive, massive, amygdaloidal and subaqueous.

Rocks			GR	R	Δt	Φ	ρ	Relation Φ and ρ curves
Felsic	Extrusive	Explosive	↑	↓	↑	↑	↓	Overlapping
		Effusive	↑	↑	↓	↓	↓ (1)	
Mafic		Amygdaloidal	↑ (2)	↓	↑	↑	↓	Separate
		Massive	↓	↑	↓	↓	↑	
		Subaqueous	↑ (3)	↑	↓	↓	↓	Predominantly separate curves with approximation on inter-pillow portion
	Intrusive		↓	?	↓	↓	↑	Separate

Caption: (1) Similar to mafic amygdaloidal ρ pattern; (2) Lower than felsic pattern; (3) Between mafic and felsic pattern.
Reference: The author, 2024

6.1.8.2 Distinctive features between volcanic, effusive felsic and mafic rocks

The felsic and mafic classification of magmatic rocks is based on their mineralogical composition, i.e., the amounts of feldspar and mafic (Mg- and Fe-rich) phases, respectively. This,

in turn, reflects the chemical composition of those rocks. Felsic rocks are formed mostly by feldspar, quartz, and feldspathoid, showing light colouring. This mineralogical assemblage is a result of a high silica content (SiO_2 > 52 wt.%), allowing them to be chemically classified as intermediate and acid rocks. Mafic rocks are rich in ferromagnesian minerals, particularly silicates, such as pyroxene and olivine, showing dark colouring and a lower rate of silica (45% < SiO_2 < 52 wt.%), implying a basic composition. Ultramafic rocks are even richer in mafic minerals and usually ultrabasic (SiO_2 < 45 wt.%) but are rare in most Phanerozoic sedimentary basins in Brazil, except for intrusions of alkaline and ultramafic lamprophyres and minor ankaramite flows (e.g. Louback *et al.*, 2021). Felsic, intermediate to acid rocks are richer in K than mafic, basic magmatic rocks, once this element is the major constituent of feldspar and feldspathoid. This also is valid for U and Th (Schön, 2015). In addition, felsic minerals are denser than mafic minerals making basic, mafic rocks, such as basalts, denser than felsic intermediate dacites and acid rhyolites, despite the fact changes in density values may result from alteration.

Probably, basalts are the most common effusive, mafic rocks found in rift-to-drift, Phanerozoic sedimentary basins worldwide, and it is certainly the case for Santos and other Gondwana-related basins in SE Brazil (e.g. Moreira *et al.*, 2007; Winter *et al.*, 2007). Effusive, felsic rocks are less common but should also be expected since the formation of rift basins during supercontinent fragmentation is often associated with bimodal, felsic-mafic volcanism of the CFB, such as Paraná-Etendeka (e.g., Peate, 1997). Thus, the magmatic section A provides a good opportunity to test for the discrimination between effusive mafic (AM section) and felsic (AF*ef* interval) rocks on the basis of their well log values and patterns (Figure 6).

The main differences between the effusive felsic and mafic rocks are depicted by their GR and ρ logs (AM and AF*ef* in Figures 6 and 10) since both are indirect compositional tools (Ellis & Singer, 2008). However, even GR and ρ logs may be deceptive due to the existence of different textures of basalts, as may be seen in detail along the three subsections of AM section (Figure 3). The top and middle subsections comprise amygdaloidal basalts but amygdales in the top subsection (AM*ag1* interval; Figure 11) coalesce greatly, enclosing angular to subangular patches of fragmented, vitrophyre (sample B53). Amygdales of amygdaloidal basalts within the middle subsection (AM*ag2* interval; Figure 11) are subcircular and isolated, with no evidence for coalescence, being immersed in a glass-rich, massive matrix (sample B54). The GR values and respective log patterns are affected by the textures of the amygdaloidal basalts within the AM*ag1* interval, becoming more variable and higher, particularly at the very top, due to the presence of K-rich minerals as zeolite and celadonite (Planke, 1994; Jerram *et al.*, 2009; Nelson *et al.*, 2009, 2015; Millett *et al.*, 2016; Rossetti *et al.*, 2019; Millett *et al.*, 2021a,b). Similarly, these basalts are less dense (lower ρ values, as a consequence of infilling of amygdales by carbonate and clay

minerals) and more porous (higher Φ values, possibly due to the presence of microfractures in the fragmented patches of vitrophyre) than those within the middle and bottom subsections (Figure 11), also leading to higher Δt values. The R patterns are also affected by the textures of basalts in the AM*ag1* and AM*ag2* intervals, being rather variable but tending to increase gradually along the latter, becoming less variable towards and along the bottom subsection, possibly as a consequence of decreasing porosity (Figure 11). Ultimately, both in AM and AF sections, the R increases from the more porous to the less porous interval (Figure 6). It shows that the resistivity is inversely proportional to porosity (Brewer *et al.*, 1998). Furthermore, the felsic rocks (both explosive and effusive) show ca. 2 times higher values of R than mafic rocks which matches with the greater porosity of the felsic ones. It is important to consider the alteration processes which can increase Φ and Δt, and decrease R and ρ (Dentith *et al.*, 2019), although it is more likely to affect greatly the explosive and amygdaloidal intervals than the effusive, massive one.

The bottom subsection of the AM section comprises massive, porphyritic basalts with plagioclase phenocrysts immersed within a medium-grained matrix with very little (<2 vol.%) volcanic glass of the AM*ms* interval (Figure 11). As a consequence, GR, R, ρ and Φ log patterns become much less variable; GR, Δt and Φ decreases whereas R and ρ values increase. In addition, all log patterns, except for GR, vary gradually along the AM*ag2* interval as a transition to the AM*ms* one. Comparatively, the AM*ag1* interval shows values of ρ, Φ and subordinately Δt, similar to those of AF*ef* flows. In turn, the AM*ms* interval has a density value ca. 1.15 times higher than AF*ef*. It is worth noting that even the porous, amygdaloidal basalts have higher density than the effusive, massive felsic rocks, as a result of the mineralogical and compositional control of density.

In conclusion, all the log patterns and values described for the amygdaloidal basalts in the AM*ag1* and AM*ag2* intervals, particularly their variability, differ from those of the cohesive, effusive felsic rocks in the AF*ef* interval (Figure 6, 10 and 11) but may be somehow comparable (apart from GR) to those of the AF*ex* interval (Figure 6). However, massive basalts and effusive, felsic rocks are readily discriminated by their little variable log patterns (including GR ones but with the exception of Δt). For instance, a markable pattern is the distance between the Φ and ρ curves; the curves overlap in felsic rock but stay apart in massive basalts (blue arrows in Figure 10 and Figure 11). Other log patterns that are useful to discriminate between basalts and effusive felsic rocks are shown in Table 3.

Figure 11: The AM magmatic section of well A with respective Gamma-ray (GR), porosity (Φ) and density (ρ) logs and microphotographs of representative samples.

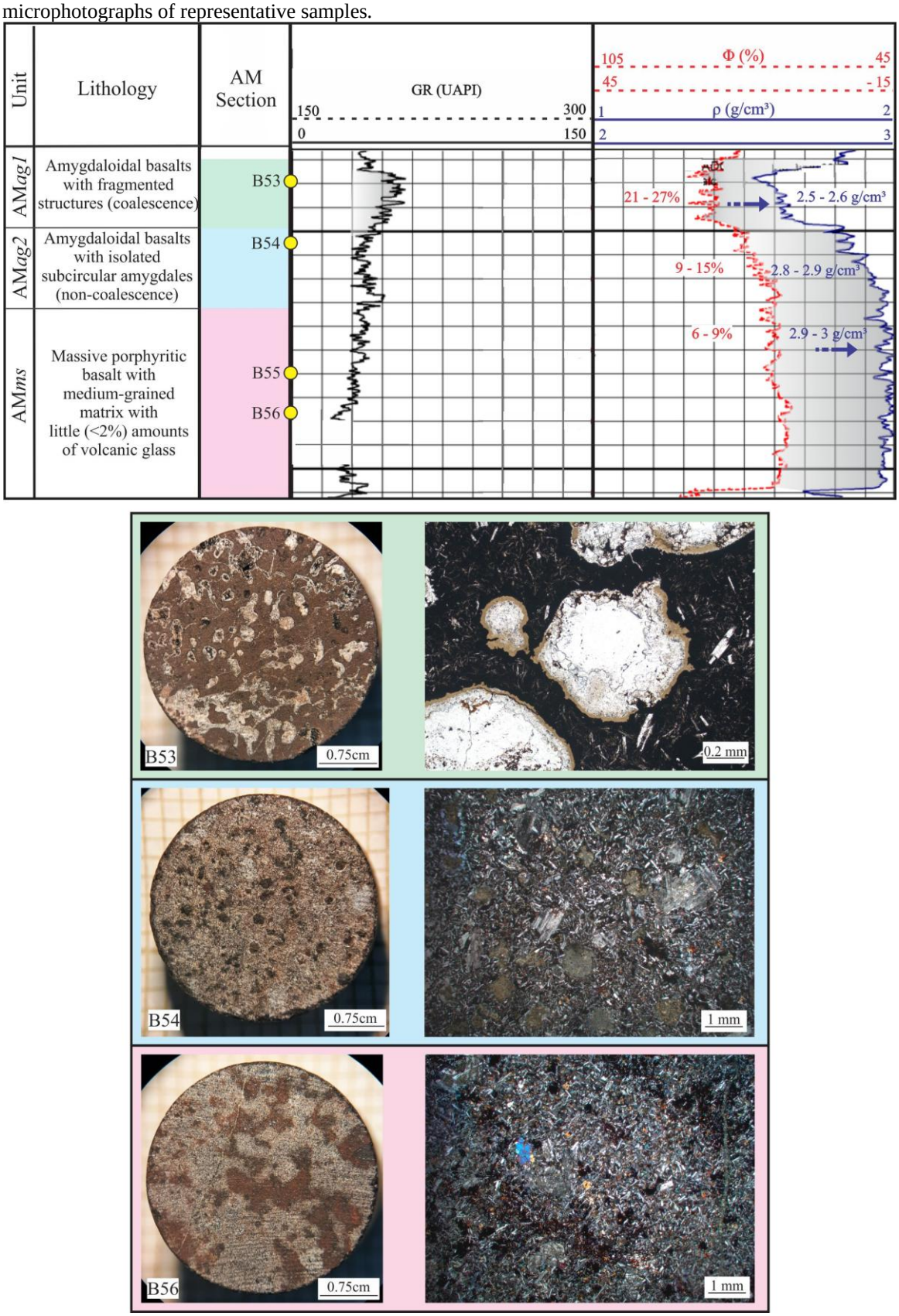

Note: The AM*ag1* interval with high GR and Φ, and low ρ is represented by an amygdaloidal basalt (coalescence; sample B53). The AM*ag2* interval with decrease of GR and Φ, and increase of ρ is represented by amygdaloidal basalt with isolated amygdales (non-coalescence; sample B54). The AM*ms* interval with lower GR and Φ, and higher ρ is represented by massive porphyritic basalt with volcanic glass (sample B56).
Reference: The author, 2024

6.1.8.3 Discriminating features for subaqueous mafic effusive volcanism

Mafic, effusive subaqueous volcanism gives rise to pillow basalts with undercooling textures in plagioclase and pyroxene, abundant vitreous matrix and micro amygdales. The underwater volcanism does not occur as spreading flows as in subaerial environments, but as overlapping pillows, lobes or sheets. Seafloor sediments, clays, and vitreous fragments (hyaloclasts) occur between lobes and pillows. Hyaloclasts there are results from cracking due to the rapid cooling of the superficial tops of the lava. In addition, basaltic clasts may also result from autobrecciation processes (McPhie *et al.*, 1993, White *et al.*, 2015). The petrophysical parameters of pillow basalts tend to reflect their uneven architecture, implying rather irregular patterns (Brewer *et al.*, 1998).

Basalts along the B section of well B are mostly amygdaloidal but their striking feature is the presence of clasts with different textures in the same sample. There is no obvious textural feature that could be regarded as hyaloclasts, such as the typical jigsaw arrangement of glass fragments. Nevertheless, the interval of B section in well B (Figure 12) displays the zigzag pattern of ρ and Φ curves associated with the intermediated GR values typical of subaqueous volcanism (Figure 7a; Bartetzko *et al.*, 2005). The intensity of the zigzag pattern in pillow lavas is dependent on the amount of inter-pillow material and the size of the pillow. The bigger the pillow, the more homogeneous will be the petrophysical log. This more homogeneous pattern of the petrophysical data appears at least 5-meter intervals, as seen by the low GR values and concomitant divergence of ρ and Φ curves (Figure 12). The undercooling textures of samples L19 and L22 resulted from the thermal difference between the water and the lava (Figure 12a). Differences in undercooling textures may indicate superimposition of different lobes along the pillow sequence. Peaks of GR values coincide with touching points of ρ and Φ curves (black dots in Figure 12), possibly representing pillow-breccias with basaltic clasts cemented by calcite (Figure 12b) or, alternatively, samples with abundant interstitial and/or larger amygdales. The presence of carbonate increases the GR values, while the Φ and ρ values slightly decrease.

The R log also is controlled by the arrangement of pillow and inter-pillow material, with high and low R values, respectively (Brewer *et al.*, 1998). The predominance of pillow intervals in B section imprints high values of R. However, R values decrease slightly due the presence of conductive pyrite, the most abundant opaque accessory phase in the amygdaloidal basalts in B section (Clavier *et al.*, 1976), although greater decreasing occurs as a consequence of greater concentrations of pyrite or the presence of stockwork structures (Bartetzko *et al.*, 2003;

Clennell *et al.*, 2010; Spacapan *et al.*, 2019). On the other hand, increasing values of R may result from sulfides oxidation (Dentith *et al.*, 2019). The reduction of the R parameter in B section is to be expected once all samples present pyrite in veins and amygdales (Figure 13). The sulfide mineralization can occur underwater (seafloor) as a result of hot hydrothermal fluids circulation, contact between fluids, seawater and rocks and precipitation on fractures, amygdales and inter-pillow space (Bartetzko *et al.*, 2003).

In general, the GR values of B section are higher than along the AM section of well A (Figure 7a and Figure 6, respectively). Comparatively, most of the B section has GR values similar to the AM*ag* intervals in well A. Only a few portions present values to the AM*ms* interval and some intervals of B section have R values higher than the AM*ag* intervals (Figure 12). Additionally, the values of ρ in B section are similar to in AM*ag*, whereas the Φ values are comparable with the AM*ms*. The R values in B section are also comparable with AM*ms*. These patterns indicate that subaqueous basaltic magmatism present compositional patterns (i.e., GR and ρ) comparable to amygdaloidal portions of subaerial basaltic magmatism, whereas parameters related with structures and textures (i.e., R and Φ) resemble those of massive portions of subaerial basalts. The subaqueous basaltic magmatism also produces smaller volumes of vesicles and amygdales due to the pressure of the water column (White *et al.*, 2015). The similarity between patterns of subaqueous basalts and subaerial amygdaloidal ones (Table 3) may be related with the alterations due to seawater interaction and the inter-pillow material interference in general petrophysical parameters of the magmatic body (Brewer *et al.*, 1998).

6.1.8.4 Discriminating features for plutonic mafic magmatism

The mafic rocks in C section of well Care dolerites, some with cumulate textures. Two marked features of the GR log pattern of C section are the box shape distinguishing abrupt changes on the lithological contact and the minor variation that gives rise to a concave pattern along its bottom subsection (Delpino & Bermudez, 2009), with an abrupt local peak (increase) that represents the maximum amounts of K, Th and U at the very base of the top subsection (black dot in Figure 14). Sample C4 was collected at this very spot, being composed almost only of medium-to-coarse grained plagioclase crystals (Figure 14a). This texture represents a plagioclase cumulate. Crystal accumulation occurs during fractional crystallization in steady-state magma chambers (e.g., Wagner *et al.*, 1960). The latter are plutonic structures, but the accumulation process has also been recorded in hypabyssal structures such as sills (e.g. Marsh, 1996; Latypov,

2003) and even massive dykes (e.g. Wilson, 1992). The petrography leaves no doubt that C section comprises one massive sill where in situ crystallization and crystal accumulation took place. The top subsection represents a cumulate interval (C*cm*; Figure 14) whereas the bottom subsection represents a dolerite interval (C*dl*; Figure 14). The variable and increasing downwards values of GR along the C*cm* interval results from gradual accumulation of plagioclase, culminating with the formation of a 5 m-thick layer of anorthosite represented by sample C4 (Figure 14a). Samples C1 to C3 and also sample C5 (Figure 14b) are glass-free leucocratic dolerite with increasing amounts (C1 to C3) of plagioclase and conspicuous ophitic textures, typical of cumulates. The C*dl* interval comprises dolerites with decreasing granulometry (Figure 14c) from top to bottom and gradual, increasing amounts of plagioclase topwards, what may explain the concave pattern of the GR log.

Figure 12: The B magmatic section of well B with respective Gamma-ray (GR), porosity (Φ) and density (ρ) logs and microphotographs of representative samples.

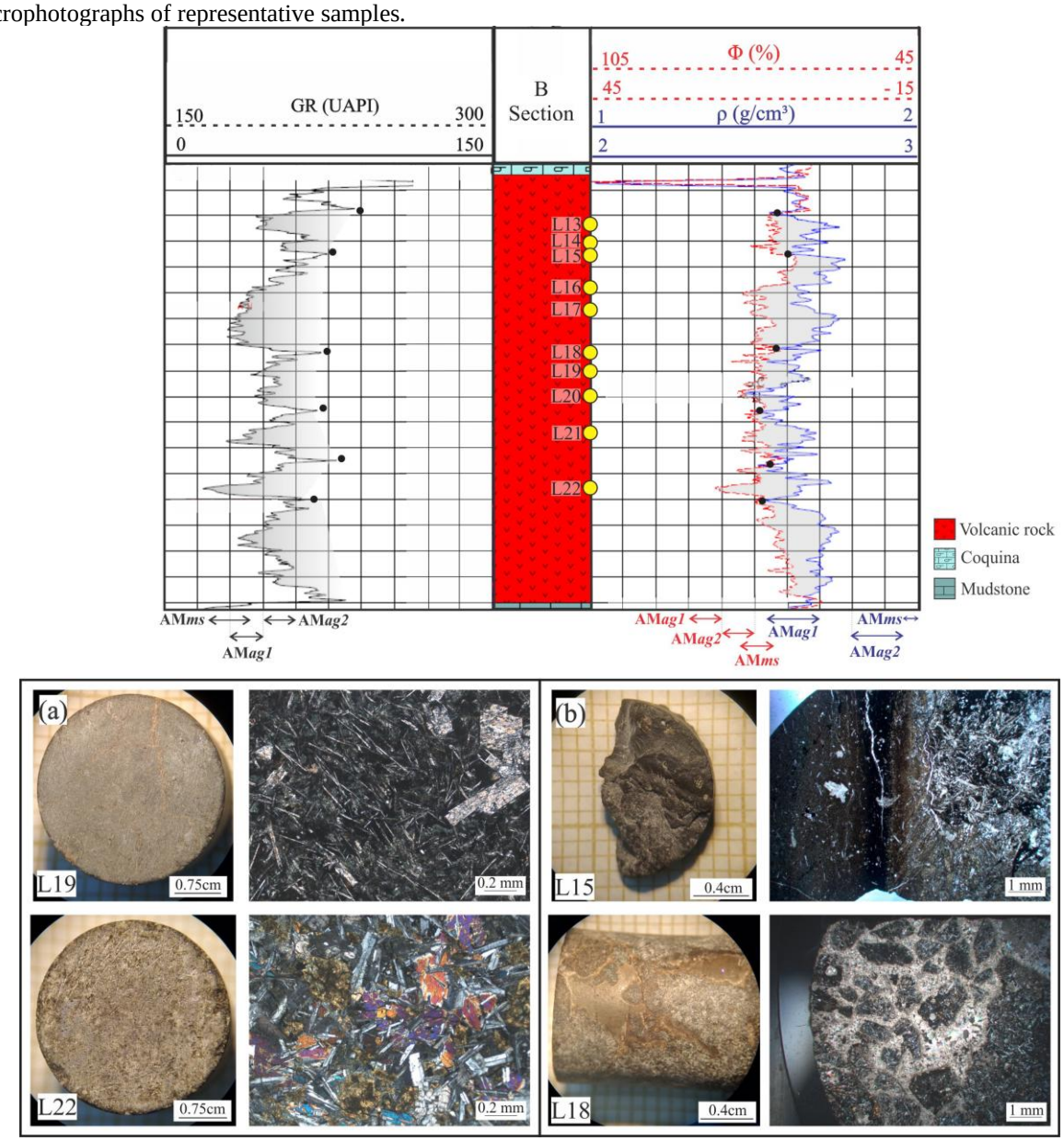

Caption: (a) Volcanics samples with different types of undercooling matrix at the low GR intervals with Φ and ρ curves distant (hatched area; samples L19 and L22); (b) Pillow-breccia and most amygdaloidal sample, featuring the inter-pillow material at the positive peaks of GR and overlap of Φ and ρ (black dots; samples L15 and L18).
Reference: The author, 2024.

Figure 13: Dissemination of pyrite in sidewall core sample L21 of well B.

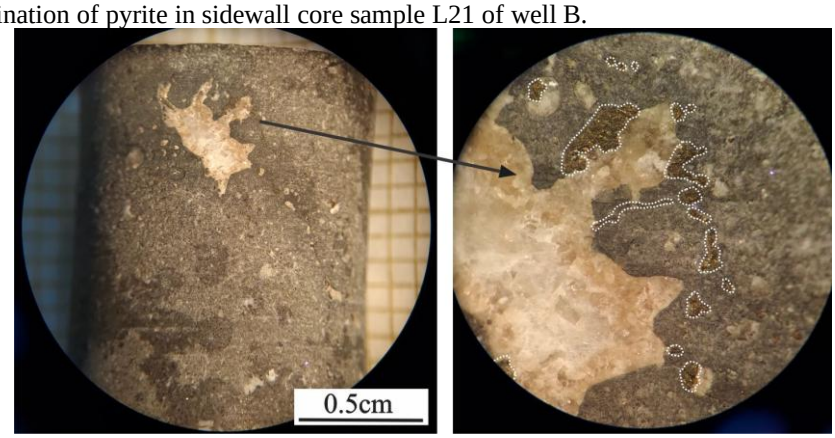

Reference: The author, 2024.

The layered architecture of the sill intrusion in C the section is also marked on the ρ profile. The concave interval in GR profile along the Cdl interval (Figure 14) coincides with a uniform interval of high ρ associate to low Φ, showing curves far from each other resembling the AM*ms* interval of the AM section of well A (Figure 6 and 11). The more variable and lower ρ values coincide with C*cm* as expected due its abundant amounts of plagioclase. There is no abrupt change in Φ values when C*cm* and C*dl* intervals are considered, but porosity decreases irregularly downwards C*dl* possibly as a consequence of decreasing granulometry of dolerites (Figure 14). Nevertheless, in the case of intrusions and cumulates, the relationship between porosity and texture must be taken with care, since the coarse-grained cumulates of C*cm* have porosity values comparable to those of the fine-grained dolerites of the C*dl* interval, although less variable (Figure 14).

The main difference between volcanic (basalts) and plutonic (dolerite) mafic rocks is their grainsize, which cannot be measured by LWD tools but only by petrography. At first glance, C*dl* and AM*ms* sections display rather similar log patterns (Figures 6 and 7b) such as low values for GR, Φ and Δt associated with high ρ, and the density and porosity curves being clearly apart from each other, as already noticed by other authors (Planke 1994; Jerram *et al.*, 2009; Nelson et al, 2009, 2015; Millett *et al.*, 2016; Rossetti *et al.*, 2019; Millett *et al.*, 2021a,b). Positive and/or negative peaks of those parameters could be justified by the alteration process (Delpino & Bermudez, 2009; Dentith *et al.*, 2019). The R log is the less useful discriminating parameter for volcanic and plutonic, cumulate mafic rocks. However, R patterns along the C*cm* interval are much more and abruptly variable when compared with the C*dl* interval. It would be worth investigating whether this pattern of R is reproducible in other wells with the occurrence of cumulates of mafic rocks. If so, the persistence of this pattern would make it a relevant discriminating parameter for the occurrence of plagioclase cumulates and, in turn, between

volcanic and plutonic mafic rocks, since crystal accumulation is not expected to happen in volcanic environments.

Figure 14: C section profile with Gamma-ray (GR), porosity (Φ) and density (ρ) patterns.

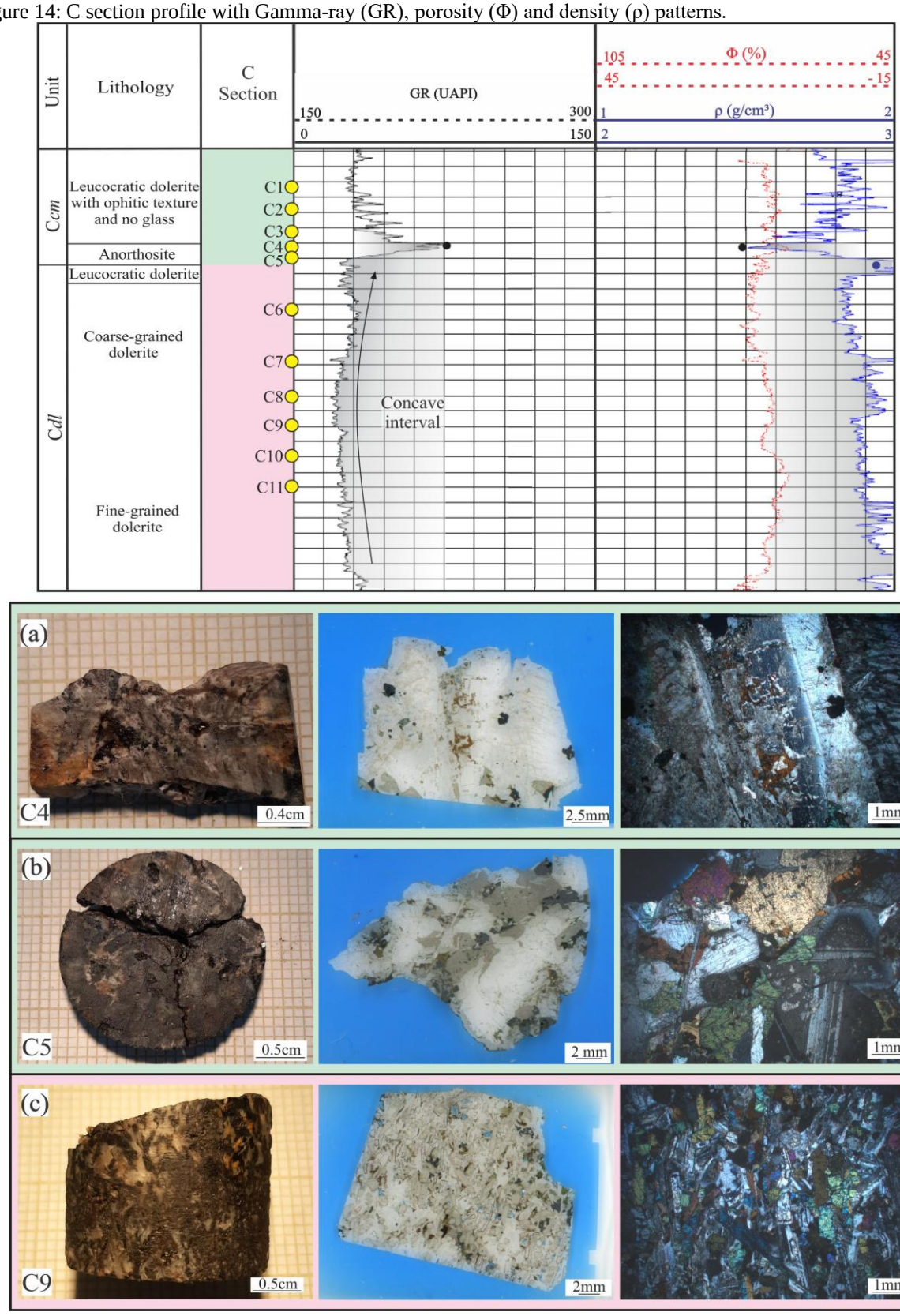

Caption: (a) representative sample from GR positive peak and ρ negative peak (black circles; sample C4); (b) gabbroic rock from petrophysically uniform and massive interval, where GR show slightly concave curves and Φ and ρ are distance themselves (sample C9); (c) gabbroic sample from above the ρ positive peak (blue circle; sample C5).
Reference: The author, 2024.

6.1.9 Conclusions

The identification of the different types of igneous rocks, as felsic or mafic, volcanic or plutonic, can be possible through integrate interpretation of parameters related with log facies. The GR patterns can show subtle variations caused by mineralogical composition, whole-rock composition or alteration. Density (ρ) and porosity (Φ) are inversely proportional, making the curves move closer together in light, porous and/or heterogeneous rocks, as acid, felsic rocks (even effusive or explosive) and inter-pillow intervals. On the other hand, denser, mafic rocks, either volcanic or plutonic, show curves that further apart each other, even in amygdaloidal portions or pillow-lavas intervals. Beyond that, felsic explosive rocks are lighter and more porous than effusive ones, imprinting a pattern to the left of the log. The same applies for amygdaloidal mafic rocks. The Δt and Φ are directly proportional and does not imprint significant differences, except for explosive felsic rocks and amygdaloidal mafic ones. On the other hand, R is inversely proportional to Δt and Φ. The subaqueous mafic volcanic rocks imprint GR, ρ and Φ intermediate patterns between mafic massive and amygdaloidal. The plutonic magmatism patterns could be similar to those of massive volcanic rocks. However, the analysis of compositional profile (as GR and ρ) shows evidence of magmatic differentiation processes that is only possible in subsurface environments.

6.2 **Artigo científico 2 (submetido): Bimodal volcanism during the Early Cretaceous in southern Santos Basin, Brazil: mantle-crust interaction, thermal regime, CO_2 influx and coeval magma generation onshore and offshore the South Atlantic volcanic rifted margins**

JMPG-D-25-00315 - Confirming your submission to Marine and Petroleum Geology

From Marine and Petroleum Geology <em@editorialmanager.com>
Date Wed 05-Mar-25 17:35
To Bárbara Santos Queiroz <b.queiroz18@hotmail.com>

Article Type: Research Paper

Dear Miss Queiroz,

We have received your article "Bimodal volcanism during the Early Cretaceous in Santos Basin, Brazil: mantle-crust interaction, thermal regimes, CO2 influx and coeval magma generation onshore and offshore the South Atlantic volcanic rifted margins" for consideration for publication in Marine and Petroleum Geology. It has been assigned the following manuscript number: **JMPG-D-25-00315**.

To track the status of your paper, please do the following:

1. Go to this URL: https://www.editorialmanager.com/jmpg/

2. Enter these login details:
Your username is: b_317
If you need to retrieve password details, please go to: click here to reset your password

3. Click [Author Login]
This takes you to the Author Main Menu.

4. Click [Submissions Being Processed]

For guidelines on how to track your manuscript in EM please go the following address:
http://help.elsevier.com/app/answers/detail/p/7923/a_id/89

Thank you for submitting your work to this journal.

Kind regards,

Editorial Manager
Marine and Petroleum Geology

6.2.1 Abstract

There are many sedimentary basins along the South Atlantic rifted margins with voluminous hydrocarbon reservoirs. It evolves from rift to drift tectonic stages that give rise to geological processes that control part of their petroleum systems. Some of these processes are related to changes in thermal regimes due to long-standing tectono-magmatic events associated to mantle-crust interactions. The Santos Basin, offshore southeast Brazil, contains the country's largest oil and gas reservoirs. Its origin is related to the rift process that led to the Gondwana breakup during the Early Cretaceous. This paper presents wellbore, petrographic, geochemical, isotopic and geochronological data obtained for an 800m-tick magmatic section recorded along the so-called pre-salt sedimentary sequence in the well 6-BG-6P-SPS in the Santos Basin. This magmatic section comprises effusive mafic and composite felsic rocks associated with long-standing bimodal volcanism (135-122 Ma). The geochemical models allowed to propose that the basic mafic and acid felsic rocks are no-cogenetic by differentiation processes, although some of the basic and intermediate liquids can be linked by AFC within the upper continental crust. The enriched isotope signature of the basic rocks can be explained by geodynamic processes involving the Tristan da Cunha plume and enriched portions of the SCLM (EMII-like mantle reservoir). The data were used to propose conceptual models for the mantle geodynamics and the tectono-magmatic settings from the Hauterivian to Aptian. These models show how mantle-crust tectonic and magmatic interactions imposed thermal regimes that may have controlled geological processes recorded by the pre-salt petroleum systems in the Santos Basin.

Keywords: Volcanic rifted margin, mantle-derived CO_2, thermal regimes, mantle-crust processes, Santos Basin

6.2.2 Introduction

Tectono-magmatic systems in volcanic margins are formed from interactions between the lithosphere and asthenosphere before, during and after continental breakup, with relevant controls on paleoenvironmental settings and the distribution of mineral resources and hydrocarbon exploration (Eldholm *et al.*, 1995, 2000). Magmatism at continental rift zones, related volcanic margins and continental flood basalt provinces (CFB) involves convective and hotspot mantle dynamics under various thermal regimes (Bailey, 1983; White & McKenzie, 1989; Eldholm & Grue, 1994; Nielsen & Hopper, 2002; Gholamrezaie *et al.*, 2018; Lu & Huismans, 2021). In turn, the thermal regimes evolve during the syn-rift and the post-rift stages of continental breakup and further drifting due to extension, sediment thickness and migration of deformation, affecting margin subsidence and the transition from a rift to a passive margin-type, sedimentary basins (Wolfenden *et al.*, 2005; Armitage *et al.*, 2010; Levell *et al.*, 2010; Biari *et al.*, 2021; Stanton *et al.*, 2014; Pérez-Gussinyé *et al.*, 2024).

The accumulation of thick sedimentary and magmatic successions during basin evolution has been long recognized along the North and South Atlantic volcanic margins; the onshore and offshore magmatism being also time-correlated (Eldholm, 1991; Hinz *et al.*, 1993; Eldholm & Grue, 1994; Gladczenko *et al.*, 1997; Menzies *et al.*, 2002; Gordon *et al.*, 2023a; Ferreira *et al.*, 2023). Tectono-magmatic systems are also correlated along conjugate volcanic rifted margins (Eldholm *et al.*, 2000; Ukstins *et al.*, 2002; Peron-Pinvidic *et al.*, 2013), as the south Brazil and north Namibia ones (Matos *et al.*, 2024). The structural, stratigraphic and magmatic correlations between the Africa-South America conjugate margins, including the Paraná-Etendeka CFB (Gladczenko *et al.*, 1997), impact the oil and gas exploration on both sides of the Atlantic Ocean (Lentini *et al.*, 2010; Beglinger *et al.*, 2012; Biari *et al.*, 2021; Basheer, 2024; Yelwa *et al.*, 2024).

Passive margin basins are widely explored by oil and gas companies around the world (e.g. Levell *et al.*, 2010; Pimentel & Reis, 2016; Zhixin *et al.*, 2016; Zalan, 2017; Schinteie *et al.*, 2023). The magmatic occurrences in rift basins are commonly related to the Pre-breakup stage and persist during basin evolution (Farooqui *et al.*, 2009; Eide *et al.*, 2017a, 2017b; Fornero *et al.*, 2019; Descovi *et al.*, 2021; Louback *et al.*, 2021; Curtis *et al.*, 2022; Marins *et al.*, 2022; Zhang *et al.*, 2023; He *et al.*, 2025). The magmatism became a relevant topic of study for oil and gas exploration, considering their effects on generation, migration, storage, trapping and sealing processes in petroleum systems in sedimentary basins worldwide (Archer *et al.*, 2005; Senger *et al.*, 2017; Jackson *et al.*, 2020; Zeng *et al.*, 2023; Mangione *et al.*, 2024).

The Santos Basin has been the most important play for oil and gas exploration and production in Brazil since 2006 when accumulations of hydrocarbons were found in the Early Cretaceous rift and post-rift strata below Aptian evaporites (Rodrigues & Sauer, 2015; Rosa *et al.*, 2018). The so-called pre-salt reservoirs are particularly large in Tupi, Búzios, Sapinhoá, and Mero oil fields, summing up to 60% and 70% of all oil and gas produced in Brazil, respectively (Mello *et al.*, 2021). Possibly, the main drawback of hydrocarbon production in Santos is the large-scale mantle-derived CO_2 emplacement and co-accumulation of CO_2 and crude oil (Ferraz *et al.*, 2019; Freitas *et al.*, 2022). The causes that led to the occurrence of highly variable amounts of CO_2 in many neighboring oil fields in the Santos Basin are still a matter of debate (Gamboa *et al.*, 2019), despite the consensus on the origin of the CO_2 within the Earth's mantle, similarly to other basins elsewhere in the world (Liu *et al.*, 2017; Zhu *et al.*, 2018; Liu *et al.*, 2023). Magmatic-related hydrothermalism under high geothermal gradients, in addition to regional crustal thinning, deep-seated faults, high fault density, and igneous intrusions are among the processes and parameters playing a role in the ascent of CO_2 from the mantle to the crust (Gamboa *et al.*, 2019; Freitas *et al.*, 2022; Yang *et al.*, 2022; Oliveira *et al.*, 2024; Plawiak *et al.*, 2024). These tectono-magmatic processes, particularly the hydrothermalism, may have consequences for shallow level processes in sedimentary basins (Kampman *et al.*, 2014; Jesus *et al.*, 2023; Vital *et al.*, 2023) such as the formation of the pre-salt, carbonate hydrocarbon reservoirs in Santos, for instance (Farias *et al.*, 2019).

The origin of the Santos Basin is related to the rift processes of Gondwana during the Early Cretaceous that culminated with the formation of a volcanic rifted margin in southeast Brazil (Chang *et al.*, 1988; Cainelli & Mohriak, 1999; Moreira *et al.*, 2007). Basaltic, effusive volcanism is the usual Pre-breakup, magmatic process in volcanic rifted margins, bimodal magmatism being rare (e.g. Morris *et al.*, 2024). The same seemed to apply for Santos Basin based on previous publications (Scribelk & Valente, 2023; Gordon *et al.*, 2023b; Queiroz *et al.*, 2024). This paper presents new well drilling, petrographic, lithogeochemical, isotope (Sr-Nd-Pb) and geochronological (U-Pb) data obtained for samples recovered from a pre-salt magmatic section in well 6-BG-6P-SPS (also known as Corcovado 1) drilled under deep-water in the distal margin of the Central Santos Basin. This is the first report of bimodal volcanism in the Santos Basin, making it likely to represent the offshore counterpart of the coeval magmatism taking place in the Paraná-Etendeka CFB. The felsic and mafic volcanic rocks in the studied magmatic section are not cogenetic by any possible differentiation process. The results of geochemical modelling are consistent with the non-cogeneticity between mafic and felsic rocks highlight the role of the upper crust as both contaminant of basic liquids and a melting source for felsic, intermediate and acid rocks. The proposed geodynamic model implies the involvement of the Tristan da Cunha mantle

plume and the EMII mantle reservoir in genesis of the mafic, basic rocks. The mantle-crust interactions established a high thermal regime during the Early Cretaceous in the area, which may explain the variable but widespread hydrothermalism and CO_2 influx recorded along the pre-salt, sedimentary sequence in the Santos Basin.

6.2.3 Geological setting

6.2.3.1 The general framework and chronostratigraphy of the Santos Basin

The Santos Basin is located along the volcanic rifted margin of southeast Brazil (Figure 15a). The basin evolved from a rift stage, related to the breakup of Gondwana and splitting of the previously amalgamated Proterozoic terranes (Heilbron *et al.*, 2000; Meisling *et al.*, 2001), to the drift stage related to the opening of the South Atlantic Ocean (Chang *et al.*, 1988; Cainelli & Mohriak, 1999; Moreira *et al.*, 2007).

The tectono-stratigraphic evolution of Santos Basin has been divided into three megasequences or stages (Figure 15b): rift, post-rift and drift (Moreira *et al.*, 2007). The sedimentary sequence lies above the crystalline basement constituted by Proterozoic to Cambrian granitoids and gneisses of the Ribeira Collisional Orogen (Valeriano *et al.*, 2016; Heilbron *et al.*, 2020a,b).

The rift-stage (138-122 Ma, Figure 15b) corresponds to the early tectonic processes of the Gondwana rifting. The sedimentation occurred over a continental environment under arid climate, with alluvial and deltaic fan deposits, inland saline and alkaline lakes, with continental biogenic deposition (Chang *et al.*, 1988; Cainelli & Mohriak, 1999). This sedimentary succession (Piçarras (PIÇ) and Itapema (ITP) formations; Figure 15b) holds the main hydrocarbon source rocks (lacustrine shales; PIÇ) and subordinate reservoirs (*coquinas*; ITP) of the pre-salt petroleum system in the Santos Basin (Anjos *et al.*, 2024). The sedimentation was preceded by tholeiitic basalt, effusive volcanism (Camboriú (CAM) Formation; Figure 15b) with a peak at *ca*. 138 Ma, being time-correlated with the tholeiitic basalt flows of the Paraná-Etendeka CFB (*ca.* 135 Ma; Plagioclase and whole-rock Ar-Ar ages; Thiede & Vasconcellos, 2010) as well as the tholeiitic basalts of the Cabiúnas Formation in Campos Basin (*ca.* 134-122 Ma; whole-rock K-Ar ages; Mizusaki *et al.*, 1992; Figure 15a). Another magmatic event at *ca.*130-121 Ma has been recorded

in the chronostratigraphic chart of the Santos Basin and described as subaqueous basalt interbedded with the sedimentary rocks of the Piçarras Formation (Moreira *et al.*, 2007).

The post-rift stage (122-113 Ma. Figure 15b) is a transitional phase between continental and shallow marine sedimentary environment during tectonic quiescence and thermal subsidence (sag basin) marked by regional unconformity (Moreira *et al.*, 2007). It is characterized by the deposition of thick limestone layers (Barra Velha (BVE) Formation; Figure 15b) during the Aptian (Brito *et al.*, 2024). These limestones are the main hydrocarbon reservoirs of the pre-salt petroleum system in the Santos Basin (Anjos *et al.*, 2024). The continuous opening process of the South Atlantic Ocean and the beginning of seawater input gave rise to a rapid (< 530 k.y.; Rodriguez *et al.*, 2018; Céline *et al.*, 2024) deposition of evaporitic rocks (Ariri (ARI) Formation; Figure 15b; Moreira *et al.*, 2007). This thick (up to 2.5 km) salt sequence comprises the sealing rocks of the pre-salt petroleum system in the Santos Basin (Anjos *et al.*, 2024). The post-rift magmatism is recorded between the Lower and Upper Barra Velha Formation, synchronous to the regional unconformity at *ca*. 117 Ma (Moreira *et al.*, 2007). Finally, the drift-stage (<113 Ma) corresponds to the effective splitting of Gondwana, with seawater entry, the deposition of marine sediments and creation of oceanic crust (Moreira *et al.*, 2007). Two drift-related magmatic events are recorded in the chronostratigraphic chart of the Santos Basin: 1) earlier alkaline magmatism during the Santonian and Campanian; 2) later alkaline magmatism during the Lower Eocene, mainly at the north of the Santos Basin (Moreira *et al.*, 2006; Oureiro *et al.*, 2008).

Figure 15: The location and chronostratigraphy of the Santos Basin in southeast Brazil.

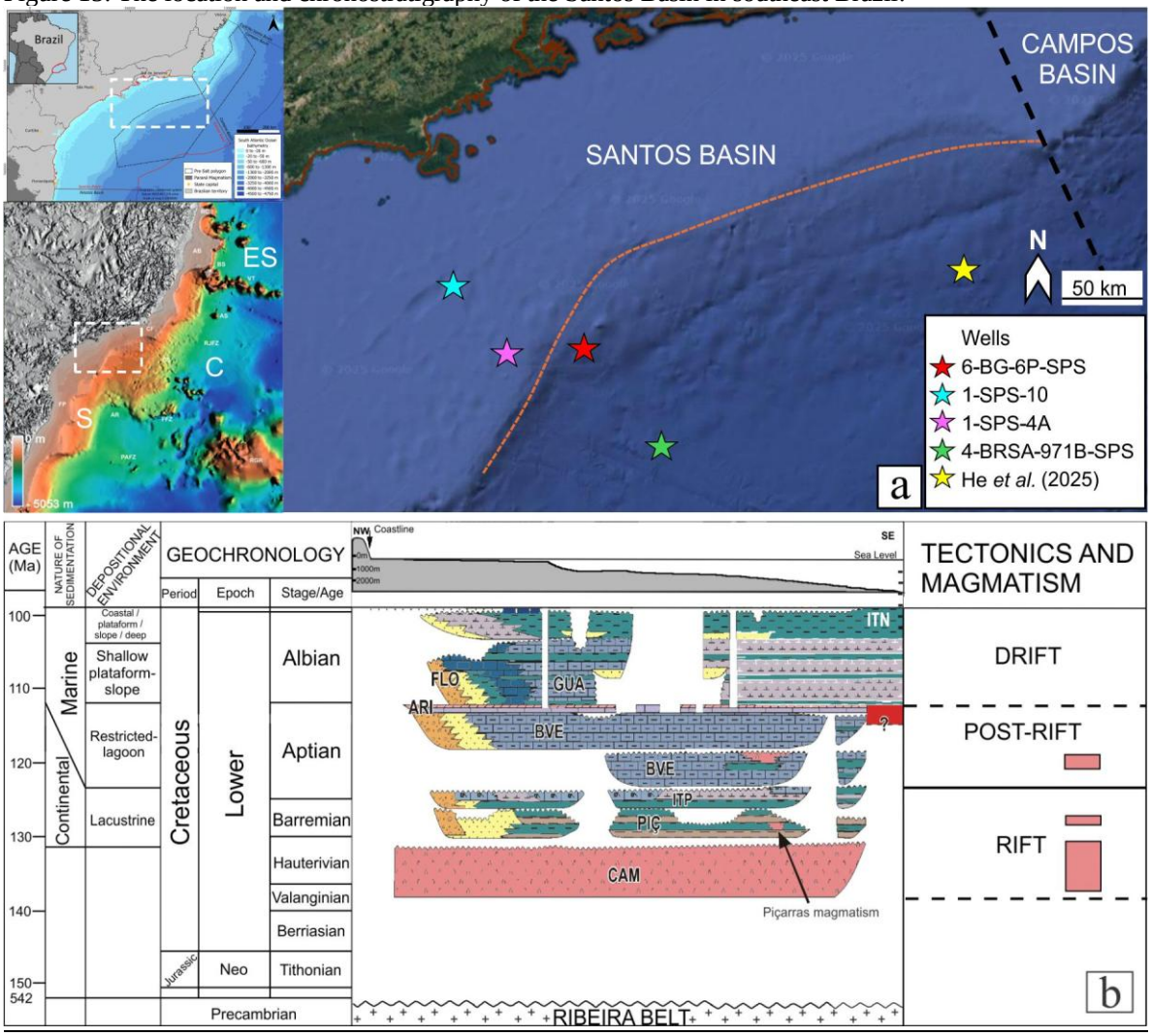

Caption: (a) The location of well 6-BG-6P-SPS (Corcovado 1) and other wells with rift- and sag-related magmatic sequences in the Santos Basin (Source: Google Earth Pro). Upper inset: bathymetry of the South Atlantic Ocean and main boundary lines in the Santos Basin (Sources: Paraná Magmatism and bathymetry from Geological Service of Brazil (CPRM); Pre-salt polygon from GeoMaps by ANP - Petroleum National Agency). Lower inset: main structural and physiographic features of the passive margin basins (ES: Espírito Santo; C: Campos; S: Santos) in SE Brazil. AR = Abimael Ridge. CF = Cabo Frio Structural High. CS = Cruzeiro do Sul Deformation Zone. FFZ = Florianópolis Fracture Zone. RJFZ = Rio de Janeiro Fracture Zone. RGR = Rio Grande Rise. SPP = São Paulo Plateau. Other features of interest in adjoining basins are: AB = Abrolhos Bank. AS = Almirante Seamount. BS = Besnard Seamounts. FP = Florianópolis Plateau. PAFZ = Porto Alegre Fracture Zone. RC = Royal Charlote Seamount. VT = Vitória-Trindade; (b) A sketch of the chronostratigraphic chart (Lower Cretaceous only) of the Santos Basin and its related tectono-magmatic events. Formations are: Camboriú (CAM), Piçarras (PIÇ), Itapema (ITP), Barra Velha (BVE), Ariri (ARI), Florianópolis (FLO), Guarujá (GUA), and Itanhaém (ITN).
Reference: Google Earth Pro; Paraná Magmatism and bathymetry from Geological Service of Brazil (CPRM); Pre-salt polygon from GeoMaps by ANP - Petroleum National Agency; Mohriak *et al.* (2010); Moreira *et al.* (2007)

6.2.3.2 The Pre-Albian magmatism in the Santos Basin

Magmatic events in the Santos Basin are recorded before and after the Albian. The pre-Albian (Hauterivian, Barremian and Aptian) magmatic events occurred during the rift and post-rift stages of basin evolution (Moreira *et al.*, 2007; Figure 15b). The post-Albian magmatic

events took place during the drift stage, at the Santonian, Campanian and the Lower Eocene (Moreira *et al.*, 2006, 2007).

The pre-Albian volcanism and plutonism in the Santos Basin have often been quoted from *ca.* > 130 Ma, at *ca.* 117 Ma, to *ca.* 113 Ma (*e.g.* Moreira *et al.*, 2007, Carminatti *et al*, 2008. Szatmari & Milani, 2016; Rancan *et al.*, 2018) but geochronological data have scarcely been published. The earliest pre-Albian magmatism occurred at the Valanginian and extended throughout the Hauterivian (Figure 1b), corresponding to the tholeiitic basalts and associated volcaniclastic rocks of the Camboriú Formation (Moreira *et al*., 2007; Figure 15b). The only published age obtained for the earliest pre-Albian magmatism is 138 ± 3.5 Ma (whole-rock, K-Ar; Fodor *et al.*, 1983), making them chronocorrelated with the basalts of the Camboriú Formation (Figure 1b), the tholeiitic basalts of the Paraná-Etendeka CFB (whole-rock and plagioclase separates, Ar-Ar, 134.7 ± 1.0 Ma; Thiede & Vasconcelos, 2010; *ca.* 134-132 Ma; Gomes & Vasconcelos, 2021), the felsic volcanic and intrusive rocks also in the Paraná-Etendeka CFB (U-Pb in baddeleyite/zircon; *ca.* 134-135Ma; Janasi *et al.*, 2011; Florisbal *et al.*, 2014, 2018) and the Cabiúnas Formation basalts from the Campos Basin (*ca.* 134-122 Ma; whole-rock K-Ar ages; Mizusaki *et al.*, 1992). Magmatic rocks are also shown in the chronostratigraphic chart of the Santos Basin interbedded with the sedimentary rocks of the Piçarras Formation (Figure 15b). They are described as subaqueous basalts formed at the Barremian (*ca.*130 Ma; Moreira *et al.*, 2007), but no geochronological data have already been published to support such time correlation.

Petrological data on the earliest, pre-Albian basalts in Santos Basin, likely to be related to the Camboriú Formation, were firstly published based on two samples recovered from wells 1-SPS-4A and 1-SPS-10 located 60 km apart (Fodor & Vetter, 1984). The Camboriú basalts were described as tholeiitic and typically composed of plagioclase, augite and pigeonite (altered), Fe-Ti-oxides and hydrated, altered and/or devitrified glass. As such, they would represent differentiated high-Ti ($2 < TiO_2 < 3.5$ wt.%) tholeiitic basalts with no primitive composition (*e.g.* $6 < MgO < 9$ wt.%, $44 < Ni < 75$ ppm, $80 < Cr < 135$ ppm). These basalts were considered to be similar to the Paraná CFB in composition and their mantle sources were attributed to T- and P-type MORB (Fodor and Vetter, 1984). The enriched MORB compositions were attributed to mixing processes involving a N-MORB, depleted source and a fertile plume-type source, similar in composition to Tristan da Cunha and Bouvet in the Jurassic. The earliest magmatism in Santos Basin was qualified as CFB and comparisons with distal portions of the Atlantic margin (São Paulo ridge; Fodor *et al.*, 1980) led to the proposition that continental crust extends as far as 600 km away from the present coast line SE Brazil (Fodor & Vetter, 1984).

The latest pre-Albian magmatic event in the Santos Basin occurred during the post-rift (or sag) stage of basin evolution, being closely associated with the Aptian (126-112 Ma) limestone

reservoirs (Barra Velha Formation; BE in Figure 15b) of the pre-salt petroleum system in the basin. Ages are often quoted by different authors without the presentation of their respective geochronological data. This is the case of the tholeiitic basalts within the Libra exploratory block in the Santos Basin with reported Ar-Ar ages of 125.5 ± 0.7 Ma (and an alternative age at 114.3 ± 1.1 Ma; Rancan *et al.*, 2018). Also, the 500 m-thick sequence of flood basalts, the so-called Tupi magmatism, which were Ar-Ar dated at 120.4 ± 0.8 Ma, as well as the Parati basalts, a 300 m-thick sequence of flood basalts with 115.7 ± 1.0 Ma, both basalt sequences being interbedded with thin layers of the Barra Velha limestone (Szatmari & Milani, 2016). Ages of *ca.* 118-113 Ma have also been reported to dominantly mafic rocks possibly related to an aborted rifting event (M0 magnetic event; Carminatti *et al.*, 2008). Magmatic rocks are also recorded at *ca.* 117 Ma in the chronostratigraphic chart of the Santos Basin based on no published geochronological data (Moreira *et al.*, 2007). More recently, Ar-Ar geochronological data have been presented for the sag-related magmatism in the Santos Basin (Louback *et al.*, 2023; He *et al.*, 2025). Diabases intrusive in a nearly 600 m-thick volcanosedimentary sequence in a well drilled in the distal northern margin of the Santos Basin have Ar-Ar (plagioclase and whole-rock) plateau ages ranging from 121.5 ± 0.2 Ma to 126.4 ± 1.0 Ma (Figure 15a). The basalts in the well were also dated but their Ar-Ar ages were inconsistently lower due to alteration of the samples. The older alkaline diabases originated from 1-5% partial melting within the shallow (spinel-garnet transition zone) lherzolitic asthenosphere whereas the younger ones display a transitional alkaline-subalkaline trend due to higher partial melting degrees (He *et al.*, 2025). Further southeast, a 500 m-thick sequence of basalts interbedded with marls in well 4-BRSA-971B-SPS within the Bacalhau field (Figure 15a) gave whole-rock Ar-Ar integrated ages at 116.93 ± 0.22 Ma, 116.16 ± 0.10 Ma, 115.21 ± 0.13 Ma and 109.95 ± 0.20 Ma (Louback *et al.*, 2023). These low-Ti, tholeiitic basalts have chondrite-normalized La/Nb and La/Yb_N ratios typical of continental flood basalt provinces. However, they cannot be related with either the low-Ti, Esmeralda and Gramado suites in Paraná-Etendeka or the low-Ti diabase suites in the Serra do Mar Dike swarm on the adjoining continental area. The low-Ti, tholeiitic basalts derived from a EM1 mantle component in the subcontinental lithospheric mantle (SCLM) with partial melting within the garnet stability zone. This magmatic event was related to the melting of the SCLM due to either the presence of the Tristan da Cunha mantle plume during the Aptian below the Santos Basin or the stretching of different portions of the blob-rich SCLM itself. This stretching was attributed to the remaining heat advected from the Tristan da Cunha mantle plume during the voluminous Early Cretaceous magmatism that gave rise to the Paraná-Etendeka CFB (Louback *et al.*, 2023).

6.2.4 Materials and methods

The well 6-BG-6-SPS was drilled in Santos Basin and the well log and samples were made public by the Petroleum National Agency (ANP) of Brazil. The Gamma Ray (GR), Resistivity (R), Sonic log (Δt), Neutron porosity (NPHI - Φ) and Density (RHOB - ρ) data were used for the qualitative interpretation of the petrophysical data.

One hundred twenty-seven sidewall core samples were recovered from the well, a hundred twenty-five were described under macroscopic scale and seventy-six thin sections were described under a transmitted light microscope. Thirty sidewall core samples from representative depth intervals were crushed and washed in a portable ultrasonic cleaning machine. After drying, samples were taken to a binocular stereoscope to select chips with no amygdales, veins or alteration portions. The batches of the chips were sent to the Activation Laboratories Ltd. (Actlabs, Canada) for whole-rock geochemical analysis on fused samples. Samples were crushed in a steel mill and powders were taken for the determination of the concentration of major elements (SiO_2, TiO_2, Al_2O_3, $Fe_2O_3^t$, MnO, MgO, CaO, Na_2O, K_2O, P_2O_5; in wt.%; $Fe_2O_3^t$ being total iron as ferric iron) by the ICP-OES (Inductively Coupled Plasma-Optical Emission Spectrometry) in a Thermo Jarrell Ash ENVIRO II equipment. Fourteen USGS and CANMET certified reference materials were used for calibration. Selected trace elements (Ba, Rb, Sr, Zr, Hf, Y, Nb, Ta, Ni, Cr, V, Co, U, Th and Pb), including the whole set of rare earth elements (REE; La, Ce, Pr, Nd, Sm, Eu, Gd, Tb, Dy, Ho, Er, Tm, Yb e Lu) were measured by ICP-MS (Inductively Coupled Plasma-Mass Spectrometry) in a Perkin Elmer Sciex ELAN 9000 equipment. The calibration was performed using ten synthetic standards. A set of ten certified materials was analyzed on the equipment before and after each batch of samples. Two samples were analyzed twice for precision control. Detection limits, accuracy and precision values are shown in Appendix C.

Fifteen samples were selected for isotope analysis (Sr-Nd-Pb) at the Isotope Lab of the New Mexico State University. The separation of Sr, Rb, Sm, Nd and Pb was done combining the methods described by Yang *et al.* (2010). Powdered samples were firstly leached in 6 M HCl for about 1 hour to remove the least strongly bonded Sr produced by alteration (Silva *et al.*, 2010). About 200-400 milligrams of powder of the leached samples were dissolved using hydrofluoric, nitric, and hydrochloric acids. The Sr purification was made by cation exchange through resin using 2.5N HCl. The Sr isotope ratios were measured in a thermal ionization mass spectrometer (TIMS) with five Faraday collectors in dynamic mode with $^{86}Sr/^{88}Sr$ ratios normalized to 0.1194 and NBS 987 standard with $^{87}Sr/^{86}Sr = 0.710284$ (n = 2) and $^{84}Sr/^{86}Sr = 0.056427$ (n = 2). The REE

purification was made using cation exchange resin and 6.0 N HCl. A HDEHP resin and 0.25 N HCl were used for the separation and purification of Nd from the remaining REE. Then, the purified Nd was dissolved in 1-2 ml of 2% HNO_3 and analyzed for 100 ratios using a ThermoScientific Neptune with seven faraday collectors in static mode. Nd isotopes were normalized to $^{146}Nd/^{144}Nd = 0.7219$ and analysis used JNdi-1 standards with $^{143}Nd/^{144}Nd = 0.512109$ (n = 9) and $^{145}Nd/^{144}Nd = 0.348412$ (n = 9). The Pb purification was made using anion exchange resin and 1.0 N HBr and dissolved in 1-2 ml of 2% HNO_3. Tl was introduced into the sample to obtain a Pb/Tl ratios between 2-5 (Wolff and Ramos, 2003). The equipment used for the analysis of samples for 100 ratios was a ThermoScientific Neptune in static model with five Faraday collectors. Pb isotope results were normalized to $^{203}Tl/^{205}Tl = 0.41892$ with standards NBS 981 with $^{206}Pb/^{204}Pb = 16.931$ (n = 11), $^{207}Pb/^{204}Pb = 15.484$ (n = 11), $^{208}Pb/^{204}Pb = 36.673$ (n = 11).

Eight thin sections of samples were selected for in situ U-Pb geochronological analysis of thirty-two zircon grains in LSP/LLA – CPGeo (USP – São Paulo University, Brazil). Each analysis was composed of 40 sequential measurements (approx.1s of integration each) on the "Neptune" ICP-MS. The first 10 seconds were done with the laser ablation turned off (to get the instrumental blank) and the remaining 30 under the action of the "analyte excite" excimer laser. Seven isotopic signals were measured simultaneously, 4 of them (206, 208, 232, 238) in Faraday cups (having higher amplitude) and the other 3 (202, 204 and 207) in Multiple Ion Counters or MICs (having higher sensitivity). The averaged value of the instrumental blank is immediately subtracted from each one of the 7 isotopic signals at the end of every measuring sequence. The 235 isotopic signal was not measured but mathematically calculated, dividing the 238 signal by the U 238/235 relative abundance (= 137.88). The participation of Hg (from the carrier gas) in the 204 signal was discounted by subtracting from it the quotient signal 202 / Hg 202/204 relative abundance (= 4.355). The relative ratios (variable with the geological age) of 206/204, 207/204 and 208/204 were calculated using the U/Pb ratios (206/238, 207/235 and 208/232) as age estimates and the equations of Stacey-Kramers. The non-radiogenic "common Pb" fraction of the isotopes 206, 207 and 208 was then discounted by subtracting, from each of them, the 204 sign multiplied by the respective relative abundances of 206/204, 207/204 and 208/204 previously calculated as above. The GJ-1 standard (Jackson et al, 2004) was periodically re-measured (nearly. every 10 minutes), in order to compensate for errors and/or instrumental variations in the subsequent samples. The (multiplicative) coefficients used to convert the 3 total signals (Pb [204+206+207+208], Th [232] and U [235+238]) into ppm units and the (fractioning) correction factors for the 4 ratios: 206/238, 207/235, 207/206 and 208/232 were obtained by comparing

tabulated *versus* measured GJ-1 values. The results were then applied before using them to calculate the respective ages.

6.2.5 Well data

The 810 m-thick (5715-4905 m) magmatic section in well 6-BG-6P-SPS comprise interbedded volcaniclastic and volcanic rocks that were included in the Camboriú Formation. The sedimentary rocks above the unconformity at the top of the magmatic section comprise limestones (Barra Velha Formation) which, in turn, lie below interbedded layers of anhydrite and halite (Ariri Formation; Figure 15b). The interpretation of petrophysical data (Appendix A) resulted in the distinction of three mafic and three felsic sections (Figure 16), hereafter identified by the letters B and A, respectively. These felsic and mafic sections are arranged (from bottom to top) as such: B1, A1, B2, A2, B3 and A3 (Figure 16).

Three effusive mafic sections (B1, B2 and B3) were discriminated based on the typical gamma-ray, resistivity, sonic and neutron porosity, and high density petrophysical patterns of basalts; opposite patterns being characteristic of amygdaloidal basalt layers (Planke 1994; Jerram *et al.*, 2009; Nelson *et al.*, 2009; Nelson *et al.*, 2015; Millett *et al.*, 2016; Rossetti *et al.*, 2019; Millett *et al.*, 2021a, 2021b, Marins *et al.*, 2022; Queiroz et al, 2024). Similarly, three felsic sections (A1, A2 and A3) were defined by their typical high gamma-ray and low density patterns. The resistivity logs of the explosive felsic rocks are low whereas sonic and neutron porosity logs are high. On the other hand, the effusive portions could be discriminated by their typical high resistivity and low sonic and neutron porosity patterns (Keys, 1979; Sanyal *et al.*, 1980; Bartetzo *et al.*, 2003; Helm-Clark *et al.*, 2004; Zou *et al.* 2013; Ran *et al.*, 2014; Oliveira *et al*., 2022; Millett *et al.*, 2021b).

The B1 effusive, mafic section comprises a 530 m-thick succession of basaltic flows, marked by distinctive lower-, intermediate (or core)-, and upper portions of the individual volcanic flows. The upper layers are formed by amygdaloidal basalts whereas massive ones comprise the intermediate and lower portions of the flows. This bottom section is overlain by the 10-meter-thick A1 explosive, felsic section. Topwards, the B2 effusive, mafic section is made by a thin (10 m) layers of effusive, massive basalt whereas the 100 m-thick. The A2 composite, felsic section comprises 80 m of effusive rocks overlain by 20 m of alternating thin (few metric thickness) layers of effusive and explosive rocks. The B3 effusive, mafic section is about 70 m-thick, comprising predominantly amygdaloidal basalt flows. The uppermost section of the well (A3 composite, felsic

section) is 80 m in thickness and comprises 50 m of alternating layers of effusive and explosive felsic rocks overlain by 19 m of effusive felsic rocks which, in turn, are overlain by 11 m of alternating thin layers of both effusive and explosive felsic rocks. The discriminating parameters and general characteristics of the mafic and felsic sections are summarized in Table 4.

Table 4: Summary of petrophysical parameters and general characteristics of the mafic and felsic magmatic sections in well 6-BG-6P-SPS in Santos Basin.

General Chemical classification		Sections	Volcanic type		Total thick (m)	GR	R	Δt	NΦ	ρb
Mafic	Felsic	A3	Co	Ef	80	H	H	L	L	L
				Ex			L	H	H	
		B3	Ef		70	L	L	L	L	H
		A2	Co	Ef	100	H	H	L	L	L
				Ex			L	H	H	
		B2	Ef		10	L	L	L	L	H
		A1	Ex		20	H	L	H	H	L
		B1	Ef		530	L	L	L	L	H

Caption: GR = Gamma Ray; R = Resistivity; Δt = Sonic; NΦ = Porosity; ρb = Density; Ef = effusive; Ex = explosive; Co = composite; L = Low; I = Intermediate; H = High.
Reference: The author, 2025.

6.2.6 Petrography

The mafic section (B1, B2 and B3) consist of volcanic rocks with variable but abundant devitrified volcanic glass depicted by spherulites. Felsic rocks in sections A1, A2 and A3 (Figure 16) are both effusive and explosive volcanics. The latter comprise tuff, welded tuff, perlite, lapillistone and pumice, being associated with epiclastic rocks at some depth intervals. Rhyolite and dacite comprise the effusive felsic rocks. In turn, massive and amygdaloidal basalts comprise most of the mafic rocks in the well.

The mafic and felsic rocks were described under macroscopic and microscopic scales (Figure 17; also refer to Appendix B for detailed petrographic descriptions and Figure 16 for the location of each sample along the well).

The mafic rocks in sections B1, B2 and B3 (Figure 17) comprise mostly very fine-grained (< 0.1 mm) to fine- (0.1 mm - 1 mm) basalt, with minor occurrence of andesite. Essential minerals are plagioclase, pyroxene and olivine, the latter often as pseudomorphs. The accessory minerals are iron oxide, leucoxene and apatite. Alteration products are represented by carbonate, calcite, talc, chlorite, zeolite, and uralite. All samples contain devitrified glass depicted by typical

spherulites. Some samples contain amygdales. The basalts are often porphyritic and glomeroporphyritic, other textures being intersertal, intergranular, synneusis, subophitic, ophitic, poikilitic, swallow tail, skeletal, and sieve.

Figure 16: The mafic and felsic magmatic sections discriminated in well 6-BG-6-SPS in Santos Basin.

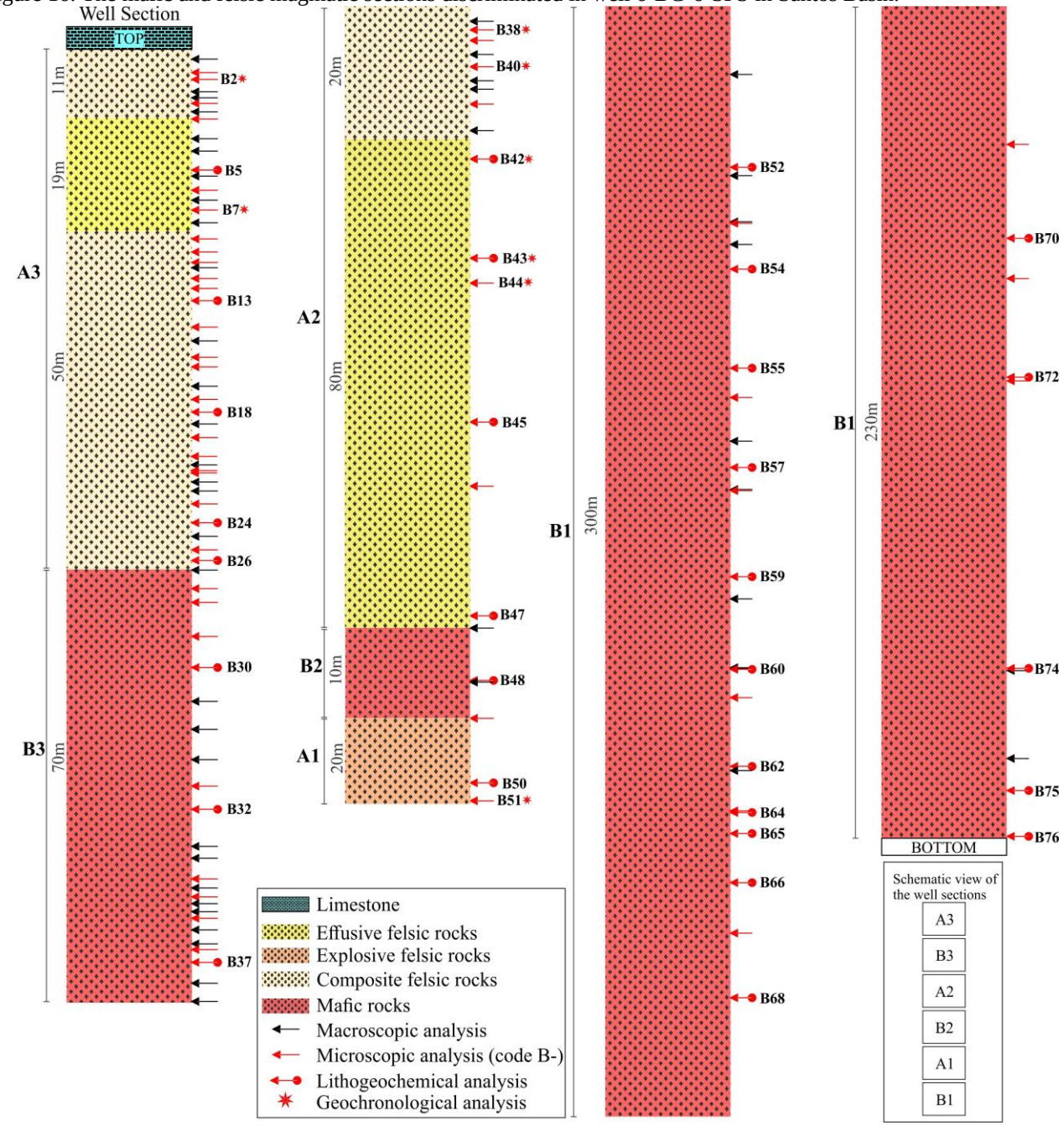

Note: Samples with macroscopic, microscopic and lithogeochemical analysis are indicated as well as the stacking of individual sections (B1, A1, B2, A2, B3 and A3). Samples described under optical microscope were previously described under a macroscopic scale and all samples selected for lithogeochemical analysis were described under the optical microscope.
Reference: The author, 2025.

The B1 mafic section comprises basalts (Figure 17a) with various textures and structures. The typical phenocryst is subedric and euedric plagioclase and structures are predominantly

massive, but basalts also have joints, and fully or partially carbonate-infilled amygdales and veins, subordinately. The B2 mafic section is a thin bed composed mostly of aphyric basalt with carbonate-infilled veins (Figure 17b). The B3 mafic section comprises massive and amygdaloidal basalts. Amygdales are filled with carbonate, subcircular and smaller than 0.5 mm in diameter, although a few are centimetric (Figure 17c).

The felsic rocks in sections A1, A2, and A3 are very fine- (< 0.1 mm) to fine-grained (0.1 mm - 1 mm) and composed of quartz, feldspar, pyroxene, plagioclase and devitrified glass. Iron oxide, apatite and zircon are accessory phases. The alteration products are carbonate, calcite, chlorite, saussurite, talc, sericite and zeolite. The felsic rocks display different textures, from porphyritic, micropoikilitic and subophitic to perlitic and eutaxitic ones. Unusual structures observed in some of the felsic rocks are spherulites and orbicules; amygdales, carbonate veins and fiammes being more common.

The commonest explosive volcanic rocks in the A1 felsic section are non-welded and welded tuffs (Figure 17d). The tuffs have fiammes and lithoclasts of basalts with textures similar to the basalts found along B1 mafic section. The thicker and lower part of A2 felsic section is composed of effusive rocks, mostly dacite and rhyolite whereas its thinner, uppermost part comprises tuffs, welded tuffs with predominantly dacitic composition (Figure 17e). The A3 section comprises rhyolite (Figure 17f), dacite, tuff, perlite, volcaniclastic rock, lapillistone and pumice.

Figure 17: Petrographic (macroscopic and microscopic) characteristics of representative samples recovered from the mafic and felsic magmatic sections of well 6-BG-6P-SPS in Santos Basin.

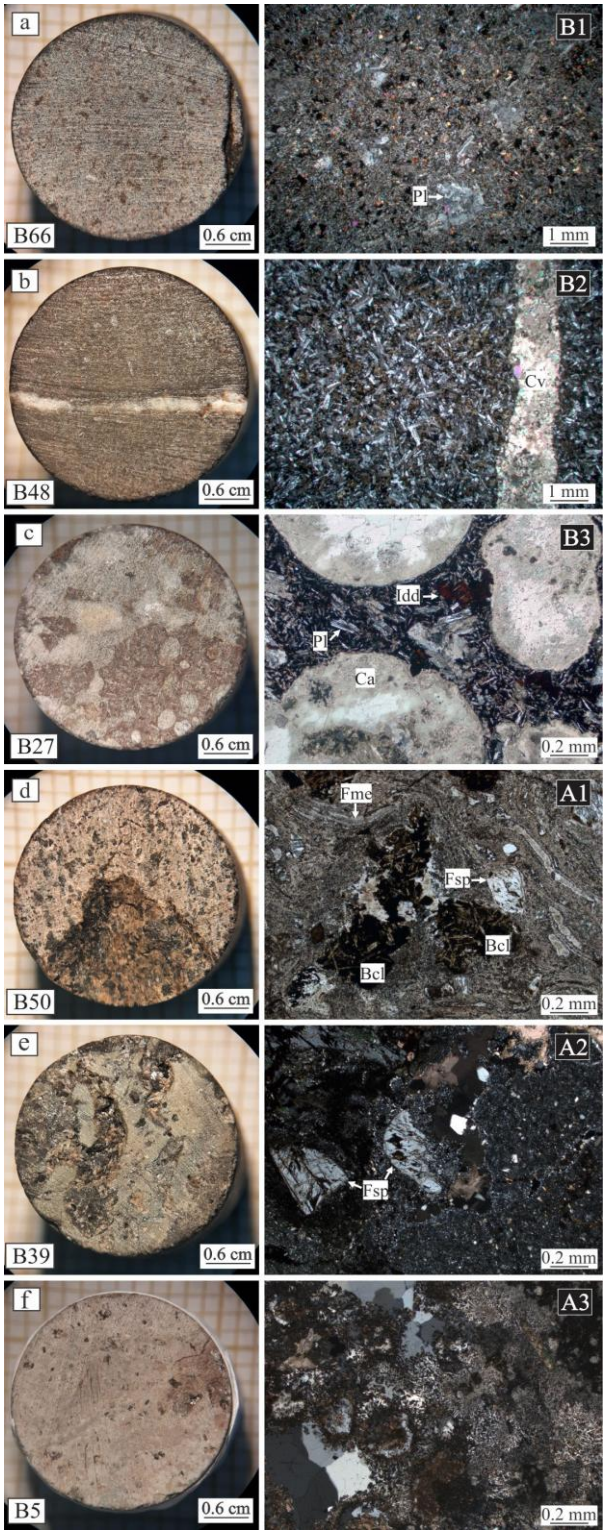

Caption: a) Plagioclase-phyric (Pl) basalt with fine-grained matrix (sample B66; B1 mafic section); b) Aphyric, fine-grained basalt with carbonate vein (Cv) (sample B48; B2 mafic section); c) Plagioclase-phyric (Pl) amygdaloidal basalt with very fine-grained matrix and the carbonate (Ca)-infilled amygdales Iddingsite (Idd) is a common alteration material (sample B27; B3 mafic section); d) Welded tuff with basaltic lithoclasts (Bcl) and fiammes (Fme) (sample B50; A1 felsic section); e) Dacite with feldspar (Fsp) crystalloclasts in very fine-grained matrix (sample B39; A2 felsic section); f) Quartz-phyric rhyolite with spherulitic matrix (sample B5; A3 felsic section).
Note: Photographs were taken under the stereoscopic microscope, photomicrographs under the transmitted light petrographic microscope.
Reference: The author, 2025.

6.2.7 U-Pb *in situ* geochronology

Eight thin sections of samples from the felsic sections (A1, A2 and A3) were selected for *in situ* U-Pb geochronology analysis of thirty-two zircon grains (Appendix D). The samples included rhyolites, dacite and tuff. The concordia ages of each sample and the average ages of each felsic sections are shown in Table 5. The total average age of the felsic rocks in well 6-BG-6P-SPS in Santos Basin is *ca.* 127 Ma, inserting the magmatism in the rift phase of Santos Basin (Figure 15b). Two tuffs (sample B51 in A1 section and sample B40 in A2 section) gave ages with high MSWD values (respectively, 2.8 and 10.2) and very low values of probability fit (respectively 0.094 and 0.0001) and their results were discarded. Sample B38 in A2 section is a thin tuff but gave reliable MSWD and probability fit values. All other dated samples are effusive rocks, being two dacites (samples B42 and B44) and one rhyolite (sample B43) from the effusive part of the A2 section, and two rhyolites (B2 and B7) from the A3 section (Table 5). The oldest ages obtained for the thin tuff in the A2 section (*ca.* 135 Ma) and the rhyolite in the A3 section (*ca.* 129 Ma) agree with the A3 section being above the A2 one (Figure 16). However, both volcanic processes could be coeval taking into account the error values. The same applies for the youngest ages obtained for samples in the A2 and A3 sections (Table 5). These geochronological data, combined with the stacking of mafic and felsic sections in well 6-BG-6P-SPS, also impose a minimum age of *ca*. 135 Ma for the recorded effusive basalt volcanism. The U-Pb ages are consistent with bimodal, long standing (135 – 122 Ma; *i.e.*13 M.y.) volcanism recorded in well 6-BG-6P-SPS in Santos Basin. As such, these geochronological data may represent the first record of a bimodal volcanism related to the Camboriú Formation in Santos Basin.

Table 5: Geochronological data of felsic volcanic rocks in well 6-BG-6P-SPS of Santos Basin, with concordia ages and average ages of samples and felsic sections.

Sample	Section	Rock	Concordia age (Ma)	MSWD	Probability	Average age
B2	**A3**	Rhyolite	128.6 ±4	0.16	0.69	125.6 ±3
B7		Rhyolite	122.6 ±2	0.32	0.57	
B38	**A2**	Thin Tuff	135.2 ±1.1	0.59	0.44	127. ±2
B40		Dacite	124.6 ±2.4	10.2	0.0001	
B42		Dacite	128.8 ±3.6	0.57	0.45	
B43		Rhyolite	124.6 ±1.3	0.028	0.87	
B44		Dacite	121.6 ±2.1	0.116	0.73	
B51	**A1**	Tuff	131.5 ±2	2.8	0.094	-

Note: Samples B51 and B40 were discarded. MSWD is Mean Square Weighted Deviation of concordance.
Reference: The author, 2025.

6.2.8 Lithogeochemistry

Twenty-nine samples were selected for whole-rock geochemical analysis (Table 6 and Appendix C for analytical data and Appendix E for statistical data), as such: twenty-one samples from the B1, B2 and B3 mafic sections and eight samples from the A1, A2 and A3 felsic sections (Figure 16).

The mafic rocks in sections B1, B2, and B3 (total of 19 samples; sample B37 in section B3 with LOI = 12.90 wt.% not being included) are basic ($43.55 < SiO_2 < 52.42$ wt.%; 50.11 ± 2.61 wt.%) and relatively evolved ($3.34 < MgO < 10.47$ wt.%; 6.10% ± 1.77 wt.%; two andesites not included), with no recorded primitive composition (*e.g.*, Ni < 170 ppm, Sc < 41 ppm, Co < 52 ppm, and Cr < 350 ppm). The samples are variably altered with LOI values between 7.17 wt.% and 1.45 wt.% (3.65 ± 1.72 wt.%). The basic rocks comprise a low-Ti suite ($TiO_2 < 1.92$ wt.%; except sample B48 from B2 with $TiO_2 = 3.09$ wt.%) based on parameters typically used to discriminate basaltic suites CFB provinces (*e.g.*, Peate, 1997 and references therein). The concentrations of incompatible and mobile trace elements such as Ba, Sr and Rb vary greatly (coefficient of variations from 47% to 136%), possibly as a consequence of alteration. The concentrations of Y, Zr and Nb also vary greatly, from 19 ppm to 35 ppm, 79 ppm to 265 ppm and 6 ppm to 21 ppm, respectively, as well as the REE ratios (*e.g.*, 3.3 < La/Yb < 10.2; basalts only), such variations unlikely to be related to alteration since these are all immobile trace elements.

The effusive and explosive felsic rocks in sections A1, A2, and A3 (10 samples, being 4 dacites, 2 rhyolites, 1 welded tuff, 1 perlite and 2 andesites) are mostly acid (SiO_2 average is 65.62 ± 4.92 wt.%) with LOI values between 9.07 wt.% and 2.15 wt.% (4.21 ± 2.07 wt.%). They are richer in K_2O (5.18 - 7.31 wt.%; 5.34 ± 1.13 wt.%) than Na_2O (0.70 – 4.11 wt.%; 1.49 ± 1.12 wt.%), with low concentrations in TiO_2 (< 1.53 wt.%) and P_2O_5 (< 0.29 wt.%). The concentrations of Rb vary between 113 ppm and 212 ppm whereas the concentrations of Sr range from 87 ppm to 142 ppm. The concentrations of Zr (286 – 512 ppm) are an order of magnitude higher than those of Y (37 – 73 ppm) and Nb (21 – 43 ppm), and the concentrations of Pb, Th and U vary between 7 – 16 ppm, 10.8 – 21.8 ppm and 1.82 – 5.4 ppm, respectively, whereas the La/Yb ratios vary greatly (10.7 ± 8.4). In general, the concentrations of Ba are very high (*e.g.*, up to1326 ppm for felsic rocks) so that petrogenetic interpretations must be done with care since there high values can be related to contamination by drilling mud.

The basic and intermediate rocks in B1, B2 and B3 mafic section classify as basalt, trachybasalt, basaltic trachyandesite and minor trachyandesite (Le Bas *et al.*, 1986) whereas the intermediate and acid rocks in the A1, A2 and A3 felsic section classify mostly as rhyolite as well

as dacite and trachyte/trachydacite in the TAS (total alkali *versus* silica) classification diagram (Figure 18a). The classifications of mafic and felsic rocks are essentially the same on the TAS and diagrams based on immobile element ratios and silica (Figure 18).

The felsic rocks plot within subalkaline field but the mafic rocks straddle the alkaline-subalkaline boundary line in the TAS diagram (Figure 18a). However, mafic rocks have Al_2O_3 < 15.28 wt.% and Alkali-Index (A.I. = $(Na_2O + K_2O)/(SiO_2-43)$ x 0.17) < 0.3 (except sample B30; A.I. = 1.57) attesting for their subalkaline, tholeiitic affinity (Middlemost, 1975). In addition, the mafic samples are all hypersthene normative according to CIPW norms calculations (except sample B70), corroborating their tholeiitic affinity (Appendix F). Finally, the mafic rocks plot as subalkaline basalt and andesite/basalt when on classification diagrams based on immobile elements ratios and silica (Winchester & Floyd, 1977; Figure 18b and 18c).

In general, the aforementioned results as well as the small (about 5 wt.%) but discernible silica gap in the TAS diagram (Figure 18a) are the first record of bimodal (*i.e.* mafic and felsic), subalkaline, tholeiitic magmatic series in the Santos Basin.

The patterns of selected basic rocks in the B1, B2 and B3 mafic sections in the chondrite-normalized multielement diagram are more spiked for the more incompatible, mobile trace elements (*e.g.*, Ba, Rb, Th and K) and relatively flat for immobile ones (from Sm to Yb; Figure 19a). The compositional range of basic rocks in B1 section (5 < Mg < 8 wt.%) includes the composition of two samples in the B3 section (MgO = 10.4 wt.%) but not of the much more evolved samples in the B2 section (MgO = 3.3 wt.%). The patterns for all basic rocks display negative anomalies of Nb and Ti, typical of low-Ti basalts in the Paraná-Etendeka CFB province. The basic rocks have higher concentrations of light REE in comparison with heavy REE, with decreasing abundances of LREE towards HREE, resulting in La/Yb_N ratios from 2.2 to 6.9 (Figure 19b). The La/Yb_N and La/Nb_N ratios greater than 1 for all basic rocks (except B75: $La/Nb_N = 1$) is also a feature commonly related to CFB (*e.g.*, Peate, 1997).

The patterns of selected intermediate and acid rocks in the A1, A2, and A3 felsic sections in the chondrite-normalized multielement diagram are spiked with prominent negative troughs in Sr, P and Ti (Figure 19c). The patterns display Nb and Ti negative anomalies that parallel those pointed for the basic rocks in the same well. Acid rocks have richer average compositions in the whole set of trace elements (exception made for Sr, P and Ti) when compared to average compositions of the intermediate rocks (Figure 19c). The intermediate and acid rocks have light REE patterns that are steeper than the nearly sub horizontal patterns of the heavy REE (Figure 17d). The acid rocks have a wider range of REE concentrations than the intermediate rocks, possibly due to the also wider silica content of the former. The REE patterns of both intermediate and acid rocks display a distinct Eu negative anomaly (Figure 19d).

Figure 18: Samples from well 6-BG-6P-SPS in Santos Basin plotted in classification and series discrimination diagrams.

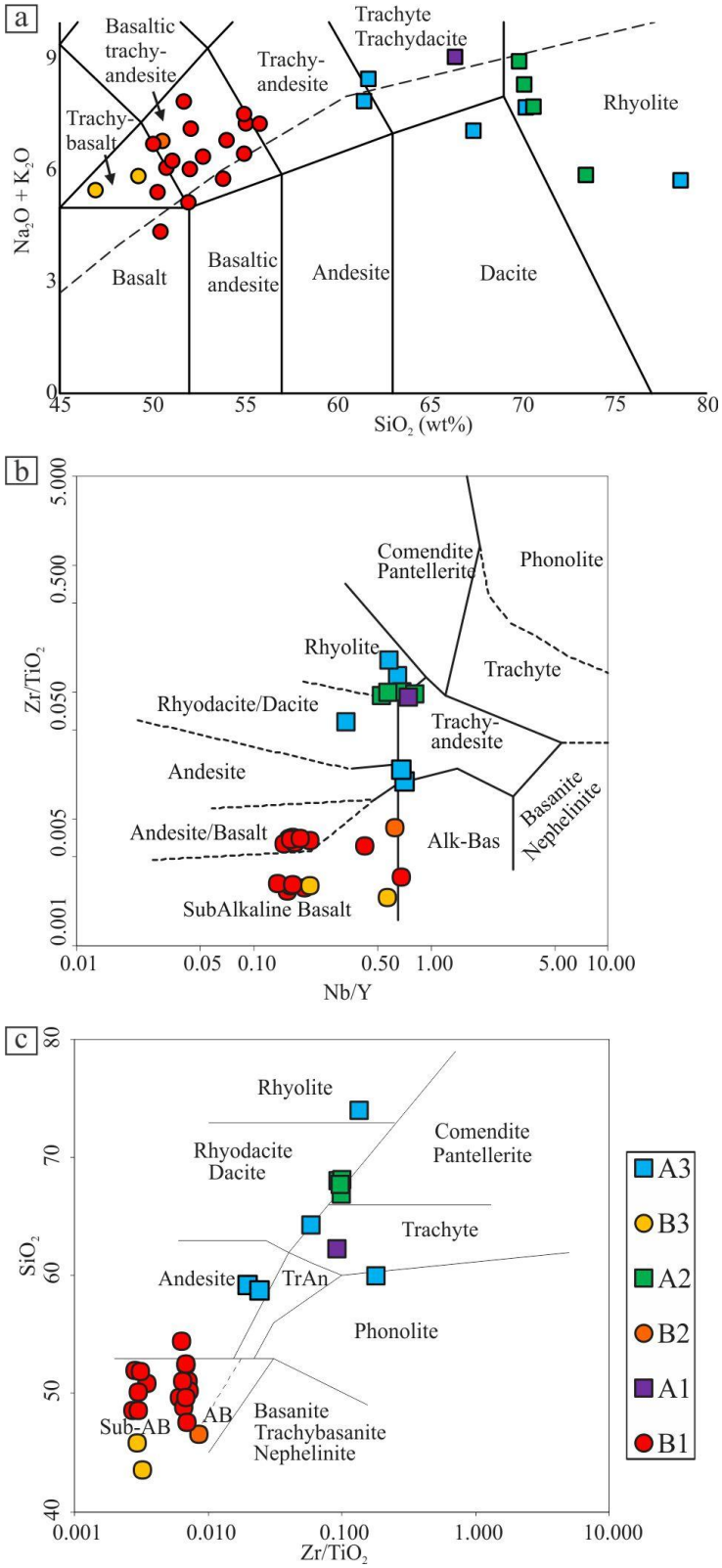

Caption: a) TAS (Total Alkalis versus Silica) diagram with the alkaline-subalkaline boundary line from. Data recalculated for 100% on a volatile-free basis; b) The Nb/Y *versus* Zr/TiO_2 discrimination diagram; c) the Zr/TiO_2 *versus* SiO_2 (wt.%) discrimination diagram.

Reference: a) Le Bas *et al.* (1986), Irvine and Baragar (1971); b) and c) (Winchester and Floyd, 1977).

Table 6: Lithogeochemical data of selected volcanic rocks in well 6-BG-6P-SPS in Santos Basin (continue).

Sample	Section	SiO_2	TiO_2	Al_2O_3	$Fe_2O_3^t$	MnO	MgO	CaO	Na_2O	K_2O	P_2O_5	LOI	Total	Ni	Cr	Co	Sc	V	Ba	Rb	Sr	Y	Zr	Hf
B-5	**A3**	74.05	0.21	10.74	1.35	0.04	0.77	1.75	0.72	4.69	bdl	4.58	98.93	bdl	bdl	1	3	10	656	141	142	42	286	6.9
B-13	**A3**	59.96	0.21	12.32	3.89	0.07	2.59	3.87	1.12	5.18	0.01	9.07	98.29	bdl	bdl	3	3	12	740	212	115	56	374	9.2
B-18	**A3**	64.32	0.59	11.81	3.41	0.04	1.63	2.86	0.70	6.36	0.09	6.54	98.35	bdl	bdl	16	12	62	888	156	87	63	345	8
B-24	**A3**	58.74	1.44	14.23	9.30	0.04	1.26	2.38	3.08	4.99	0.29	4.23	99.98	40	bdl	21	18	135	425	124	125	38	349	8.4
B-26	**A3**	59.22	1.53	14.11	9.69	0.04	0.97	3.48	4.11	3.48	0.27	3.55	100.40	50	bdl	19	22	184	516	115	128	37	302	7.8
B-30	**B3**	43.55	1.88	14.45	14.92	0.24	10.41	2.85	3.62	1.46	0.24	6.81	100.40	130	220	50	39	337	628	32	249	23	90	2.3
B-32	**B3**	45.86	1.46	15.28	13.40	0.15	10.47	1.61	4.36	1.09	0.17	6.41	100.30	160	190	45	35	358	468	27	254	23	86	2.3
B-42	**A2**	68.04	0.40	9.71	4.93	0.07	0.77	3.48	0.75	4.70	0.07	5.90	98.80	bdl	bdl	10	9	35	999	113	114	56	374	8.4
B-43	**A2**	68.12	0.44	11.91	7.04	0.06	0.37	1.41	1.96	5.49	0.07	2.34	99.22	bdl	bdl	1	9	26	967	179	98	55	435	9.9
B-45	**A2**	66.91	0.52	12.84	4.25	0.08	0.47	2.32	2.02	6.55	0.09	3.86	99.91	bdl	bdl	3	11	25	1326	172	138	73	512	11.8
B-47	**A2**	67.74	0.49	12.06	6.91	0.05	0.46	1.18	1.77	6.27	0.07	2.15	99.15	bdl	bdl	3	9	34	1280	166	128	54	475	11.9
B-48	**B2**	46.53	3.09	12.45	13.49	0.20	3.34	7.06	2.64	3.62	0.37	7.17	99.95	50	bdl	29	30	354	669	65	367	35	265	6.3
B-50	**A1**	62.31	0.55	13.09	6.43	0.07	0.82	2.36	1.20	7.31	0.10	4.18	98.40	bdl	bdl	4	12	33	1022	186	112	57	504	11.5
B-52	**B1**	50.87	1.29	13.19	11.02	0.15	7.52	2.05	3.11	3.61	0.19	6.00	99.00	130	240	48	35	169	444	63	141	21	90	2.1
B-54	**B1**	52.42	1.50	13.80	11.76	0.16	5.30	7.33	2.69	2.94	0.13	1.86	99.88	60	60	36	37	282	472	79	248	22	102	2.7
B-55	**B1**	51.07	1.65	14.22	12.53	0.21	5.47	8.61	3.25	1.81	0.17	1.77	100.80	60	70	38	40	336	304	60	271	26	116	3.1
B-57	**B1**	48.54	1.70	12.85	13.98	0.29	8.00	5.01	4.74	1.07	0.21	4.30	100.70	170	280	52	37	284	433	20	313	26	92	2.3
B-59	**B1**	49.65	1.82	14.38	13.27	0.22	6.10	9.21	3.09	1.20	0.21	1.45	100.60	70	110	46	39	393	282	38	262	29	110	2.7
B-60	**B1**	50.23	1.83	13.99	13.11	0.24	5.47	5.14	2.94	4.70	0.21	2.74	100.60	20	40	38	39	368	646	107	443	28	131	3.4
B-62	**B1**	51.95	1.65	14.21	10.75	0.17	5.93	5.35	5.24	1.32	0.19	3.53	100.30	110	350	41	41	344	219	24	255	25	94	2.3
B-64	**B1**	54.40	1.72	12.14	11.12	0.20	4.95	6.32	4.98	2.10	0.16	1.90	99.98	30	90	31	40	344	112	35	104	27	109	3
B-65	**B1**	48.84	1.92	14.06	12.89	0.26	5.16	6.96	3.33	2.66	0.23	2.90	99.20	bdl	70	37	38	362	1045	66	330	29	125	3.6
B-66	**B1**	51.02	1.63	13.74	12.30	0.18	5.04	7.16	3.21	2.96	0.17	1.67	99.07	bdl	80	36	36	316	221	83	332	25	105	3.1
B-68	**B1**	50.11	1.33	15.13	10.79	0.21	6.22	7.16	3.36	2.46	0.13	2.64	99.55	30	160	37	35	287	604	66	530	19	79	2.2
B-70	**B1**	51.84	1.46	12.34	9.09	0.22	6.23	7.38	5.51	0.58	0.16	4.57	99.39	30	150	34	40	278	405	10	86	27	90	2.5
B-72	**B1**	49.67	1.53	13.38	12.17	0.26	6.69	5.37	2.39	4.41	0.16	3.05	99.07	bdl	90	38	39	334	2126	115	498	26	104	2.9
B-74	**B1**	48.61	1.53	13.79	12.46	0.23	6.66	8.66	2.68	2.56	0.16	2.95	100.30	50	160	43	40	338	1092	87	313	23	92	2.4
B-75	**B1**	52.53	1.61	13.94	9.49	0.29	5.72	5.13	4.04	3.15	0.19	3.29	99.37	40	120	32	37	320	518	59	111	24	109	2.8
B-76	**B1**	47.59	1.57	14.61	13.20	0.36	7.44	4.47	2.05	4.34	0.17	3.91	99.74	60	120	41	35	331	5163	109	382	26	109	3.1

Table 6: Lithogeochemical data of selected volcanic rocks in well 6-BG-6P-SPS in Santos Basin (conclusion).

Sample	Section	Nb	Ta	La	Ce	Pr	Nd	Sm	Eu	Gd	Tb	Dy	Ho	Er	Tm	Yb	Lu	U	Th	Pb
B-5	**A3**	27	2.29	57.3	85.1	7.73	25.8	4.84	0.831	5.15	1.04	7.2	1.58	4.8	0.711	4.77	0.775	3.3	21.8	16
B-13	**A3**	33	2.44	69.3	83.3	14.4	52.4	10.6	1.78	9.97	1.81	10.8	2.1	6.31	0.966	6.59	1.05	1.82	21.7	7
B-18	**A3**	21	2.04	69.1	139	14.6	53.7	10.7	2.15	10.3	1.75	10.8	2.26	6.61	1.03	6.67	1.13	5.4	16.1	8
B-24	**A3**	26	1.92	57.2	117	12.8	47.8	9.21	1.84	7.5	1.14	7	1.38	4.07	0.609	4.11	0.662	3.05	11.9	9
B-26	**A3**	26	1.86	42	84.1	9.41	35.8	7.28	1.5	7.05	1.12	7.01	1.39	4.16	0.639	4.46	0.701	2.7	11.4	10
B-30	**B3**	13	0.68	16.9	32.6	3.72	15.6	3.44	1.37	4.01	0.65	4.34	0.9	2.64	0.386	2.38	0.365	0.42	1.45	52
B-32	**B3**	9	0.53	12.5	25.7	3.2	14.3	3.63	1.36	4.08	0.64	4.09	0.85	2.48	0.364	2.38	0.38	0.24	1.05	21
B-42	**A2**	29	2.12	79	146	16.6	64.8	13.3	2.97	12.9	1.93	11.5	2.1	5.59	0.822	5.35	0.863	2.93	10.8	11
B-43	**A2**	38	2.66	67.2	126	14.4	55.4	10.7	2.27	9.4	1.61	10.6	2.13	6.31	0.977	6.54	1.09	3.33	15	14
B-45	**A2**	42	3.1	76.8	156	17.4	67.8	14.2	3.32	13.4	2.33	14.2	2.76	8.01	1.23	8.14	1.27	3.75	15	9
B-47	**A2**	43	2.91	55.4	104	11.8	44.8	8.98	2.11	8.62	1.56	10.3	2.04	6.18	0.95	6.39	1.03	2.93	14.8	14
B-48	**B2**	22	1.48	33.9	69.6	8.51	35.4	7.8	2.38	7.79	1.22	7.04	1.32	3.56	0.505	3.32	0.539	0.78	3.4	14
B-50	**A1**	42	2.74	73.8	139	17.1	65.2	13.5	3.29	12.1	1.86	11	2.16	6.71	1.03	6.86	1.11	2.81	14.1	10
B-52	**B1**	14	0.66	17.7	35.5	4.07	17.2	3.6	1.08	3.61	0.6	3.66	0.78	2.32	0.337	2.28	0.349	0.3	1.61	23
B-54	**B1**	7	1.57	11.9	25	3.14	13.7	3.45	1.19	3.96	0.66	4.05	0.82	2.37	0.341	2.22	0.363	0.2	1.12	17
B-55	**B1**	8	0.59	13.4	29	3.66	16.6	4.24	1.42	4.7	0.78	4.96	0.95	2.59	0.374	2.46	0.403	0.27	1.23	bdl
B-57	**B1**	8	0.66	9.56	22	3.07	15.7	4.04	1.33	4.7	0.79	5.09	1.01	2.86	0.403	2.7	0.434	0.29	0.66	9
B-59	**B1**	12	0.74	15.2	32.7	4.04	18.3	4.75	1.52	4.75	0.84	5.38	1.05	3.05	0.433	2.55	0.411	0.39	1.87	bdl
B-60	**B1**	9	1.14	12.3	29	3.89	18.4	4.85	1.57	5.11	0.86	5.54	1.06	2.99	0.419	2.74	0.445	0.28	1.41	bdl
B-62	**B1**	10	0.63	10.6	24.8	3.41	15.1	3.63	1.18	4.34	0.78	4.75	0.95	2.65	0.382	2.59	0.442	0.22	0.93	bdl
B-64	**B1**	8	0.62	8.54	22.2	3.14	15.5	4.29	1.41	4.25	0.78	4.97	0.96	2.8	0.425	2.61	0.411	0.32	1.41	5
B-65	**B1**	10	0.7	13.4	31.1	4	18.8	4.84	1.61	5.2	0.9	5.42	1.07	3.04	0.43	2.78	0.438	0.4	1.51	5
B-66	**B1**	9	0.56	12.9	27.7	3.64	15.4	4.4	1.35	4.27	0.79	4.86	0.94	2.69	0.37	2.4	0.366	0.34	1.3	bdl
B-68	**B1**	6	0.34	8.59	19.2	2.6	11.3	2.94	1.09	3.38	0.59	3.84	0.75	2.06	0.298	1.91	0.303	0.17	0.8	bdl
B-70	**B1**	7	0.53	8.8	22	3.12	13.4	4.33	1.43	4.38	0.76	4.87	1.02	2.88	0.413	2.64	0.415	0.61	1.11	16
B-72	**B1**	8	0.83	10.7	26	3.3	16	4.56	1.15	4.49	0.84	4.91	0.98	2.64	0.384	2.51	0.382	0.4	2.04	bdl
B-74	**B1**	8	0.57	10.1	22.8	2.92	14.2	4.39	1.18	4	0.69	4.25	0.86	2.51	0.348	2.13	0.323	0.24	0.95	6
B-75	**B1**	10	0.65	9.43	25.3	3.44	16.8	4.48	1.19	4.61	0.78	4.48	0.92	2.64	0.403	2.49	0.377	0.28	1.63	6
B-76	**B1**	10	0.72	12.9	31	4	18.8	4.42	1.55	4.8	0.82	4.82	0.96	2.71	0.391	2.53	0.382	0.34	1.61	6

Caption: $Fe_2O_3^t$ is total iron as ferric iron, LOI is loss on ignition and bdl is below detection limit. Oxides in wt.%; elements in ppm).
Reference: The author, 2025

Figure 19: The compositional patterns of selected samples from well 6-BG-6P-SPS in Santos Basin in chondrite-normalized diagrams.

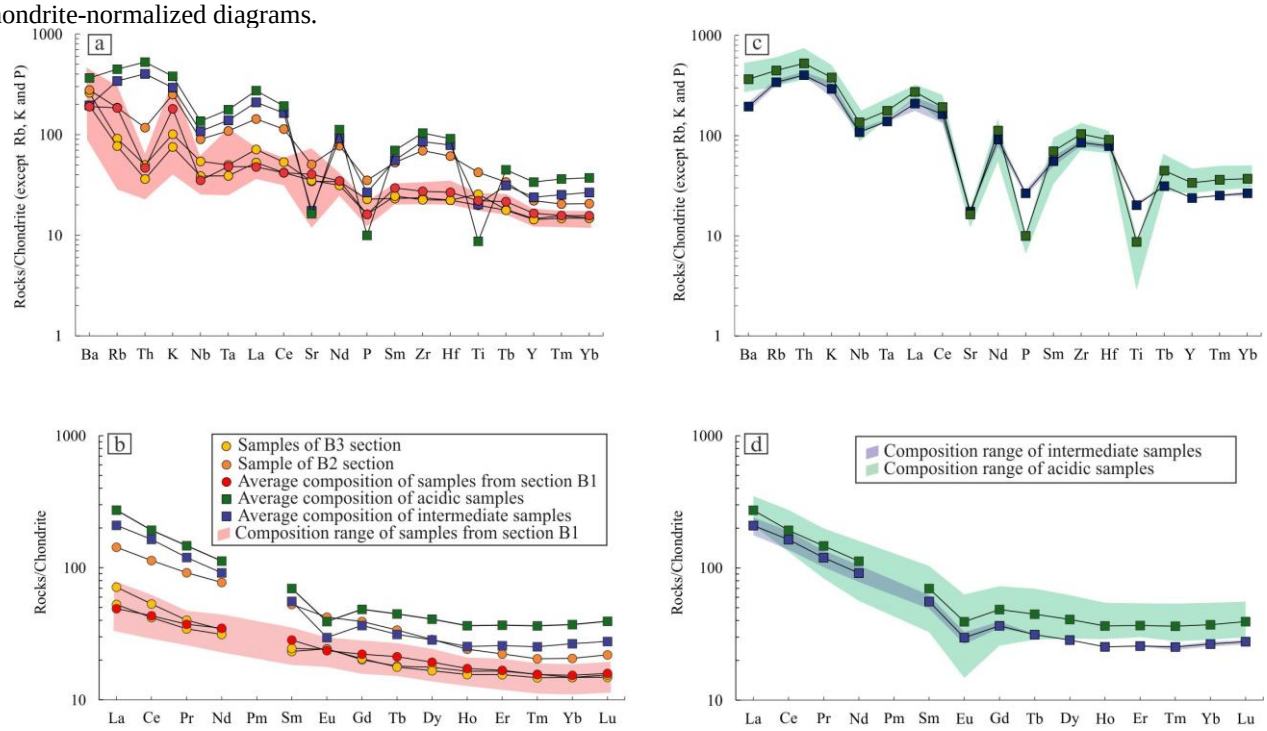

Caption: (a) Compositions, average and range of compositions of basic rocks in B1, B2 and B3 mafic sections as well as average compositions of acid and intermediate rocks in chondrite-normalized multielement diagram. (b) Same as (a) but plotted in chondrite-normalized REE diagram. (c) Same as (a) but samples from A1, A2 and A3 felsic section. (d) Same as (c) but plotted in chondrite-normalized REE diagram. Captions of diagrams shown in (c) and (d).
Reference: Normalizing factors from McDonough and Sun (1995), except for Rb, K and P that are from Thompson (1982).

6.2.9 Isotope data (Sr, Nd and Pb systems)

The isotope data were obtained for fifteen samples from the felsic and mafic sections in well 6-BG-6P-SPS in Santos Basin (Table 7). Four samples recovered from the felsic sections were selected for analysis. Sample B50 is an acid (SiO_2 = 62.3 wt.%) volcanic tuff in the A1 felsic section. Sample B45 is an acid (SiO_2 = 66.9 wt.%), effusive trachydacite in the A2 felsic section. Two samples were selected from A3 felsic section, as such: an intermediate (samples B26, SiO_2 = 59.2 wt.%) trachyandesite and a rhyolite (sample B5; SiO_2 = 74.1 wt.%) (Table 7). The four samples are slightly altered (3.6 < LOI < 4.6 wt.%) and, therefore, their analysis was proceeded by acid leaching.

Eleven samples were selected from the mafic section in well 6-BG-6P-SPS, as such: B30 and B32, from the B3 section, B48, from the B2 section, and samples B52, B55, B57, B60, B64, B66, B68 and B70 (Sr and Pb data only) from the B1 section (Table 7). The samples were selected on the basis of the following criteria: absence of amygdales, low degree of alteration as seen by petrographic (macroscopic and microscopic scales) analysis, low values of LOI, samples

representative of the least and more evolved compositions based on their MgO contents, samples with similar MgO contents but different La/Yb_N values. The isotope data were all recalculated to 127 Ma, according to the average U-Pb age obtained for the intermediate and acid rocks in the well.

Samples from the mafic and felsic sections have rather different Sr-Nd isotope ratios (Table 7).

The samples from the B1, B2 and B3 mafic section have values of $^{87}Sr/^{86}Sr_{(127)}$ ratios ranging between 0.706482 and 0.711788 and $^{143}Nd/^{144}Nd_{(127)}$ ratios ranging between 0.512259 to 0.512421 ($\varepsilon_{Nd(127)}$ = -1.0 to -4.2) (Table 7). The $^{206}Pb/^{204}Pb_{(127)}$ ratios of those samples are between 18.08 and 18.75, $^{207}Pb/^{204}Pb_{(127)}$ between 15.57 and 15.95, and the $^{208}Pb/^{204}Pb_{(127)}$ ratio ranges from 38.27 and 39.07 (Table 7). The samples from the A1, A2 and A3 felsic section have values of $^{87}Sr/^{86}Sr_{(127)}$ ratios ranging between 0.708989 to 0.729133, whereas the $^{143}Nd/^{144}Nd_{(127)}$ ratios range from 0.512144 to 0.512258 ($\varepsilon_{Nd(127)}$ = -4.2 to -6.5) (Table 7). The ranges of Pb isotope data for those same samples are: $^{206}Pb/^{204}Pb_{(127)}$ between 18.61 and 19.28, $^{207}/Pb/^{204}Pb_{(127)}$ between 15.69 and 15.73, $^{208}Pb/^{204}Pb_{(127)}$ ratio between 38.25 and 39.23 (Table 7).

Samples from the mafic sections spread over a wider range of Nd isotope initial ratios when compared with the samples from the felsic section (Figure 20a). On the other hand, the range of Sr isotope initial ratios of the samples from the felsic sections is wider than that of the samples in the mafic sections. In general, the samples from the mafic sections are more Sr and Nd radiogenic than the Sr-Nd isotope composition of the Tristan da Cunha mantle plume; sample B52 (B1 mafic section) has the highest radiogenic Sr isotope composition ($^{87}Sr/^{86}Sr_{(127)}$ = 0.711991; Table 7) and being displaced towards typical EMII Sr isotope compositions (Figure 20a). There is no consistent variation of Sr-Nd isotope data among the three mafic sections. For instance, the Sr-Nd isotope compositions of the samples in the B3 mafic section fall within the range obtained for samples in the B1 mafic section (Figure 20a). All samples in the mafic section of well 6-BG-6P-SPS plot within the enriched quadrant of the Sr-Nd isotope diagram (Figure 20a), having negative values (-1.0 to -4.2) of $\varepsilon_{Nd(127)}$ (Table 7). No consistent Pb isotope variations are seen among the three mafic sections, similarly to the Sr-Nd isotope variations, despite the linear trend displayed by the samples towards the EMII mantle component: those from the B3 mafic section having the highest Pb isotope compositions (Figure 20b). The $^{206}Pb/^{204}Pb_{(127)}$ *versus* $^{207}/Pb/^{204}Pb_{(127)}$ in Figure 20b show the high values of Pb isotopic ration, and a correlation between basic samples and EMII reservoir and lower continental crust.

Figure 20: Diagrams with isotopic data obtained for samples from the mafic and felsic sections in the well 6-BG-6P-SPS in Santos Basin.

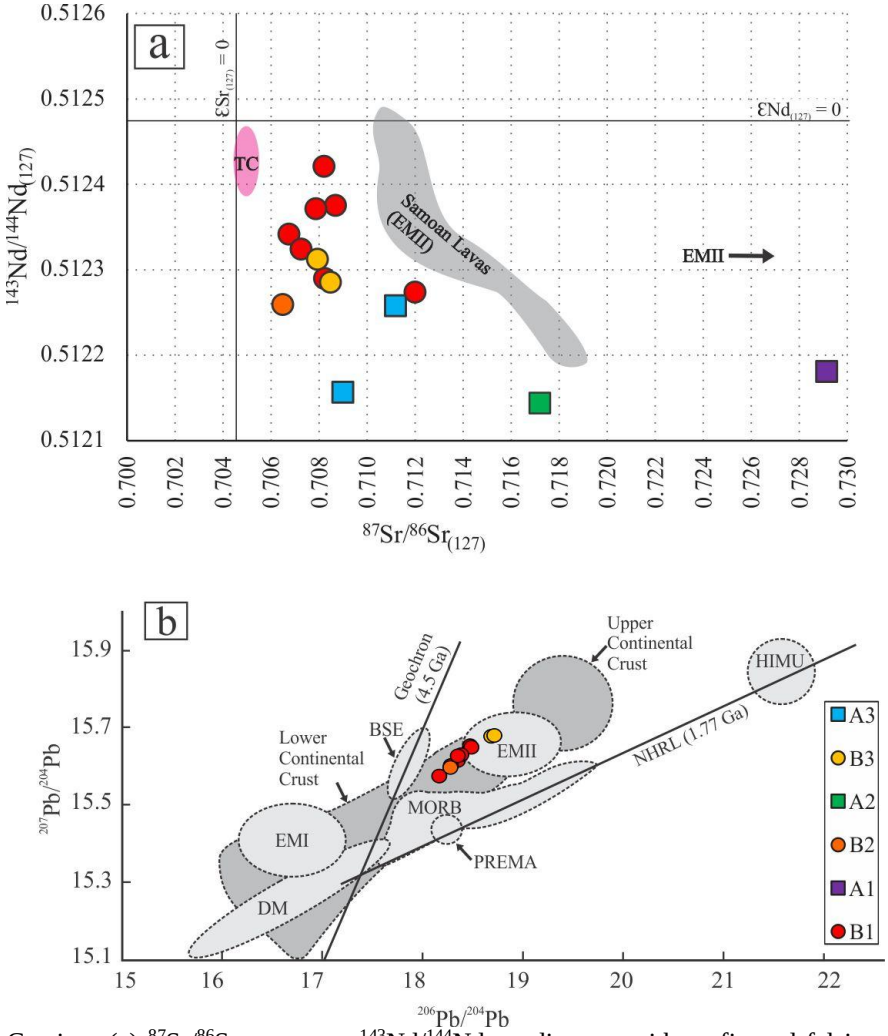

Caption: (a) $^{87}Sr/^{86}Sr_{(127)}$ *versus* $^{143}Nd/^{144}Nd_{(127)}$ diagram with mafic and felsic rocks ($^{87}Sr/^{86}Sr_{(127,\ UR)}$ = 0.704547; $^{143}Nd/^{144}Nd_{(127,\ UR)}$ = 0.512475) (b) $^{206}Pb/^{204}Pb$ versus $^{207}Pb/^{204}Pb$ with samples from the mafic section only. Mantle components are: HIMU (mantle with high U/Pb ratio (high-μ)); DM (depleted mantle); EMI and EMII (enriched mantle I and II); BSE (Bulk Silicate Earth); MORB (Mid-Ocean Ridge Basalts); PREMA (Prevalent Mantle).
Reference: The typical isotopic compositions of the enriched mantle type 2 (EMII; Zindler & Hart, 1986) is show by the arrow. The Tristan da Cunha (TC; Newson, 1986 and Le Roex *et al.*, 1990) and the Samoan islands (Jackson *et al.*, 2007) isotopic compositions are also shown. Source for the mantle components is Zindler & Hart (1986).

Table 7: Measured and age-corrected (127 Ma) Sr-Nd-Pb isotopic data and their respective 2σ standard errors obtained for samples within the mafic and felsic section in well 6-BG-6P-SPS in Santos Basin. (continue)

Sample	**B5**	**B26**	**B30**	**B32**	**B45**	**B48**	**B50**
Section	**A3**	**A3**	**B3**	**B3**	**A2**	**B2**	**A1**
$^{87}Sr/^{86}Sr_{(m)}$	0.714175	0.715872	0.708596	0.709026	0.723699	0.707407	0.737806
Error	0.000010	0.000008	0.000011	0.000008	0.000008	0.000011	0.000008
$^{84}Sr/^{86}Sr_{(m)}$	0.056432	0.056423	0.056438	0.056378	0.056425	0.05644	0.056409
$^{87}Sr/^{86}Sr_{(127)}$	0.708989	0.711180	0.707925	0.708471	0.717190	0.706482	0.729133
$\varepsilon_{Sr(127)}$	63.1	94.1	47.9	55.7	179.4	27.5	349.0
$^{143}Nd/^{144}Nd_{(m)}$	0.512251	0.512360	0.512423	0.512413	0.512249	0.512370	0.512285
Error	0.000007	0.000014	0.000021	0.000016	0.000008	0.000016	0.000008
$^{145}Nd/^{144}Nd_{(m)}$	0.348407	0.348413	0.348399	0.348394	0.348402	0.348428	0.348400
Error	0.000005	0.000006	0.000012	0.000011	0.000010	0.000008	0.000004
$^{143}Nd/^{144}Nd_{(127)}$	0.512157	0.512258	0.512312	0.512286	0.512144	0.512259	0.512181
$\varepsilon_{Nd(127)}$	-6.2	-4.2	-3.2	-3.7	-6.5	-4.2	-5.7
T_{DM} **(Ga)**	1172	1119	1141	1488	1334	1228	1259
$^{206}Pb/^{204}Pb_{(m)}$	19.538	18.940	18.684	18.713	19.191	18.276	19.427
Error	0.002	0.002	0.001	0.001	0.001	0.001	0.001
$^{206}Pb/^{204}Pb_{(127)}$	19.285	18.608	18.674	18.699	18.679	18.208	19.082
$^{207}Pb/^{204}Pb_{(m)}$	15.724	15.706	15.676	15.678	15.735	15.596	15.751
Error	0.002	0.002	0.001	0.001	0.001	0.001	0.002
$^{207}Pb/^{204}Pb_{(127)}$	15.712	15.690	15.676	15.677	15.710	15.593	15.734
$^{208}Pb/^{204}Pb_{(m)}$	39.778	39.020	38.634	38.668	38.918	38.437	39.107
Error	0.004	0.004	0.003	0.002	0.004	0.002	0.003
$^{208}Pb/^{204}Pb_{(127)}$	39.23024	38.56169	38.62279	38.64790	38.24795	38.33936	38.54014
$^{208}Pb/^{206}Pb_{(m)}$	2.03588	2.06009	2.07036	2.06639	2.02791	2.10310	2.01305
Error	0.00008	0.00007	0.00005	0.00004	0.00007	0.00004	0.00006
$^{207}Pb/^{206}Pb_{(m)}$	0.80479	0.82919	0.83896	0.83784	0.81989	0.85336	0.81082
Error	0.00002	0.00002	0.00001	0.00001	0.00002	0.00001	0.00002

Table 7: Measured and age-corrected (127 Ma) Sr-Nd-Pb isotopic data and their respective 2σ standard errors obtained for samples within the mafic and felsic section in well 6-BG-6P-SPS in Santos Basin. (conclusion)

Sample	B52	B55	B57	B60	B64	B66	B68	B70
Section	B1	B1	B1	B1	B1	B1	B1	B1
$^{87}Sr/^{86}Sr_{(m)}$	0.714324	0.707905	0.709001	0.709133	0.709984	0.708541	0.708850	0.708248
Error	0.000010	0.000008	0.000010	0.000010	0.000010	0.000008	0.000011	0.000010
$^{84}Sr/^{86}Sr_{(m)}$	0.056412	0.056439	0.056435	0.056423	0.056433	0.056427	0.056414	0.056438
$^{87}Sr/^{86}Sr_{(127)}$	0.711991	0.706749	0.708667	0.707872	0.708226	0.707235	0.708200	0.707641
$\varepsilon_{Sr(127)}$	105.6	31.2	58.5	47.2	52.2	38.2	51.8	43.9
$^{143}Nd/^{144}Nd_{(m)}$	0.512379	0.512470	0.512505	0.512504	0.512429	0.512468	0.512552	-
Error	0.000015	0.000012	0.000014	0.000015	0.000010	0.000010	0.000018	-
$^{145}Nd/^{144}Nd_{(m)}$	0.348409	0.348401	0.348389	0.348417	0.348418	0.348415	0.348404	-
Error	0.000010	0.000008	0.000008	0.000010	0.000006	0.000006	0.000010	-
$^{143}Nd/^{144}Nd_{(127)}$	0.512274	0.512342	0.512376	0.512372	0.512290	0.512325	0.512421	-
$\varepsilon_{Nd(127)}$	-3.9	-2.6	-1.9	-2.0	-3.6	-2.9	-1.0	-
T_{DM} **(Ga)**	1130	1384	1329	1410	1809	1884	1256	-
$^{206}Pb/^{204}Pb_{(m)}$	18.472	18.166	18.486	18.349	18.385	18.281	18.351	18.79
Error	0.001	0.002	0.002	0.002	0.001	0.002	0.002	0.100
$^{206}Pb/^{204}Pb_{(127)}$	18.456	18.083	18.446	18.263	18.306	18.177	18.299	18.75
$^{207}Pb/^{204}Pb_{(m)}$	15.652	15.574	15.648	15.614	15.629	15.601	15.626	15.95
Error	0.001	0.002	0.002	0.002	0.001	0.002	0.002	0.100
$^{207}Pb/^{204}Pb_{(127)}$	15.651	15.570	15.646	15.610	15.625	15.596	15.623	15.95
$^{208}Pb/^{204}Pb_{(m)}$	38.537	38.398	38.499	38.462	38.495	38.478	38.469	39.09
Error	0.002	0.005	0.003	0.005	0.003	0.004	0.004	0.600
$^{208}Pb/^{204}Pb_{(127)}$	38.50886	38.27438	38.46952	38.32028	38.38163	38.34734	38.38859	39.06511
$^{208}Pb/^{206}Pb_{(m)}$	2.08616	2.11379	2.08257	2.09801	2.09378	2.10484	2.09629	2.08053
Error	0.00006	0.00007	0.00006	0.00008	0.00006	0.00007	0.00006	0.00150
$^{207}Pb/^{206}Pb_{(m)}$	0.84731	0.85731	0.84650	0.85097	0.85007	0.85346	0.85150	0.84888
Error	0.00001	0.00002	0.00002	0.00002	0.00001	0.00002	0.00002	0.00800

Caption: The ages were estimated at 127 Ma. An arbitrary value (4 ppm) was used for age corrections of the Pb ratios for samples B55, B60, B66 e B68. The Nd isotope ratios are expressed also in the epsilon notation. The depleted mantle model ages (T_{DM}) are also shown.
Reference: The author, 2025

6.2.10 Discussions

6.2.10.1 The compositional gap and possible differentiation processes

Large igneous provinces (LIPs) are often associated with compositional gap between basic and acid compositions, imprinting a bimodal distribution of geochemical data (Daly, 1925; Chayes, 1963; Zao *et al.*, 2023). This silica gap appears between the basic, intermediate and acid rocks, when the samples within the mafic and felsic magmatic sections of well 6-BG-6P-SPS are

plotted in a Harker diagram (Figure 21). However, the roughly curvilinear, inverse correlation between MgO and SiO_2 in the Harker diagram is a common feature related with cogeneticity by fractional crystallization, meaning that the compositional gap may be a consequence of sampling being restricted to a single drilling well. Furthermore, some of the basic, intermediate and acid rocks present patterns in the chondrite-normalized multielement diagrams (Figure 19a and 19c) that at face value would be consistent with magmatic cogeneticity by fractional crystallization, either as a open-system (i.e., with crustal assimilation or AFC).

The likelihood of a genetic relationship of the mafic and felsic rocks in the well 6-BG-6P-SPS by differentiation can be firstly investigated on the basis of their elemental and isotope data (Table 6, Table 7, Figure 20). The closed-system, fractional crystallization is not capable of imprinting variations greater than the analytical errors of isotope ratios (Table 7). Closed-system, fractional crystallization of a typical fractionating assemblage in basalts (i.e., olivine, clinopyroxene and plagioclase) will enrich the evolved basaltic magmas in incompatible elements (e.g., the large-ion lithophile elements or LILE, and the high field strength elements or HFSE) without much fractionation between the light and heavy REE. On the other hand, open-system, fractional crystallization will result in differences in the isotope ratios of the less evolved and more evolved magma compositions beyond the analytical errors. Besides, trace elements enrichment will be greater than that produced during close-system, fractional crystallization.

Figure 21: Samples from the six magmatic sections in well 6-BG-6P-SPS in Santos Basin plotted in the Harker diagram for MgO with a compositional silica gap (about 5 wt.%) between the basic rocks from the B1, B2 and B3 mafic sections and the intermediate and acid rocks from the A1, A2 and A3 felsic sections.

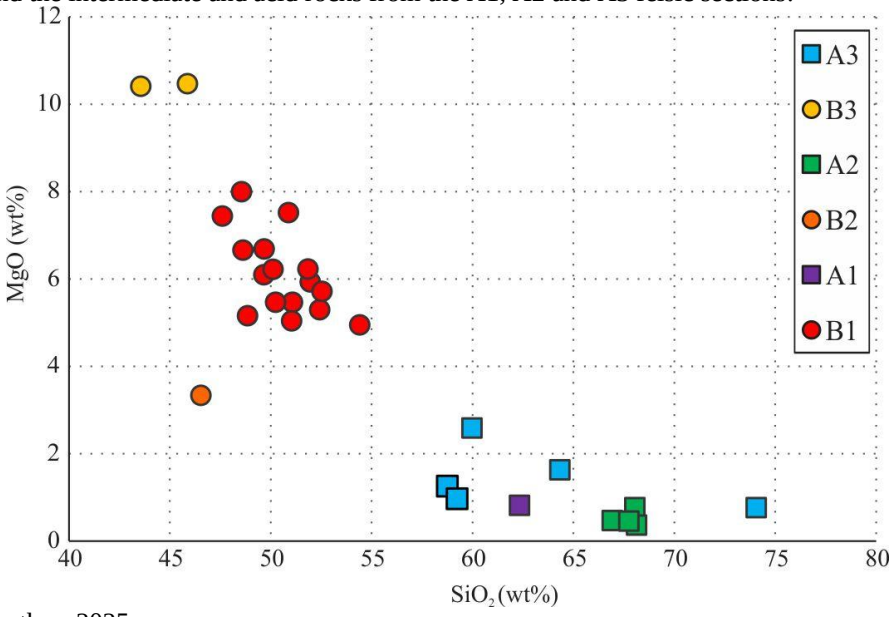

Reference: The author, 2025.

The relationship among basic, intermediate and acid rocks in the mafic and felsic sections of the well 6-BG-6P-SPS by closed-system fractional crystallization can be excluded on the basis of their initial isotope ratios (Figure 20). The same applies to genetic relationships within the mafic and felsic sections. For instance, the initial Sr-Nd isotope ratios of the samples representing the least and more evolved basalts lavas in the B1 mafic section (respectively, B57; MgO = 8.00 wt.%, and B64; MgO = 4.95 wt.%; Table 3) differ in the fourth decimal place (Table 7). Similarly, differences of the initial Sr-Nd isotope ratios in the third decimal place are seen between samples B57 and sample B48 (MgO = 3.34 wt.%), in the B1 and B2 mafic sections, respectively. The initial Sr-Nd isotope ratios of the least evolved sample in the well (B30 and B32, B3 mafic section, both with MgO = 10.40 wt.%; Table 6) are also different of the more evolved basic compositions in the B1 and B2 mafic sections. Finally, differences in the values of Sr-Nd-Pb isotope ratios also preclude genetic relationships by fractional crystallization between basic and intermediate rocks as well as between intermediate and acid rocks in the well (Figure 20).

Despite the fact that the rocks in the well 6-BG-6P-SPS are not related by closed-system, fractional crystallization, their isotope ratios do not preclude the hypothesis of cogeneticity by AFC. This differentiation process has been often related to the basic volcanism in CFB provinces. This is the case of the voluminous Gramado low-Ti basalts flows in the Paraná Magmatic Province (e.g. Petrini *et al.*, 1987; Peate, 1997; Ewart *et al.*, 1998; Barreto *et al.*, 2016; Almeida *et al.*, 2019) and similarly to other CFB worldwide (e.g., Krans *et al.*, 2024).

The existence of a genetic link within and between the mafic sections and between the mafic sections and the intermediate rock in the A3 felsic section was tested by geochemical modelling using the equation for isotope variations proposed by DePaolo (1981). The main drawback for the modelling was the selection of a local crustal contaminant. The basement rocks of the Santos Basin, where the AFC processes are prone to have happened, comprise the Ediacaran to Cambrian high-grade, strongly deformed metamorphic rocks of the Ribeira collisional orogen (Valeriano *et al.*, 2016; Heilbron *et al.*, 2020a,b). The local upper crust is likely to include granitic to granodioritic orthogneisses and Al-rich schists (metapelites) that form the basement and supracrustal units of the orogen, with a lower crust mostly constitute by granulites (Heilbron *et al.* 2008). However, the average elemental and isotope compositions of the lower and upper crust in the southeast Brazil are still to be determined and the average compositions of the continental crust available in the literature (e.g. Taylor & McLennan, 1981; Weaver & Tarney, 1984; Wedepohl, 1995; Rudnick & Gao, 2004; Hawkesworth & Kemp, 2006) are largely variable and may not parallel that in SE Brazil. Alternatively, the AFC modelling performed here assumed that initial Sr-Nd isotope compositions of the local crustal contaminants would fall within the wide isotopic range represented by the acid rocks in well 6-BG-6P-SPS. This assumption took into consideration

that the isotope compositions of acid liquids are unlikely to be changed due to crustal contamination processes and, as such, they can be good proxies to their crustal sources. The acid rock represented by sample B5 in the A3 felsic section has initial Sr-Nd isotope ratios that are too low to represent a likely contaminant during AFC in order to generate the intermediate rock (sample B26) in the A3 felsic section. The isotope compositions of the two crustal contaminants used in geochemical modelling are shown in Table 8.

Models were done considering a typical basaltic fractionating assemblage with 50% olivine, 40% clinopyroxene and 10% plagioclase, the partition coefficient (KD) values from the compiled data in Rollinson (1993) and a contaminant/fractionating ratio (r value) of 0.3 and 0.7, to represent the AFC process in the upper and lower crust, respectively (Taylor, 1980; DePaolo, 1981). The higher value of r can also be a consequence of the existence of an anomalously upper crust at ca. 127 Ma underneath the Santos Basin.

Table 8: Elemental and isotope compositions of crustal contaminants used in the AFC modelling. Elements in ppm.

Contaminant	Type	Sample	Sr	Nd	$^{87}Sr/^{86}Sr_{(127)}$	$^{143}Nd/^{144}Nd_{(127)}$
CC1	Acid	B45	138	68	0.7171	0.51214
CC2	Acid	B50	112	65	0.7281	0.51218

Reference: The author, 2025.

The wide range of the initial Sr and Nd isotope ratios of the basic and intermediate rocks in the well 6-BG-6P-SPS (Table 7; Figure 20) can be related to various AFC trends (Figure 22 and Appendix G).

The least evolved basic rocks (samples B30 and B32; MgO = 10 wt.%) cannot produce the isotope compositions of any of the more evolved basic rocks. The same applies to sample B52 and between samples B57 and B68. Similarly, the samples B55, B60, B64 and B66 cannot be related with a single AFC trend with sample B68 representing the least evolved composition (Figure 22, AFC trend 3). Finally, sample B48 cannot represent a least evolved composition within any AFC trend since it has the lowest initial Sr isotope ratio and MgO content (Figure 22). The best result of the AFC modelling was obtained with the least evolved composition represented by sample B55. This basalt could give rise to the isotope compositions of samples B66 and B64 by 7% and 28% fractional crystallization of 70% plagioclase and 30% clinopyroxene (DSr = 1.2990; DNd = 0.1257) and concomitant assimilation of an upper crust contaminant represented by CC2 at r = 0.31 (Figure 22). The same AFC process could give rise to the intermediate rock in the A3 felsic section after 60% fractional crystallization of the same fractionating assemblage (Figure 22). The curvature of AFC trends does not change for the r values (0.3 and 0.7) applied to the models, differences being related to a smaller amount of fractional crystallization needed for the AFC

process to occur in the lower crust (in this case, less than 8% rather the 28% required to generate the AFC trend within the basic range). Altogether, the AFC model is consistent with the derivation of the intermediate rock in well 6-BG-6P-SPS from parental basic liquids with MgO = 6 wt.% in the B1 mafic section. This MgO concentration is largely capable of producing the fractionating assemblage used in the AFC model. On the other hand, the least evolved basaltic compositions represented by samples B30 and B32 cannot be related to any more evolved basic compositions in the B1 and B2 mafic sections. They must represent parental basaltic liquids in other two liquid lines of descent, considering their rather different initial Sr-Nd isotope ratios, whose evolved basalts are not sampled in the well 6-BG-6P-SPS. The curvature of the AFC trend related with these two basalts, represented by the dashed lines 2 and 3 in Figure 22, also preclude any genetic relationship with the intermediate rock in the A3 felsic section. Finally, it seems impossible that the initial Sr-Nd isotope ratios of the acid rocks in the A3 felsic section (sample B5 and B45, the latter also taken as the CC1 contaminant in the AFC modelling) would fit an AFC trend starting with the intermediate composition in the A3 felsic section. It would require a crustal contaminant much more Sr and Nd radiogenic than CC2, also implying the migration of the viscous intermediate liquid away from the magma chamber in which it was generated in the first place.

Figure 22: AFC trend for the rocks in the magmatic sections of well 6-BG-6P-SPS in the Santos Basin.

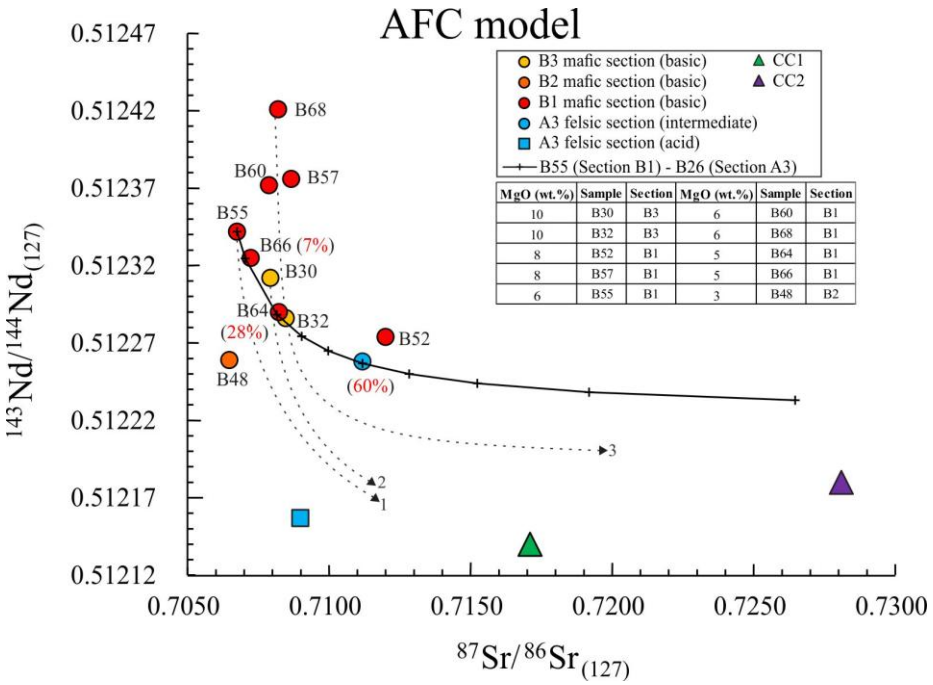

Note: The isotope composition of crustal contaminants CC1 and CC2 are indicated, as some sample codes of the basalts in the mafic section. The amount of fractional crystallization of the AFC curve (crosses) is indicated (red figures). Approximate curvatures of AFC trends are shown by the dashed lines 1, 2 and 3.
Reference: The author, 2025

In conclusion, the compositional gap between basic and intermediate compositions represented by the mafic and felsic rocks in the well 6-BG-6P-SPS is related with scarce sampling.

The least and more evolved basalts in this well, respectively in the B3 and B2 mafic sections, are associated with flows that erupted from vents other than the one that gave rise to the basalts in the B1 mafic section. The same applies to some basalts in the B1 mafic section (B52, B57, B60 and B68) whose isotope compositions do not fit the AFC trend having the least evolved basic composition represented by sample B55. On the other hand, processes other than closed- and open-system fractional crystallization must have been operated to generate the acid rocks in the well 6-BG-6P-SPS in the Santos Basin.

6.2.10.2 The origin of the acid rocks

The acid rocks, including those in LIP's such as the Paraná-Etendeka, can be generate by partial melting of the continental crust (Harris & Milner, 1997), or partial melting of basic rocks. They can also be the final products of fractional crystallization from basic rocks, with or without crustal contamination (e.g., Bellieni *et al.*, 1986, Garland *et al.*, 1995).

The studied acid rocks recovered from well 6-BG-6P-SPS in the Santos Basin cannot be the product of partial melting of the basic rocks in the same well due to their distinct initial isotope ratios (Table 7 and Figure 20). Also, those rocks cannot be result from AFC in the basic rocks by AFC as demonstrated in previous sections (Figure 22). Therefore, the hypothesis of an origin by partial melting of the continental crust is a plausible process to be tested by geochemical modelling.

The modelling was done using the equations of batch modal partial melting (Wood & Fraser, 1976). The published concentrations of the immobile trace elements Zr, Y and Nb of the upper and lower continental crust were used to produce different possible settings for the partial melting process (Table 9 and Appendix H). The acid rocks in the A1 (sample B50), A2 (sample B45) and A3 (sample B5) felsic sections are taken as representative acid melts related with three different crustal compositions on the basis of their initial Sr and Nd isotope ratios (Table 7). Tests were performed for typical amphibolitic and granulitic mineral compositions representing the local lower continental crust as well as mineral compositions of felsic orthogneisses to represent the upper continental crust (Valeriano *et al.*, 2016; Heilbron *et al.*, 2020a,b). The amount of melting associated with the generation of felsic melts is rather variable (e.g., 20-60%; Vielzeuf & Holloway, 1988; Patiño Douce & Beard, 1995), but melt generation is likely to require between 10% and 30% melting (e.g. Sawyer, 1994; 2001). The aims of the modelling was to reproduce the modelled bulk partition coefficients (D) needed to generate the concentrations of Zr, Y and Nb of

the acid rocks within this melting range (10-30%) typically associated with the production of rhyolitic melts (Appendix H). The best result obtained for the rhyolite with the highest silica values (sample B5; A3 felsic section; Table 6) was 28% partial melting of a felsic gneiss (K-feldspar = 39%; plagioclase = 58%; biotite = 3%) with the concentrations of Zr, Y and Nb close to their lowest values and within analytical error (Table 9; Appendix H). A mineral composition including 35% quartz, equal amounts (30%) of K-feldspar and plagioclase plus 5% of biotite would require a higher degree of partial melting (F = 44%) of the same felsic upper crust. The concentrations of Zr, Y and Nb in the rhyolite represented by sample B45 (A2 felsic section) cannot be explained by the amounts of partial melting (28% and 45%) derived for rhyolite (sample B5) in the A3 felsic section using the range of trace element compositions and modes of the felsic gneiss of the upper continental crust (Table 9 and Appendix H). The same applies to the rhyolite represented by the sample B50 in the A1 felsic section. Models with typical granulitic and amphibolitic compositions of the lower continental crust did not produce good results due to the high partition coefficients of Y and Nb between acid liquids and hornblende and orthopyroxene and clinopyroxene (Appendix H).

The results of the modelling are consistent with the origin of the rhyolite in the three felsic sections in well 6-BG-6P-SPS in the Santos Basin by partial melting of felsic rocks with different trace element compositions in the upper continental crust, as also supported by the different initial Sr and Nd isotope ratios of the felsic volcanic rocks in the well.

Table 9: The concentrations of Zr, Y and Nb (in ppm) in the continental upper crust and the lower continental crust.

	Upper Crust			**Lower Crust**			**Samples (Section)**	**Zr**	**Y**	**Nb**	**SiO_2**
	Zr	**Y**	**Nb**	**Zr**	**Y**	**Nb**	**B5 (A3)**	286	42	27	74.05
n	16	17	11	19	17	18	**B45 (A2)**	512	73	42	66.91
Mode	193	21	26	68	16	5	**B50 (A1)**	504	57	42	62.31
Average	203	22	19	116	20	8	**Average**	434	57	37	67.76
SD	31	3	7	56	8	4	**SD**	128	16	9	5.92
CV (%)	15	13	38	48	4	45	**CV (%)**	30	28	24	8.73
Lowest	160	17	10	30	7	4	**Lowest**	504	57	42	62.31
Highest	240	32	26	206	40	15	**Highest**	512	73	42	74.05

Note: SD = standard deviation. CV = coefficient of variation (Average: SD ratio). n = amount of values.
References: Taylor & McLennan, 1981, Taylor *et al.*, 1983, Weaver & Tarney 1984, Shaw *et al.*, 1986, Condie, 1993, Rudnick & Fountain, 1995, Taylor & McLennan, 1985, Wedepohl, 1995, Plank & Langmuir, 1998, Kemp & Hawkesworth 2003, Rudnick & Gao, 2004.

6.2.10.3 Mantle sources

Basalts are originated by partial melting of the mantle, which constitute a rather heterogeneous reservoir in the Earth, despite its predominantly peridotitic composition. The variable isotopic and trace element compositions of basalts can be generally explained by either variable amounts of partial melting from a common source or by derivation from different mantle sources.

The AFC models presented in a previous section allowed to conclude that the basalts in mafic section in well 6-BG-6P-SPS in Santos Basin are associated with different vents, although some samples in the B1 mafic section have initial Sr and Nd isotope ratios that are consistent with single AFC trend. This means that volcanic vents at the surface are most probably linked with shallow-seated magma chambers where contamination processes may have changed the original isotopic compositions of the basaltic liquids. Therefore, the mantle sources and partial melting regime are to be investigated on the basis of the isotopic and trace elements compositions of the least evolved basalts since they represent uncontaminated or the least contaminated liquids during the AFC processes (e.g., DePaolo, 1981).

The partial melting process was investigated using the equation of modal batch model (Wood & Fraser, 1976). It is well known that there are no major differences in the results obtained by this equation when compared to the results obtained by using the non-modal model considering the range of partial melting (F values) degrees to generate tholeiitic basalts. Using the batch model also overcomes the debate about the struggling to segregate the very small fractions of melt when the fractional model is used in modeling.

The samples B30 and B32 were selected due to their high MgO values (10.41 and 10.47 wt.%, respectively) and low SiO_2 values (43.44 and 45.86 wt.%, respectively), taken as representative of uncontaminated liquids. Samples B30 and B32 present similar values of La/Nb and Zr/Y (1.3 and 3.9, respectively), but distinct values of La/Yb ratios (7.1 and 5.3, respectively) and initial Sr and Nd isotope ratios (Table 7). The aims of the model were to reproduce the different La/Yb ratios of those two samples within the spinel and garnet stability zones in the lherzolitic mantle with 55 vol.% of olivine, 20 vol.% of orthopyroxene and 15 vol.% clinopyroxene plus 10% of the Al-phase, considering a range of 20-30% partial melting to generate tholeiitic basalt liquids (e.g. Green, 1970). The two least evolved basalts cannot be related to the same mantle source according to the results of the analytical modelling (Appendix I and Figure 23). The La/Yb ratios of these least evolved basalts cannot be explained by partial melting within the spinel stability zone. In addition, the two samples have La/Yb ratios that will not fall

within the range of partial melting required to generate tholeiitic basalts considering either a mantle composition with chondritic La/Yb ratio or an enriched mantle composition with La/Yb ratio 1.8 times the chondritic value (Figure 23). These results are corroborated by the differences in the initial Sr and Nd ratios of the two least evolved basalts, implying the melting of different source reservoirs deeper than 80 km in the mantle.

Figure 23: Results of modal batch partial melting model using the least evolved basalts in the well 6-BG-6P-SPS in Santos Basin.

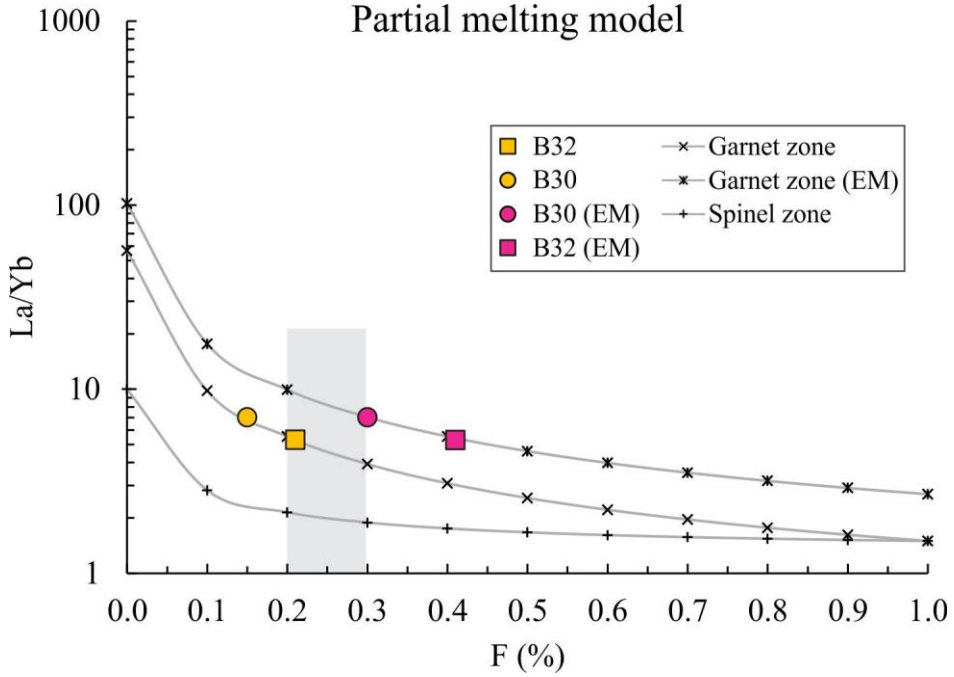

Note: The average interval of degree of partial melting (F value) is shown by the shaded area. EM = enriched mantle with La/Yb ratio 1.8 times chondritic value.
Reference: The author, 2025.

6.2.10.4 Mantle reservoir and geodynamic processes

The La/Yb_N and La/Nb_N >1 for all basic, intermediate and acid samples, the negative values of ℇNd (from -1 to -6.5) and high values of $^{87}Sr/^{86}Sr_{(127)}$ (> 0.7064) suggest that the partial melting involved enriched components within the mantle. The deep-seated, fertile Tristan da Cunha mantle reservoir (TC mantle plume) also seems to have played a role in the mantle melting process (Figure 20a) being taken as with during the formation of the coeval Paraná-Etendeka CFB in the continental area close to the Santos Basin (e.g., White & Mckenzie, 1989; Gibson *et al.*, 1999; Meisling *et al.*, 2001, Thomaz Filho *et al.*, 2005). Besides, an enriched mantle component such as EMII may have imprinted the high $^{87}Sr/^{86}Sr$ and Pb isotope ratios of the uncontaminated, least evolved basalts (Figure 20).

The interplay between the deep-seated, fertile sublithospheric and shallow-seated enriched subcontinental lithospheric mantle during the petrogenesis of the studied basalts was tested by binary mixing analytical modelling. The compositions of TC from Newson (1986) (sample TR-1, Rb = 105 ppm, Sr = 1490 ppm, Sm = 14 ppm, Nd = 90.6 ppm, $^{87}Sr/^{86}Sr_{(127)}$ = 0.704682, $^{143}Nd/^{144}Nd_{(127)}$ = 0.512456) and two extreme lava compositions of EMII from Jackson (2007) (sample D115-18, Rb = 97.4 ppm, Sr = 511 ppm, Sm = 10.66 ppm, Nd = 55.89 ppm, $^{87}Sr/^{86}Sr_{(127)}$ = 0.717597, $^{143}Nd/^{144}Nd_{(127)}$ = 0.512218; Sample D111-26, Rb = 99.8 ppm, Sr = 528 ppm, Sm = 11.24 ppm, Nd = 55.43 ppm, $^{87}Sr/^{86}Sr_{(127)}$ = 0.715407, $^{143}Nd/^{144}Nd_{(127)}$ = 0.512287) were used in the modelling. The initial Sr and Nd isotope ratios of samples B30 and B32 can be explained by nearly equal amounts of TC and EMII endmembers (Figure 24). The best consistent results were obtained using an isotopic composition of the EMII component with high $^{87}Sr/^{86}Sr_{(127)}$ (> 0.714) and low $^{143}Nd/^{144}Nd_{(127)}$ (< 0.5123) for a less variable TC isotope composition (Figure 24).

The origin of the EMII has been largely debated. Its genesis was initially associated with recycling and storage of continental or oceanic lithosphere and terrigenous sediments subducted into the mantle (Zindler & Hart, 1986; Jackson, 2007). An alternative origin involves metasomatic processes which enriched the oceanic lithosphere during subduction events, followed by storage and recycling (Workman *et al.*, 2004). The EMII fingerprints are its high $^{87}Sr/^{86}Sr$ (> 0.710) and low $^{143}Nd/^{144}Nd$ (< 0.5126) (Zindler & Hart, 1986), although the different elemental compositions of sediments related with distinct tectonic environments resulted in a wide range of EMII compositions. Based on the partial melting models shown in previous sections, the petrogenesis of the studied basalts is likely to have involved different mantle sources. As such, the EMII component may reflect the melting of the enriched subcontinental lithospheric mantle underneath the Santos Basin in Early Cretaceous time, probably triggered by the TC upwelling.

Figure 24: The mixing curves between Tristan da Cunha (TC) and Enriched-Mantle II (EMII) endmembers in the Sr-Nd isotope diagram.

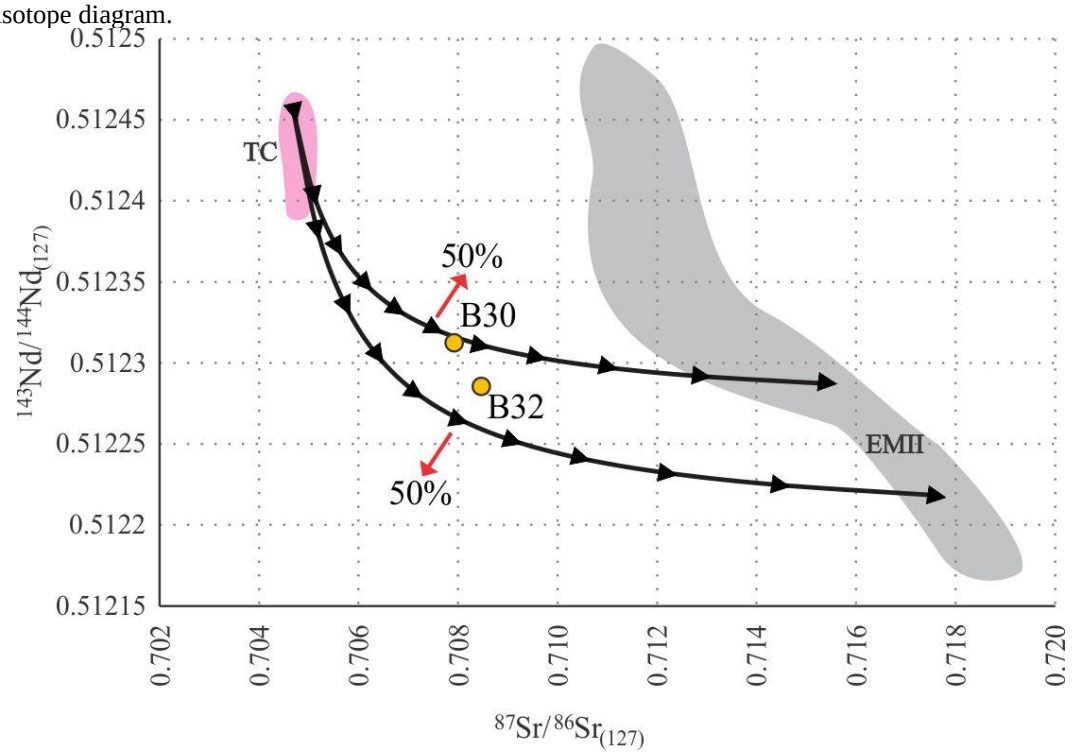

Note: The samples B30 and B32 plot nearly 50% TC and 50% EMII.
References: The TC and EMII fields (shaded areas) include data from Newsom (1986), Le Roex *et al.* (1990) and Jackson *et al.* (2007).

A conceptual geodynamic model for the mantle processes related to the petrogenesis of the magmatic rocks in the well 6-BG-6P-SPS in the Santos Basin is shown in Figure 25. The basement of the Santos Basin includes Archean and Paleoproterozoic collisional terranes that agglutinated during the Neoproterozoic (Heilbron *et al.*, 2000, 2008) to give rise to the Gondwana supercontinent. These multiple Wilson Cycles contributed to the trace element enrichment of the shallow-seated although thick lithospheric mantle of the Gondwana supercontinent (Figure 25a and 25b). The first signs of rupture were probably accompanied by mantle uprise and of the arrival of the Tristan da Cunha plume, producing the voluminous magmatism of the Paraná-Etendeka CFB (e.g., White & Mckenzie, 1989; Gibson *et al.*, 1999; Meisling *et al.*, 2001, Thomaz Filho *et al.*, 2005), but also reaching the site of the basemen of the Santos Basin, resulting in the basalts of the Camboriú Formation. The heat advected from the TC plume must have triggered the melting of the low-temperature, volatile-rich, portions of the SCLM and the magmatism proceeded from the Hauterivian to the Aptian (Figure 25c). As consequence, various long-lived magma chambers could form in the upper continental crust in which basaltic magmas evolved mostly by AFC giving rise to more evolved, contaminated basic and intermediate magmas (Figure 25d) that fed multiple vents at the surface.

Figure 25: Schematic geodynamic context proposes to explain the enriched (EMII) and Tristan da Cunha (TC) isotope signature, mafic rocks differentiation (AFC modelling) and partial melt (PM) processes that originated felsic rocks.

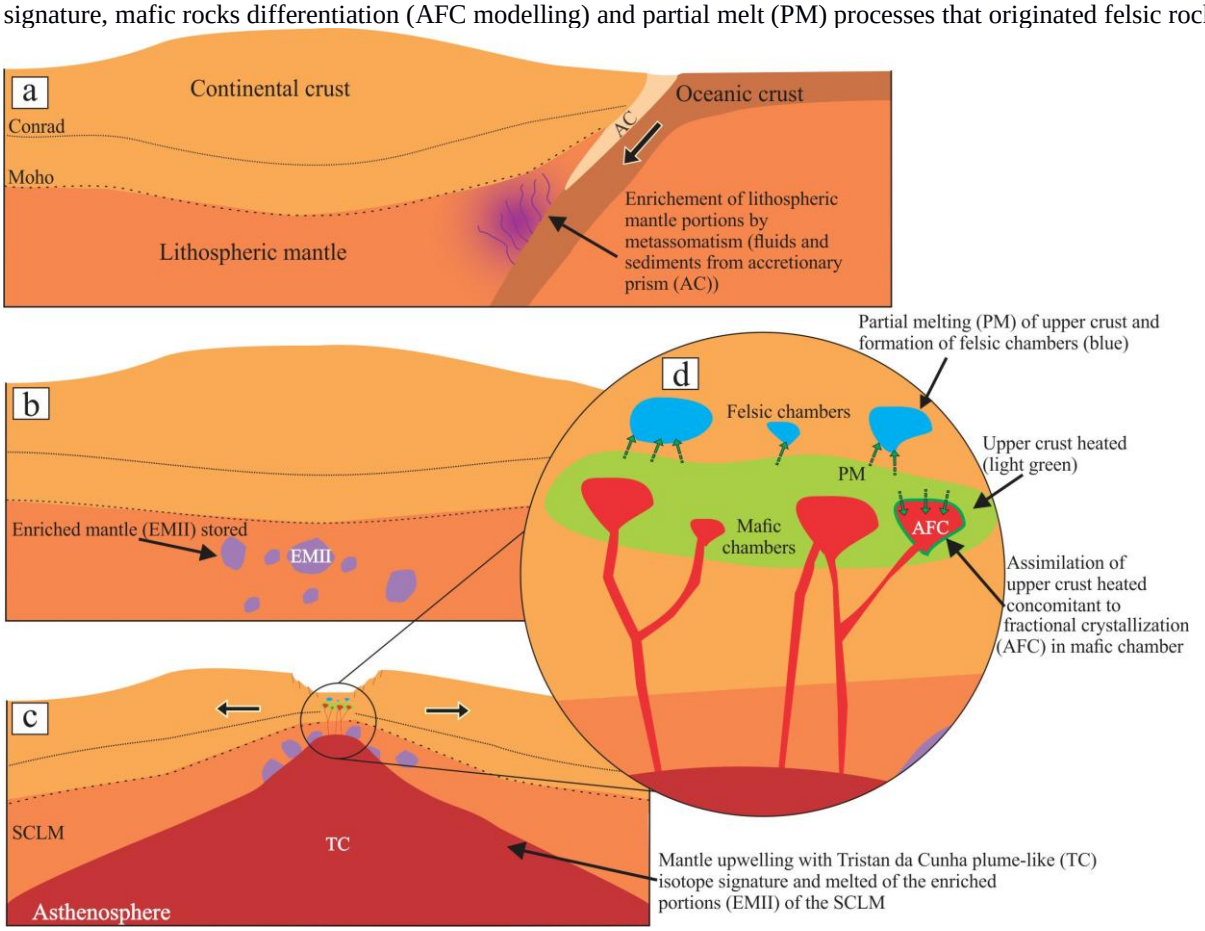

Note: AC = Accretionary Prism. SCLM = Subcontinental Lithospheric Mantle. Discordances are in dotted line.
Reference: The author, 2025.

6.2.10.5 Mantle-crust interaction, thermal regimes and CO_2 influx

A tectonic-magmatic conceptual model (Figure 26) is proposed in this section based on the well data and the petrographic and geochemical data, as well as the conceptual geodynamic model presented in previous sections.

The U-Pb geochronological data (Table 5) record two major events of felsic and mafic volcanism (V1 and V2) starting at the Hauterivian and extending to the Aptian. These two volcanic events can be related to a pre-rift stage and three rift stages (rift 1, 2 and 3) related to the evolution of the Santos Basin before the Gondwana breakup (Figure 26a). The V1 event was voluminous, bimodal although mostly basaltic and probably short-lived (*ca.* 137 – 135 Ma), occurring during the pre-rift and rift 1 stages. The basaltic flows of the B1 mafic section and possibly the explosive volcanism recorded in the A1 felsic section were probably formed during the pre-rift stage earlier than *ca.* 136 Ma. This bimodal volcanism may represent the offshore counterpart of the bimodal effusive and intrusive magmatism recorded in the Paraná-Etendeka CFB within South America

(Janasi *et al.*, 2011; Florisbal *et al.*, 2017, 2018). Explosive, felsic volcanic processes have also been documented al the onset of the silicic volcanism in the Paraná-Etendeka CFB (Guimarães *et al.*, 2019), as it seems to be the case of the volcanism recorded in the A1 felsic section of the studied well in the Santos Basin. Doming focused on the crustal portion of the continental lithosphere as a consequence of the impingement of the TC plume head occurred during the pre-rift stage (Figure 26b). Heat from the TC plume was mostly concentrated in the poorly conductive SCLM, producing low fraction melts within more fusible enriched portions of the latter. These low fractions melts mixed with melts derived from the proto-head of the TC plume giving rise to the basalts in the B1 mafic section. Melt migration towards MOHO and possible underplating, a common process during voluminous basaltic magmatism, advected enough heat to melt the close-to-eutectic portions of the upper crust to produce the volatile-rich acid liquids (rocks in the A1 felsic section) by anatexis. This can result in high heat flow from the mantle towards the overlying continental crust. The temperature required for crustal melting during the heat flow from the mantle due to plume-related mafic magmatism at rifts or at CFB provinces is about 700 ºC. The typical felsic rock types in the upper crust may begin to partially melt when the temperature exceeds 650°C and the melt they produce is acid in composition. Biotite-bearing rocks will produce melt progressively as the temperature rises up to 800°C but amphibolites will melt only at higher temperatures but they produce melt of tonalitic composition rather than rhyolitic ones. The rate of melt production also decreases and the composition of the melt is no longer rhyolitic after all the mica is consumed at about 925°C (Sawyer et al., 2011). Despite the fact most models favor crustal anatexis in the lower crust, recent thermobarometric calculations showed that anatexis can also occur at upper crustal depths (< 5 kbar or 18 km depth, at 750–800°C and 3 wt% water content; Morris *et al.*, 2024). The advected heat may have been enough to produce crustal melting but not to change the rheology of the cold thermal and brittle mechanical boundary layers (TBL and MBL, respectively) between the base of the lithosphere and the top of the ascending plume head (Figure 26b). As a consequence, incipient doming and extension were concentrated in the continental crust, during the pre-rift stage. The rapid advection of TC plume head incremented the crustal extension and the continuing short-lived magmatism producing the effusive basaltic flows and the composite felsic volcanism of the B2 mafic and A2 felsic sections, respectively, during the rift 1 stage (Figure 26b). The rift 1 stage marked the onset of the mechanical subsidence of the Santos Basin. The rift 2 stage was characterized by predominance of the advection of the TC plume head over the adiabatic decompression, resulting in lesser mantle melting and a period of quiescence that lasted for about 5 Myr. The erosion of the pre-rift and rift 1 topography led to the deposition of the lacustrine sediments that will originate the organic rich shales of the Piçarras Formation. These rocks will become the major hydrocarbon sources of the pre-salt petroleum

system in the Santos Basin. The extension became concentrated in the crustal portion of the lithosphere since the advection of the heat from the TC plume head was distributed over a large area underneath the SCLM, keeping it more brittle and resistant to deformation than the overlying continental crust. The poorly conductive SCLM retained most of the heat flow near the MBL during the advection of the TC plume head along nearly 5 Myr., becoming more ductile and prone to extension during the rift 3 stage (Figure 26b). In addition, the heat loss by the continental crust over this long quiescence period as well as the concentration of the heat in the underlying SCLM due to mantle advection produced the conditions for the thermal subsidence of the Santos Basin during the rift 3 stage (Figure 26b). The SCLM-focused extension allowed renewed adiabatic decompression restarting the melting process that will generate the V2 volcanism that will last from *ca.* 129 to *ca.* 121 Ma (Figure 26a), forming the rocks in the B3 and A3 magmatic sections of the well. The Hauterivian U-Pb age (*ca.* 136 Ma) of the volcanic tuff in the A2 felsic section might have been obtained from a detrital zircon crystal formed during the composite felsic volcanism of the A1 section of the well. However, the predominant ages in the A2 and A3 felsic sections spread over the 129, 125 and 121 Ma range (Figure 26a). A restricted lagoon sedimentary environment took place, being characterized by the chemical sedimentation that will originate the limestones of the lower Barra Velha Formation. These rocks will become the main hydrocarbon reservoirs of the pre-salt petroleum system in the Santos Basin. The heat flow at this new high thermal regime during the Barremian-Aptian rift 3 stage easily crossed the basement of the Santos Basin since it was strongly thinned during the previous rifting stages, reaching its overlying sedimentary sequence. Heat was then mostly consumed to produce hydrothermal processes rather than melting, promoting the main influx of mantle-derived CO_2 into the basin, affecting the petrophysical parameters of the limestones of the lower Barra Velha Formation in southern Santos Basin.

6.2.11 Conclusions

This study presents the first record of bimodal volcanic processes in Santos Basin. The petrographic, geochemical and geochronological data are consistent with the assumption that the Hauterivian pre-salt magmatic sequences in the Santos Basin represent the offshore counterpart of the bimodal magmatism of the Paraná-Etendeka CFB. The results are also consistent with a geodynamic process involving the Tristan da Cunha mantle plume and the overlying SCLM underneath the Santos Basin during the Early Cretaceous. This mantle interplay and interactions with the continental crust caused changes in the thermal regime in this part of the Santos Basin

from the Hauterivian to the Aptian, resulting in two volcanic events separated by a nearly 5 Myr period of general quiescence. These different thermal regimes may explain not only the recurrent bimodal volcanism but also the influx of the mantle-derived CO_2 into the main hydrocarbon reservoirs of the pre-salt petroleum system in the Santos Basin.

Figure 26: Tectonic-magmatic conceptual model for the mantle-crust interactions during the Early Cretaceous in the Santos Basin, Brazil.

a

Dated sections	Dated samples	Ages (Ma)		Basin tectonics	Sedimentary environments	Formations	Basin subsidence	Volcanic events
A3/A2	B7/B44	121	Aptian	Post-rift (sag)	Restricted lagoon	(Lower) BVE	Thermal	V2
A2	B43	125						
A3/A2	B5/B42	129	Barremian	Rift	Lacustrine	PIÇ	Mechanical	
A1	B38	136	Hauterivian			CAM		V1

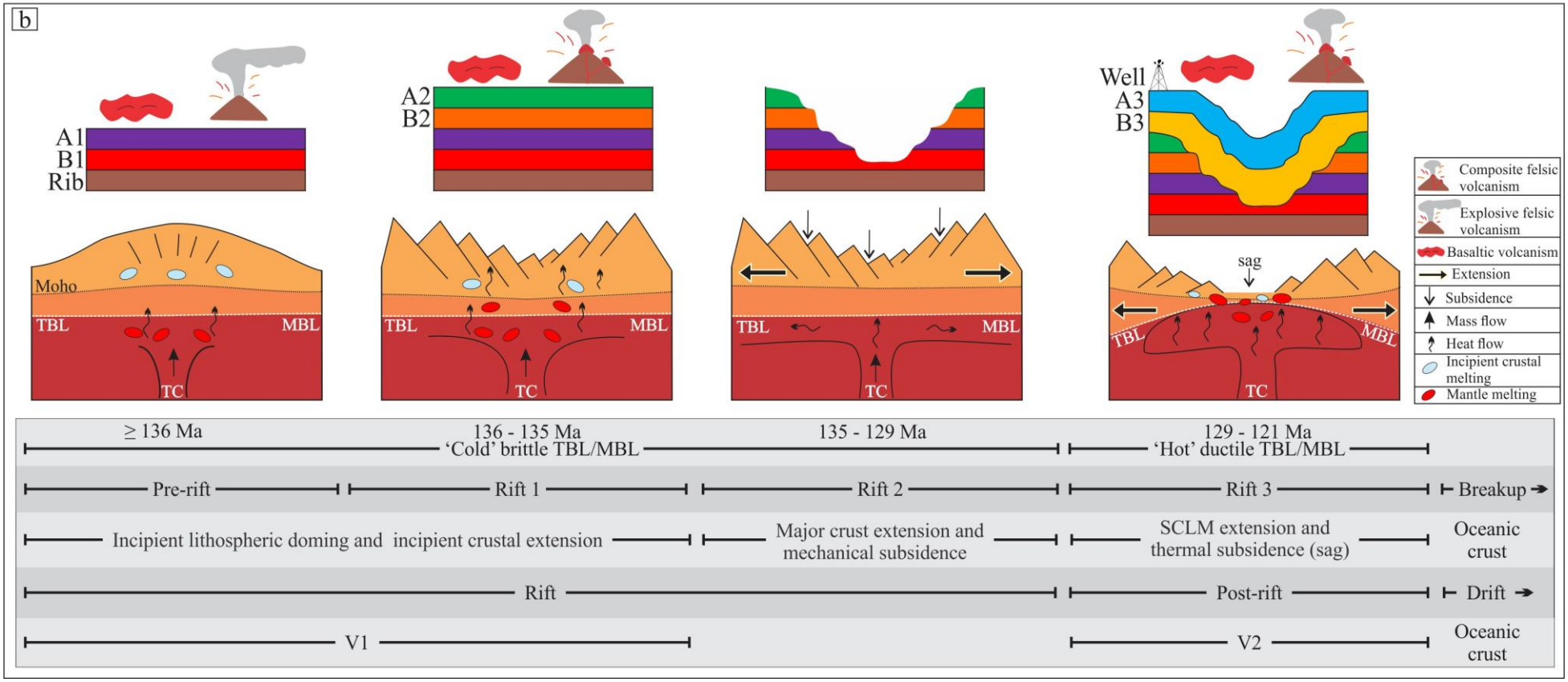

Caption: (a) Table with U-Pb ages, basin tectonics and subsidence processes and related sedimentary environments and respective formations and volcanic events. (b) Schematic tectonic-magmatic model. Thicknesses of the well sections, the mechanical portions of the lithosphere and the asthenosphere not on scale.
Note BVE = Barra Velha Formation. PIÇ = Piçarras Formation. CAM = Camboriú Formation. Rib = Ribeira Belt. TBL/MBL = Thermal/Mechanical Boundary Layers. TC = Tristan da Cunha. SCLM = Subcontinental Lithospheric Mantle.
Reference: The author, 2025.

CONSIDERAÇÕES FINAIS

Esta tese de doutorado apresenta dados obtidos a partir do estudo de seções magmáticas da sequência pré-sal de três poços exploratórios de hidrocarbonetos localizados em diferentes partes da Bacia de Santos (6-BG-6P-SPS, 3-BRSA-1267A-RJS e 1-BRSA-886-RJS).

Inicialmente, os dados petrofísicos destes poços foram interpretados qualitativamente e combinados com dados petrográficos obtidos para amostras laterais de modo a propor possíveis paleoambientes magmáticos. As análises integradas dos dados petrográficos e petrofísicos dos três poços permitiram a identificação de ocorrências magmáticas subaéreas explosivas e efusivas, subaquosas e intrusivas na sequência pré-sal da Bacia de Santos. O poço 6-BG-6P-SPS registra vulcanismo máfico efusivo, com intercalação entre porções maciças e amigdaloidais, identificadas por meio da interpretação qualitativa de dados petrofísicos (raio gama, sônico, resistividade, porosidade e permeabilidade) corroborados pela análise petrográfica. Interpretações similares permitiram atribuir o vulcanismo félsico registrado no poço a eventos efusivos e explosivos. O vulcanismo registrado no poço 6-BG-6P-SPS ocorreu em paleoambiente continental. A seção estudada do poço 3-BRSA-1267A-RJS apresenta vulcanismo máfico subaquoso, com padrões petrofísicos e texturas petrográficas representativas de intervalos de *pillow-lavas* e *inter-pillow* carbonáticos. Além disso, as seções sobrepostas e sotopostas às seções magmáticas são representadas por coquinas, o que está de acordo com a existência de um paleoambiente lacustre e marinho raso. No poço 1-BRSA-886-RJS, diferentemente do vulcanismo subaéreo e subaquoso pré-Albiano, as seções magmáticas registram intrusões basálticas pós-Albianas, algumas com até 150 m de espessura, com gabros com texturas cumuláticas. Estas características devem estar associadas a um ambiente tectônico de relativa estabilidade na parte central da bacia naquele período de tempo, o que permitiu o estabelecimento de condições de câmara magmática em ambiente hipabissal.

Posteriormente, o poço 6-BG-6P-SPS, também conhecido como Corcovado 1, foi escolhido para estudos petrológicos em função da diversidade de rochas vulcânicas registrada por abundante amostragem lateral. Estes estudos resultaram no primeiro registro de vulcanismo bimodal (máfico e félsico) na sequência pré-sal da Bacia de Santos.

O poço 6-BG-6P-SPS registra eventos vulcânicos félsicos e máficos de longa duração (135 a 122 Ma, análise U-Pb in situ em grãos de zircão das rochas félsicas), em camadas de diferentes espessuras. Estas camadas foram agrupadas em três seções máficas (B1, B2 e B3) e três seções félsicas (A1, A2 e A3) que somam cerca de 800 m. As rochas félsicas são riolito, dacito e, subordinadamente, traquito/traquidacito, enquanto as rochas máficas são basalto, traquibasalto, traquiandesito e, subordinadamente, traquiandesito basáltico. As rochas magmáticas das seis

seções do poço integram uma série subalcalina, com afinidade toleítica. As rochas básicas e ácidas não são cogenéticas por diferenciação magmática. Por outro lado, foi possível demonstrar que as rochas de composição intermediária estão vinculadas a algumas rochas básicas por meio de cristalização fracionada com assimilação (AFC) na crosta superior. A origem das rochas félsicas ácidas foi atribuída à fusão parcial de rochas com composição modal e litogeoquímica típicas da crosta superior. Por sua vez, a gênese das rochas básicas menos evoluídas e não contaminadas foi relacionada à fusão parcial de diferentes fontes mantélicas na zona de estabilidade da granada. As assinaturas isotópicas das rochas básicas podem ser explicadas por mistura de reservatórios mantélicos do tipo Tristão da Cunha e EMII. Este último é atribuído às porções mais enriquecidas do manto litosférico subcontinental.

Esta tese propõe um modelo conceitual geodinâmico mantélico e outro modelo conceitual tectono-magmático para explicar vários processos geológicos registrados nos sistemas petrolíferos da sequência pré-sal da Bacia de Santos. Estes modelos propõem que a presença da pluma de Tristão da Cunha impões regimes térmicos distintos durante a evolução da Bacia de Santos deste o Hauteriviano até o Aptiano. O calor advectado a partir da pluma nos primeiros estágios de rifteamento (pré-rifte; >136 Ma) e rifte 1; 136 a 135 Ma) permitiu a fusão parcial de porções enriquecidas do manto litosférico subcontinental (MLSC) com razões isotópicas similares a EMII, que misturaram-se à fusões da proto-cabeça da pluma, dando origem às rochas máficas das seções B1 e B2. De forma semelhante, a presença da pluma foi responsável pelo aumento de calor e fusão incipiente de porções da crosta superior, gerando as rochas félsicas das seções A1 e A2. O avanço da extensão crustal foi acompanhado por aumento da cabeça da pluma, subsidência mecânica e implementação de sedimentação em ambiente lacustre no estágio rifte 2 (135 a 129Ma). Por fim, no estágio rifte 3 (129 a 121 Ma), a extensão focada no MLSC e subsidência térmica (*sag*), resultaram em novos episódios de fusão mantélica e crustal que formaram as rochas das seções B3 e A3, respectivamente. As interações entre o manto e a crosta continental superior e os seus diferentes regimes térmicos desde o Hauteriviano até o Aptiano são usadas para explicar algumas características marcantes do sistema petrolífero do pré-sal da Bacia de Santos como, por exemplo, o influxo de CO_2 advindo do manto.

REFRÊNCIAS

Abelha, M. 2017. Bacia de Santos: sumário geológico e áreas em oferta. Disponível em: http://rodadas.anp.gov.br/pt/partilha-de-producao/3-rodada-de-partilha-de-producao-pre-sal/areas-oferecidas. Acessado em 05 de maio de 2021 às 14:25h.

Almeida, J., Dios, F. Mohriak, W. U., Valeriano, C. M., Heilbron, M., Eirado, L. G. & Tomazzoli, E. 2013. Pre-rift tectonic scenario of the Eo-Cretaceous Gondwana break-up along SE Brazil-SW Africa: insights from tholeiitic mafic dykes swarms. In: Mohriak, W. U., Danforth, A., Post, P. J., Brown, D. E., Tari, G. C., Nemcok, M. & Sinha, S. T. (eds) Conjugate Divergent Margins. Geological Society, London, Special Publications, 369.

Almeida, V.V., Janasi, V.A., Azzone, R.G. Faleiros, F.M. 2019. Crustal contamination and genesis of transitional alkaline-tholeiitic intrusions: Insights from the José Fernandes Suite, Paraná Magmatic Province, Brazil. Lithos, 342-343, 59-75.

Amarante, F.B., Jackson, C.A., Pichel, L.M. 2023. Post-salt magmatism in the Campos Basin, offshore SE Brazil: style, distribution, and relationship to salt tectonics. Journal of South American Earth Sciences. 125: 104314.

Anjos, S.M.C., Sombra, C.L., Spadini, A.R. 2024. Petroleum exploration and production in Brazil: From onshore to ultra-deepwaters. Petroleum Exploration and Development, 51(4), 912-924.

Antobreh, A. A., Faleide, J. I., Tsikalas, F. & Planke, S. 2009. Rift-shear architecture and tectonic development of the Ghana margin deduced from multichannel seismic reflection and potential field data. Marine and Petroleum Geology, Amsterdam. v. 26, n. 3, p. 345–368.

Archer, S.G., Bergman, S.C., Iliffe, J., Murphy, C.M. & Thornton, M. 2005. Palaeogene igneous rocks reveal new insights into the geodynamic evolution and petroleum potential of the Rockall Trough, NE Atlantic Margin. Basin Research. 17:171-201.

Armitage, J.J., Collier, J.S., Minshull, T.A. 2010. The importance of rift history for volcanic margin formation. Letters, 465(17).

Bailey, D.K. 1983. The chemical and thermal evolution of rifts. Tectonophysics, 94.

Barreto, C.J.S., Lafon, J.M., Lima, E.F., Sommer, C.A. 2016. Geochemical and Sr-Nd-Pb isotopic insight into the low-Ti basalts from southern Paraná Igneous Province, Brazil: the role of crustal contamination. International Geology Review.

Bartetzko, A., H. Paulick, G. Iturrino, and J. Arnold. 2003. Facies reconstruction of a hydrothermally altered dacite extrusive sequence: Evidence from geophysical downhole logging data (ODP Leg 193). Geochem. Geophys. Geosyst., 4(10), 1087, doi:10.1029/2003GC000575.

Bartetzko, A., Delius, H. & Pechnig, R. 2005. Effect of compositional and structural variations on log responses of igneous and metamorphic rocks. I: mafic rocks. In: Harvey, P. K., Brewer, T.S., Pezard, P. A. & Petrov, V. A. (eds) 2005. Petrophysical Properties of Crystalline Rocks. Geological Society, London, Special Publications, 240, 255-278.

Basheer, A.A. 2024. Deep crustal and upper mantle structures in North Africa: A review. In: Hamimi, Z., Chabou, M.C., Errami, E., Fowler, A-R., Fello, N., Masrouhi, A., Leprêtre, R. The geology of North Afric. Regional Geology Reviews, Springer.

Beglinger, S.E., Doust, H., Cloetingh, S. 2012. Relating petroleum system and play development to basin evolution: West African South Atlantic basins. Marine and Petroleum Geology, 30, 1-25.

Bell, B., & Butcher, H. 2002. On the emplacement of sill complexes: evidence from the Faroe-Shetland Basin. Geological Society, London, Special Publications. v: 197, 307-329.

Bellieni, G., Comin-Chiaramonti, P., Marques, L. S., Melfi, A. J., Nardy, A. J. R., Papatrechas, C., Piccirillo, E. M., Roisenberg, A., Stolfa, D. 1986. Petrogenetic aspects of acid and basaltic lavas from the Paraná Plateau (Brazil): Geological, mineralogical and petrochemical relationships. Journal of Petrology. V.27 (4), 915-944.

Biari, Y., Klingelhoefer, F., Franke, D., Funck, T., Loncke, L., Sibuet, J., Basile, C., Austin, J.A., Rigoti, C.A., Sahabi, M., Benabdellouahed, M., Roest, W.R. 2021. Structure and evolution of the Atlantic passive margins: A review of existing rifting models from wide-angle seismic data and kinematic reconstruction. Marine and Petroleum Geology, 126.

Boyer, S. & Mari, J-L. 1997. Seismic surveying and well logging. Oil and gas Exploration Techniques. Institut Français Du Pétrole. Éditions Technip, Paris.

Brewer, T. S., Harvey, P. K., Lovell, M. A., Haggas, S., William-Son, G., Pezard, P. 1998. Ocean floor volcanism: constraints from the integration of core and downhole logging measurements. Core Log Integration, 136, 341-362.

Brito Neves, B. B. & Cordani, U. G., 1991. Tectonic Evolution of South America during the Late Proterozoic. Precambrian Research, 53: 23-40

Brito Neves, B. B; Sá, J. M.; Nilson A. A.; Botelho, N. F. 1995. A tafrogênese Estateriana nos blocos Paleoproterozóicos da América do Sul e processos subseqüentes. Geonomos, 3:1-21

Brito, J.P.S., Santos, R.V., Gonçalves, G.O., Barbosa, P.F., Souza Cruz, C.E., Ushirobira, C.A., Souza, V.S., Richer, F., Abreu, C.J. 2024. U-Pb dating of Barra Velha carbonates reveals the influence of Santos Santos Basin sedimentary and tectonothermal history on pre-salt carbonate ages. Marine and petroleum Geology, 168.

Bullock, A. D. & Minshull, T. A. 2005. From continental extension to seafloor spreading: Crustal structure of the Goban Spur rifted margin, southwest of the UK. Geophysical Journal International, [Oxford], v. 163, n. 2, p. 527–546.

Cainelli, C. & Mohriak, W. U. 1999. Some remarks on the evolution of sedimentary basins along the eastern Brazilian continental margin. Episodes, Vol. 22, no. 3.

Carminatti, M., Wolff, B., Gamboa, L. 2008. New exploratory frontiers in Brazil. 19th World Petroleum Congress, Spain.

Carvalho, H., Tassinari, C., Alves, F., Guimarães, D. & Simões, M. C. 2000. Geochronological review of the precambrian in western Angola: links with Brazil. Journal of African Earth Sciences, 31, 383–402.

Chang, H. K., Kowsmann, R. O. & Figueiredo, A. M. F. 1988. Novos conceitos sobre o desenvolvimento das bacias marginais do leste brasileiro. In: Raja Gabaglia, G.P. & Milani, E. J. 1990. Origem e Evolução de Bacias Sedimentares. PETROBRÁS. p. 269-289.

Chang, H. K., Kowsmann, R. O., Figueiredo, A. M. F. & Bender, A. 1992. Tectonics and stratigraphy of the East Brazil Rift system: an overview. Tectonophysics, 213:97-138.

Chang, H. K., Assine, M. L., Correa, F. S., Tinen, J. S., Vidal, A. C. & Koike, L. 2008. Sistemas petrolíferos e modelos de acumulação de hidrocarbonetos na Bacia de Santos. Revista Brasileira de Geociências, 38, 29-46.

Chayes, F. 1963. Relative abundance of intermediate members of the oceanic basalt trachyte association. Journal of Geophysical Research, vol. 68, no. 5 pp. 1519-1534.

Cioccari, G. M. & Mizusaki, A. M. P. 2019. Sistemas petrolíferos atípicos nas bacias paleozoicas brasileiras - uma revisão. Geociências. 38:367-390.

Clavier, C., Heim, A., and C. Scala. 1976. Effect of pyrite on resistivity and other logging measurements. SPWLA 17th Annual Logging Symposium.

Clennell, M. B., Josh, M., Esteban, L., Hill, D., Woods, C., McMullan, B., Piane, C. D., Schmid, S., Verrall, M. 2010. The influence of pyrite on rock electrical properties: a case study from NW Australian gas reservoirs. SPWLA 51st Annual Logging Symposium.

Condie, K.C. 1993. Chemical composition and evolution of the upper continental crust: Contrasting results from surface samples and shales. Chemical Geology, 104(1-4), 1–37.

Curtis, M. S., Holford, S. P., Bunch, M. A. & Schofield, N. J. 2022. Seismic, petrophysical and petrological constraints on the alteration of igneous rocks in the Northern Carnarvon Basin, Western Australia: implications for petroleum exploration and drilling operations. The APPEA Journal. 62:196-222.

Curtis, M. S., Holford, S. P., Bunch, M. A. & Schofield, N. J. 2022. Seismic, petrophysical and petrological constraints on the alteration of igneous rocks in the Northern Carnarvon Basin, Western Australia: implications for petroleum exploration and drilling operations. The APPEA Journal. 62:196-222.

Daly, R.A. 1925. The geology of Ascension Island. Proceedings of the American Academy of Arts and Sciences, vol. 60, no. 1, pp. 3-80.

Dani, A. P. O., Remus, M. V. D., Dani, N. & Lima, E. F. 2017. Magmatismo basáltico do Andar Alagoas (Bacia de Campos). Geologia USP, Série Científica, São Paulo. v.17, n.2, p. 269-287.

Delpino, D. H. & Bermúdez, A. M. 2009. Petroleum systems including unconventional reservoirs in intrusive igneous rocks (sills and laccoliths). Special Section: Unconventional Resources and CO_2 monitoring. The Leading Edge. 804-811.

Dentith, M., Enkin, R. J., Morris, W., Adams, C., Bourne, B. 2019. Petrophysics and mineral exploration: a workflow for data analysis and a new interpretation framework. Geophysical Prospecting, 68, 178–199.

DePaolo, D. J., 1981. Trace Element and isotopic effects of combined wallrock assimilation and fractional crystallization. Earth and Planetary Science Letters, 53, 189-202.

Descovi, P. L. M., Ade, M. V. B., Avellar, G. O., Bermúdez, L. B., Vieira, F. P. 2021. Volcanic reservoirs: historic and current context. Pesquisas em Geociências. V.48, n. 1:e104451.

Dezhi, B., Zigang, Q., Minggao, L. 1991. Method and Application Effects of the Identifying Igneous Lithology Based on Fuzzy Mathematics: Geological Application of the Well Logging Data. Petroleum Industry Press, Beijing.

Dias, J. L. 1998. Análise sedimentológica e estratigráfica do andar Aptiano em parte da margem leste do brasil e no platô das Malvinas: considerações sobre as primeiras incursões e ingressões marinhas do Oceano Atlântico Sul Meridional. 2v. Tese (Doutorado) – Universidade Federal do Rio Grande do Sul, Porto Alegre.

Dias, J. L. 1993. Evolução da fase rift e a transição rift/drift nas bacias das margens leste e sudeste do Brasil. In: SBGf, International Congress of the Brazilian Geophysical Society, 3, Rio de Janeiro, Expanded Abstracts, 2:1328-1332.

Duraiswami, R. A., Dole, G., & Bondre, N. 2003. Slabby pahoehoe from the western Deccan Volcanic Province: evidence for incipient pahoehoe-aa transitions. Journal of Volcanology and geothermal Research, 121, 195-217.

Duraiswami, R. A., Bondre, N. R., & Managave, S. 2008. Morphology of rubbly pahoehoe (simple) flows from the Deccan Volcanic Province: implications for style of emplacement. Journal of Volcanology and Geothermal Research, 177, 822-836.

Duraiswami, R. A., Gadpallu, P, Shaikh, T. N., Cardin, N. 2014. Pahoehoe-a'a transitions in the lava flow fields of the western Deccan Traps, India-implications for emplacement dynamics, flood basalt architecture and volcanic stratigraphy. Journal of Asian Earth Sciences (84): 146-166.

Eide, C.H., Schofield, N., Jerram, D.A., Howell, J.A. 2017a. Basin-scale architecture of deeply emplaced sill complexes: Jameson Land, East Greenland. Journal of the Geological Society. 174:23-40.

Eide, C.H., Schofield, N., Lecomte, I., Buckley, S.J., Howell, J.A. 2017b. Seismic interpretation of sill complexes in sedimentary basins: implications for the sub-sill imaging problem. Journal of the Geological Society. v:175, 193-209.

Eldholm, O. 1991. Magmatic-tectonic evolution of a volcanic rifted margin. Marine geology, 102.

Eldholm, O. & Grue, K. 1994. North Atlantic Volcanic margins: Dimensions and production rates. Journal of Geophysical research. 99, 2955-2968.

Eldholm, O., Skogseid, J., Planke, S. Gladczenko, T.P. 1995. Volcanic margin concepts. In: Banda, E., Torné, M., Talwani, M. (eds) Rifted Ocean-Continent Boundaries, 1-16. Kluwer Academic Publishers.

Eldholm, O. Gladczenko, T.P., Skogseid, J., Planke, S. 2000. Atlantic volcanic margins: a comparative study. In: Nøttvedt, A. et al. (eds) Dynamics of the Norwegian Margin. Geological Society, London, Special Publication, 167, 411-428.

Ellis, D. V. & Singer, J. M. 2008. Well Logging for Earth Scientists. 2º Ed. Springer.

Evain, M., Afilhado, A., Rigoti, C., Loureiro, A., Alves, D., Klingelhoefer, F., Schnurle, P., Feld, A., Fuck, R., Soares, J., Vinicius de Lima, M., Corela, C., Matias, L., Benabdellouahed, M., Baltzer, A., Rabineau, M., Viana, A., Moulin, M. & Aslanian, D. 2015. Deep structure of the Santos Basin-São Paulo Plateau System, SE Brazil, J. Geophys. Res. Solid Earth, 120.

Ewart. A., Milner, S.C., Armstrong, R.A., Duncan, A.R. 1998. Etendeka volcanism of the Goboboseb Mountains and Messum Igneous Complex, Namibia. Part I: Geochemical evidence of Early Cretaceous Tristan plume melts and the role of crustal contamination in the Paraná-Etendeka CFB. Journal of Petrology, 39(2), 191-225.

Farias, F., Szatmari, P., Bahniuk, A., França, A.B. 2019. Evaporitic carbonates in the pre-salt of Santos Basin – Genesis and tectonic implications. Marine and Petroleum Geology, 105, 251-271.

Farooqui, M.Y., Hou, H., Li, G., Machin, N., Neville, T., Pal, A., Shrivastva, C., Wang, Y., Yang, F.,Yin, C., Zhao, J. & Yang, X. 2009. Evaluating volcanic reservoirs. Oilfield Review, 21(1): 36-47.

Feijó, F. J. 1996. O início da livre circulação das águas no Oceano Atlântico. Bol. Geoc. Petrobras, 10:157-164.

Fernandez, R. O. 2017. Bacia de Santos: sumário geológico e setores em oferta. 15ª Rodada – Concessão de Petróleo e Gás. Disponível em www.anp.gov.br

Fernandez, R. O. & Santos, A. J. 2017. Bacia de Santos: sumário geológico e setores em oferta. 14ª Rodada – Licitações de Petróleo e Gás Disponível em www.anp.gov.br

Ferraz, A., Gamboa, L., Neto, E., Baptista, R. 2019. Crustal structure and CO2 occurrences in the Brazilian basins. Interpretation.

Ferreira, L.C., Stanton, N., Gordon, A.C., Schmitt, R. 2023. The magmatic rifting of Santos Basin: Aeromagnetic mapping of dykes, terranes and marginal structures and the interplay between tectonism and volcanism. Tectonics, 42.

Figueiredo A. M. F. & Mohriak W. 1984. A tectônica salífera e as acumulações de petróleo na Bacia de Campos. SBG. Cong. Bras. Geol. Anais. 33:1380-1384

Flores, A. C. C., Dupuy, I. S. S., Forbrig, L. C., Silva, R. R. & Campinho, V. S. 2006. Apostila Perfilagem: Conceitos e aplicações.

Florisbal, L.M., Heaman, L.M., Janasi, V.A., Bitencourt, M.F. 2014. Tectonic significance of the Florianópolis Dyke Swarm, Paraná–Etendeka Magmatic Province: A reappraisal based on precise U–Pb dating. Journal of Volcanology and Geothermal Research, 289, 140-150.

Florisbal, L.M., Janasi, V.A., Bitencourt, M.F., Nardi, L.V.S., Marteleto, N.S. 2018. Geological, geochemical and isotope diversity of ~134Ma dykes from the Florianópolis Dyke Swarm, Paraná Magmatic Province: Geodynamic controls on petrogenesis. Journal of Volcanology and Geothermal Research, 355, 181-203.

Fodor, R. V., Kumar, N., Bornhorst, T. J. & Husler, J. W. 1980. Petrology of basaltic rocks from the São Paulo Ridge, Southwestern Atlantic Ocean. Marine Geology, 36, 127-141.

Fodor, R. V., McKee, E. H. e Asmus, H. E. 1983. K-Ar Ages and the opening of the South Atlantic Ocean: basaltic rock from the Brazilian margin. Marine Geology, 54, B1-M8.

Fodor, R. V. & Vetter, S. K. 1984. Rift-zone magmatism: Petrology of basaltic rocks transitional from CFB to MORB, southeastern Brazil margin. Contributions to Mineralogy and Petrology, 88, 307-321.

Fodor, R. V. & Vetter, S. K. 1985. Mineral chemistry and petrography of passive-margin basalt, Southeastern Brazil. Revista Brasileira de Geociências. v. 15(1): 36-47.

Fornero, S.A., Marins, G.M., Lobo, J.T., Freire, A.F.M. & de Lima, E.F. 2019. Characterization of subaerial volcanic facies using acoustic image logs: Lithofacies and log-facies of a lava-flow deposit in the Brazilian Pre-salt, deepwater of Santos Basin. Marine and Petroleum Geology, 99: 156-174

Francis, E. H. 1982. Magma and sediment-I Emplacement mechanis of late Carboniferous tholeiite sills in northern Britain. J. geol. Soc. London, Vol. 139, p. 1-20.

Freitas, V.A., Vital, J.C.S., Rodrigues, B.R., Rodrigues, R. 2022. Source rock potential, main depocenters, and CO2 occurrence in the pre-salt section of Santos Basin, southeast Brazil. Journal of South American Earth Sciences, 115.

Gamboa, L., Ferraz, A., Baptista, R., Neto, E.V.S. 2019. Geotectonic controls on CO2 formation and distribution processes in the Brazilian pre-salt basins. Geosciences, 9, 252.

Gao, Z., Tian, W., Wang, L., Shi, Y. & Pan, M. 2017. Emplacement of intrusions of the Tarim Flood Basalt Province and their impacts on oil and gas reservoirs: A 3D seismic reflection study in Yingmaili fields, Tarim Basin, northwest China. Interpretation, 5 (3): SK51–SK63.

Garcia, S. F. M., Danderfer Filho, A., Lamotte, D. F. & Rudkiewicz, J. 2012. Análise de volumes de sal em restauração estrutural: um exemplo na Bacia de Santos. Revista Brasileira de Geociências. v.42(2): 433-450.

Garland, F., Hawkesworth, C. J., Mantovani, M. S. M. 1995. Description and Petrogenesis of the Parana Rhyolites, Southern Brazil. Journal of Petrology. V.36 (5), 1193-1227.

Gholamrezaie, E., Scheck-Wenderoth, M., Sippel, J., Strecker, M.R. 2018. Variability of the geothermal gradient across two differently aged magma-rich continental rifted margins of the Atlantic Ocean: the Southwest African and the Norwegian margins. Solid Earth, 9, 139-158.

Gibson, S. A., Thompson, R. N., Leonardos, O. H, Dickin A. P & Mitchell, J. G. 1999. The limited extent of plume-litosphere interactions during continental flood basalt genesis: geochemical evidence from Cretaceous magmatism in southern Brazil. Contrib. Min. Petrol., 137:147-169.

Gladczenko, T.P., Hinz, K., Eldholm, O., Meyer, H., Neben, S., Skogseid, J. 1997. South Atlantic volcanic margins. Journal of the Geological Society, London, 154, 465-470.

Gomes, A.S. & Vasconcelos, P.M. 2021. Geochronology of the Paraná-Etendeka large igneous province. Earth-Science reviews, 220.

Gordon, A. C., Mohriak, W. U., Stanton, N., Santos, A. C. 2023a. Magmatic cycles in Santos Basin (S.E. Brazil): Tectonic control in the temporal-spatial distribution and geophysical signature. Journal of South American Earth Science, 121.

Gordon, A.C., Santos, A.C., Caitano, G.R., Stanton, N., Mohriak, W.U. 2023b. Magmatic cycles in Santos Basin (S.E. Brazil): Geochemical characterization and magmatic sources. Journal of South American Earth Sciences, 126.

Green, D.H. 1970. A review of experimental evidence on the origin of basaltic and nephelinitic magmas. Phys. Earth Planet. Interiors, 3, 221-235.

Guimarães, L.F., Hornby, A., Kueppers, U., Alves, A., Janasi, V.A., Dingwell, D.D. 2019. Generation of block-and-ash flows at the onset of silicic volcanism in the Paraná Magmatic Province (Brazil): evidence from photoanalysis of Caxias do Sul breccias. Bulletin of Volcanology, 81:65.

Hamada, G.M., Al-Awad, M.N.J., Almalik, M.S. 2001. Log Evaluation of low resistivity sandstone reservoirs. SPE – Society Petroleum Engineers.

Harris, C. & Milner, S. 1997. Crustal origin for the Paraná Rhyolites: Discussion of 'Description and Petrogenesis of the Paraná Rhyolites, Southern Brazil' by Garland et al. (1995). Journal of Petrology. V.38 (2), 299-302.

Hawkesworth, C.J. & Kemp, A.I.S. 2006. Evolution of the continental crust. Nature, 443(19).

He, W., Wang, H., Su, J., Wang, Q., Zhao, J., Zuo, G., Wang, T., Yang, L., Ren K., Wang, C., Zhao, J., Guo, Y., Zhang, Y., Sun, J. 2025. Magma evolution during the post-rift phase of the Santos Basin, Brazil: petrogenesis and geochemistry of ~126-121 Ma basalts and diabases. Frontiers in Earth Science, 12.

Heilbron, M., Mohriak, W.U., Valeriano, C.M., Milani, E, J., Almeida, J., Tupinambá, M. 2000. From collision to extension: The roots of the Southeastern Continental Margin of Brazil. Atlantic Rifts and Continental Margins, Geophysical Monograph, 115.

Heilbron, M., Pedrosa-Soares, A. C., Campos Neto, M. C., Silva, L. C., Trouw, R. A. J. & Janasi, V. 2004. A Província Mantiqueira. In: Mantesso-Neto, V., Bartorelli, A., Carneiro, C. D. R. & Brito-Neves, B. B. (eds) Geologia do Continente Sul-Americano: Evolução da Obra de Fernando Flávio Marques de Almeida. Beca, São Paulo, 203–234.

Heilbron, M., Valeriano, C., Tassinari, C. G., Almeida, J. C. H., Tupinamba, M., Siga, O. Jr. & Trouw, R. A. J. 2008. Correlation of Neoproterozoic terranes between the Ribeira Belt, SE Brazil and its African counterpart: comparative tectonic evolution and open questions. In: Pankhurst, R. J., Trouw, R. A. J., Brito-Neves, B. B. and de Wit, M. J. (eds) West Gondwana: Pre-Cenozoic Correlations across the South Atlantic Region. Geological Society, London, Special Publications, 294, 211–237.

Heilbron, M., Silva, L.G.E., Almeida, J.C.H., Tupinambá, M., Peixoto, C.A., Valeriano, C.M., Lobato, M., Rodrigues, S.W.O., Ragatki, C.D., Silva, M. A., Monteiro, T.L.V, Freitas, N. C., Miguens, D., Girao, R. 2020a. Proterozoic to Ordovician geology and tectonic evolution of Rio de Janeiro State, SE-Brazil: insights on the central Ribeira Orogen from the new 1:400,000 scale geologic map. Brazilian Journal of Geology, v. sp vol, p. 1-25.

Heilbron, M., Valeriano, C.M., Peixoto, C., Tupinambá, M., Neubauer, F., Dussin, I., Corrales, F., Bruno, H., Lobato, M., Almeida, J.C.H., Silva, L.G.E. 2020b. Neoproterozoic magmatic arc systems of the central Ribeira belt, SE-Brazil, in the context of the West-Gondwana pre-collisional history: A review. Journal of South American Earth Sciences, v. 105, p. 102710.

Helm-Clark, C. M., Rodgers, D. W., Smith, R. P. 2004. Borehole geophysical techniques to define stratigraphy alteration and aquifers in basalts. Journal of Applied Geophysics (55), 3-38.

Hinz, K., Eldholm, O., Block, M., Skogseid, J. 1993. Evolution of North Atlantic volcanic continental margins. Petroleum Geology of Northwest Europe: Proceedings of the 4th Conference. The Geological Society, London, 901-013.

Huismans, R. & Beaumont, C. 2011. Depth-dependent extension, two-stage breakup and cratonic underplating at rifted margins. Nature, [S.I.], v. 473, n. 7345, p. 74–78.

Irvine, T. N. and baragar, W. R. A. 1971. A guide to the chemical classification of common volcanic rocks. Canadian Journal of Earth Sciences, Canadá. 8: 523-547.

Jackson, S. E., Pearson, N. J., Griffin, W. L., Belousova, E. A. 2004. The application of laser ablation-inductively coupled plasma-mass spectrometry to in situ U–Pb zircon geochronology. Chemical Geology, 211. 47–69

Jackson, M. G., Hart., S. R., Koppers, A. A. P., Staudigel, H., Konter, J., Blusztajn, J., Kurz, M., Russell, A. 2007. The return of subducted continental crust in Samoan lavas. Nature, vol. 449 (9).

Jackson, C.A.L., Magee, C., Jacquemyn, C. 2020. Rift-related magmatism influence petroleum system development in the NE Irish Rockall Basin, offshore Ireland. Petroleum Geoscience. v: 26: 511-524.

Janasi, V.A., Freitas, V.A., Heaman, L.H. 2011. The onset of flood basalt volcanism, Nothern Paraná Basin, Brazil: A precise U-Pb baddeleyite/zircon age for Chapecó-type dacite. Earth and Planetary Science Letters, 302, 147-153.

Jerram, D. A., Single, R. T., Hobbs, R. W. & Nelson, C. E. 2009. Understanding the offshore flood basalt sequence using onshore volcanic facies analogues: an example from the Faroe-Shetland basin. Geol. Mag. 146 (3):353-367.

Jesus, I.L., Abrantes Jr., F.R., Ferreira, D.J.A., Lupinacci, W.M. 2023. Carbonate Reservoir quality and permoporosity obliteration due to silification processes in the Barra Velha Formation, Santos Basin, Southeastern Brazil. Brazilian Journal of Geology, 53(2).

Kampman, N., Bickle, M., Wigley, M., Dubacq, B. 2014. Fluid flow and CO2-fluid-mineral interactions during CO2-storage in sedimentary basins. Chemical Geology, 369, 22-50.

Kemp, A.I.S. & Hawkesworth, C.J. 2003. Granitic Perspectives on the Generation and Secular Evolution of the Continental Crust. In: Holland, H.D. & Turekian, K.K. (eds) Treatise on Geochemistry., Elsevier, Amsterdam. 3: 349-410.

Keys, W.S., 1979. Borehole geophysics in igneous and metamorphic rocks. Society of Professional Well Log Analysts Annual Logging Symposium, 20th, Tulsa, Okla., pp. 1–26

Klingelhoefer, F., Evain, M., Afilhado, A., Rigoti, C., Alves, D., Leprêtre, A., Moulin, M., Schnurle, P., Benabdellouahed, M., Baltzer, A., Rabineau, M., Feld, A., Viana, A. & Aslanian, D. 2014. Imaging proto-oceanic crust off the Brazilian Continental Margin. Geophysical Journal International, Oxford. v. 200, p. 471–488.

Krans, S.R., Rooney, T.O., Kappelman, J.W., Yirgu, G., Ayalew, D. 2024. Magma evolution during main-phase continental flood basalt volcanism: A case for

recharge-evacuating-assimilation-fractional crystallization in the Ethiopian Low-Ti province. Geochemistry, Geophysics, Geosystems, 25.

Latypov, R.M. 2003. The origin of basic-ultrabasic sills with S-, D-, and I-shaped compositional of profiles by in Situ crystallization of a single input of phenocryst-poor parental magma. Journal of Petrology. v: 44(9), 1619-1656.

Lavier, L. L. & Manatschal, G. 2006. A mechanism to thin the continental lithosphere at magma-poor margins. Nature, [S.I.], v. 440, n. 7082, p. 324–8.

Le Bas, M.J.; Le Maitre, R.N.; Streckeisen, A.; Zanettin, B. 1986. A chemical classification of volcanic rock based on total silica diagram. J. Petrol. 27 (3), 745–750.

Le Roex, A. P., Cliff, R. A., Adair, J. I. 1990. Tristan da Cunha, South Atlantic: Geochemistry and petrogenesis of basanite-phonolite lavas series. Journal of Petrology, vol. 31. 779-812

Leite, C. O. N., Silva, C. M. A. & De Ros, L. F. 2020. Depositional and diagenetic processes in the pre-salt rift section of s Santos Basin area, SE Brazil. Journal of Sedimentary Research. v.90, 584-608.

Lentini, M.R., Fraser, S.I., Summer, H.S., Davies, R. 2010. Geodynamics of the central South Atlantic conjugate margins: implications for hydrocarbon potential. Petroleum Geoscience, 16, 217-229.

Levell, B., Argent, J., Doré, A.G., Fraser, S. 2010. Passive margins: overview. Geological Society, London, Petroleum Geology Conference Series. vol. 7, 823 - 830

Leyden, R. 1976. Salt distribution and crustal models for the eastern Brazilian margin. Anais da Academia Brasileira de Ciências, 48:159- 168.

Lister, G. S., Etheridge, M. A. & Symonds, P. A. 1986. Detachment faulting and the evolution of passive continental margins. Geology, [S.I.], v. 14, p. 246–250.

Liu, Q., Zhu, D., Jin, Z., Meng, Q., Wu, X., Yu, Hao. 2017. Effects of deep CO2 on petroleum and thermal alteration: The case of the Huangqiao oil and gas field. Chemical Geology, 469, 214-229.

Liu, J., Pujol, M., Zhou, H., Selby, D., Li, J., Cheng, B. 2023. Origin and evolution of a CO2-Rich gas reservoir offshore Angola: Insights from the Gas Composition and isotope analysis. Applied Geochemistry, 148.

Louback, V. S., Valente, S.C., de Almeida, C. N., Ross, J., & Borghi, L. 2021. Petrogenesis and geodynamics of Eocene alkaline intrusions in the pre-salt sedimentary sequence of Santos Basin, Brazil. Lithos, 401, 106400.

Louback, V.S., Valente, S.C., de Almeida, C. N., Ross, J., & Borghi, L. 2023. Aptian flood basalts in Bacalhau oil and gas field: petrogenesis and geodynamics of post‑rift tholeiites in the pre‑salt sequence of Santos Basin, Brazil. Contributions to Mineralogy and Petrology, 178:15.

Lu, G. & Huismans, R.S. 2021. Melt volume at Atlantic volcanic rifted margins controlled by depth-dependent extension and mantle temperature. Nature Communications, 12, 3894.

Lutonda, E. M. 2014. Modelagem térmica de uma sequência de rochas magmáticas pré-aptianas na Bacia de Santos. Trabalho de conclusão de curso, Universidade Federal Rural do Rio de Janeiro – Seropédica.

Macdonald, G. A. 1953. Pahoehoe, aa, and block lava. American Journal of Science, 251, 169-191.

Macedo, J. M. 1989. Evolução tectônica da Bacia de Santos e áreas continentais adjacentes. Boletim de Geociências da PETROBRAS, Rio de Janeiro, 3(3):159-173.

Mackenzie, W. S.; Donaldson, C. H.; and Guilford, C. 1982. Atlas of igneous rocks and their textures. London: Longman. 148p.

Manatschal, G. 2004. New models for evolution of magma-poor rifted margins based on a review of data and concepts from West Iberia and the Alps. International Journal of Earth Sciences, [S.I.], v. 93, p.432-466.

Mangione, A.; Schofield, N.; Holford, C.; Grove, C.; Ellis, C.; Foster, C.; Schenk, O.; Gardiner, D.; Hedley, B.; Broadley, L.; & Underhill, J.R. 2024. Petroleum generation and migration through the Faroe–Shetland Basin – the role of igneous intrusions. Petroleum Geoscience, 30 (1), petgeo2022-084.

Marins, G. M., Parizek-Silva, Y., Millet, J. M.., Jerram, D. A., Rossetti, L. M. M., Souza, A. J., Planke, S., Bevilaqua, L. A., Carmo, I. O. 2022. Characterization of Volcanic reservoirs; insights from the Badejo and Linguado oil field, Campos Basin, Brazil. Marine and Petroleum Geology, 146.

Mark, N.J., Schofield, N., Pugliese, S., Watson, D., Holford, S., Muirhead, D., Brown, R., Healy, D. 2017. Igneous intrusions in the Faroe Shetland basin and their implications for hydrocarbon exploration: new insights from well and seismic data. Marine and Petroleum Geology, 92:733-753.

Mark, N.J., Schofield, N., Gardiner, D. Holt, L., Grove, C., Watson, D., Alexander, A., Poore, H. 2018. ‘Overthickening’ of sedimentary sequences by igneous intrusions. Journal of the Geological Society. v: 176, 46-60.

Mark, N.J.; Schofield, N.; Watson, D.A.; Holford, S.; Pugliese, S. & Muirhead, D. 2024. The impact of igneous intrusions on sedimentary host rocks: insights from field outcrop and subsurface data. Petroleum Geoscience, 30 (1), petgeo2022-086.

Marsh, B.D. 1996. Solidification fronts and magmatic evolution. Mineralogical Magazine. v: 60, 5-40.

Marsh, B. D. 2015. The encyclopedia of volcanoes, Cap. 8. London: Academic Press. pp. 185-201.

Matos, R.M.D., Fernandes, F.L., Fetter, M., Norton, I. 2024. Santos Basin as an example of shear-driven core complex in a transform marginal plateau. Brazilian Journal of Geophysics 42(2), 1-63. .

McDonough, W. F. and Sun, S. S. 1995. The composition of the Earth, Chem. Geol., 120; 223-253.

McKenzie, D. 1978. Some Remarks on the Development of Sedimentary Basins. Earth and Planetary Science Letters, 40:25-32.

McPhie, J. 1993. Volcanic textures: a guide to the interpretation of textures in volcanic rocks. Tasmanian: Tasmanian Government Printing Office.

Meisling K. E., Cobbold P. R. & Mount V. S., 2001. Segmentation of an oblique rifted margin, Campos and Santos Basins, southeastern Brazil. AAPG Bull., 85:1903-1924

Mello, M.R., Peres, W., Rostirolla, S.P., Pedrosa, O.A., Jr., Piquet, A., Becker, S., Yilmaz, P.O. 2021. Chapter 1: The Santos Basin pre-salt super giant petroleum system: An incredible journey from failure to success. AAPG Datapages Combined Publications database, 1-34.

Menzies, M.A., Klemperer, S.L., Ebinger, C.J., Baker, J. 2002. Characteristics of volcanic rifted margins. In: M.A., Klemperer, S.L., Ebinger, C.J., Baker, J., (eds) Volcanic Rifted Margins. Boulder, Colorado, Geological Society of America Special Paper 362, p. 1–14

Middlemost, E. A. K. 1975. The Basalt Clan. Earth-Science Reviews, 11 (1975) 337-364.

Miller, R. McG. & Grote, W. 1998. Geological Map of the Damaran Orogen of South West Africa/Namibia, 1:5,000,000. Geological Survey of Namibia, Windhoek.

Millett, J. M., Wilkins, A. D., Campbell, E., Hole, M. J., Taylor, R. A., Healy, D., Jerram, D. A., Jolley, D. W., Planke, S., Archer, S. G. & Blischke, A. 2016. The geology of offshore drilling through basalt sequences: Understanding operational complications to improve efficiency. Marine and Petroleum Geology, 77:1177-1192.

Millett, J. M., Jerram, D. A., Planke, S., Mund, B. K., Konar, S., Sharda, R., Maharjan, D., Patankar, T. 2021a. Volcanic facies architecture of early bimodal volcanism of the NW Deccan Traps: Volcanic reservoirs of the Raageshwari Deep Fas Field, Barmer Basin, India. Basin Research, 33:3348-3377.

Millett, J. M., Jerram, D. A., Manton, B., Planke, S., Ablard, P., Wallis, D., Hole, M. J., Brandsem, H., Jolley, D. W., Dennehy, C. 2021b. The Rosebank Field, NE Atlantic: Volcanic characterization of an inter-lava hydrocarbon discovery. Basin Research, 00:1-31.

Millward, D., Young, S. R., Beddoe-Stephens, B., Phillips, E. R., and Evans, C. J. 2002. Gamma-ray, spectral gamma-ray, and neutron-density logs for interpretation of Ordovician volcanic rocks, west Cumbria, England. In: M. Lovell and N. Parkinson, eds., Geological applications of well logs: AAPG Methods in Exploration No. 13, p. 251–268.

Miranda, F., Vettorazzi, A. L., Cunha, P. R. C., Aragão, F. B. Michelon, D., Caldeira, J. L., Porsche, E., Martins, C., Ribeiro, R. B., Vilela, A. F., Corrêa, J. R., Silveira, L. S. & Andreola, K. 2018. Atypical igneous-sedimentary petroleum systems of the Parnaíba Basin, Brazil: seismic, well logs and cores. In: Daly, m. C., Fuck, r. A., Julià, j., Macdonald, d. I. M. & Watts, a. B. (eds) Cratonic Basin Formation: A Case Study of the Parnaíba Basin of Brazil. Geological Society, London, Special Publications, 472.

Mizusaki, A. M. P., Petrini, R., Bellieni, G., Comin-Chiaramonti, P., Dias, J., De Min, A., Picirillo, E. M. 1992. Basalt magmatism along the passive continental margin of SE Brazil (Campos basin). Contributions to Mineralogy and Petrology, 111, 143-160.

Mizusaki, A. M. P. & Mohriak, W. U. 1993. Sequências vulcânico-sedimentares na região da plataforma continental de Cabo Frio. (RJ). Simpósio de Geologia do Sudeste, Rio de Janeiro. p. 52-56.

Mizusaki, A. M. P. & Thomaz Filho, A. 2004. O magmatismo pós-paleozoico no Brasil. In: Mantesso-Neto, V., Bartorelli, A., Carneiro, C. D. R. & Brito-Neves, B. B. (eds) Geologia do Continente Sul-Americano: Evolução da Obra de Fernando Flávio Marques de Almeida. Beca, São Paulo, 281-291.

Mohriak, W.U., Nóbrega, M., Odegard, M.E., Gomes, B.S., Dickson, W.G. 2010. Geological and geophysical interpretation of the Rio Grande Rise, south-eastern Brazilian margin: extensional tectonics and rifting of continental and oceanic crusts. Petroleum Geoscience, 16, 231-245.

Mohriak, W. U. & Fainstein, R. 2012. Phanerozoic regional geology of the eastern Brazilian margin. In: Regional Geology and Tectonics: Phanerozoic Passive Margins, Cratonic Basins and Global Tectonic Maps. 222-282.

Mohriak, W. U. 2020. Genesis and evolution of the South Atlantic volcanic islands offshore Brazil. Geo-Marine Letters, Springer Nature. V.40: 1-33.

Moreira, J. L. P., Esteves, C. A., Rodrigues, J. J. G. & Vasconcelos, C. S. 2006. Magmatismo, sedimentação e estratificação da porção norte da Bacia de Santos. Boletim de Geociências da Petrobrás. v. 14(1), p. 161-170.

Moreira, J. L. P., Madeira, C. V., Gil, J. A. & Machado, M. A. P. 2007. Bacia de Santos. Boletim de Geociências da Petrobras. v. 15(2), p. 531-549.

Morris, A.M., Lambart, S., Stearns, M.A., Bowman, J.R., Jones, M.T., Mohn, G., Andrews, G., Millet, J., Tegner, C., Chatterjee, S., Frieling, J., Guo, P., Jolley, D.W., Cunningham, E.H., Berndt, C., Planke, S., Alvarez Zarikian, C.A., Betlem, P., Brinkhuis, H., Christopoulou, M., Ferré, E., Filina, I.Y., Harper, D.T., Longman, J., Scherer, R.P., Varela, N., Xu, W., Yager, S.L., Agarwal, A., Clementi, V.J. 2024. Evidence for low-pressure crustal anatexis during the Northeast Atlantic break-up. Geochemistry, Geophysics, Geosystems, 25.

Muirhead, D.K., Bowden, S.A.; Parnell, J. & Schofield, N. 2017. Source rock maturation owing to igneous intrusion in rifted margin petroleum systems. Journal of the Geological Society, 174, 979-987.

Nelson, C. E., Jerram, D. A. & Hobbs, R. 2009. Flood basalts facies from borehole data: implications for prospectivity and volcanology in volcanic rifted margins. Petroleum Geoscience. v. 15, p. 313-324.

Nelson, C. E., Jerram, D. A., Clayburn, J. A. P., Halton, A. M. & Roberge, J. 2015. Eocene volcanis in offshore southern Baffin Bay. Marine and Petroleum Geology (67). p. 678-691.

Newsom, H. E., White, W. M., Jochum, K. P., Hofmann, A. W. 1986. Siderophile and chalcophile element abundances in oceanic basalts, Pb isotope evolution and growth of the Earth's core. Earth and Planetary Science Letters, 80, 299-313.

Nielsen, T.K. & Hopper, J.R. 2002. Formation of Volcanic rifted margins: Are temperature anomalies required? Geophysical Research Letters, 29 (21).

Ning, L., Dexing, Q., Qingfeng, L., Hongliang, W., Youshen, F., Lixin, D., Qingfu, F., Kewen, W. 2009. Theory on logging interpretation of igneous rocks and its application. Petroleum Exploration and Development. v: 36(6), 683-692.

Nunes, M. V, Viviers, M. & Lana, C. C. 2004. Bacias Sedimentares Brasileiras: Bacia de Santos. Fundação Paleontológica Phoenix, Aracaju- SE, nº 66, p 1-6.

Oliveira, F. V. C. S. R. S., Gomes, R. T. M., Calonio, L. W., Silva., K. M. S., Carmo, I. O., Bittencourt, B. T., Imbuzeiro, B. M., Silveira, C. S., Silva, C. G., Freire, A. F. M. 2022. Igneability feature: an effective, easy and low-cost way to identify basic igneous rocks using wireline well logs in open hole wells. Brazilian Journal of Geophysics. v.40, 1, 1–32

Oliveira, L.C., Penna, R.M., Rancan, C.C., Carmo, I.O., Marins, G.M. 2024. Seismic interpretation of the Mero Field igneous rocks and its implications for pre- and post-salt CO2 generation – Santos Basin, offshore Brazil. Marine and Petroleum Geology, 163.

Oreiro, S. G. 2006. Magmatismo e sedimentação em uma área na Plataforma Continental de Cabo Frio, Rio de Janeiro, Brasil, no intervalo Cretáceo Superior – Terciário. Boletim de Geociências da Petrobrás, Rio de Janeiro. v.14, n.1, p. 95-112.

Oreiro, S. G., Cupertino, J. A., Szatmari, P. & Thomas Filho, A. 2008. Influence of pre-salt in post-Aptian magmatism in the Cabo Frio High and its surroundings, Santos and Campos basins, SE Brazil: An example of non-plume-related magmatism. Journal of South American Earth Sciences, 25, 116-131.

Osborne, M.J. & Swarbrick, R.E. 1997. Mechanisms for generating overpressure in sedimentary basins: a revaluation. AAPG Bull. 81:1023-1041.

Patiño Douce, A. E. & Beard, J. S. 1995. Dehydration-melting of biotite gneiss and quartz amphibolite from 3 to 15 kbar. Journal of Petrology, 36, 707-738.

Peate, D. W. 1997. The Paraná-Etendeka province. In: Mahoney, J.J. & Coffin, M.F. (Eds.) Largue igneous provinces: continental, oceanic and planetary flood volcanism. USA: Geophysical Monograph Series. p. 438.

Peixoto, P. P. 2004. Estratigrafia e modelagem do preenchimento sedimentar cenozoico em seção na margem sul da bacia de santos. 113p. Tese (Mestrado) – Universidade Federal do Rio Grande do Sul, Porto Alegre.

Pérez-Gussinyé, M. Morgan, J. P., Reston & T. J., Ranero, C. R. 2006. The rift to drift transition at non-volcanic margins: Insights from numerical modelling. Earth and Planetary Science Letters, Amsterdam. v. 244, p. 458–473.

Pérez-Gussinyé, M., Xin, Y., Cunha, T., Ram, R., Andrés-Martínez, M., Dong, D., García-Pintado, J. 2024. Synrift and post-rift thermal evolution of rifted margins: a re-evaluation of classic models of extension. In: Kilhams, B., Holford, S., Gardiner, D., Gozzard, S., Layfield, L., McLean, C., Thackrey, S., Watson, D. (eds) 2024. The Impacts of Igneous Systems on Sedimentary Basins and their Energy Resources. Geological Society, London, Special Publications, 547, 13–38.

Péron-Pinvidic, G. 2010. The formation and evolution of crustal blocks at rifted margins: new insights from the interpretation of the Jan Mayen microcontinent. In: Central & North Atlantic Conjugate Margins Conference, 2., 2010, Lisboa. Extended Abstracts… Lisboa: S.n. v. 5, p. 231–235.

Petrini, R., Civetta, L., Piccirillo, E.M., Bellieni, G., Comin-Chiaramonti, P., Marques, L.S., Melfi, A.J. 1987. Mantle heterogeneity and crustal contamination in the genesis of Low-Ti continental flood basalts from the Paraná Plateau (Brazil): Sr-Nd isotope an geochemical evidence. Journal of Petrology, 28(4), 791-126.

Pezard, P.A. 1990. Electrical Properties of Mid-Ocean Ridge Basalt and implications for the structure of the Upper oceanic crust in Hole 504B. Journal of Geophysical Research. v: 95 (B6), 9237-9264.

Pimentel, N. & Reis, R.P. 2016. Petroleum systems of the West Iberian margin: a review of the Lusitanian Basin and the deep offshore Peniche Basin. Journal of Petroleum Geology, Vol. 39(3), 305-326.

Plank, T. & Langmuir, C.H. 1998. The chemical composition of subducting sediments and its consequences for the crust and mantle. Chemical Geology, 145, 325-394.

Planke, S. 1994. Geophysical response of flood basalts from analysis of wire line logs: Ocean Drilling Program Site 642, Vøring volcanic margin. Journal of Geophysical Research, v. 19, p. 9279-9296.

Plawiak, R.A.B., Carvalho, M.J., Sombra, C.L., Brandão, D.R., Mepen, M., Ferrari, A.L., Gambôa, L.A.P. 2024. Structural controls of the migration of mantle-derived CO2 offshore in the Santos Basin (Southeastern Brazil). Frontiers in Earth Science, 11:1284151.

Poprawa, P., Nejbert, K., Krzywiec, P., Krzeminska, E., Krzeminski, L., Mazur, S., Slaby, E. 2023. Alkaline magmatism from the Lublin-Baltic area of Poland (SW slope of the East European Craton) – Manifestation of hitherto unrecognized early Carboniferous igneous province. Terra Nova. 1-12.

Queiroz, B.S., Valente, S.C., Santos, A.C., Heilbron, M. 2024. Petrophysical and petrographic data correlation and the discrimination of magmatic environments and processes in Santos Basin, offshore SE Brazil. Journal of South American Earth Sciences, 147.

Ran, Q., Wang, Y., Sun, Y., Yan, L., & Tong, M. 2014. Volcanic gas reservoir characterization. Waltham: GPP. Cap. 5, pp. 163-202

Rancan, C. C., Oliveira, L. C., Carmo, I. O., Marins, G. M., Pessoa, V. C. O., Andrade, H., Penatti, A. P. R., Borges, T. A., Silva, R. C. B., Carlotto, M. A., Bassetto, M. & Zanatta, A. S. 2018. Rochas ígneas do bloco de Libra, Bacia de Santos. 49º Congresso Brasileiro de Geologia, Rio de Janeiro.

Ranero, C. R. & Pérez-Gussinyé, M. 2010. Sequential faulting explains the asymmetry and extension discrepancy of conjugate margins. Nature, [S.I.], v. 468, n. 7321, p. 294–299.

Rangel, H. D. 2006. Manifestações magmáticas na parte sul da Bacia de Campos (Área de Cabo Frio) e na Bacia de Jequitinhonha. Boletim de Geociências da Petrobrás, Rio de Janeiro. v.14, n.1, p. 155-160.

Reston, T. J. 2009. The structure, evolution and symmetry of the magma-poor rifted margins of the North and Central Atlantic: A synthesis. Tectonophysics, [Amsterdam], v. 468, n. 1-4, p. 6–27.

Rider, M. 2000. The Geological Interpretation of Well Logs. Second Edition. Rider-French Consulting Ltd, Scotland.

Rigoti, C. A., 2015. Evolução tectônica da bacia de Santos com ênfase na geometria crustal: interpretação integrada de dados de sísmica de reflexão e refração, gravimetria e magnetometria. Dissertação (Mestrado), Universidade do Estado do Rio de Janeiro – Faculdade de Geologia, Rio de Janeiro.

Riley, T. R., Leat, P. T., Curtis, M. L., Millar, L. L. & Fazel, A. 2005. Early-Middle Jurassic dolerite dykes from western Dronning Maud Land (Antarctica): identifying mantle sources in the Karoo large igneous province. Journal of Petrology, 46, 1489–1524.

Rodrigues, L.A. & Sauer, I.L. 2015. Exploratory assessment of the economic gains of a pre-salt oil fiel in Brazil. Energy Policy, 87.

Rollinson, H.R. 1993. Using geochemical data: evaluation, presentation, interpretation. Geochemistry Series. Longman Scientific & Technical.

Rosa, M.B, Cavalcante, J.S.A, Miyakawa, T.M, Freitas, L.C.S. 2018. The giant Lula oil field: world's largest oil production in ultra-deep water under a fast-track development. In: Offshore technology conference, 30 April–3 May, Houston, Texas, USA

Rossetti, L., Lima, E. F., Waichel, B.L., Hole, M.J., Simões, M.S., Scherer, C.M.S. 2018. Lithostratigraphy and volcanology of the Serra Geral Group, Paraná-Etendeka Igneous Province in Southern Brazil: Towards a formal stratigraphical framework. Journal of Volcanology and Geothermal Research. v: 355, 98-114

Rossetti, L. M., Healy, D., Hole, M. J., Millett, J. M., Lima, E. F., Jerram, D. A., Rossetti, M. M. M. 2019. Evaluating petrophysical properties of volcano-sedimentary sequences: A case study in the Paraná-Etendeka Large Igneous Province. Marine and Petroleum Geology. 102. 638-656.

Rudnick, R.L. & Fountain, D.M. 1995. Nature and composition of the continental crust: A lower crustal perspective. Reviews of Geophysics, 33.

Rudnick, R.L. & Gao, S. 2004. Composition of the Continental Crust. The Crust, Treatise on Geochemistry, 3, 17-18.

Sanyal, S. K., Juprasert, S., Jusbasche, M. 1980. An evaluation of a rhyolite-basalt-volcanic ash sequence from well logs. Log Analyst, 21, n. 1, 3-9.

Sawyer, E.W. 1994. Melt segregation in the continental crust. Geology, 22, 1019-1022.

Sawyer, E.W. 2001. Melt segregation in the continental crust: distribution and movement of melt in anatectic rocks. Journal of Metamorphic Geology, 9(3), 291-309.

Schattner, U. & Mahiques, M. M. 2020. Post-rift regional volcanism in southern Santos Basin and the uplift of the adjacent South American coastal range. Journal of South American Earth Sciences. v.104.

Schinteie, R., Ross, A.S., Boreham, C.J., Kempton, R.H., Talukder, A., Trefry, C. 2023. Petroleum source rocks in the Bight Basin, Australia: An updated view. Marine and Petroleum Geology (151).

Schofield, N., Holford, S., Millet, J., Brown, D. Jolley, D., Passey, S.R., Muirhead, D., Grove, C., Magee, C., Murray, J., Hole, M., Joackson, C.A.L., Stevenson, C. 2015. Regional magma plumbing and emplacement mechanism of the Faroe-Shetland Sill Complex: implications for magma transport and petroleum systems within sedimentary basins. Basin Research. 1-23.

Schofield, N., Jerran, D.A., Holford, S., Archer, S., Mark, N., Hartley, A., Howell, J., Muirhead, D.; Green, P., Hutton, D. & Stevenson, C. 2016. Sills in Sedimentary Basins and Petroleum Systems. In: Breitkreuz, C., Rocchi, S. (eds) Physical Geology of Shallow Magmatic Systems. Advances in Volcanology. Springer, Cham., p. 273 – 294.

Schön, J. H. 2015. Physical Properties of Rocks. Elsevier, London, UK.

Scribelk, L. S. & Valente, S. C. 2023. Petrogenesis of Early Cretaceous volcanic rocks in Santos Basin, offshore SE Brazil: evidence for the Tristan da Cunha plume. International Geology Review, DOI: 10.1080/00206814.2023.2201928

Self, S., Keszthelyi, L., & Thordarson, T. 1998. The importance of pahoehoe. Annual Reviews Earth Planet, 26, 81-110.

Senger, K., Millett, J., Planke, S., Ogata, K., Eide, C.H., Festoy, M., Galland, O. & Jerram, D.A. 2017. Effects of igneous intrusions on the petroleum system: a review. First Break, 35 (6), online publication.

Shaw, D.M., Cramer, J.J., Higgins, M.D., Truscott, M.G. 1986. Composition of the Canadian Precambrian shield and the continental crust of the Earth. In: Dawson, J.B., Carswell, D.A., Hall, J., Wedepohl, K.H. (eds). The nature of the lower continental crust. Geological Society Special Publication, 24, 275-282.

Silva, I. G. G., Weis, D. & Scoates, J. S. 2010. Effects of acid leaching on the Sr-Nd-Hf isotopic compositions of ocean island basalts. Geochem. Geophys. Geosyst., 11, Q09011.

Souza, L. M. 2010. Mapeamento Sísmico 3D das rochas vulcânicas terciárias da região do Alto de Cabo frio – Bacia de Campos – RJ. Trabalho de conclusão de curso (Bacharelado em Geofísica) – Universidade Federal Fluminense, Niterói.

Souza, L. S. & Sgarbi, G. N. C. 2019. Bacia de Santos no Brasil: geologia, exploração e produção de petróleo e gás natural. Boletim de Geologia, 41(1), 175-195.

Spacapan, J. B., Palma, O., Galland, O., Senger, K., Ruiz, R., Manceda, R., & Leanza, H. A. 2019. Low resistivity zones at contacts of igneous intrusions emplaced in organic-rich formations and their implications on fluid flow and petroleum systems: A case study in the northern Neuquén Basin, Argentina. Basin Research, 32 (1), 3-24.

Sruoga, P., Rubinstein, N., Hinterewimmer, G. 2004. Porosity and permeability in volcanic rocks: a case study on the Serie Tobífera, South Patagonia, Argentina. Journal of Volcanology and Geothermal Research 132, 31-43.

Stanistreet, I. G. & Charlesworth, E. G. 2001. Damaran basement-cored fold nappes incorporating pre-collisional basins, Kaoko belt, Namibia, and controls on Mesozoic supercontinental break-up. South African Journal of Geology, 104, 1–12.

Stanton, N., Ponte-Neto, C., Bijani, R., Masini, E., Fontes, S., Flexor, J.-M. 2014. A geophysical view of the Southeastern Brazilian margin at Santos Basin: Insights into rifting evolution. Journal of South American Earth Sciences, 55.

Stica, J. M., Zalán, P. V. & Ferrari, A. L. 2014. The evolution of rifting on the volcanic margin of the Pelotas Basin and the contextualization of the Paraná-Etendeka LIP in the separation of Gondwana in the South Atlantic. Marine and Petroleum Geology, [Amsterdam], v. 50, p. 21.

Sun, W., Lou, Y., Lenwoue, A.R.K., Li, Z., Zhu, L., Wu, H. 2022. Classification and evaluation of volcanic rock reservoirs based on the Constraints of Energy Storage Coefficient. Frontiers in Earth Science. 10:914383.

Sun, W., Lou, Y., Lenwoue, A.R.K., Li, Z., Zhu, L., Wu, H. 2022. Classification and evaluation of volcanic rock reservoirs based on the Constraints of Energy Storage Coefficient. Frontiers in Earth Science. 10:914383.

Sutra, E. & Manatschal, G. 2012. How does the continental crust thin in a hyperextended rifted margin? Insights from the Iberia margin. Geology, [S.I.], v. 40, n. 2, p. 139–142.

Szatmari, P., Milani, E.J., Lana, M.C., Conceição, J. & Lobo, A.P. 1985. How South Atlantic rifting affects Brazilian oil reserves distribution. Oil and Gas Journal, 14:107-113.

Szatmari, P. 2000. Habitat of petroleum along the South Atlantic margins. In: Mello, M.R., Katz, B.J. (eds.). Petroleum systems of South Atlantic margins, AAPG Memoir 73:69-75.

Szatmari, P. & Milani, E. 2016. Tectonic control of the oil-rich large igneous-carbonate-salt province of the South Atlantic rift. Marine and Petroleum Geology, 77, 567-596.

Taylor, H.P. 1980. The effects of assimilation of country rocks by magmas on 18O/16O and 87Sr/86Sr systematics in igneous rocks. Earth and Planetary Science Letters, 47, 243-254.

Taylor, S.R. & McLennan, S.M. 1981. The composition and evolution of the continental crust: rare earth element evidence from sedimentary rocks. Phil. Trans. R. Soc., A301, 381-399.

Taylor, S.R., McLennan, S.M., McCulloch, T. 1983. Geochemistry of loess, continental crustal composition and crustal model ages. Geochimica et Cosmochimica Acta, 47, 1897-1905.

Taylor, S.R. & McLennan S.M. 1985, The continental crust: its composition and evolution. Blackwell, Oxford.

Theys, Ph. 1991. Log data acquisition and quality control. Editions Technip, Paris.

Thiede, D. S. & Vasconcelos, P. M. 2010. Paraná flood basalts: rapid extrusion hypothesis confirmed by new 40Ar/39Ar results. Geology, 38, 747–750.

Thomaz Filho, A., Mizusaki, A. M. P., Milani. E. J. & Cesero, P. 2000. Rifting and magmatism associated with the South America and Africa break up. Revista Brasileira de Geociências. 30(1):017-019.

Thomaz Filho, A., Mizusaki, A. M. P., Césero, P. & Leão, J.G. 2005 Hot Spot Volcanic Tracks and their Implications for South American Plate Motion, Campos Basin (Rio de Janeiro state), Brazil. J. South Am. Earth Sci. 18: 383-389

Thomaz Filho, A., Mizusaki, A.M.P. & Antonioli, L. 2008. Magmatismo nas Bacias Sedimentares Brasileiras e sua Influência na Geologia do Petróleo. Revista Brasileira de Geociências. 38:128-137.

Thompson, R. N. 1982. Magmatism of the British Tertiary volcanic province. Scottish Geology, Scotland. 18: 49-107.

Thompson, R. N., Gibson, S. A., Dickin, A. P. & Smith, P. M. 2001. Early Cretaceous basalt and picrite dykes of the southern Etendeka region, NW Namibia: windows into the role of the Tristan mantle plume in Parana-Etendeka magmatism. Journal of Petrology, 42, 2049–2081.

Tiab, D. & Donaldson, E. C. 2003. Petrophysics. 2º Ed. Elsevier.

Trouw, R., Heilbron, M., Ribeiro, A., Paciullo, F., Valeriano, C., Almeida, J. C. H., Tupinambá, M. & Andreis, R. 2000. The Central Segment of The Ribeira Belt. In: Milani, E. J. & Thomás Filho, A. (org) Geotectonics of South America, Int. Geol. Cong., 31. p. 287-310

Tucker, D. S., Scott, K. M. 2009. Structure and facies associated with the flow of subaerial basaltic lava into a deep freswatter lake: The Sulphur Creek lava flow, North Cascades, Washington. Journal of volcanology and Chemical Research. 185, 311-322.

Ukstins, I.A., Renne, P.R., Wolfenden, E., Baker, J., Ayalew, D., Menzies, M. 2002. Matching conjugate volcanic riftes margins: 40Ar/39Ar chrono-stratigraphy of pre- and syn-rift bimodal flood volcanism in Ethiopia and Yemen. Earth and Planetary Science Letters, 198, 289-306.

Valente, S. C., Dutra, T., Heilbron, M., Corval, A. & Szatmari, P. 2009. Litogeoquímica de Diques de Diabásio da Faixa de Colatina, ES. Geochimica Brasiliensis, 23, 177–192.

Valeriano, C.M., Mendes, J., Tupinambá, M., Bongiolo, E.M., Heilbron, M., Junho, M.C.B. 2016. Cambro-Ordovician post-collisional granites of the Ribeira belt, SE-Brazil: A case of terminal magmatism of a hot orogen. Journal of South American Earth Sciences, v. 68, p. 269-281.

Vielzeuf, D. & Holloway, J. R. 1988. Experimental determination of the vapour-absent melting relations in the pelitic system: consequences for crustal differentiation. Contributions to Mineralogy and Petrology, 98, 257–276.

Vital, J.C.S., Ade, M.V.B., Morelatto, R., Lupinacci, W.M. 2023. Compartmentalization and stratigraphic-structural trapping in pr-salt carbonate reservoirs of the Santos basin: A case study in the Iara complex. Marine and Petroleum Geology, 151.

Waichel, B.L., de Lima, E.F., Lubachesky, R., Sommer, C.A., 2006. Pahoehoe flows from the central Paraná Continental Flood Basalts. Bull Volcanol 68, 599–610. https://doi.org/10.1007/s00445-005-0034-5

Waichel, B.L., de Lima, E.F., Sommer, C.A., Lubachesky, R., 2007. Peperite formed by lava flows over sediments: An example from the central Paraná Continental Flood Basalts, Brazil. Journal of Volcanology and Geothermal Research 159, 343–354. https://doi.org/10.1016/j.jvolgeores.2006.07.009

Waichel, B.L., de Lima, E.F., Viana, A.R., Scherer, C.M., Bueno, G.V., Dutra, G., 2012. Stratigraphy and volcanic facies architecture of the Torres Syncline, Southern Brazil, and its role in understanding the Paraná–Etendeka Continental Flood Basalt Province. Journal of Volcanology and Geothermal Research 215–216, 74–82. https://doi.org/10.1016/j.jvolgeores.2011.12.004

Walker, G.P.L. 1971. Compound and simple lava flows and flood basalts. Bull Volcanol 35, 579–590. https://doi.org/10.1007/BF02596829

Walker, G. P. L. 1992. Morphometric study of pillow-size spectrum among pillow lavas. Bulletin of Volcanology, 54, 459-474.

Watton, T. J., Cannon, S., Brown, R. J. Jerram, D. A., Waichel, B. L. 2014. Using formation micro-imaging, wireline logs and onshore analogues to distinguish volcanic lithofacies in borehole: examples from Palaeogene successions in the Faroe-Shetland Basin, NE Atlantic. Geological Society, London, Special Publications, 397, 173-192.

Weaver B. & Tarney, J. 1984. Empirical approach to estimating the composition of the continental crust. Nature, 310, 575-57

Wedepohl, K.H. 1995. The composition of the continental crust. Geochimica et Cosmochimica Acta, 59(7), 1217-1232.

White R. & McKenzie D. J., 1989. Magmatism at Rift Zones: the generation of volcanic continental margins and flood-basalts. J. Geophis. Res., 94(B6):7685-7729

White, J. D. L., McPhie, J., Soule, S. A. 2015. Submarine Lavas and Hyaloclastite. Haraldur Sigurdsson, The Encyclopedia of Volcanoes (Second Edition), Academic Press, 363-375.

Wilson, A.H. 1992. The geology of the Great Dyke, Zimbabwe: crystallization, layering and cumulative formation in the P1 pyroxenite of cyclic unit 1 of the Darwendale Subchamber. Journal of Petrology. v: 33 (3), 611-663.

Winchester, J.A., and Floyd, P.A. 1977. Geochemical discrimination of different magma series and their differentiation products using immobile elements. Chemical Geology, v. 20, p. 325–343.

Winter, W. R., Jahnert, R. J. & França, A. B. 2007. Bacia de Campos. Boletim de Geociências da Petrobras, 15(2), 511-529.

Wolfenden, E., Ebinger, C., Yirgu, G., Renne, P.R., Kelley, S.P. 2005. Geological Society of American Bulletin, 117 (7/8), 846-864.

Wolff, J.A., Ramos, F.C., 2003. Pb isotope variations among Bandelier Tuff feldspar: no evidence for a long-lived silicic magma chamber. Geology 31 (6), 533–536.

Wood, B.J. & Fraser, D.C. 1976. Elementary Thermodynamics for Geologists. Oxford University Press, London.

Workman, R. K., Hart, S. R., Jackson, M., Regelous, M., Farley, K. A., Blusztajn, J., Kurz, M., Staudigel, H. 2004. Recycled metasomatized lithosphere as the origin of the Enriched Mantle II (EM2) end-member: Evidence from the Samoan Volcanic Chain. Geochem. Geophys. Geosyst., 5, Q04008.

Wyllie, M. R. J., Gregory, A. R., & Gardener, L. W. 1956. Elastic wave velocities in heterogeneous and porous media. Geophysics, 21(1): 41-70.

Yang, Y. H., Zhang, H. F., Chu, Z. Y., Xie, L. W., Wu, F. Y., 2010. Combined chemical separation of Lu, Hf, Rb, Sr, Sm and Nd from a single rock digest and precise and accurate isotope determinations of Lu-Hf, Rb-Sr and Sm-Nd isotope systems using Multi-Collector ICP-MS and TIMS. Int. J. Mass Spectrom. 290 (2–3), 120-126.

Yang, Xf., Tian, Zj., Liu, Ym., Zhao, Yb., Zhou, Yb., Ma, Zz., Wang, Dd. 2022. Distribution of pre-salt carbon dioxide and controlling factors of structural styles in offshore Brazil. In: Lin, J. (eds) Proceedings of the International Field Exploration and Development Conference 2022. IFEDC 2022. Springer Series in Geomechanics and Geoengineering. Springer, Singapore

Yelwa, N.A., Mustapha, K.A., Opuwari, M., Qadri, S.M.T., Christanis, K. 2024. Hydrocarbon prospectivity of the South Atlantic Orange Basin. Journal of Sedimentary Environments, 9, 747-789.

Zalán, P. V., Severino, M. C. G., Rigoti, C. A., Magnavita, L. P., Oliveira, J. A, B. & Vianna, A. R. 2011. An Entirely New 3D-View of the Crustal and Mantle Structure of a South Atlantic

Passive Margin – Santos, Campos and Espírito Santo Basins, Brazil. In: Aapg Annual Convention And Exhibition, 2011, Houston, Texas, USA. Expanded abstract. p. 12.

Zao, K., Xu, X., Bachmann, O., Nan, T., Xia, Y. 2023. H2O-controlled eruptive filtering on the bimodality of continental volcanism across tectonic settings. Journal of Petrology. v. 64, 1-15.

Zeng, H.; Loucks, R.G. & Reed, R.M. 2023. Three-dimensional seismic architecture of an Upper Cretaceous volcanic complex and associated carbonate systems; Taylor Group, Elaine field, South Texas, USA. Marine and Petroleum Geology, 155, 106350.

Zhang, C., Liu, D., Liu, Q., Jiang, S., Wang, X., Wang, Y., Ma, C., Wu, A., Zhang, K., Na, Y. 2023. Magmatism and hydrocarbon accumulation in sedimentary basins: A review. Earth-Science Reviews 244, 104531.

Zhixin, W., Hong, X., Zhaoming, W., Zhengjun, H., Chengpeng, S., Xi, C., Yonghua, W. 2016. Classification and hydrocarbon distribution of passive continental margin basins. Petroleum Exploration and Development. 43(5).

Zhu, D., Liu, Q., Meng, Q., Jin, Z. 2018. Enhanced effects of large-scale CO2 transportation on oil accumulation in oil-gas-bearing basins – Implications from supercritical CO2 extraction os source rocks and a typical case study. Marine and Petroleum Geology, 92, 493-504.

Zindler, A. & Hart, S. 1986. Chemical Geodynamics. Annual Reviews Earth Planetary Science. 14: 493-571.

Zou, C., Zhang, G., Zhu, R., Yuan, X., Zhao, X., Hou, L., Wen, B., Wu, X. 2013. Volcanic Reservoirs in Petroleum Exploration. Elsevier.

APÊNDICE A - Interpretação petrofísica (Poço 6-BG-6P-SPS)

Perfil composto do poço 6-BG-6P-SPS com fluxos de derrame inferidos a partir da interpretação das ferramentas petrofísicas.

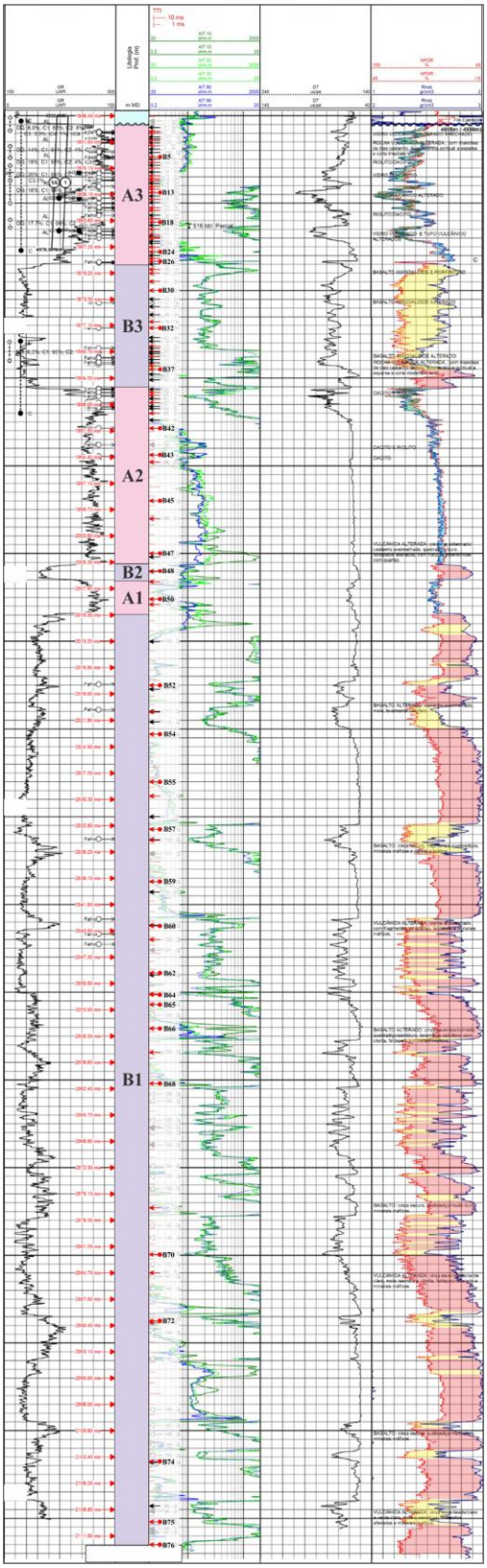

As setas indicam a localização de cada amostra (seta preta para amostras que foram descritas apenas em escala macroscópica; seta vermelha para descrições macroscópicas e microscópicas, círculo vermelho para amostras com análise litogeoquímica). As litologias e descrições apresentadas no perfil podem contrastar com as definidas no estudo.

Nas seções A1, A2 e A3, os intervalos hachurados em verde indicam vulcanismo explosivo, e os hachurados em azul indicam vulcanismo efusivo, Nas seções B1, B2 e B3, os intervalos hachurados em amarelo indicam as porções amigdaloidais do derrame efusivo máfico, enquanto os intervalos hachurados em vermelho indicam as porções maciças do derrame.

APÊNDICE B - Dados petrográficos (macroscópicos e microscópicos)

A lista a seguir apresenta o link com as descrições macroscópicas e microscópicas de todas as amostras estudadas dos poços 6-BG-6P-SPS, 3-BRSA-1267A-RJS e 1-BRSA-886-RJS. O link direciona à página da Plataforma LabMEG referente à cada amostra. Amostras apenas com descrições macroscópicas foram codificadas como Macro-.

Poço	Seção	Código	Link
6-BG-6P-SPS	A3	Macro1	http://labmeg.com/amostra/2718
		B1	http://labmeg.com/amostra/2719
		B2	http://labmeg.com/amostra/2720
		Macro2	http://labmeg.com/amostra/2830
		Macro3	http://labmeg.com/amostra/2832
		B3	http://labmeg.com/amostra/2831
		Macro4	http://labmeg.com/amostra/2827
		B4	http://labmeg.com/amostra/2721
		Macro5	http://labmeg.com/amostra/2722
		Macro6	http://labmeg.com/amostra/2828
		B5	http://labmeg.com/amostra/2833
		Macro7	http://labmeg.com/amostra/2724
		B6	http://labmeg.com/amostra/2725
		Macro8	http://labmeg.com/amostra/2834
		B7	http://labmeg.com/amostra/2726
		Macro9	http://labmeg.com/amostra/2727
		B8	http://labmeg.com/amostra/2729
		B9	http://labmeg.com/amostra/2730
		B10	http://labmeg.com/amostra/2835
		Macro10	http://labmeg.com/amostra/2731
		B11	http://labmeg.com/amostra/2836
		B12	http://labmeg.com/amostra/2732
		B13	http://labmeg.com/amostra/2733
		Macro11	http://labmeg.com/amostra/2837
		Macro12	http://labmeg.com/amostra/2734
		B14	http://labmeg.com/amostra/2736
		Macro13	http://labmeg.com/amostra/2737
		B15	http://labmeg.com/amostra/2838
		B16	http://labmeg.com/amostra/2839
		Macro14	http://labmeg.com/amostra/2738
		B17	http://labmeg.com/amostra/2840
		B18	http://labmeg.com/amostra/2841
		Macro15	http://labmeg.com/amostra/2739
		B19	http://labmeg.com/amostra/2842
		B20	http://labmeg.com/amostra/2740
		Macro16	http://labmeg.com/amostra/2741
		B21	http://labmeg.com/amostra/2743
		B22	http://labmeg.com/amostra/2742
		Macro17	http://labmeg.com/amostra/2744
		Macro18	http://labmeg.com/amostra/2829

Poço	Seção		Código	Link
6-BG-6P-SPS	B3		B23	http://labmeg.com/amostra/2745
			B24	http://labmeg.com/amostra/2746
			Macro19	http://labmeg.com/amostra/2747
			B25	http://labmeg.com/amostra/2843
			B26	http://labmeg.com/amostra/2748
			Macro20	http://labmeg.com/amostra/2749
			B27	http://labmeg.com/amostra/2750
			B28	http://labmeg.com/amostra/2751
			B29	http://labmeg.com/amostra/2844
			B30	http://labmeg.com/amostra/2845
			Macro21	http://labmeg.com/amostra/2752
			Macro22	http://labmeg.com/amostra/2753
			Macro23	http://labmeg.com/amostra/2754
			B31	http://labmeg.com/amostra/2755
			B32	http://labmeg.com/amostra/2756
			Macro24	http://labmeg.com/amostra/2757
			Macro25	http://labmeg.com/amostra/2758
			B33	http://labmeg.com/amostra/2759
			Macro26	http://labmeg.com/amostra/2760
			B34	http://labmeg.com/amostra/2761
			Macro27	http://labmeg.com/amostra/2762
			Macro28	http://labmeg.com/amostra/2763
			B35	http://labmeg.com/amostra/2764
			Macro29	http://labmeg.com/amostra/2765
			Macro30	http://labmeg.com/amostra/2766
			B36	http://labmeg.com/amostra/2767
			B37	http://labmeg.com/amostra/2846
			Macro31	http://labmeg.com/amostra/2847
			Macro32	http://labmeg.com/amostra/2768
	A2	Seção AF - Artigo 1	Macro33	http://labmeg.com/amostra/2769
			B38	http://labmeg.com/amostra/2770
			B39	http://labmeg.com/amostra/2771
			Macro34	http://labmeg.com/amostra/2826
			B40	http://labmeg.com/amostra/2772
			Macro35	http://labmeg.com/amostra/2773
			Macro36	http://labmeg.com/amostra/2774
			B41	http://labmeg.com/amostra/2775
			Macro37	http://labmeg.com/amostra/2776
			B42	http://labmeg.com/amostra/2777
			Macro38	http://labmeg.com/amostra/2778
			B43	http://labmeg.com/amostra/2848
			B44	http://labmeg.com/amostra/2782
			B45	http://labmeg.com/amostra/2779
			B46	http://labmeg.com/amostra/2780
			B47	http://labmeg.com/amostra/2781

Poço	Seção		Código	Link
6-BG-6P-SPS	B2		Macro39	http://labmeg.com/amostra/2783
			B48	http://labmeg.com/amostra/2785
			Macro40	http://labmeg.com/amostra/2784
			B49	http://labmeg.com/amostra/2786
	A1		B50	http://labmeg.com/amostra/2787
			B51	http://labmeg.com/amostra/2795
	B1		Macro41	http://labmeg.com/amostra/2788
			B52	http://labmeg.com/amostra/2789
			Macro42	http://labmeg.com/amostra/2790
		Seção AM - Artigo 1	Macro43	http://labmeg.com/amostra/2793
			B53	http://labmeg.com/amostra/2791
			Macro44	http://labmeg.com/amostra/2792
			B54	http://labmeg.com/amostra/2794
			B55	http://labmeg.com/amostra/2954
			B56	http://labmeg.com/amostra/2796
			Macro45	http://labmeg.com/amostra/2797
			B57	http://labmeg.com/amostra/2798
			B58	http://labmeg.com/amostra/2849
			Macro46	http://labmeg.com/amostra/2799
			Macro47	http://labmeg.com/amostra/2800
			B59	http://labmeg.com/amostra/2801
			Macro48	http://labmeg.com/amostra/2802
			Macro49	http://labmeg.com/amostra/2803
			B60	http://labmeg.com/amostra/2804
			B61	http://labmeg.com/amostra/2805
			B62	http://labmeg.com/amostra/2806
			Macro50	http://labmeg.com/amostra/2807
			B63	http://labmeg.com/amostra/2808
			B64	http://labmeg.com/amostra/2809
			B65	http://labmeg.com/amostra/2810
			B66	http://labmeg.com/amostra/2811
			B67	http://labmeg.com/amostra/2812
			B68	http://labmeg.com/amostra/2813
			B69	http://labmeg.com/amostra/2816
			B70	http://labmeg.com/amostra/2817
			B71	http://labmeg.com/amostra/2818
			B72	http://labmeg.com/amostra/2819
			B73	http://labmeg.com/amostra/2820
			B74	http://labmeg.com/amostra/2822
			Macro51	http://labmeg.com/amostra/2821
			Macro52	http://labmeg.com/amostra/2823
			B75	http://labmeg.com/amostra/2824
			Macro53	http://labmeg.com/amostra/2955
			Macro54	http://labmeg.com/amostra/2850
			B76	http://labmeg.com/amostra/2825

Poço	Seção	Código	Link
3-BRSA-1267A-RJS	B - Artigo 1	L13	http://labmeg.com/amostra/3253
		L14	http://labmeg.com/amostra/3254
		L15	http://labmeg.com/amostra/3255
		L16	http://labmeg.com/amostra/3256
		L17	http://labmeg.com/amostra/3257
		L18	http://labmeg.com/amostra/3258
		L19	http://labmeg.com/amostra/3259
		L20	http://labmeg.com/amostra/3262
		L21	http://labmeg.com/amostra/3263
		L22	http://labmeg.com/amostra/3264
1-BRSA-886-RJS	C - Artigo 1	C1	http://labmeg.com/amostra/3886
		C2	http://labmeg.com/amostra/3887
		C3	http://labmeg.com/amostra/3888
		C4	http://labmeg.com/amostra/3889
		C5	http://labmeg.com/amostra/3890
		C6	http://labmeg.com/amostra/3891
		C7	http://labmeg.com/amostra/3892
		C8	http://labmeg.com/amostra/3893
		C9	http://labmeg.com/amostra/3894
		C10	http://labmeg.com/amostra/3895
		C11	http://labmeg.com/amostra/3896

APÊNDICE C - Precisão e acurácia

Limites de detecção, acurácia e precisão de elementos maiores (em %peso) e elementos traço (em ppm). $Fe_2O_3^t$ é ferro total como ferro férrico. Med é medido; Cert é certificado; Orig é original; Dup é duplicata. A acurácia média de MnO, K_2O e P_2O_5 foi descartada devido ao desvio padrão.

Análise	SiO_2	TiO_2	Al_2O_3	$Fe_2O_3^t$	MnO	MgO	CaO	Na_2O	K_2O	P_2O_5	Total	Ni	Cr	Co	Sc	V	Ba	Rb	Sr	Y	Zr	Nb
Limite de detecção	0,01	0,001	0,01	0,01	0,001	0,01	0,01	0,01	0,01	0,01	0,01	20	20	1	1	5	2	1	2	0,5	1	0,2
DNC-1 Med	47,1	0,47	18,04	9,75	0,15	10,02	11,48	1,92	0,22	0,07					31	156	104		143		31	
DNC-1 Cert	47,15	0,48	18,34	9,97	0,15	10,13	11,49	1,89	0,234	0,07					31	148	118		144		38	
Acurácia (%)	0,1	2,1	1,6	2,2	0,0	1,1	0,1	1,6	6,0	0,0					0,0	5,4	11,9		0,7		18,4	
BIR-1a Med	48,62	0,96	15,44	11,15	0,17	9,72	13,56	1,88	0,02	0,03		180	400	54	44	341	8		110	15,3	13	
BIR-1a Cert	47,96	0,96	15,5	11,3	0,175	9,7	13,3	1,82	0,03	0,021		170	370	52	44	310	6		110	16	18	
Acurácia (%)	1,4	0,0	0,4	1,3	2,9	0,2	2,0	3,3	33,3	42,9		5,9	8,1	3,8	0,0	10,0	33,3		0,0	4,4	27,8	
W-2b Med	53,21	1,1	15,89	10,9	0,17	6,41	11,09	2,3	0,62	0,14		70	90	45	35	281	180	20	199	21	81	7,5
W-2b Cert	52,4	1,06	15,4	10,7	0,163	6,37	10,9	2,14	0,626	0,14		70	92	43	36	262	182	21	190	24	94	7,9
Acurácia (%)	1,5	3,8	3,2	1,9	4,3	0,6	1,7	7,5	1,0	0,0		0,0	2,2	4,7	2,8	7,3	1,1	4,8	4,7	12,5	13,8	5,1
Média da acurácia	1,0	2,0	1,7	1,8	-	0,6	1,3	4,1	-	-		2,9	5,1	4,2	0,9	7,6	15,4	4,8	1,8	8,4	20,0	5,1
B5 Orig	73,74	0,216	10,87	1,39	0,039	0,78	1,74	0,74	4,77	0,02	98,89	< 20	< 20	1	3	10	668	139	145	41,7	288	26,1
B5 Dup	74,37	0,211	10,61	1,31	0,039	0,76	1,75	0,7	4,61	< 0,01	98,97	< 20	< 20	1	2	10	644	142	139	41,5	284	27,6
Precisão (%)	0,8	2,4	2,5	6,1	0,0	2,6	0,6	5,7	3,5	-	0,1	-	-	0,0	50,0	0,0	3,7	2,1	4,3	0,5	1,4	5,4
B76 Orig	47,51	1,561	14,45	13,18	0,365	7,43	4,48	2,04	4,34	0,17	99,42	60	130	42	35	330	5149	111	378	26,9	108	9,9
B76 Dup	47,68	1,584	14,77	13,23	0,364	7,46	4,47	2,06	4,35	0,18	100,1	50	110	40	35	332	5177	106	386	25,2	109	9,2
Precisão (%)	0,4	1,5	2,2	0,4	0,3	0,4	0,2	1,0	0,2	5,6	0,7	20,0	18,2	5,0	0,0	0,6	0,5	4,7	2,1	6,7	0,9	7,6
Media da precisão	0,6	1,9	2,3	3,2	0,1	1,5	0,4	3,3	1,9	5,6	0,4	20,0	18,2	2,5	25,0	0,3	2,1	3,4	3,2	3,6	1,2	6,5

Análise	La	Ce	Pr	Nd	Sm	Eu	Gd	Tb	Dy	Ho	Er	Tm	Yb	Lu	Hf	Pb	Ta	Th	U
Limite de detecção	0,05	0,05	0,01	0,05	0,01	0,005	0,01	0,01	0,01	0,01	0,01	0,005	0,01	0,002	0,1	5	0,01	0,05	0,01
DNC-1 Med																			
DNC-1 Cert																			
Acurácia (%)																			
BIR-1a Med	0,7	2,1		2,4	1,2	0,54	1,9						1,8	0,26	0,6	< 5			
BIR-1a Cert	0,63	1,9		2,5	1,1	0,55	2						1,7	0,3	0,6	3			
Acurácia (%)	11,1	10,5		4,0	9,1	1,8	5,0						5,9	13,3	0,0	-			
W-2b Med	11	24,7		13,6	3,4			0,66		0,79	2,3	0,35	2,2	0,32	2,5		0,61	2,3	0,51
W-2b Cert	10	23		13	3,3			0,63		0,76	2,5	0,38	2,1	0,33	2,6		0,5	2,4	0,53
Acurácia (%)	10,0	7,4		4,6	3,0			4,8		3,9	8,0	7,9	4,8	3,0	3,8		22,0	4,2	3,8
Média da acurácia	10,6	9,0		4,3	6,1	1,8	5,0	4,8		3,9	8,0	7,9	5,3	8,2	1,9		22,0	4,2	3,8
B5 Orig	57,8	85,6	7,83	25,8	4,72	0,853	5,19	1,06	7,22	1,57	4,9	0,713	4,66	0,756	6,8	15		21,8	3,29
B5 Dup	56,9	84,5	7,63	25,8	4,97	0,809	5,11	1,03	7,18	1,58	4,69	0,708	4,88	0,793	7	17	2,29	21,7	3,32
Precisão (%)	1,6	1,3	2,6	0,0	5,0	5,4	1,6	2,9	0,6	0,6	4,5	0,7	4,5	4,7	2,9	11,8	100,0	0,5	0,9
B76 Orig	13,5	32,1	4,24	19,4	4,69	1,61	5,06	0,84	5,12	0,99	2,73	0,394	2,44	0,358	3,1	7	0,73	1,67	0,38
B76 Dup	12,3	30	3,76	18,1	4,15	1,49	4,54	0,81	4,52	0,93	2,69	0,388	2,62	0,405	3	5	0,71	1,54	0,3
Precisão (%)	9,8	7,0	12,8	7,2	13,0	8,1	11,5	3,7	13,3	6,5	1,5	1,5	6,9	11,6	3,3	40,0	2,8	8,4	26,7
Media da precisão	5,7	4,2	7,7	3,6	9,0	6,7	6,5	3,3	6,9	3,5	3,0	1,1	5,7	8,1	3,1	25,9	51,4	4,5	13,8

APÊNDICE D - Dados geocronológicos de U-Pb *in situ*

O leitor deve consultar a planilha Excel via abaixo para acesso aos dados:
(https://docs.google.com/spreadsheets/d/1VpgT6GVs5VzvVck4EamKL7y6N_uOsc6O/edit?usp=sharing&ouid=102535274687644767604&rtpof=true&sd=true)

APÊNDICE E - Dados estatísticos

Média, desvio padrão (DP), valores máximos e mínimos para elementos maiores das amostras básicas, intermediárias e acidas são apresentados abaixo. Elementos maiores em %peso; LOI é Perda ao Fogo (*Loss On Ignition*); $Fe_2O_3^t$ é ferro total como ferro férrico; N = número de amostras.

Amostras básicas (N = 19)	**SiO_2**	**TiO_2**	**Al_2O_3**	**$Fe_2O_3^t$**	**MnO**	**MgO**	**CaO**	**Na_2O**	**K_2O**	**P_2O_5**	**LOI**	**Total**
Média	50,11	1,63	13,94	12,46	0,22	6,10	6,32	3,25	2,56	0,17	3,05	99,95
DP	2,61	0,38	0,88	1,51	0,05	1,77	2,15	1,00	1,24	0,05	1,81	0,60
Máximo	54,40	3,09	15,28	14,92	0,36	10,47	9,21	5,51	4,70	0,37	7,17	100,80
Mínimo	43,55	1,29	12,14	9,09	0,15	3,34	1,61	2,05	0,58	0,13	1,45	99,00

Amostras ácidas e intermediárias (N = 10)	**SiO_2**	**TiO_2**	**Al_2O_3**	**$Fe_2O_3^t$**	**MnO**	**MgO**	**CaO**	**Na_2O**	**K_2O**	**P_2O_5**	**LOI**	**Total**
Média	65,62	0,50	12,19	5,68	0,05	0,80	2,37	1,49	5,34	0,09	4,21	99,04
DP	4,92	0,47	1,39	2,64	0,01	0,67	0,91	1,12	1,13	0,10	2,07	0,74
Máximo	74,05	1,53	14,23	9,69	0,08	2,59	3,87	4,11	7,31	0,29	9,07	100,40
Mínimo	58,74	0,21	9,71	1,35	0,04	0,37	1,18	0,70	3,48	0,01	2,15	98,29

APÊNDICE F - Norma CIPW

Quantidade calculada de nefelina (Ne) normativa, hiperstênio (Hy), olivina (Ol) e quatzo (Q) para as amostras do poço 6-BG-6P-SPS na Bacia de Santos. As razões de ferro são de acordo com Middlemost (1989).

Sample	Section	Total	(Ne)	(Hy)	(Ol)	(Q)
B30	**B3**	99,13		8,81	18,05	
B32	**B3**	99,16		15,88	12,76	
B48	**B2**	99,20		3,47		1,54
B52	**B1**	99,33		25,00		1,98
B54	**B1**	99,34		10,87		4,28
B55	**B1**	99,25		9,87		1,80
B57	**B1**	99,17		3,04	13,32	
B59	**B1**	99,26		11,74		1,40
B60	**B1**	99,25		3,32	7,62	
B62	**B1**	99,37		6,20	5,39	
B64	**B1**	99,37		6,56		0,69
B65	**B1**	99,26		7,34	2,86	
B66	**B1**	99,29		9,81		0,83
B68	**B1**	99,36		8,12	4,48	
B70	**B1**	99,46	0,15		6,10	
B72	**B1**	99,30		11,41	4,33	
B74	**B1**	99,28		5,71	5,17	
B75	**B1**	99,46		10,77	1,58	
B76	**B1**	99,20		12,77	8,07	

APÊNDICE G - Modelagem de processos evolutivos - AFC

O leitor deve consultar a planilha Excel via abaixo para acesso aos dados:
(https://docs.google.com/spreadsheets/d/1nLi-TTM5ov_cGcoHpisN_Cd8gXej4nQk/edit?usp=sharing&ouid=102535274687644767604&rtpof=true&sd=true)

APÊNDICE H - Modelagem de fusão crustal

O leitor deve consultar a planilha Excel via abaixo para acesso aos dados:
(https://docs.google.com/spreadsheets/d/1O7htr4LNL5pEgVIKZ_A5QOyom__3eKMO/edit?usp=sharing&ouid=102535274687644767604&rtpof=true&sd=true)

APÊNDICE I - Modelagem de fusão mantélica

O leitor deve consultar a planilha Excel via abaixo para acesso aos dados:
(https://docs.google.com/spreadsheets/d/1XT3332-v1cOWySxQLhw2sHEd3_IfYbFU/edit?usp=sharing&ouid=102535274687644767604&rtpof=true&sd=true)